‎&EPA

Remote Monitoring of Gaseous Pollutants by Differential Absorption Laser Techniques

RESEARCH REPORTING SERIES

Research reports of the Office of Research and Development, U.S. Environmental Protection Agency, have been grouped into nine series. These nine broad categories were established to facilitate further development and application of environmental technology. Elimination of traditional grouping was consciously planned to foster technology transfer and a maximum interface in related fields. The nine series are:

1. Environmental Health Effects Research

2. Environmental Protection Technology

3. Ecological Research

4. Environmental Monitoring

5. Socioeconomic Environmental Studies

6. Scientific and Technical Assessment Reports (STAR)

7. Interagency Energy-Environment Research and Development

8. "Special" Reports

9. Miscellaneous Reports

This report has been assigned to the ENVIRONMENTAL PROTECTION TECH-NOLOGY series. This series describes research performed to develop and demonstrate instrumentation, equipment, and methodology to repair or prevent environmental degradation from point and non-point sources of pollution. This work provides the new or improved technology required for the control and treatment of pollution sources to meet environmental quality standards.

REMOTE MONITORING OF GASEOUS POLLUTANTS
BY DIFFERENTIAL ABSORPTION LASER TECHNIQUES

by

S. A. Ahmed, J. S. Gergely, and F. Barone
Electrical Engineering Department
The City College of the City University
140th Street and Convent Avenue
New York, New York 10031

Project Officer

ENVIRONMENTAL SCIENCES RESEARCH LABORATORY
OFFICE OF RESEARCH AND DEVELOPMENT
U.S. ENVIRONMENTAL PROTECTION AGENCY
RESEARCH TRIANGLE PARK N.C. 27711

DISCLAIMER

This report has been reviewed by the Environmental Sciences Research Laboratory, U.S. Environmental Protection Agency, and approved for publication. Approval does not signify that the contents necessarily reflect the views and policies of the U.S. Environmental Protection Agency, nor does mention of trade names or commercial products constitute endorsement or recommendation for use.

ABSTRACT

A single-ended laser radar (LIDAR) system was designed, built, and successfully operated to measure range-resolved concentrations of NO_2, SO_2, and O_3 in the atmosphere using a Differential Absorption of Scattered Energy (DASE) LIDAR technique. The system used a flash-lamp pumped dye laser as the primary source of laser energy. For the NO_2 measurements, the dye laser output was used directly in a novel simultaneous two wavelength output mode in which two wavelengths, one on and one off the resonance absorption of NO_2 molecules are transmitted simultaneously and the relative attenuation determined for the two backscattered signals detected. This mode of operation effectively reduces errors due to scintillation and aerosol drift. For the SO_2 and O_3 measurements, it was necessary to frequency double the output of the dye laser to match the absorption spectra of the SO_2 and O_3 molecules. Field measurements, which were carried out over the Upper East Side of Manhattan for all three pollutants, produced range-resolved concentrations at ranges of over two kilometers. The ambient pollutant concentrations measured ranged from 0.04 ppm to 0.31 ppm, depending on location and time of day. In general, these showed reasonably good correlation with measurements obtained from conventional pollution monitoring stations in the area and demonstrated the potential of DASE LIDAR systems for range-resolved ambient pollutant measurements.

CONTENTS

LIST OF FIGURES

LIST OF TABLES

CHAPTER 1   INTRODUCTION AND BACKGROUND

1.1 The Need for Effective Pollution Monitoring

The adverse effects of pollution on health are well known, and
hence the need for effectively monitoring such pollution in heavily
populated areas is apparent.[1]

The use of lasers for atmospheric pollution monitoring has re-
ceived considerable attention.[2-5,19] The potential advantages of
using lasers for this purpose are simple in essence.

Existing methods for monitoring air pollution utilize fixed-site
chemical stations. However, to effectively cover a large metropolitan
area, such as that of New York City, very many fixed-site stations are
required with attendant expenses. In addition, such stations only
provide information in their immediate vicinity and not in the air
between or above them.

Optimally, the intelligent planning of selective and more local-
ized pollution control measures, which would be less disruptive than
general ones, would require a three-dimensional pollution map of the
area. Moreover, it should ideally, instantaneously reflect changes in
conditions. An additional desirable goal would be the ability to track
moving clouds of pollutants.

Greatly increasing the number of fixed-site monitoring stations and
using aircraft sample collections would be prohibitively expensive
methods for attaining these goals. It is for these reasons that laser
monitoring schemes, with their potential ability to instantaneously and
remotely determine pollutant concentration and spatial distribution.

1.2 Background

1.2.1 Introduction

LIDAR, an acronym for Light Detection and Ranging, was the name given to laser ranging systems. The first recorded backscattered echoes from the atmosphere were reported in 1963 by Ficco and Smullin, and by Ligada, who measured backscattered signals from haze.[6,7] Since then, research and development have concentrated on developing LIDAR into an effective method for air pollution monitoring.

1.2.2 Raman

Raman scattering was first used to detect molecular constituents of the atmosphere in 1967 by Leonard, Cooney, and Melfi.[8-10] Later, Inaba and Kobayashi discussed the possibility of pollution detection by Raman scattering, and subsequently remotely detected SO_2 and CO_2 in the atmosphere.[11,12] Unfortunately, the pollution detection sensitivity that the Raman scheme offers is not adequate for trace contaminant measurements typically found in polluted urban areas. However, considerable effort has been directed to monitor water vapor and major atmospheric constituents using the Raman scattering method.[13-15]

An advantage of the Raman scheme is that a single frequency laser can be used as a source to obtain the Raman backscatter from the constituents of interest. On the other hand, Raman schemes are greatly limited in their attainable sensitivities by the relatively small Raman scattering cross sections.

Using a nitrogen laser operating at 3371 Å at 20 KW peak power 10 ns halfwidth at 50 HZ, Kobayashi and Inaba (1971) have detected Raman sig-

nals from clear air and from an oil smoke plume.[3] The reveiving system consisted of a 30 cm diameter telescope followed by an f/8.5 half meter grating monochrometer and spectral interference filter. They were able to show the presence of H_2O, CH_4, H_2S, CO, NO, and SO_2 in the oil smoke plume at a distance of 30 m.

Progress in laser sources led to improvement in Raman detection systems. Thus, in 1973 Hirschfeld described a system using a frequency doubled Ruby laser transmitter with a 3 m aperture telescope as the receiver.[16] This was used in field tests to detect CO_2, H_2O, and SO_2 over a 200 m range. Concentrations of approximately 10^4 ppm of water vapor, 310 ppm of CO_2, and 300 ppm of SO_2 were detectable. The SO_2 was dispersed in controlled amounts to create detectable plumes for monitoring. The SO_2 concentration is of course much higher than those present in ambient conditions.

The 2 j, 2 HZ Ruby laser source was doubled in KDP with 8 percent efficiency and the returned signal was processed by photon counting techniques referenced against the nitrogen system and probably represents the state of the art for sensitivity and range.[17,18]

The advent of tunable dye lasers opened possibilities for other LIDAR pollution detection methods with inherent advantages over the Raman scheme.[2] The four LIDAR schemes for which tunable dye lasers are particularly important and that presently appear to be the most promising for the detection of molecular pollutants with resonant absorption in the visible and near ultraviolet are: resonance Raman, long path absorption, resonance fluorescence, and differential absorption of scattered energy (DASE).

1.2.3 Resonance Raman

Observations of resonance Raman scattering in gases have been very few. Bernstein (1973) measured resonant Raman enhancements in gaseous Cl_2, Br_2, and I_2. He obtained intensities of 10 to 1000 times stronger than the normal Raman effect.[72]

Rosen (1975) estimated the feasibility of using resonance Raman scattering for the remote detection of pollutants.[73] He estimated that for 10^4 pulses of 0.05 mj each, 100 ppm of NO_2 and 10 ppm of SO_2 could be detected at 1 km at night, and 100 ppm of NO could be detected during daytime. These are for a signal to noise ratio of 10. These concentrations are 3 to 4 orders of magnitude higher than ambient pollution concentrations encountered.

1.2.4 Long Path Absorption

Hanst (1968) described the measurement of average pollutant concentration along a laser beam path by laser resonance absorption.[20,21] More recently, Zaromb (1969), Nakahara and Ito (1970), Inomota and Igarashi (1972), and Hodgeson, McClenney and Hanst (1973), suggested the long path absorption scheme for determining average pollutant densities.[22-25] Kidal and Byer have given a detailed analysis of the doubled-ended long path absorption method.[2] This analysis was later extended to the single ended absorption method using topographical targets by Byer and Garbuny.[26]

To determine the average pollutant density along a laser beam path, absorption measurements have been carried out using low power diode lasers by Hinkley (1970).[27-29] Using a $Pb_{0.88}Sn_{0.12}Te$ diode laser mounted onto a cold-finger of a cryogenic Dewar, concentrations ranging

from 74 to 1000 ppm of C_2H_4 in N_2 were detected in a laboratory in a sample chamber 30 cm long. Similar experiments were carried out by Snowman using a CO_2 laser.[30]

More recently, O'Shea and Dodge (1974) measured NO_2 absorption coefficients for the most prominent argon-ion laser lines.[31] Measurements using the long path absorption of argon-ion lines by NO_2 in an urban atmosphere were carried out. A corner cube reflector was positioned 3.54 km from the laser site to reflect the laser signal back to the receiver. Integrated pollutant concentrations ranging from 0.05 ppm to 0.15 ppm of NO_2 were detected.

The topographical single ended absorption method was first demonstrated by Henningsen, Garbuny and Byer in 1974.[32] The transmitter consisted of a CaLaSOAP:Nd laser source electro-optically Q-switched and operated in a TEM_{00} mode with 10 mj/pulse output energy at 1.06 um.

The 1.06 um output from the laser was frequency doubled in a 2 cm long CDA crystal with an efficiency of 25 percent. The output from the frequency doubler was focused into a temperature-tuned $LiNbO_3$ parametric oscillator. An etalon within the laser cavity was fine tuned piezoelectrically which allowed the infrared frequency to be tuned on and off a resonance peak of CO.

Using a wooded area as a topographical target a concentration of 47 ppm of CO was detected at a range of 107 m. The CO was released from containers situated below the laser beam path.

1.2.5 Resonance Fluorescence

In 1969, Bowman, Gibson and Sandford used a flashlamp-pumped dye

laser tuned by a tilted Fabry-Perot interferometer to obtain nighttime measurements of sodium in the upper atmosphere.[33] The output of the dye laser was used to induce fluorescence from sodium at altitudes up to 150 km. Concentrations ranging from 1.8×10^{14} m^{-2} to 9×10^{12} m^{-2} were detected at altitudes of 80 to 100 km.

By 1970, regular measurements were being made of the sodium double layer at 90 km altitude.[34] Since that time, observations of the sodium layer have been numerous.[35-39] In 1972, Gibson and Sandford extended the use of the resonance fluorescence scheme into daytime operation by using a narrow band optical receiver.[40,41]

The use of resonance fluorescence backscattering for probing the troposphere has been limited. However, the method has been extensively analyzed by Kidal and Byer, and by C.M. Penny.[2,42] Resonance backscattering also has been discussed by ourselves, Kobayashi and Inaba, and Measures and Pilon.[44,3,43]

In 1972, Gelbwachs utilized resonance fluorescence of NO_2 excited by an argon-ion laser to detect NO_2 locally with a sensitivity of one part per billion.[45] The laser excitation was at 4480 Å and the fluorescence was monitored at 7000 to 8000 Å. Local Los Angeles air, drawn through filters, was monitored, and NO_2 variations measured over a period of a few hours showed concentrations ranging from 0.03 ppm to 0.1 ppm. Filtering was necessary to eliminate interferring fluorescence from particulates in the air.

The increased sensitivity of resonance fluorescence backscattering makes it appear useful as a remote monitoring method compared to the Raman method. As will be shown later, the sensitivity of the resonance

6

fluorescence scheme is greatly surpassed by the differential absorption of scattered energy method (DASE).

1.2.6 Differential Absorption of Scattered Energy (DASE)

The DASE method was first suggested by Schotland in 1964 using a searchlight as a source.[46] The method was recently extended to LIDAR pollution monitoring by Ahmed and Gergely, Igarashi, and others.[47,50,2, 26,43,48,49]

The earliest experimental work was performed by Schotland who used a temperature tuned Ruby laser to measure the water vapor vertical profile by the DASE method.[46] DASE measurements in the atmosphere were first reported by ourselves and by Igarashi.[47,50] DASE measurements also were later reported by Rothe, Brinkman and Walther of Cologne, Germany.[51,53] Calibration measurements of the differential absorption method were made by Grant et al.[52] Using a flashlamp-pumped dye laser operating near 4450 Å at 4 to 8 mj pulse energy, they measured NO_2 of known concentration in a sample chamber.

The DASE system with its superior operating capabilities is the topic of interest in this work and a detailed theoretical comparison between the aforementioned LIDAR schemes is given in Chp. 2.

1.3 Summary and Outline of This Study

The tasks accomplished are summarized below:

1. The basic laser radar system was designed built and tested. It consists of a flashlamp-pumped dye laser and an optical receiver with a 38cm Fresnel lens.

2. The optical arrangements of the dye laser system were designed for two alternate modes of operation. In one mode, outputs at the two required wavelengths, on and off the resonance absorption of the pollutant, are obtainable in rapid sequence, with frequency selection by an electromagnetically driven grating. In the second mode of operation, an intracavity polarizing-prism beam splitter is used to obtain simultaneously a pair of close-lying independently tunable wavelengths.

3. Field tests of the LIDAR system were carried out from City College and extended over the upper East Side of Manhattan. In these tests ambient levels of NO_2 concentrations were measured. These measurements showed that ambient levels below 0.2 ppm could readily be detected at ranges of more than 1 km.

4. The LIDAR system makes use of a calibration cell containing the pollutant gas to be monitored, so that a calibration signal is automatically available with each outgoing pulse. This makes the system independent of the slight variations in laser output characteristics that occur from pulse to pulse.

5. To improve flashlamp-pump laser output and efficiency, and to obtain simultaneously laser outputs at wavelengths suitable for monitoring NO_2 and other pollutants whose absorptions lie within the visible band, experiments were also carried out on energy transfer processes in dye mixtures. In this work, simultaneous outputs were successfully obtained at desired wavelengths. An investigation of the excitation energy transfer indicates an optical process. This work led to the first tunable three-color dye

mixture laser spanning the visible spectrum.[77]

The following is a chronological listing of the material presented in this work:

1. In Chp. 1, the need for an effective method of pollution monitoring is explained, and the historical development of LIDAR systems is given. Finally, an outline of this thesis is presented.

2. In Chp. 2, atmospheric scattering mechanisms are presented, first in a qualitative manner, then scattering relationships are detailed under Atmospheric Parameters. Towards this end, the four LIDAR schemes, Raman and resonance Raman, long path absorption, resonance fluorescence, and differential absorption of scattered energy (DASE) are described, and a comparison of operating parameters is given in Table 2.4:1.

3. In Chp. 3, the LIDAR system developed in this work, is described in detail. Sequential mode of operation is described first, then the necessity and operating characteristics of Simultaneous Two-Wavelength operation is presented. Experimental results showing the fluctuations in output beam quality, including bandwidth changes, indicate a strong need for calibrated output signals.

4. In Chp. 4, results of field tests are given along with uncertainties associated with the LIDAR readings.

5. In Chp. 5, theoretical and experimental results are given on energy transfer processes in dye mixtures.

6. In Chp. 6, a summary and conclusions are presented on the work reported.

CHAPTER 2 LIDAR TECHNIQUES

2.1 Introduction

All laser radar techniques depend upon atmospheric scattering mech-
anisms for their operation. Possible techniques for pollution monitor-
ing include the following:

1. Raman and resonance Raman (Raman backscatter),

2. long path absorption (resonance absorption),

3. resonance fluorescence (resonance fluorescence backscatter),
    and

4. differential absorption of scattered energy (DASE) (Rayleigh
    and Mie backscatter).

In the following section, the atmospheric scattering mechanisms
are explained qualitatively, then scattering relationships are detailed
in Sect. 2.3 under Atmospheric Parameters. A comparison of the LIDAR
schemes is made in Sect. 2.4 which shows the superior operating char-
acteristics of the DASE system.

2.2 Atmospheric Scattering Mechamisms

2.2.1 Raman Scattering

The Raman effect consists of the appearance of displaced lines in
the spectrum of monochromatic light scattered by molecules. The degree
of displacement, $\Delta \bar{\nu}$, is characteristic of the molecules causing the
scattering. The intensity of the spectral line is proportional to the
density of scattering molecules.

The Raman effect is essentially a detail of the Rayleigh scattering

process. In the Rayleigh process, incident light on a molecule is virtually absorbed and immediately re-emitted. The absorbed light does not raise the molecule to an excited energy level, as in classical resonance absorption. Instead, after absorption, the molecule is in a virtual excited state. This has two consequences. First, the molecule re-emits the energy in a very short time--about 10^{-12} sec. Second, the absorption and scattering cross sections are very small. It has been estimated that, for a typical liquid irradiated at 6328 Å, 1 part in 10^4 of the incident light will be scattered in a path length of 1 cm.[60,61] Gases have fewer molecules per unit volume, and the fraction of light will obviously be much less.

A small portion of the molecules excited (10^{-2} to 10^{-6} or less) will emit (Raman) light of a slightly different wavelength than the incident light.[60,61] This phenomenon is known as Raman scattering. The process is shown in Fig. 2.2:1. Light is absorbed by molecules in the ground state, and for some molecules Raman light is re-emitted, with these molecules returning not to the ground state, but to an excited vibrational level. The emitted light is naturally of a lower energy or frequency than the incident light. The difference in frequency is equal to one of the natural vibrational frequencies of the molecule. Several such shifted lines are usually observed in a Raman spectrum. Each molecule has its own set of vibrational frequencies and therefore its unique Raman spectrum, which can thus be used to uniquely identify the scattering (or re-emitting) molecule.

A few molecules initially absorb light while they are in an excited vibrational state and decay to a lower energy level, so that their Raman scattered light has a higher frequency. Therefore, the complete
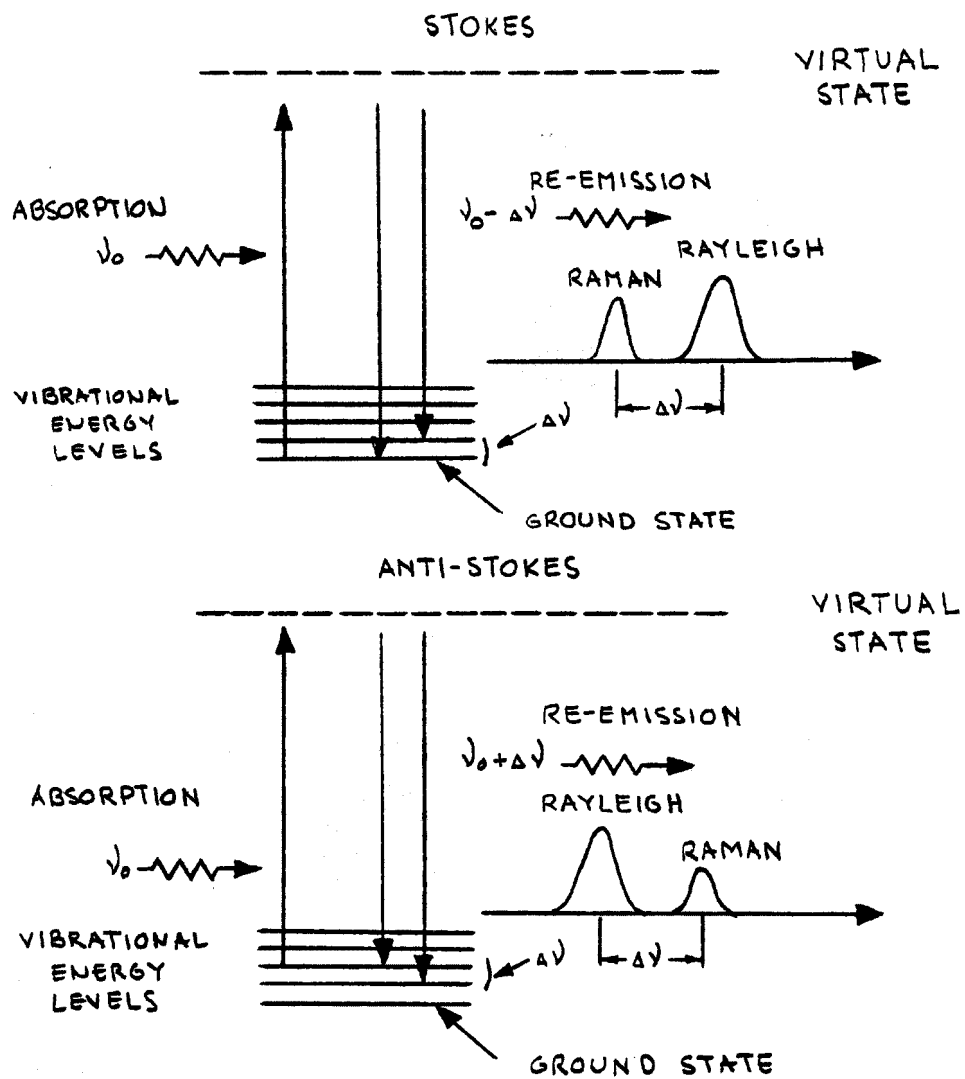
FIGURE 2.2:1   THE RAMAN PROCESS

12

scattering spectrum is made up of the Rayleigh scattering (predominant) at the same frequency as the incident light and the two components of the Raman spectrum, the Stokes lines (which are shifted to a lower frequency), and the anti-Stokes lines (which are shifted to a higher frequency. The Stokes lines are more intense because under most circumstances most molecules are in the ground energy level. To summarize, the typical Rayleigh scattering ratio is 1 in 10^4 (for a 1 cm liquid path).[60,61] Of this 10^{-4}, only 1 in 10^2 to 10^4 of the scatterings exhibits the displaced wavelengths characteristic of Raman scattering. For atmospheric gases, the Raman scattering ratio is much less. For N_2 at atmospheric pressure, this scattering ratio is approximately 1 in 10^{10} for a 1 cm path length.[18]

The Raman cross section determines the fraction of an incident light beam which will be scattered at Raman wavelengths. It is a critical piece of information needed for determining pollutant detectabilities and necessary for quantitative measurements. The cross section is a function of the fourth power of the frequency of the incident radiation, and it may be enhanced by resonance effects.

2.2.2 Resonance Raman Scattering

The resonance Raman effect can best be explained if the first step in scattering is considered to be the quasi-absorption of the incident light. As the light is scanned in frequency and approaches an absorption band, the fraction of the light absorbed increases, and the fraction of the scattered light increases proportionally, thus a larger apparent cross section results.

13

2.2.3 Absorption and Fluorescence Scattering

Absorption and fluorescence scattering is in actuality a description of the classical resonance absorption and fluorescence mechanisms. As an example, when monochromatic light propagates through the atmosphere and encounters a species of molecules whose absorption band coincides with the propagation frequency of the transmitted light, a portion of the light is absorbed. Subsequently, some of the absorbed monochromatic radiation will be re-emitted by the molecules over a wide spectrum characteristic of the absorbing species. The fluorescence scattered will be in all directions, shifted toward the longer wavelength end of the spectrum and will resemble the absorption spectrum of the molecules.

2.2.4 Rayleigh Scattering

Scattering from atoms or molecules for which the particle diameter is small compared to the wavelength of the incident light is called Rayleigh scattering. The scattered light is directional and is of the same frequency of the incident radiation. In the atmosphere, Rayleigh scattering is due to molecules normally present in the air, such as, N_2, O_2, H_2O, and CO_2.[2,18,58]

Rayleigh scattering occurs because molecules, for example, react to nonresonant radiation. When incident radiation passes over molecules, a general vibration is set up within the molecules, not at the resonance frequency, w_0, but at the frequency, w, of the field. The vibrating molecules are the sources of the scattered radiation.

2.2.5 Mie Scattering

Scattering from particles for which the particle diameter is large

14

compared to the wavelength of incident light is called Mie scattering. In this process, the scattered light is of the same frequency of the incident radiation. In the atmosphere, Mie scattering is due to particulates and aerosols.[2,18,58]

The DASE scheme makes use of both Rayleigh and Mie scattering. The next section details scattering relationships which are then used in Sect. 2.4 in a comparison of the four types of LIDAR schemes that have potential for use as pollution monitoring systems.

2.3 Atmospheric Parameters

The atmosphere attenuates a transmitted light beam by elastic (Rayleigh, Mie) scattering and by absorption.

The propagation of a light beam of intensity I_0 through the atmosphere may be expressed by:

$$I = I_0 \exp(-\alpha_A r), \qquad (2.3:1)$$

where,

I = the transmitted intensity over a distance r,

α_A = the atmospheric volume extinction coefficient which is composed of a sum of terms:

$$\alpha_A = \alpha_R + \alpha_M + \alpha_{ABS}. \qquad (2.3:2)$$

where,

α_R, α_M, α_{ABS} are respectively the Rayleigh, Mie, and absorption extinction coefficients.

The Rayleigh extinction coefficient is due to molecular scattering and can be calculated as a function of altitude for known atmospheric molecular densities. Mie scattering is due to particulates and aerosols

15

in the atmosphere and is highly variable in both particulate size, wavelength, and particle distribution. For identical molecules of density N, the volume extinction coefficient can be written in terms of a cross section $\alpha = \sigma N$ where, σ is the total cross section (cm^2) for the optical interaction with the molecule or particle.

In general, the scattering of light from molecular or particulate matter is not isotropic. The cross section is then specified by the differential cross section $\sigma(\theta, \varphi) = d\sigma/d\Omega$ where, θ is the scattering angle and φ is the polarization angle.[54] For isotropic scattering, the scattering cross section per unit solid angle is $d\sigma/d\Omega = \sigma/4\pi$. For backscattering ($\theta = \pi$) the volume backscatter coefficient $\beta = N\sigma(\pi)$.[54]

For molecular Rayleigh scattering, the differential cross section is:[54]

$$\frac{d\sigma_R}{d\Omega} = \frac{\pi^2(n^2 - 1)^2}{3\lambda^4 N^2}(\cos^2\theta \cos^2\varphi + \sin^2\varphi), \quad (2.3\!:\!3)$$

where,

  n = the refractive index,

  N = the density of molecules, and

  λ = the wavelength of incident light.

For unpolarized light, the angular factor averaged over φ reduces to $(\cos^2\theta + 1)/2$. Finally, for backscattering ($\theta = \pi$), the Rayleigh backscatter coefficient is uniquely given by:[54]

$$B_R = \frac{8\pi N\sigma_R(\pi)}{3}. \quad (2.3\!:\!4)$$

In the above discussion, the Raman volume extinction coefficient has been neglected since it is at least two orders of magnitude less than the Rayleigh extinction coefficient. However, the Raman differ-

ential cross section is given by:[2,55,56]

$$\frac{d\sigma_{RAM}}{d\Omega} = \left(\frac{1}{2\pi\epsilon_0 c^2}\right)^2 w_1 w_2 r^2 \alpha^2, \qquad (2.3:5)$$

where,

w_1 = the pump frequency,

w_2 = the Raman frequency, and

$r\alpha$ = the Raman polarizability.

The two frequencies differ by the vibrational mode frequency, w_v, so that $w_2 = w_1 - w_v$.

The large variation in size, density distribution and properties of atmospheric aerosols preclude an accurate calculation of the Mie scattering cross section. However, a useful empirical relation relating the Mie scattering coefficient is given below:[2,57,58]

$$\beta_M = \frac{3.91}{V} \left[\frac{0.55}{\lambda}\right]^{0.585(V^{1/3})} km^{-1}, \qquad (2.3:6)$$

where,

λ = the wavelength of incident light in um, and

V = the visibility in km.

This empirical expression is an approximation which has been found experimentally to hold under normal visibility conditions when ambient particulate concentrations are relatively low.[18]

The final parameter in the atmospheric volume extinction coefficient is absorption. Atmospheric absorption is not serious for wavelengths longer than 2500 Å. Below 2500 Å, absorption due to atmospheric oxygen becomes important with an absorption coefficient reaching 1 km^{-1} at 2450 Å.[2]

Now, having discussed both the atmospheric scattering mechanisms

and atmospheric parameters, a comparative analysis can be made of the four types of pollution monitoring schemes mentioned in Chp. 1, namely:

1. differential absorption of scattered energy (DASE),

2. resonance fluorescence,

3. Raman and resonance Raman, and

4. long path absorption.

From the discussion which follows, it will be seen that the DASE approach has inherent advantages over the other pollution monitoring schemes.

2.4 LIDAR Schemes: A Comparative Analysis

2.4.1 Introduction

For all four schemes, except the Raman, laser sources are needed at wavelengths that match the resonance absorption of the pollutants of interest. Dye lasers are now available with outputs tunable over the entire near ultraviolet and visible spectral ranges. They are capable of narrow band operation, less than 1 Å, with good frequency stability.[59] Pulse energies of over 1 j (per pulse) are typically available from flashlamp-pumped dye lasers. If coaxial flashlamps and appropriate discharge circuitry are utilized, these energies are available in pulses only a few hundred nanoseconds in duration, as is required for obtaining desired depth resolution in LIDAR applications. Several of the important commonly encountered pollutants have absorption spectra in the visible and near ultraviolet due to electronic transitions. These pollutants include NO_2, NO, SO_2, and O_3. This work centers on a pollution monitoring scheme to detect trace contam-

inant levels of NO_2 in the atmosphere.

2.4.2 NO_2 Absorption Spectrum

As can be seen in Fig. 2.4:1, NO_2 has a clearly structured absorption spectrum in the blue, with well defined peaks and troughs.[95]

2.4.3 General Formulation

The backscattered signal from a target at range R is given by:[18]

$$P_r(R) = \left(\frac{\rho}{\pi}\right) K P_0 \frac{A}{R^2} \exp\left(-2 \int_0^R \alpha_A(r)dr\right) , \qquad (2.4:1)$$

where,

$P_r(R)$ = the received power from range R,

P_0 = the transmitted power,

K = the optical system efficiency,

A = the area of the receiving telescope,

$\frac{\rho}{\pi}$ = the effective reflectivity of the remote target, and

$\alpha_A(r)$ = the volume extinction coefficient at range r.

The transmitted radiation interacts with the pollutant molecules through the atmospheric volume extinction coefficient, α_A, as defined in Eq. 2.3:1. The portion of the returned signal due to Raman and fluorescence scattering is taken into account in the effective reflectivity term ρ/π. The depth resolution attainable by backscatter methods is shown schematically in Fig. 2.4:2. The depth resolution is given by

$$\Delta R = \frac{c\tau}{2}, \qquad (2.4:2)$$

where,

19
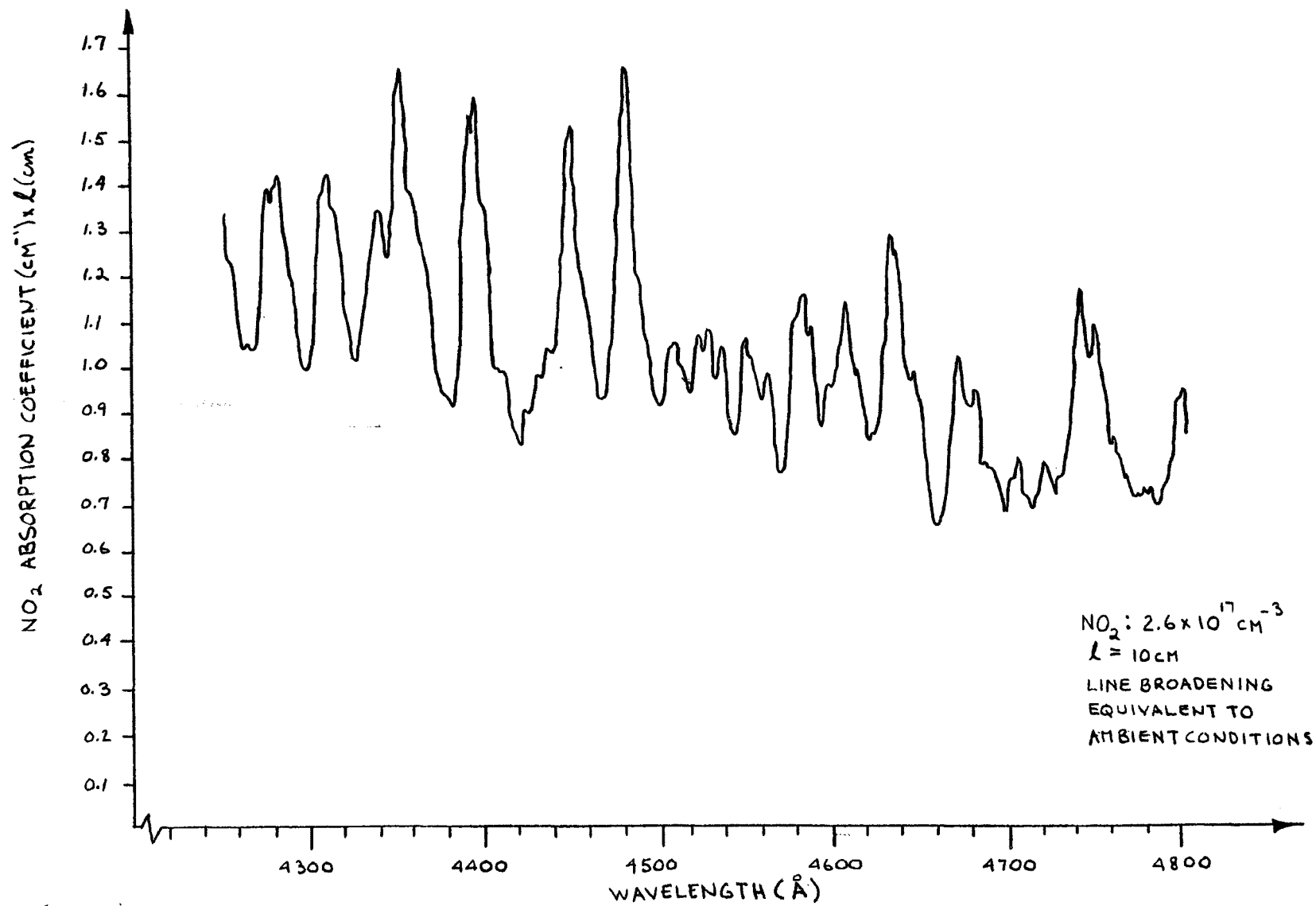
FIGURE 2.4:1   NO$_2$ ABSORPTION CURVE
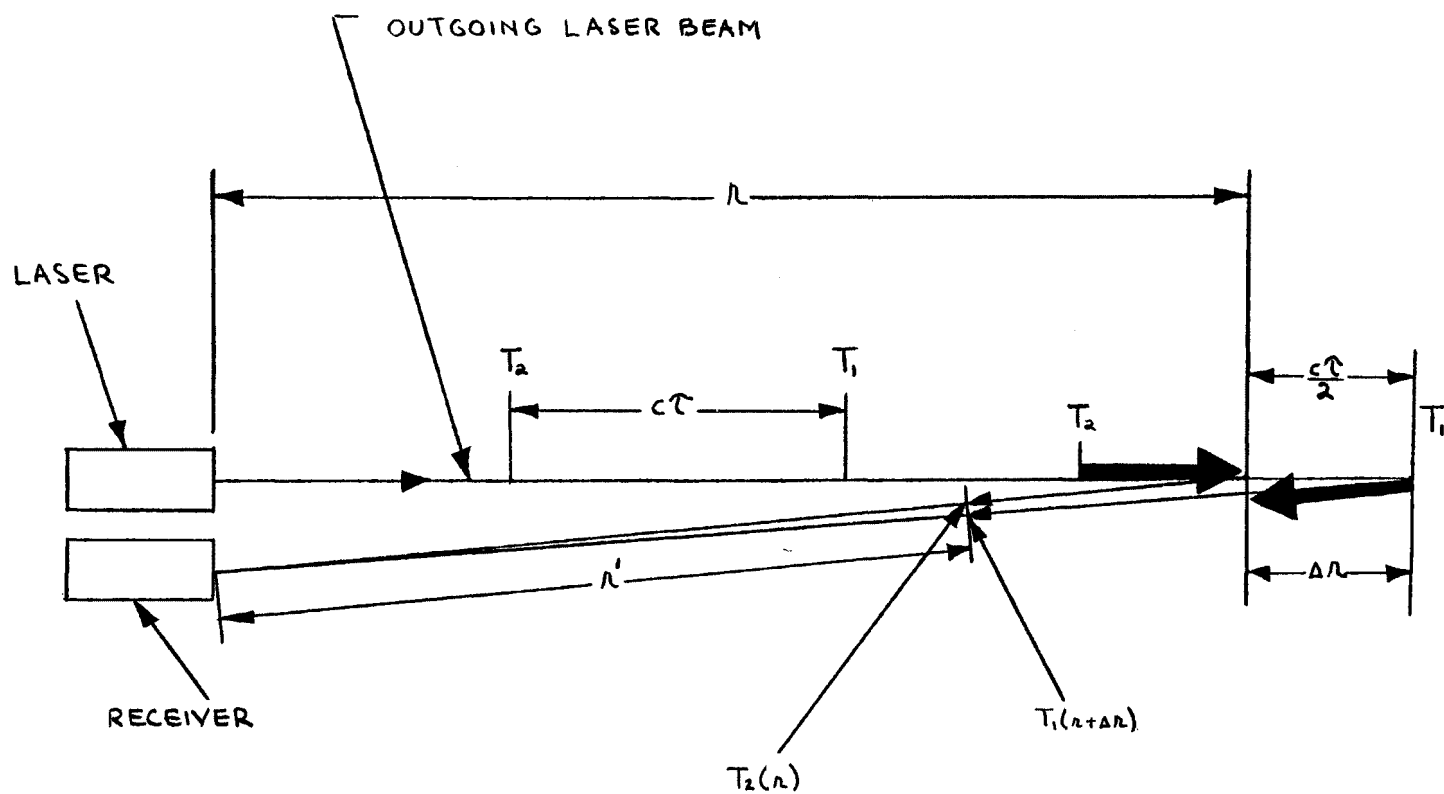
FIGURE 2.4:2   OBTAINABLE DEPTH RESOLUTION FOR BACKSCATTER LIDAR SCHEMES

$\tau = \tau_p + \tau_D + \tau_F$, the sum of the laser pulse width τ_p, the
detector integration time, τ_D, and the molecular fluo-
rescence time, τ_F (τ_F only comes into effect in the
resonance fluorescence backscatter scheme).

In the discussion that follows, a comparison among the DASE,
resonance fluorescence, Raman and resonance Raman, and long path ab-
sorption schemes is made. For the purpose of comparison the DASE
LIDAR system developed here were used as a basis.

2.4.4 Differential Absorption of Scattered Energy (DASE)
2.4.4.1 Basic Theory

In its simplest form, this scheme determines the concentration of a
pollutant at an arbitrary point, distance r in space, by measuring the
optical resonance absorption due to the pollutant across an incremental
path length, Δr. This is shown schematically in Fig. 2.4:3. The ab-
sorption across Δr is obtained from the relative attenuation of two
collinear laser beams at close-lying wavelengths, λ_1 and λ_2, respect-
ively on and off the resonance absorption of the pollutant molecule in
question. The relative attenuation is determined from comparisons (at
the receiver) of the Rayleigh and Mie atmospheric elastic backscatter
from the two laser beams as they traverse Δr. Appropriate temporal
resolution at the receiver permits determination of r and Δr, the range
and spatial resolution of the pollutant distribution.

Several features of this scheme should be noted at this stage:

1. As mentioned earlier, dye lasers are now capable of narrow band
   operation, less than 1 Å, with good frequency stability. Since
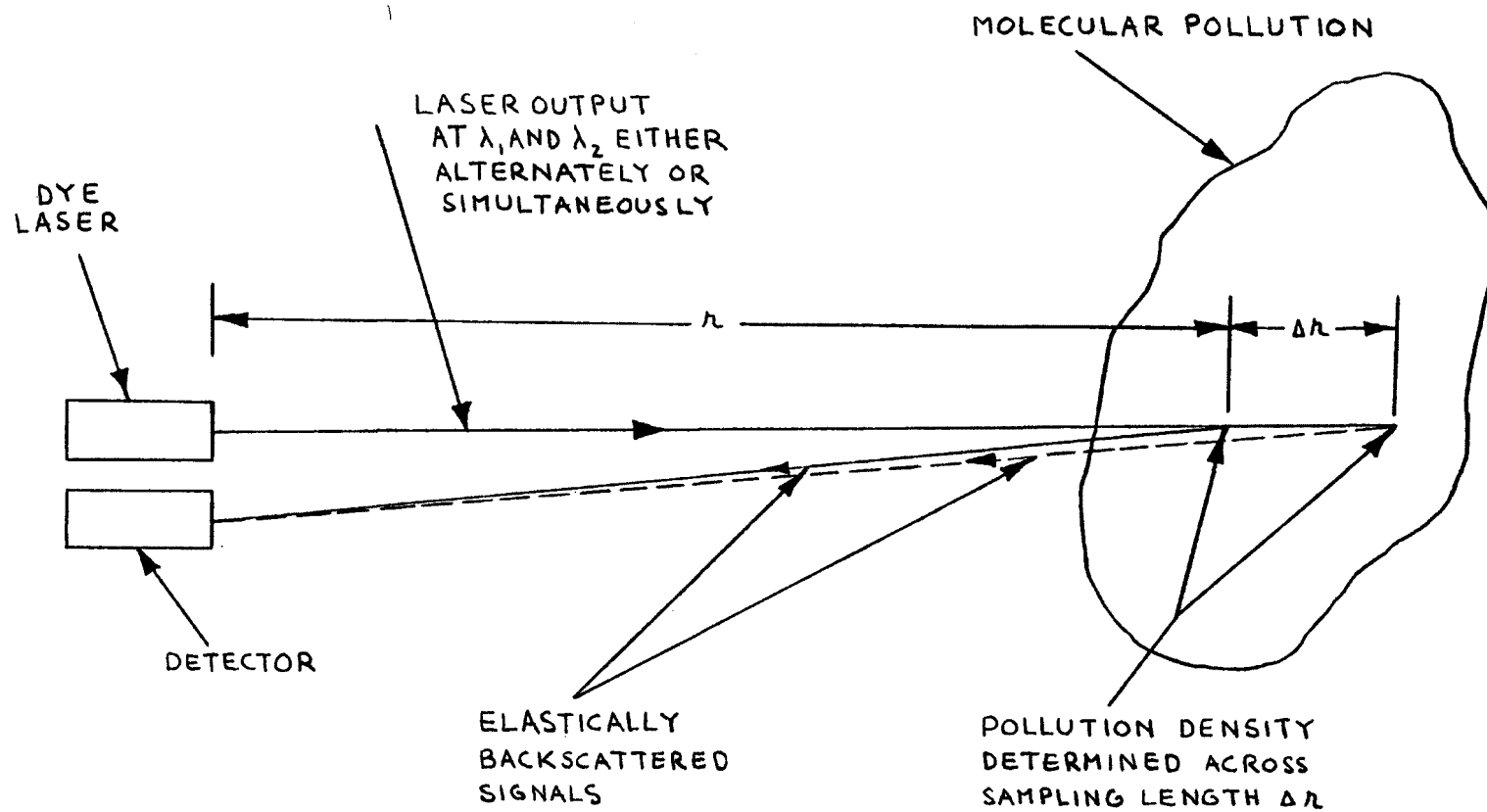
FIGURE 2.4:3   THE DASE SCHEME

the receiver signal is simply the elastic backscattered compo-
nent of the transmitted signal, this permits the use of very
narrow bandwidth receivers (if possible, down to the bandwidth
of the transmitted signal). This is an important factor in re-
ducing undesirable background noise and the limitations that it
places on LIDAR monitoring schemes.

2. The received signal that is due to the elastic scattering from
   the atmosphere is relatively large and thus easily detected.

3. Since this scheme determines the pollutant concentration by an
   absorption method, the achievable detection sensitivity is high
   even where the required spatial resolution is high (or equiva-
   lently, where the sampling lengths are small).

The backscattered power observed by a LIDAR system with collinear
transmitting and receiving optical axes is given by Eq. 2.4:1. For the
DASE case the effective reflectivity of the atmosphere is given by:[18]

$$\frac{\rho}{\pi} = \frac{ct_p}{2}\left[\beta_R(R,\lambda) + \beta_M(R,\lambda)\right], \qquad (2.4:3)$$

where,

c = the speed of light,

t_p = the laser pulse length,

$\beta_R(R,\lambda)$ = the Rayleigh backscatter coefficient, and

$\beta_M(R,\lambda)$ = the Mie backscatter coefficient.

Substituting this relation into Eq. 2.4:1 yields,

$$P_r(R,\lambda) = \frac{ct_p}{2}[\beta_R(R,\lambda) + \beta_M(R,\lambda)]KP_0(\lambda)\frac{A}{R^2}\exp\left\{-2\int_0^R[\alpha_{SC}(R,\lambda) + \sigma_{ABS}(R,\lambda)N_r]dr\right\}, \qquad (2.4:4)$$

where,

24

$\alpha_{SC}(R,\lambda) = \alpha_R(R,\lambda) + \alpha_M(R,\lambda)$, the atmospheric volume scatter-

ing coefficient without absorption,

$\alpha_R(R,\lambda)$ = the Rayleigh volume scattering coefficient, and

$\alpha_M(R,\lambda)$ = the Mie volume scattering coefficient. The other

parameters were previously defined.

An expression for $\bar{N}_r$ averaged over a distance ΔR can be obtained

from Eq. 2.4:4 by forming the difference of the logarithm of $P_r(R)$ eval-

uated at R and $R + \Delta R$ for both a frequency on the absorption peak (λ_1)

and to the absorption trough (λ_2). These equations are shown below:

$$\ln P_r(R,\lambda_1) - \ln P_r(R + \Delta R, \lambda_1) = -2\frac{\Delta R}{R} + \ln[\beta_R(R,\lambda_1) +$$

$$\beta_M(R,\lambda_1)] - \ln[\beta_R(R + \Delta R, \lambda_1) + \beta_M(R +$$

$$\Delta R,\lambda_1)] + 2\bar{\alpha}_{SC}(\lambda_1)\Delta R + 2\sigma_{ABS}(\lambda_1)\bar{N}_r\Delta R,$$

$$(2.4:5)$$

$$\ln P_r(R,\lambda_2) - \ln P_r(R + \Delta R, \lambda_2) = -2\frac{\Delta R}{R} + \ln[\beta_R(R,\lambda_2) +$$

$$\beta_M(R,\lambda_2)] - \ln[\beta_R(R + \Delta R,\lambda_2) + \beta_M(R +$$

$$\Delta R,\lambda_2)] + 2\bar{\alpha}_{SC}(\lambda_2)\Delta R + 2\sigma_{ABS}(\lambda_2)\bar{N}_r\Delta R.$$

$$(2.4:6)$$

An expression for $\bar{N}_r$, the value of N_r averaged for the depth resolu-

tion ΔR at range r can be obtained from Eqs. 2.4:5 and 2.4:6 as:

$$\bar{N}_r = \frac{1}{2\Delta\sigma\Delta R}[\ln \frac{P_r(R,\lambda_1)}{P_r(R + \Delta R,\lambda_1)} - \ln \frac{P_r(R,\lambda_2)}{P_r(R + \Delta R,\lambda_2)} +$$

$$S + S'], \qquad (2.4:7)$$

where,

$$S = -2[\bar{\alpha}_{SC}(\lambda_1) - \bar{\alpha}_{SC}(\lambda_2)]\Delta R, \qquad (2.4:8)$$

$\bar{\alpha}_{SC}(\lambda) = \bar{\alpha}_R(\lambda) + \bar{\alpha}_M(\lambda)$, the total volume scattering coeffi-

cient neglecting absorption, averaged over ΔR, and

$\Delta\sigma = \sigma_{ABS}(\lambda_1) - \sigma_{ABS}(\lambda_2)$, the difference in absorption cross

sections.

$$S' = \ln\left[\frac{\beta_R(R + \Delta R, \lambda_1) + \beta_M(R + \Delta R, \lambda_1)}{\beta_R(R, \lambda_1) + \beta_M(R, \lambda_1)}\right] -$$

$$\ln\left[\frac{\beta_R(R + \Delta R, \lambda_2) + \beta_M(R + \Delta R, \lambda_2)}{\beta_R(R, \lambda_2) + \beta_M(R, \lambda_2)}\right]. \tag{2.4:9}$$

In order to evaluate Eq. 2.4:7, it is necessary to know the magnitudes of S and S'. These quantities are, in general, unknown. However, if if the absorption peak and trough measurements are taken nearly simultaneously, so that the β's and α's remain constant in time, and if these coefficients do not change significantly over the spectral interval $\lambda_1 - \lambda_2$, then S and S' can be taken to be zero.[49,52,62] Therefore, making these assumptions, Eq. 2.4:7 reduces to:

$$\bar{N}_r = \frac{1}{2\Delta\sigma\Delta R}\ln\left[\frac{\dfrac{P_r(R, \lambda_1)}{P_r(R, \lambda_2)}}{\dfrac{P_r(R + \Delta R, \lambda_1)}{P_r(R + \Delta R, \lambda_2)}}\right], \tag{2.4:10}$$

or,

$$\bar{N}_r = \frac{\ln(1 + \Delta F_r)}{2\Delta\sigma\Delta R}, \tag{2.4:11}$$

where,

ΔF_r = the fractional change in the ratio of ratios of the received signals.

As can be seen from Eq. 2.4:11, the sensitivity of pollutant detection is improved by:

1. the ability of the instrumentation to detect smaller changes in ΔF_r,

2. increasing the sampling length, Δr (at a cost of decreasing spatial resolution), and

3. a large resonance absorption cross section, σ_{λ_1}, and a small off-

26

resonance cross section, σ_{λ_2}.

2.4.4.2 Evaluation of Required System Parameters for Detection of NO_2

2.4.4.2.1 Received Signal Requirements

Assuming a relative change in the ratio of ratios of received signals of 5 percent, a range of 1000 m, minimum spatial resolution of 100 m, and taking the absorption cross sections from Fig. 2.4:1 as $\sigma_{ABS}(4478.5\ \mathring{A}) = 6.38 \times 10^{-19}\ cm^2$ and $\sigma_{ABS}(4500\ \mathring{A}) = 3.5 \times 10^{-19}\ cm^2$ (the curve in Fig. 2.4:1 was run with a resolution of 5 $\mathring{A}$ which matches the typical laser bandwidth used), the minimum detectable pollutant concentration, $\overline{N}_r$, equal to 0.315 ppm is obtained.

In order to obtain maximum difference in absorption cross sections, and hence achieve better detection sensitivity, laser wavelengths of $\lambda_1 = 4480\ \mathring{A}$ (peak) and $\lambda_2 = 4497\ \mathring{A}$ (trough) were chosen. It should be noted that for narrow filters such as is required in the system described, manufacturers encounter difficulty producing filters exactly to the specifications, and the above was the closest fit that could be obtained.

The received signal power in this DASE LIDAR system is the elastically backscattered fraction of the outgoing laser beam. Since this received power, and therefore the effective range of the system, is determined by the fraction of the power that is reflected, this aspect is considered next.

A detector is dark current limited if

$$2q\left(\frac{B}{n}\right)\left(\frac{S}{N}\right)^2_{min} < i_d,$$

where,

(2.4:12)

q = the electronic charge,

B = the electronic bandwidth of the detection system,

n = the number of pulses,

$\left(\dfrac{S}{N}\right)_{min}$ = the minimum acceptable signal to noise ratio, and

i_d = the detector dark current.

For photon limited detection the opposite of Eq. 2.4:12 is true. Inserting the values of the detector used, Amperex type 56AVP, (B = 3 MHZ, i_d = 15 nA) into Eq. 2.4:12, it is found that the system is dark current limited for an acceptable signal to noise ratio of 10.

The minimum detectable signal power, $P_{r,min}$, for dark current limited detectors is given by:[2]

$$P_{r,min} = \frac{[2q(B/n)(S/N)_{min}i_d]^{1/2}}{S_D},\qquad (2.4:13)$$

where,

S_D = the detector sensitivity.

For the system described, $P_{r,min}$ is found to be equal to 6.32×10^{-9} W. The minimum detectable change, ΔP_{min}, relative to the signal power, P_r, at the detector is given by the following relationship:[2]

$$\frac{\Delta P_{min}}{P_r} = \left[\frac{4qB}{nS_D P_r}\left(\frac{S}{N}\right)_{min}\left(1 + \frac{i_d}{S_D P_r}\right)\right]^{1/2},\qquad (2.4:14)$$

Using Eq. 2.4:14 and the parameters for the system ($S_D = 60 \times 10^{-3}$ A/W), a minimum acceptable signal to noise ratio of 10, and a minimum detectable change of 5 percent, it is found that for single pulse operation a received power, P_r, of 0.25 uW is required.

2.4.4.2.2 Transmitted Power Requirements

It is useful at this stage to get an idea of the power requirements

for the laser transmitter for a system of this type.

Assuming an NO_2-polluted-free atmosphere up to the sampled region, ΔR, solving Eq. 2.4:4 for the transmitted power yields:

$$P_0(\lambda) = \frac{P_r(R + \Delta R, \lambda)}{\frac{ct_p}{2}[B_R(R + \Delta R, \lambda) + B_M(R + \Delta R, \lambda)]} \times$$

$$\frac{1}{\frac{KA}{(R + \Delta R)^2}\exp\left\{-2[\bar{\alpha}_{SC}(\lambda)(R + \Delta R) + \sigma_{ABS}(\lambda)\bar{N}_r\Delta R]\right\}}, \qquad (2.4:15)$$

where,

$\bar{\alpha}_{SC}(\lambda) = \bar{\alpha}_R(\lambda) + \bar{\alpha}_M(\lambda)$, the total atmospheric volume scattering coefficient without absorption, averager over R + ΔR, and

$\bar{N}_r$ = the average pollutant concentration over ΔR.

An average pollution concentration of 0.315 ppm of NO_2 over the sampled region of 100 m, a range of 1000 m, a visibility of 10 km, and a received signal power of 0.25 uW for each outgoing wavelength (to give a fractional change of ratio of ratios of received powers of 5 percent), yield the on-line and off-line transmitted powers as 0.0395 MW (9.88 mj) and 0.0375 MW (9.38 mj) respectively.

Increasing the output energies of each line to 1/2 j, the received power increases to 15.9 uW off-line and 15.8 uW on-line, which corresponds to a minimum detectable pollution concentration of 0.029 ppm.

2.4.4.2.3 Pump Depletion

The foregoing discussion considered the Rayleigh and Mie return assuming an NO_2-polluted-free atmosphere up to the sampled region. It is still necessary to consider the problem of pump depletion if the

pollutant is at a density of, say, 0.315 ppm over the entire 1000 m range. Since 100 m cause approximately a 10 percent reduction in received signal power (and approximately a 5 percent reduction in ΔF_r), 1000 m will cause a reduction by a factor of exp(-1.0%) = 0.34. The received signal will be down approximately 34 percent of its original value of 5.41 uW off-line and 5.37 uW on-line, and it would be possible to detect a minimum concentration of 0.051 ppm, which corresponds to a 0.45 percent change in ratio of ratios. Thus, a laser pulse energy of 1/2 j per line is sufficient to detect a change of NO_2 concentration of 0.051 ppm averaged over 100 m at a range of 1000 m even when pollution concentrations as high as 0.315 ppm exist along the entire probe beam path.

If the range is decreased to 100 m, a minimum concentration as low as 1.6 ppb could be detected (corresponding to a change in the ratio of ratios of 2.6 X 10^{-2} percent), with the same optics and output power described above.

2.4.5 Resonance Fluorescence

2.4.5.1 Basic Theory

This scheme determines the pollution concentration at a distance r in space by measuring the fluorescence backscatter induced by the probe beam as it is absorbed by the polluted species. This is shown schematically in Fig. 2.4:4.

2.4.5.2 Evaluation of Required System Parameters for Detection of NO_2

The backscattered fluorescence intensity from range r observed by

LASER OUTPUT
AT λ_1

MOLECULAR POLLUTION

DYE
LASER

h

DETECTOR

MOLECULAR FLUORESCENCE
RETURN
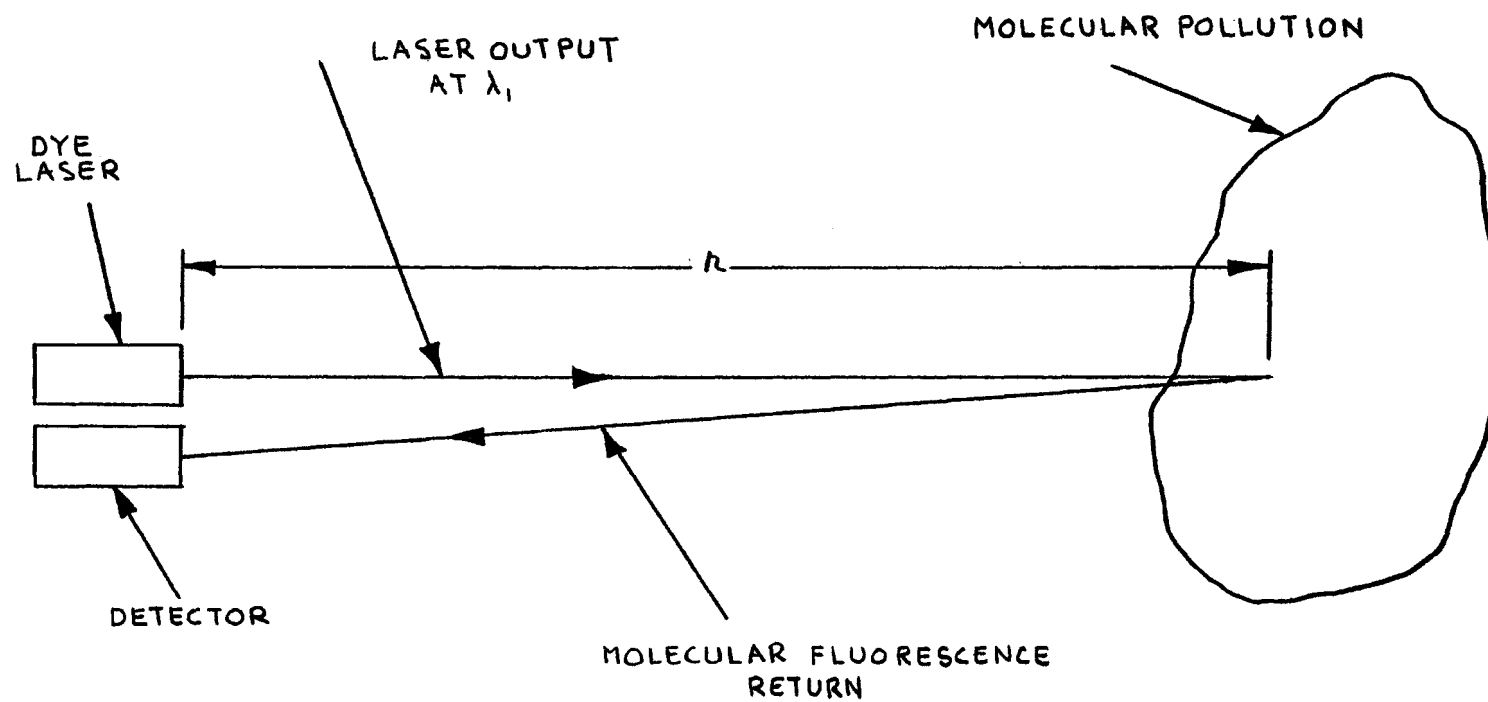
FIGURE 2.4:4   THE RESONANCE FLUORESCENCE SCHEME

a LIDAR system with collinear transmitting and receiving axes is given by Eq. 2.4:1 with the effective reflectivity $\frac{\rho}{\pi}$ given as:[2]

$$\frac{\rho}{\pi} = \frac{ctN_r\sigma_F}{2}, \qquad (2.4:16)$$

where,

$$\sigma_F = \sigma_{ABS}(\lambda)Q, \text{ and} \qquad (2.4:17)$$

$$Q = \frac{1}{1 + \frac{t_{SP}}{t_{COL}}\left(\frac{1}{Z}\right)} \frac{t_{COL}}{t_{SP}}Z, \qquad (2.4:18)$$

where,

$\frac{1}{Z}$ = the probability of quenching per collision,

t_{COL} = the collision time, and

t_{SP} = the spontaneous decay time.

Substituting these terms into Eq. 2.4:1 and assuming an NO_2-polluted-free atmosphere up to the sampled region, ΔR, yields:

$$P_r(R) = KP_0\frac{ct\sigma_{ABS}(\lambda)\bar{N}_rQAF}{2} \frac{}{4\pi} \frac{}{R^2} \exp[-2\bar{\alpha}_{SC}(\lambda)R -$$

$$\sigma_{ABS}(\lambda)\bar{N}_r\Delta R], \qquad (2.4:19)$$

where,

F = the fraction of the total fluorescence detected by the re-
   ceiver,

$\bar{N}_r$ = the average pollutant concentration over the sampled region,
   ΔR, and

$\bar{\alpha}_{SC}(\lambda) = \bar{\alpha}_R(\lambda) + \bar{\alpha}_M(\lambda)$, the atmospheric volume scattering coeffi-
   cient without absorption averaged over R.

For an average pollution concentration of 0.029 ppm across the sampled region, a range of 1000 m, a depth resolution of 100 m, and a received

signal of 6.32×10^{-9} W (the minimum detectable received power for the detector used) the required transmitted power of 382 MW is obtained. This power is equivalent to 95.5 j for a dye laser with a pulse length of 250 ns.

The discussion above considered nighttime operation, that is, the entire backscattered spectrum (F = 1) was detected. In daytime operation the noise attributed to background radiation must be blocked. This has the effect of reducing the observed fluorescence backscattered signal. Therefore, to detect 0.029 ppm for daytime operation (F = 0.1) a transmitted energy of 955 j is required.

These energy requirements are, of course, only to be used as a relative basis for a comparison among the other LIDAR schemes presented. For realistic power requirements, a range of 100 m, a sampled depth of 100 m, an average pollution concentration of 0.1 ppm of NO_2, yields for nighttime operation a required transmitted power of 3.52×10^5 W (8.80×10^{-2} j). For daytime operation, the required transmitted power increases to 3.52×10^6 W (8.80×10^{-1} j).

To summarize, the resonance fluorescence backscatter scheme has the following disadvantages:

1. Daytime operation severely limits detection sensitivities, resulting from the blockage of background radiation.

2. The fluorescent backscattered signal at the receiver is dependent upon the concentration of the pollutant in the region being probed.

2.4.6 Raman and Resonance Raman

2.4.6.1 Basic Theory

The Raman scheme determines the concentration of the pollutant at an arbitrary point in space by measuring the Raman backscattered intensity induced as the probe beam interacts with the polluted atmosphere. This is shown schematically in Fig. 2.4:5.

2.4.6.2 Evaluation of Required System Parameters for Detection of NO_2

The backscattered Raman intensity at the receiver due to the pollutant is of the same form as that for the resonance fluorescence scheme, but with the effective reflectivity term $\frac{\rho}{\pi}$ given as:[18]

$$\frac{\rho}{\pi} = \frac{ctN_n\sigma_{RAM}(\lambda)}{8},$$ (2.4:20)

where,

σ_{RAM} = the Raman scattering cross section.

Subsitiuting this relation into Eq. 2.4:1 and assuming an NO_2-polluted-free atmosphere up to the sampled region, ΔR, yields for the received power:

$$P_r(R) = KP_0\frac{ct}{2}\sigma_{RAM}(\lambda)\overline{N}_n\frac{AF}{4\pi}\frac{1}{R2}\exp[-2\overline{\alpha}_{SC}(\lambda)R -$$

$$\sigma_{ABS}(\lambda)\overline{N}_r\Delta R].$$ (2.4:21)

For an average pollution concentration of 0.029 ppm across the sampled region, a range of 1000 m, a depth resolution of 100 m, and a received power of 6.32×10^{-9} W (the minimum detectable received power), the required transmitted power of 1.77×10^8 MW (4.43×10^7 j) is obtained.

To reduce the transmitted power requirements, this LIDAR scheme can be run in the resonance Raman mode. This has the effect of increasing the received backscattered Raman intensity by increasing the Raman scat-
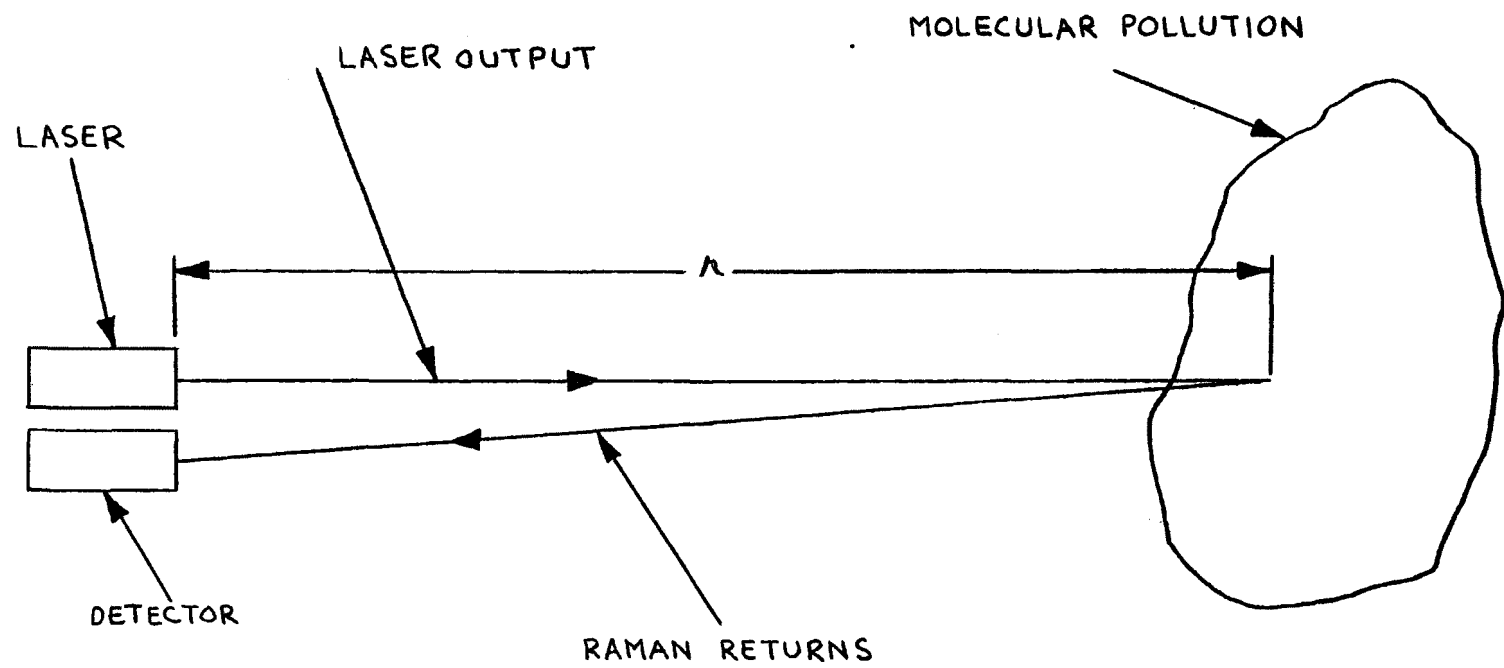
FIGURE 2.4:5   THE RAMAN SCHEME

tering cross section as:[2]

$$\left(\frac{d\sigma}{d\Omega}^{RAM}\right)_{RES} \sim \left(\frac{d\sigma}{d\Omega}^{RAM}\right)_{NONRES} \frac{\nu_0^2}{(\nu_1 - \nu_0)^2 + (\Delta\nu/2)^2} ,$$

$$(2.4:22)$$

where,

ν_1 = the laser pump frequency,

ν_0 = the electronic transition frequency, and

$\Delta\nu$ = the linewidth of the electronic transition.

For NO_2, $\nu_1 = 6.69 \times 10^{14}$ HZ, $\nu_0 = 6.69 \times 10^{14}$ HZ, and $\nu = 2.24 \times 10^{12}$ HZ, Eq. 2.4:22 yields $\left(\frac{d\sigma}{d\Omega}^{RAM}\right)_{RES} = 1.21 \times 10^{-23}$ cm^2. Inserting the value for the resonance Raman backscattering cross section into Eq. 2.4:21 and evaluating the expression for the same conditions as for the Raman case, 504 MW (126 j) is obtained for the required transmitted power.

Thus far, it has been assumed that the entire backscattered Raman signal was detected. Actually, since the laser probe beam is both Stokes and anti-Stokes shifted, that part of the Raman return signal that the elastic backscatter interferes with must be rejected. Also, since the Raman effect is not a selective process, the backscattered signal consists of many Raman returns from different species of molecules present in the atmosphere. Therefore, the signal of interest must be distinguished from the other Raman returns. This in effect increases the transmitted energy requirement by approximately 10 percent.[18]

The energy requirements for both the Raman and resonance Raman schemes, as for the case of resonance fluorescence, are of course only

36

to be used in a comparison among the LIDAR schemes presented. The magnitude of the nonresonance Raman backscattering coefficient limits the range of this type of LIDAR system to less than 50 m for any practical transmitted energy requirements for monitoring pollution levels present in ambient conditions (0.01 to 5 ppm), and limits the range to less than 75 m for the resonance Raman scheme.[2]

The disadvantages of the Raman and resonance Raman schemes are summarized below:

1. The Raman backscattering cross sections are 10 to 10^3 smaller than the Rayleigh and Mie backscattering cross sections.

2. The strength of the Raman and resonance Raman returns depend upon the concentration of the pollutant present in the atmosphere. This dependency is the main factor in limiting detection sensitivities. Even though for NO_2 detection, the resonance Raman backscattering cross section is larger than the sum of the Rayleigh and Mie backscattering cross sections (1.21×10^{-23} cm^2 as compared to 3.21×10^{-28} cm^2 respectively), the backscattering coefficient which is a function of pollutant concentration in the resonance Raman (and Raman) case, and a function of air in the elastic (Rayleigh and Mie) case, determines the strength of the return signal.

3. The Raman and resonance Raman returns that are anti-Stokes shifted are interferred with by the Rayleigh and Mie backscatter. It is therefore necessary to reject that part of the Raman return as well as the elastically backscattered signal, which results in a decrease of detected signal power at the

37

receiver.

4. In the resonance Raman scheme, since Raman returns are induced
   by probing approximately with an absorption frequency, and the
   fluorescence frequency shift for molecules is of the same order
   as the Raman shift, discrimination problems exist at the receiv-
   er. Finally, the magnitude of the backscattered fluorescence
   intensity may be larger by orders of magnitude than the reso-
   nance Raman intensity.[2]

2.4.7 Long Path Absorption

2.4.7.1 Basic Theory

In this technique, the average pollution concentration along the
probe beam, Fig. 2.4:6, is determined from measurements of the relative
attenuation along the length of the probed path, R, of two collinear
laser beams at close-lying wavelengths, λ_1 and λ_2, respectively on and
off a resonance absorption peak of the pollutant in question. This
scheme has the disadvantages of needing a remote detector or reflective
target to receive the transmitted beam, and lacks depth resolved meas-
urements. The advantages of this scheme are its good sensitivity and
the use of low power light sources.

Since monostatic LIDAR schemes are the ones of interest, two types
of long path absorption schemes are considered, namely:

1. long path absorption utilizing a retroreflector, and

2. long path absorption utilizing a topographical target.

The received power at the detector is given by Eq. 2.4:1 with the
appropriate effective reflectivity terms inserted. For absorption meas-

DYE
LASER

LASER OUTPUT
AT λ_1 AND λ_2
ALTERNATELY OR
SIMULTANEOUSLY

MOLECULAR POLLUTION

h

DETECTOR

RETROREFLECTOR OR
TOPOGRAPHICAL TARGET

REFLECTED LASER
SIGNALS

FIGURE 2.4:6   THE LONG PATH ABSORPTION SCHEME

urements with a retroreflector and a collimated transmitted beam, the
range-squared dependence is effectively cancelled. Thus, all the
transmitted power is collected except for a collection efficiency
factor, ξ, which is near unity, and the effective target reflectivity
is orders of magnitude better than for a Lambertian scatterer. The
effective reflectivity term for such a case is given by:[18]

$$\left(\frac{\rho}{\pi}\right)_{RETRO} = \frac{R^2 \xi}{A} \, . \tag{2.4:23}$$

For long path absorption by scattering from topographical targets:

$$\left(\frac{\rho}{\pi}\right)_{TOPOG} = \frac{\rho}{\pi} \, , \tag{2.4:24}$$

where,

$$\rho \approx 0.1 \text{ for visible and u.v. wavelengths.}[18]$$

An expression for the average pollutant concentration over R can
be obtained by taking the difference between the logarithms of the
received powers from the off-line and on-line wavelengths respective-
ly:

$$\ln P_r(R,\lambda_2) - \ln P_r(R,\lambda_1) = \ln P_0(\lambda_2) - \ln P_0(\lambda_1) +$$
$$2[\bar{\alpha}_{SC}(\lambda_1) - \bar{\alpha}_{SC}(\lambda_2)]R +$$
$$2[\sigma_{ABS}(\lambda_1) - \sigma_{ABS}(\lambda_2)]\bar{N}_r R, \tag{2.4:25}$$

where,

$$\bar{\alpha}_{SC}(\lambda) = \bar{\alpha}_R(\lambda) + \bar{\alpha}_M(\lambda),$$ the total atmospheric volume scattering
coefficient without absorption averaged over R, and

$\bar{N}_r$ = the average pollutant concentration over R.

Solving for the average pollutant concentration yields:

$$\bar{N}_r = \frac{1}{2\Delta\sigma R}\left[\ln\frac{P_0(\lambda_1)}{P_0(\lambda_2)} - \ln\frac{P_r(R,\lambda_1)}{P_r(R,\lambda_2)} + S''\right], \tag{2.4:26}$$

40

where,

$$S'' = -2[\bar{\alpha}_{SC}(\lambda_1) - \bar{\alpha}_{SC}(\lambda_2)]R, \text{ and}$$

$$\Delta\sigma = \sigma_{ABS}(\lambda_1) - \sigma_{ABS}(\lambda_2), \text{ the difference in absorption cross}$$

sections.

In order to evaluate Eq. 2.4:26 exactly, it is necessary to know the magnitude of the S'' term. This quantity is, in general, unknown. As in the DASE scheme, if the peak and trough measurements are taken nearly simultaneously, so that the α's remain constant in time, and if these coefficients do not change significantly over the spectral interval, $\lambda_1 - \lambda_2$ (which is true for the case for close-lying wavelengths), then S'' can be taken to be zero.[49,52,62] Therefore, Eq. 2.4:26 reduces to:

$$\bar{N}_r = \frac{1}{2\Delta\sigma R} \ln \left[\frac{\frac{P_0(\lambda_1)}{P_0(\lambda_2)}}{\frac{P_r(R,\lambda_1)}{P_r(R,\lambda_2)}} \right], \tag{2.4:27}$$

or,

$$\bar{N}_r = \frac{\ln(1 + \Delta F_r)}{2\Delta\sigma R}, \tag{2.4:28}$$

where,

ΔF_r = the fractional change in the ratio of ratios of the on-line and off-line transmitted and received powers respectively.

To make a comparison between the long path absorption and the other LIDAR schemes mentioned, an average pollution concentration of 0.029 ppm of NO_2 along a probed path of 1000 m are assumed. The required on-line and off-line transmitted powers are then found.

41

2.4.7.2 Evaluation of Required System Parameters for Detection of NO_2

For both the long path absorption methods, utilizing a retroreflector and a topographical target, the received power at the detector is given by Eq. 2.4:1 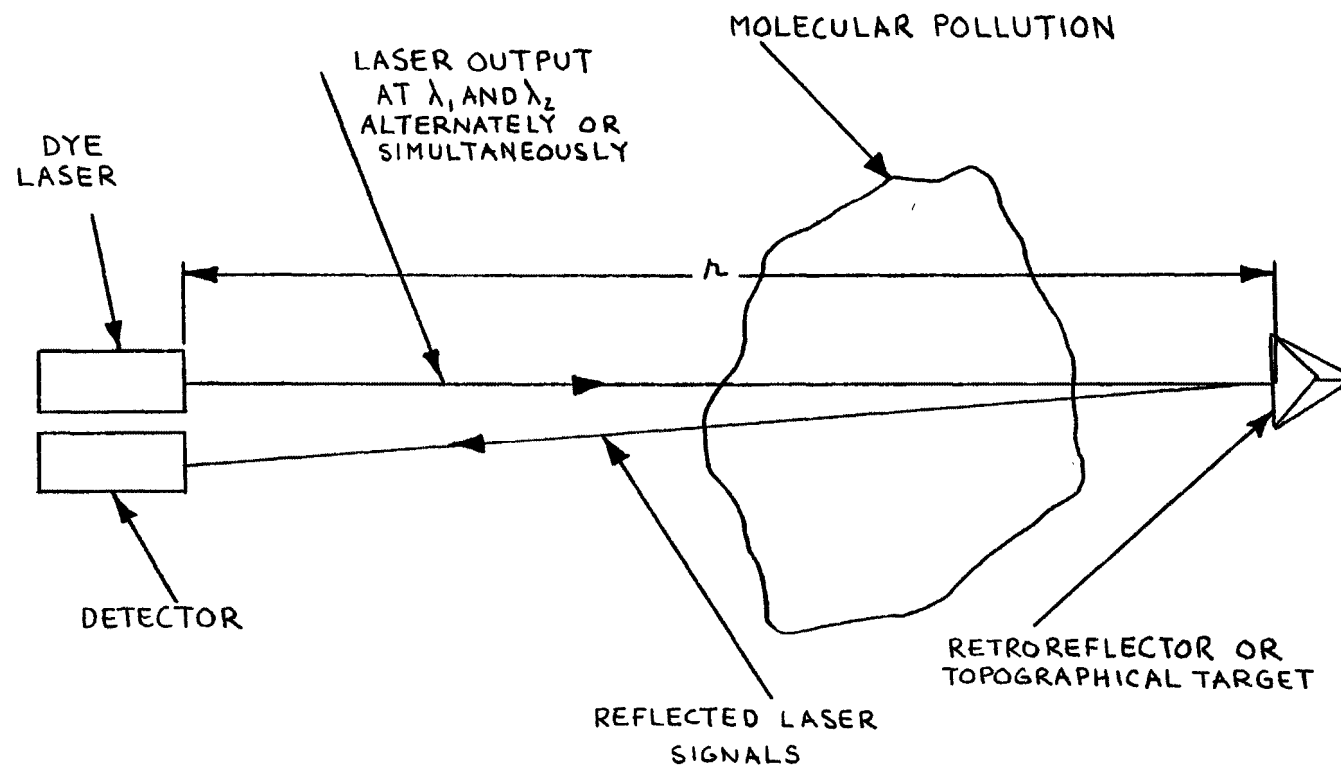with the proper effective reflectivity terms inserted for each case. Solving Eq. 2.4:1 for the transmitted power for the topographical target case yields:

$$P_0(\lambda) = \frac{P_r(R,\lambda)}{\frac{0.1KA}{\pi}\frac{}{R^2} \exp\{-2[\sigma_{SC}(\lambda) + \sigma_{ABS}(\lambda)N_r]R\}} \cdot$$

$$(2.4:29)$$

Inserting the appropriate values into Eq. 2.4:29 yileds the on-line and off-line transmitted powers as 1.22×10^5 W (3.05×10^{-2} j) and 1.17×10^5 W (2.93×10^{-2} j) respectively.

The use of a specular retroreflector has the effect of cancelling out the R^2 dependence. This is seen by the reduced on-line and off-line transmitted power requirements, which are 4.44×10^{-4} W (1.11×10^{-10} j) and 4.23×10^{-4} W (1.06×10^{-10} j) respectively.

As can be seen from the above results, the long path absorption scheme offers required sensitivities needed to monitor pollutant concentrations found in urban areas (.01 to 5 ppm). This is done with more than conservative transmitted power requirements. Unfortunately, this is accomplished at the expense of losing depth-resolved measurements.

2.5 Summary

A tabulated summary showing the relative merits for each LIDAR system considered in the comparison is given in Table 2.4:1. The compari-

son was made by first calculating the operating characteristics for the DASE system: an assumed minimum detectable change of received powers of 5 percent, the received power needed to observe the minimum detectable change (0.25 uW for each on-line and off-line wavelengths), an assumed range of 1000 m, and a depth resolution of 100 m. These conditions led to the attainable sensitivity of 0.029 ppm of NO_2 with moderate transmitted energy requirements of 9.88 mj (on-line) and 9.38 mj (off-line). Then, the required received powers were calculated for the above parameters, assuming output energies of 1/2 j in each lasing line.

Since the Raman, resonance Raman, and resonance fluorescence schemes require orders of magnitude higher output energy levels than the long path absorption and DASE methods, the received power was assumed to be equal to the minimum detectable power for our system, namely, 6.32×10^{-9} W. This was done in order to show that under optimum operating conditions, these systems still fall short of the long path absorption and DASE output energy requirements to detect the same pollutant concentration of NO_2 (0.029 ppm).

As can be seen, the long path absorption schemes require the least output energies to monitor a given pollutant concentration, or equivalently the best sensitivity for a given output energy. Unfortunately, this is accomplished at the expense of losing depth-resolved measurement capabilities. The DASE scheme, therefore, combines the spatial resolution offered in the Raman, resonance Raman, and resonance fluorescence schemes, with the greater attainable sensitivities of the long path absorption schemes.

LIDAR Meth.	Range (m)	Res. (m)	Concen. NO_2 (ppm)	Received Power		Required Transmitted Power		Required Transmitted Energy	
				On-Line (W)	Off-Line (W)	On-Line (MW)	Off-Line (MW)	On-Line (J)	Off-Line (J)
Raman	1000 *	100 *	0.029 *	*	6.32×10^{-9} *	*	1.77×10^{9} *	*	4.43×10^{8} *
Reson. Raman	1000 **	100 **	0.029 **	6.32×10^{-9} **	**	5.04×10^{3} **	**	1.26×10^{3} **	**
Reson. Fluor. (night)	1000 (100)	100 (100)	0.029 (0.1)	6.32×10^{-9} (6.32×10^{-9})		3.82×10^{2} (3.52×10^{-1})		9.55×10^{1} (8.80×10^{-2})	
Reson. Fluor. (day)	1000 (100)	100 (100)	0.029 (0.1)	6.32×10^{-9} (6.32×10^{-9})		3.82×10^{3} (3.52)		9.55×10^{2} (8.80×10^{-1})	
Long Path Abs. Topog.	1000	1000	0.029	15.8×10^{-6}	15.9×10^{-6}	1.22×10^{-1}	1.17×10^{-1}	3.05×10^{-2}	2.93×10^{-2}
Long Path Abs. Retro.	1000	1000	0.029	15.8×10^{-6}	15.9×10^{-6}	4.44×10^{-10}	4.23×10^{-10}	1.11×10^{-10}	1.06×10^{-10}
DASE	1000	100	0.029	15.8×10^{-6}	15.9×10^{-6}	2.00	2.00	5.0×10^{-1}	5.0×10^{-1}

( ): For realistic power requirements
*: Limited to less than 50m for detection of ambient pollution levels
**: Limited to less than 75m for detection of ambient pollution levels

TABLE 2.4:1   TABULATED COMPARISON OF MONOSTATIC LIDAR SCHEMES

44

CHAPTER 3   THE LIDAR SYSTEM

3.1   Introduction

The basic LIDAR system consists of a flashlamp-pumped dye-laser transmitter, and an optical receiver.[63]   Figs. 3.1:1a and b show a schematic for the combination. Two arrangements and modes of operation are possible. In one mode, signals at the "on" and "off" resonance absorption wavelengths were generated and detected sequentially. In the other mode they were generated and detected simultaneously. The arrangement shown in Fig. 3.1:1a is for sequential operation and that shown in Fig. 3.1:1b is for simultaneous.

3.2   Optical Receiver

The primary lens of the optical receiver is an acrylic Fresnel lens (purchased from Fresnel II, Inc.) mounted on a light-tight steel frame which was designed for the purpose. This lens is basically a flat thin piece of a plastic on which a series of concentric stepped zones extending from the center to the edge are molded. Fig. 3.2:1 illustrates the geometric relationship between the zones on the Fresnel lens and the surface of an ordinary lens. Each zone refracts the incident light so that the combined action of each refracting facet focuses light essentially in the same manner as a conventional lens.

The lens used has a focal length of 24 inches, a diameter of 15 inches, and a thickness of 1/8 inch. With concentric zones spaced approximately 125 grooves per inch, the lens is capable of forming a sharp image for objects near the optical axis. This is appropriate,

APERTURE

IRIS

FRESNEL LENS

HOOD

PHOTOMULTIPLIER

COLLIMATOR

SLIDE TO CALIBRATION SYSTEM

ELECTROMAGNETICALLY-CONTROLLABLE GRATING

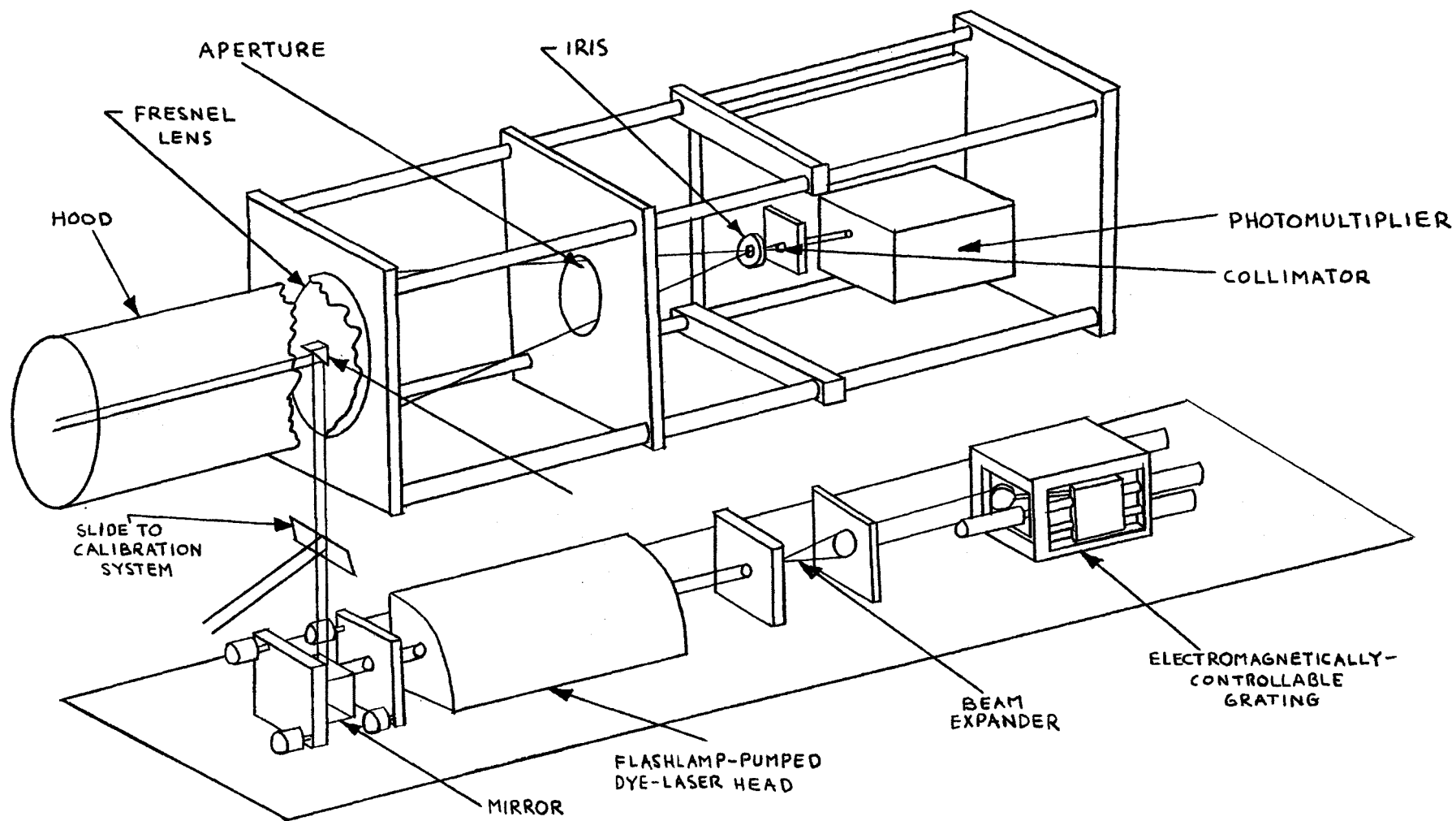BEAM EXPANDER

FLASHLAMP-PUMPED DYE-LASER HEAD

MIRROR

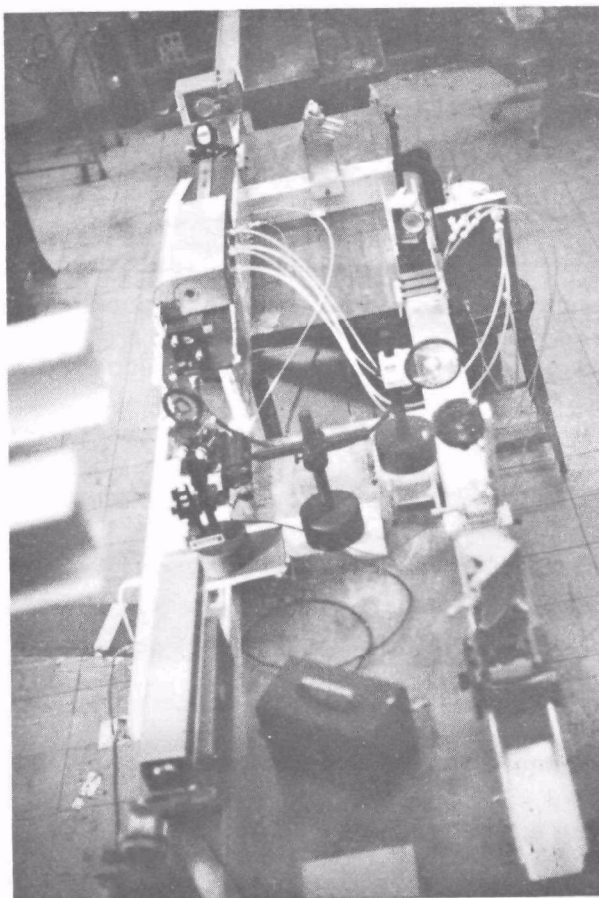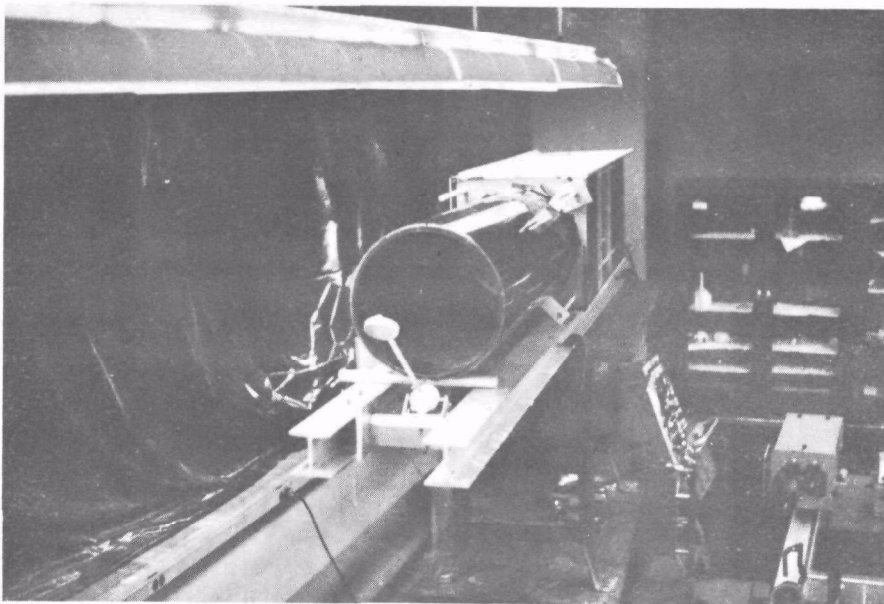FIGURE 3.1:1a   THE LIDAR SYSTEM FOR SEQUENTIAL OPERATION

FIGURE 3.1:1b PHOTOGRAPHS OF THE LIDAR SYSTEM FOR SIMULTANEOUS
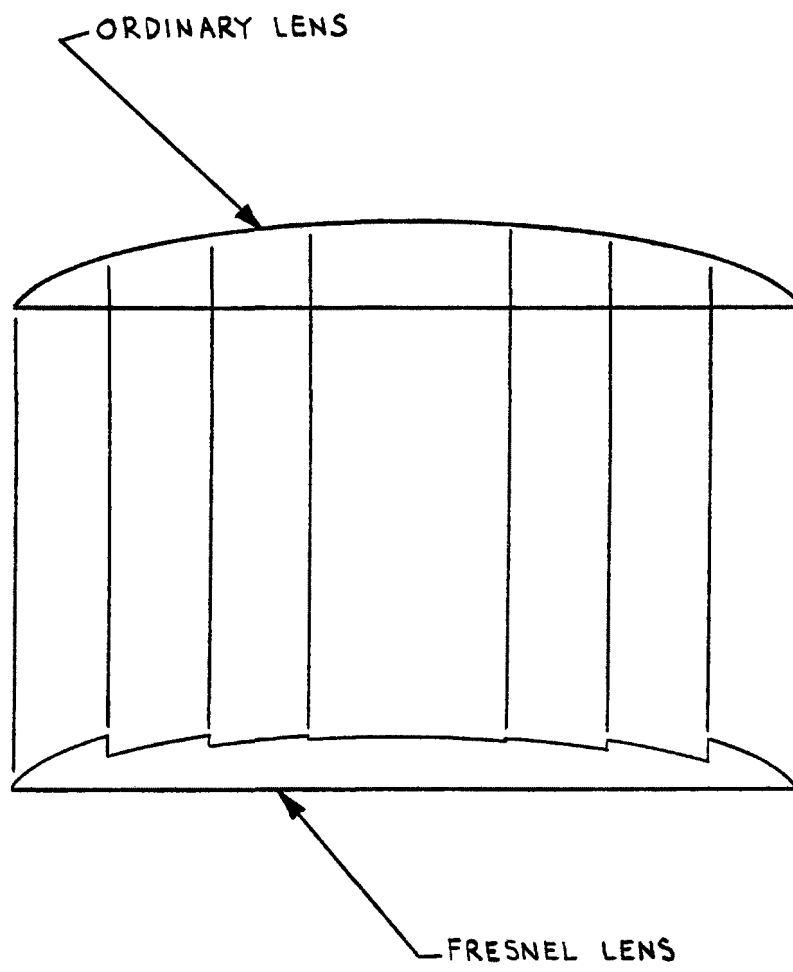OPERATION

47

FIGURE 3.2:1   FRESNEL LENS

since a LIDAR receiver does not require a wide field of view for col-
lecting the backscattered light from the region scanned.

For this Fresnel lens, the circle of least confusion for collimated
light directed parallel to the optical axis was measured and found to
be approximately one centimeter. In the plane containing the circle
of least confusion, the spatial distribution of the collected light is
a bright spot of the above diameter with the surrounding area weakly
illuminated by light spuriously scattered at the edges of the concen-
tric zones of the Fresnel lens. To eliminate the spurious light, an
iris was placed in the plane containing the circle of least confusion.
Since LIDAR receivers do not require a wide field of view, this remedy
does not pose a problem. The Fresnel lens used in this system costs
far less than a comparable parabolic mirror, yet its quality is certain-
ly acceptable for our LIDAR application.

The backscattered light collected by the Fresnel lens is then col-
limated by a 1.5 inch diameter lens, and for the sequential mode of op-
eration, passes through a 58 Å bandwidth three-period filter onto an
Amperex 56 AVP photomultiplier. The center wavelength of the filter
and its bandwidth are such that the "on" and "off" resonance absorption
wavelengths are both passed by it. To further reduce spurious light
pick-up, a three foot cylindrical lens hood is mounted on the front of
the receiver.

In the simultaneous wavelength mode of operation, the collimated
light entering the receiver is split by means of a partial reflector (beam
splitter) into two beams. Each of these beams is then directed to a separate
photomultiplier covered with a narrow filter of the appropriate fre-

49

quency. The photomultipliers used are Amperex type 56 AVP. See Figs. 3.2:2a and b. The interference filters have measured half bandwidths of 8.3 Å and 7.7 Å centered at 4478.5 Å and 4500 Å respectively. See Spec. Sheet 3.6:1.

The photomultiplier outputs, corresponding to the backscatter return signals are displayed on Tektronix type 549 oscilloscopes and recorded photographically.

3.3 The Dye Laser

3.3.1 The Laser Head

The basic laser system consists of a flashlamp-pumped organic-dye laser. The laser head is constructed in a coaxial arrangement in which the flowing dye is uniformily excited by an annular discharge surrounding the active medium. See Figs. 3.3:1a and b. The laser head, model DL2100B, and discharge circuitry was purchased from the Phase-R Company, and was chosen for maximum energy output and shortest possible pulse width. Fig. 3.3:1b shows the laser head situated in the LIDAR system, and Fig. 3.3:2 shows a typical output pulse.

The organic dye, 7-diethylamino-4-methyl coumarine, dissolved in ethanol was used as the lasing medium. A concentration of 3 X 10^{-5} M/l was found to give maximum output energy consistent with a laser linewidth that was less than the halfwidth of the absorption peak of NO_2 to be measured, i.e., less than approximately 10 Å for the 4478.5 Å absorption peak. In this manner, it was possible to maximize the return signal, thereby increasing range, and still retain the maximum difference between absorption peak and trough, and thus attain the sen-

50

FRESNEL
LENS

APERTURE

IRIS

MIRROR

INTERFERENCE
FILTERS

PHOTOMULTIPLIERS
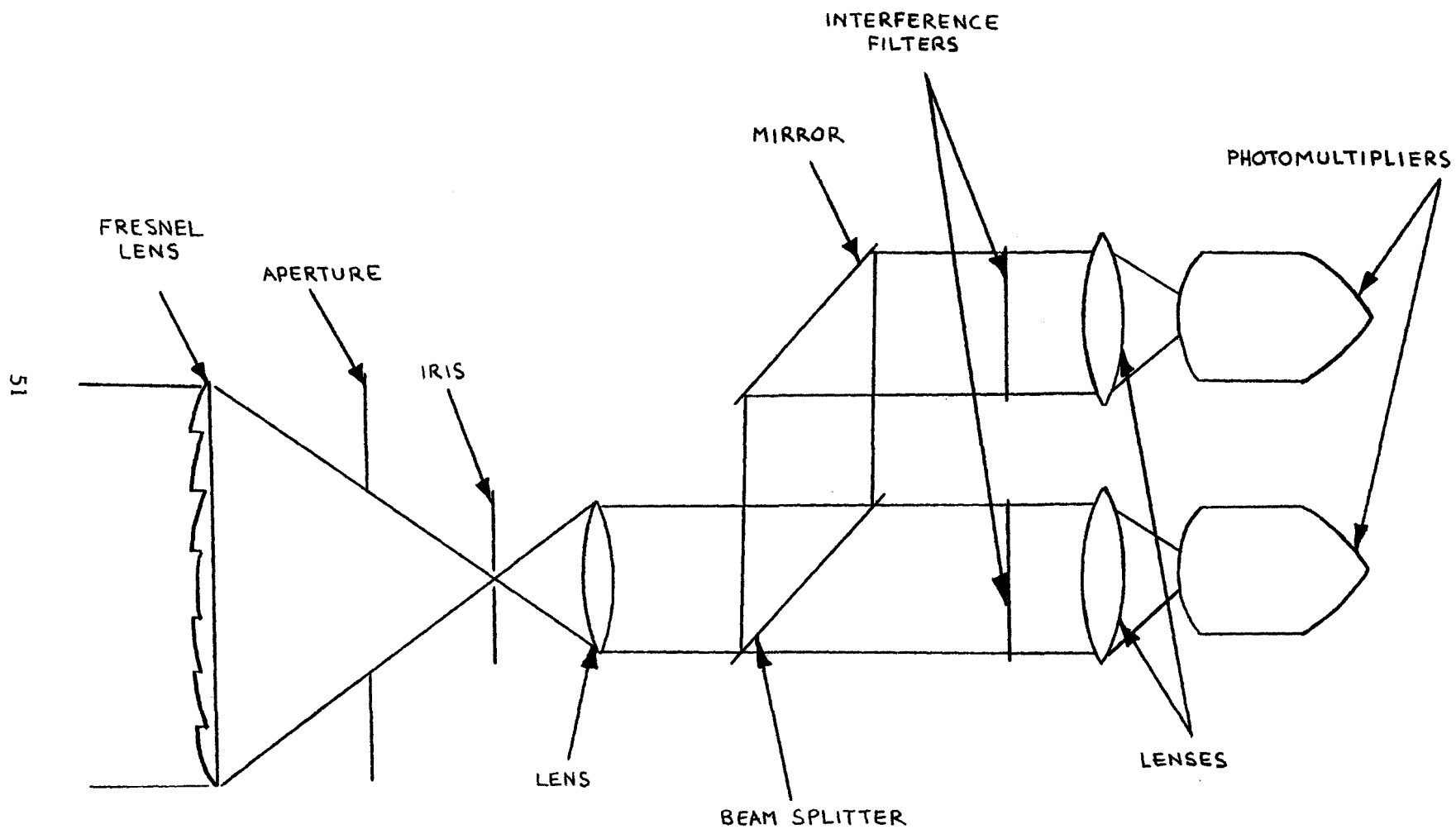
LENS

BEAM SPLITTER

LENSES

FIGURE 3.2:2a   THE OPTICAL RECEIVER SYSTEM FOR SIMULTANEOUS OPERATION
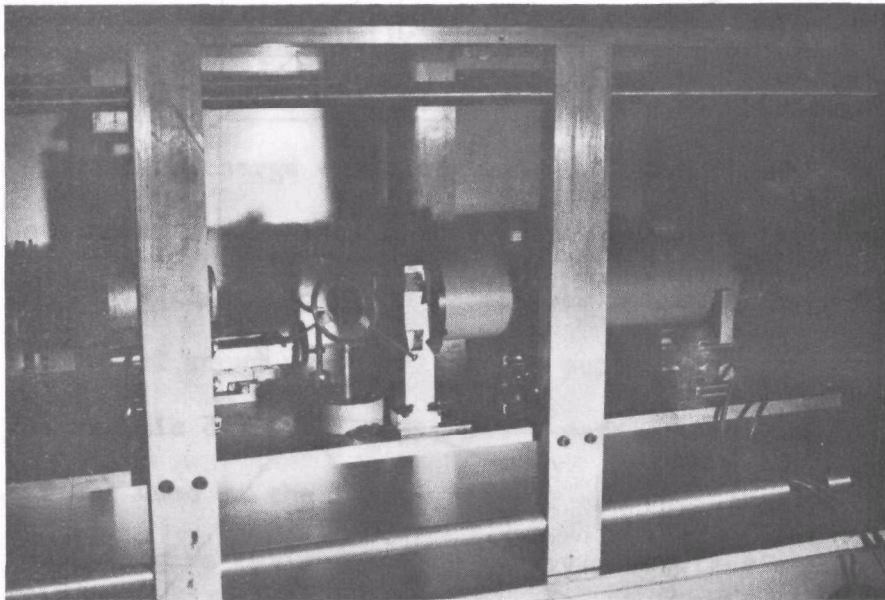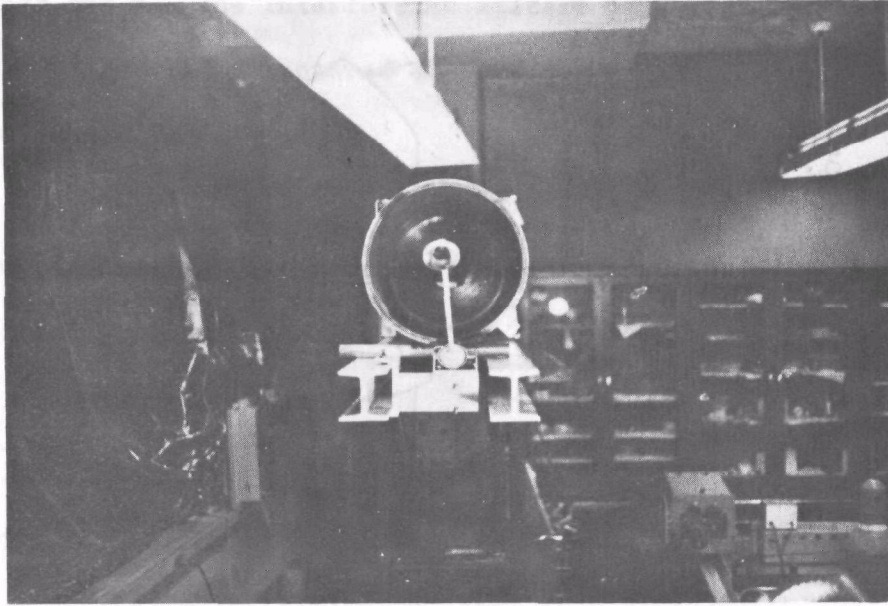
FIGURE 3.2:2b PHOTOGRAPHS OF THE OPTICAL RECEIVER SYSTEM FOR
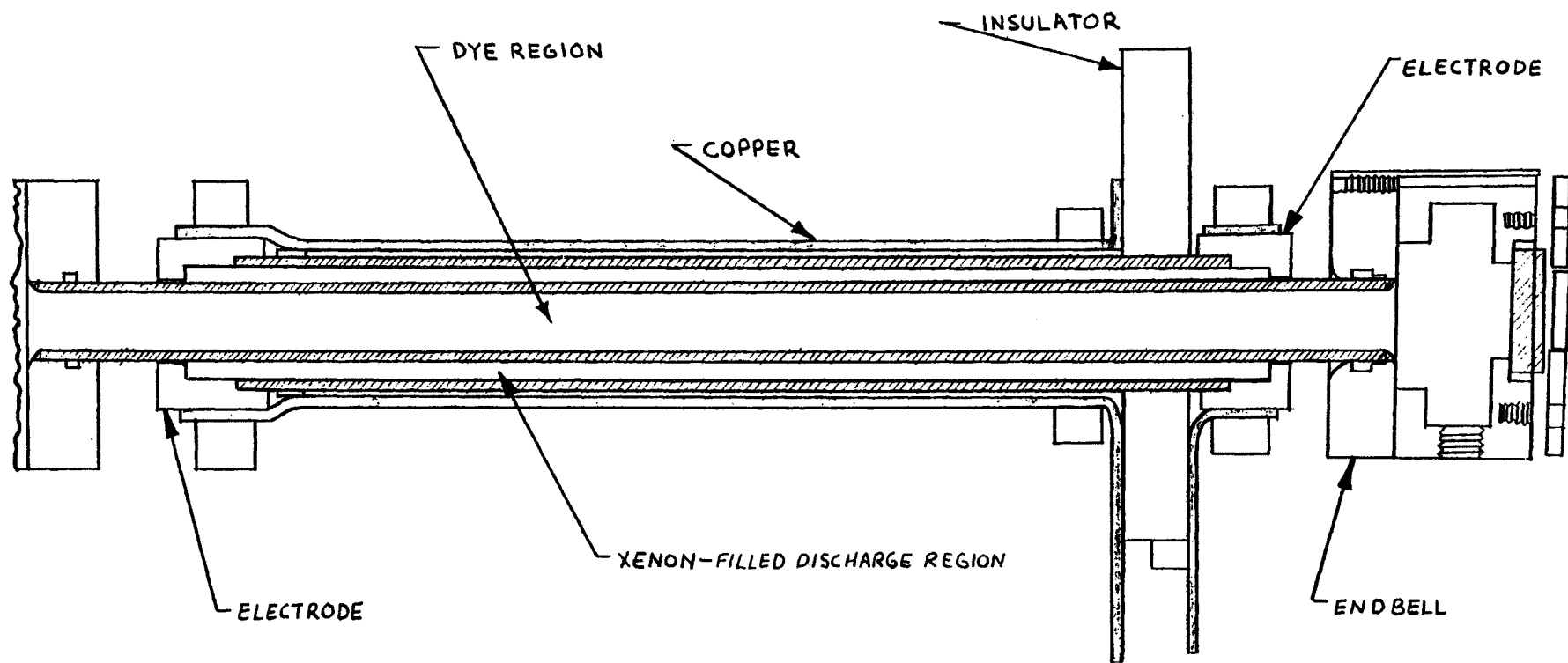
SIMULTANEOUS OPERATION

52

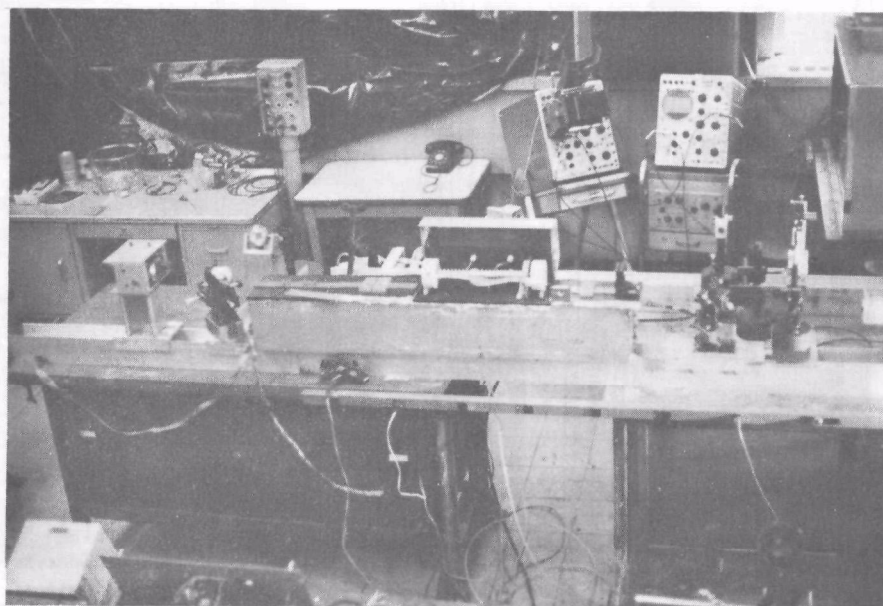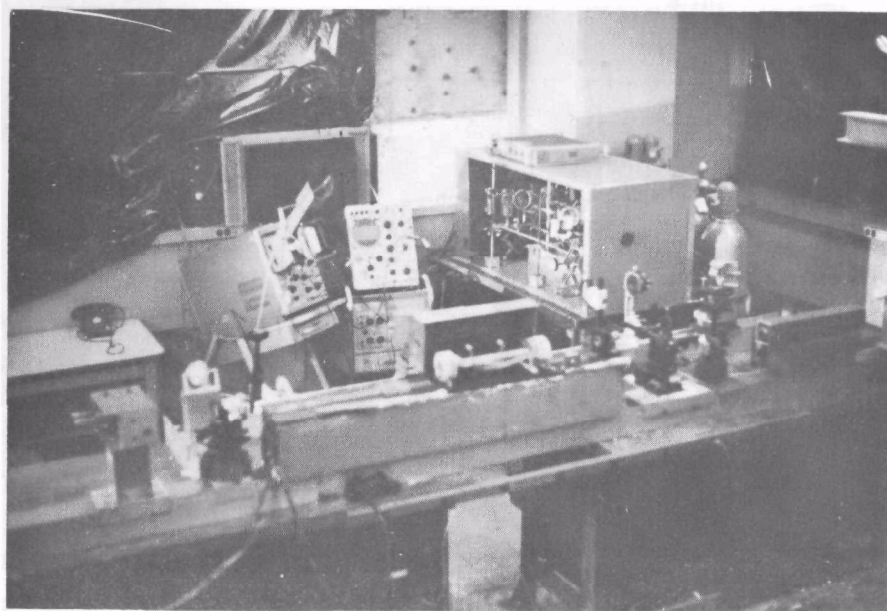FIGURE 3.3:1a   COAXIAL ARRANGEMENT OF THE FLASHLAMP-PUMPED DYE-LASER HEAD

53

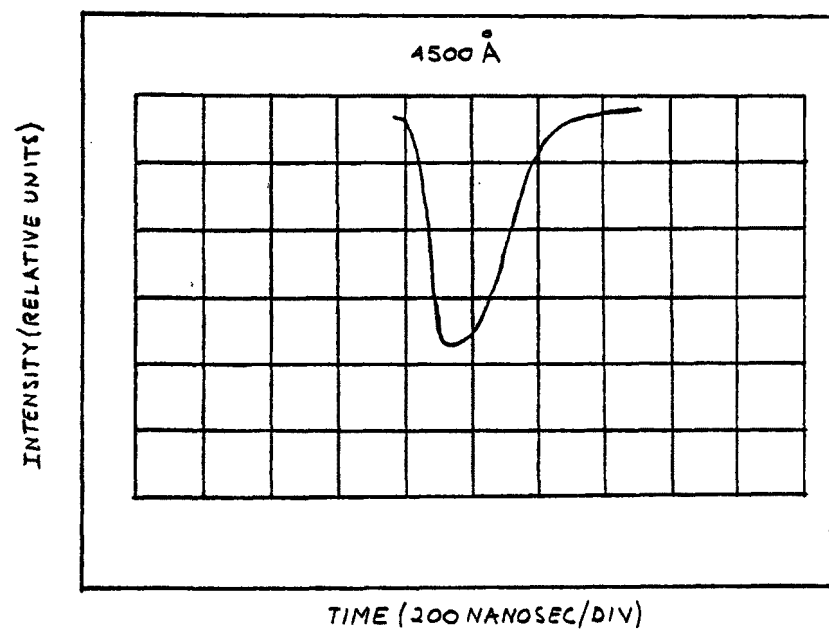FIGURE 3.3:1b PHOTOGRAPHS OF THE LASER HEAD SITUATED IN THE LIDAR
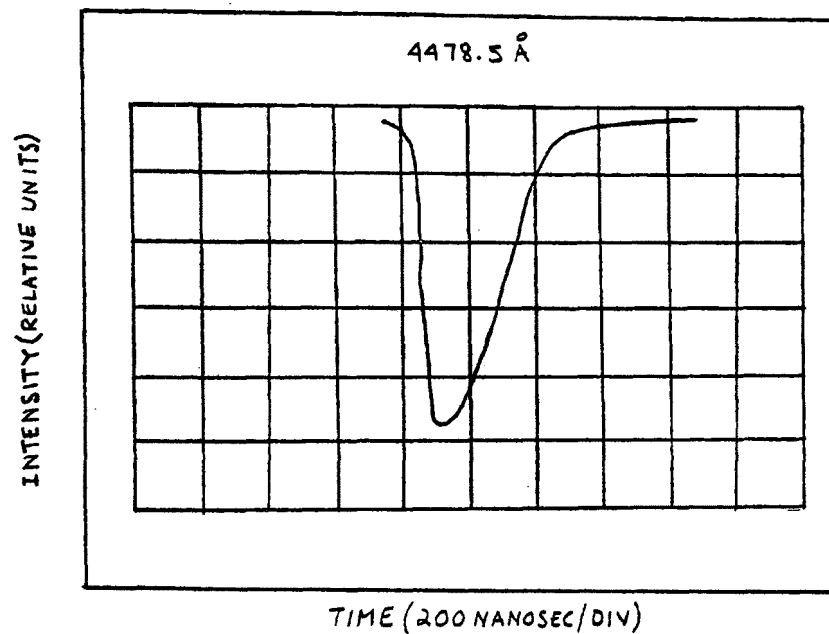SYSTEM

FIGURE 3.3:2   TYPICAL FLASHLAMP-PUMPED DYE-LASER OUTPUT PULSE

sitivities that the system is capable of.

3.3.2 Dye Laser Mechanism--Brief Description

Organic molecules possess a lowest excited singlet state, $^1S_0^*$, and fluorescsnce when it occurs, originates from this state. In making a fluorescent transition the molecule reverts back to its ground state, $^1S_0$, while simultaneously emitting radiation.

The spectrum of the fluorescent radiation from an organic dye often has more than one maximum, and it usually spans a region no less than several hundred angstroms wide. The reason for this large bandwidth is that the radiation is actually made up of hundreds of components, corresponding to transitions originating from various sublevels of the first excited singlet state and terminating at various sublevels of the ground state. These sublevels are associated with specific vibrations of the molecule as a whole. See Fig. 3.3:3. Since some of the vibrational sublevels of the ground state may be high enough in energy so that they are normally unoccupied, a population inversion sufficient for laser action can be established between the states from which fluorescence originates and some of the higher vibrational levels of the ground state.

Once threshold conditions are reached, the laser light that is produced has frequencies centered about one of the broad fluoresence peaks. The bandwith of such broadband operation can range up to 200 Å for flashlamp-pumped dye lasers.

To reduce the naturally large bandwidth of the flashlamp-pumped dye laser output, a tuning element such as a diffraction grating can be
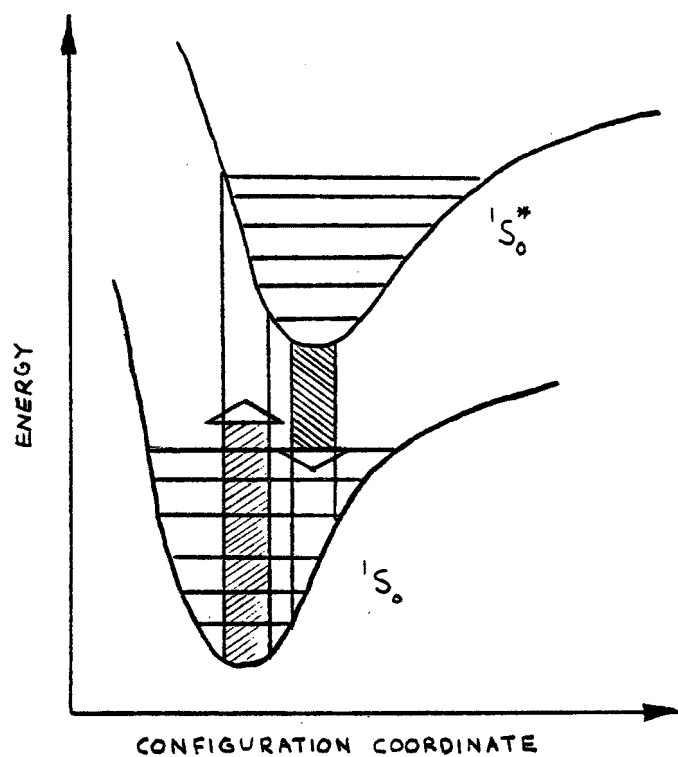
FIGURE 3.3:3 ENERGY LEVELS OF ORGANIC DYE MOLECULES

placed in the laser cavity. With the proper choice of grating characteristics, such as blaze wavelength, grooves per millimeter, and power-density handling capabilities, etc., the desired laser frequency and bandwidth are attainable, and may be chosen to match the absorption peak and troughs for NO_2.

3.3.3 Intra-Cavity Grating for Wavelength Selection

To obtain laser outputs at the required wavelengths, 4478.5 Å and 4500 Å, and linewidths, a grating with the specifications given in Spec. Sheet 3.6:1 was chosen, tested, and found suitable. In both sequential and simultaneous modes of operation, gratings are used in the Littrow configuration with the Blaze angle in the first order. In this manner, all the other orders extinguish and the diffracted energy is concentrated in the first order (at the wavelength desired).

Gratings have different efficiencies (percentage of light incident on a grating that is diffracted into the desired order) for light that is polarized perpindicularly or in parallel to the groove profile. For the gratings used, perpindicularly polarized light gives the better efficiency. See Spec. Sheet 3.6:1. Since a polarizing element is inserted intra-cavity for the simultaneous mode of operation, this factor must be taken into account.

For both modes of operation the bandwidth of the laser lines obtained are determined by the dispersion of the grating and the effective aperture created by the geometry of the lasing medium, which in turn depends upon the distance of the grating from the laser head. This is readily seen in Fig. 3.3:4. The dispersion of the grating is the angular sepa-
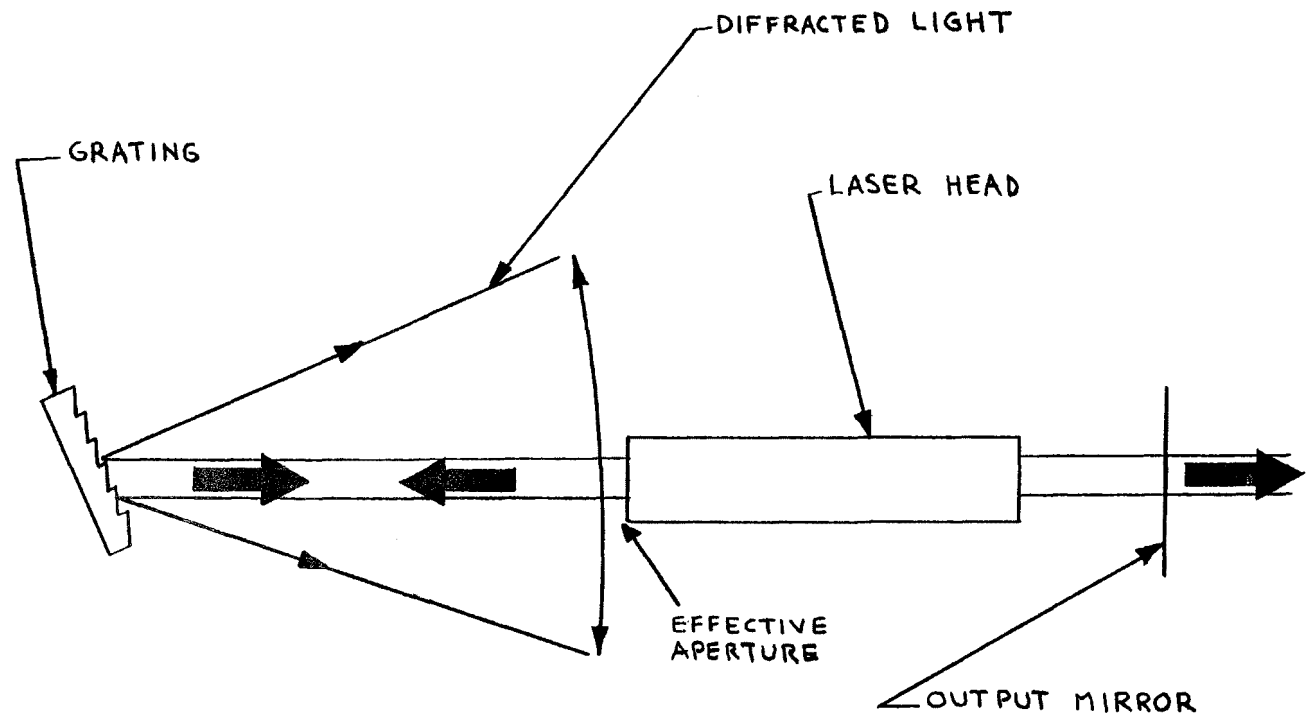
FIGURE 3.3:4   DISPERSION OF GRATING AND EFFECTIVE APERTURE CREATED BY THE LASER HEAD

ration obtained for two different radiations. Therefore, the farther the grating is from the laser head containing the lasing medium the smaller the lasing bandwidth.

3.4 Experimental Arrangement for Sequential Operation

Sequential operation of the dye laser at two desired wavelengths was achieved with the arrangement shown in Figs. 3.3:1 and 3.4:1.

The grating at one end of the laser cavity is used to obtain the desired wavelengths of laser oscillation. With a overall cavity length of approximately 2.5 m, and a 30 percent output mirror, the desired wavelengths at 4478.5 Å and 4500 Å (on and off resonance absorption respectively) are obtained with approximately 5 Å linewidths.

Mechanical stops are adjusted to define the grating orientation at these two wavelengths. The grating is then switched from the setting for one wavelength to the other by means of an electromagnetic drive after each firing of the laser. The time between shots is approximately 5 seconds, the time required for the capacitors to recharge after firing a pulse.

3.5 Simultaneous Two-Wavelength Operation
3.5.1 The Need for Simultaneous Two-Wavelength Operation

Thermal effects and consequent index changes in the atmosphere cause perturbations in both the outgoing and backscattered signals. In addition, particulate drift in existing winds can also cause fairly rapid changes of the scene being scanned by the LIDAR beam. Both these factors argue in favor of the use of simultaneous two-wavelength

60

DETECTORS

SPECTROMETER

ELECTROMAGNETICALLY-
CONTROLLABLE
GRATING

SLIDE

CALIBRATION
CELL

GRATING-CONTROL
CIRCUIT

SLIDE

OSCILLOSCOPES

FLASHLAMP-PUMPED
DYE-LASER
HEAD

PHOTODIODE

OUTPUT
MIRROR

BEAM
EXPANDER

PELLICLE

LASER OUTPUT
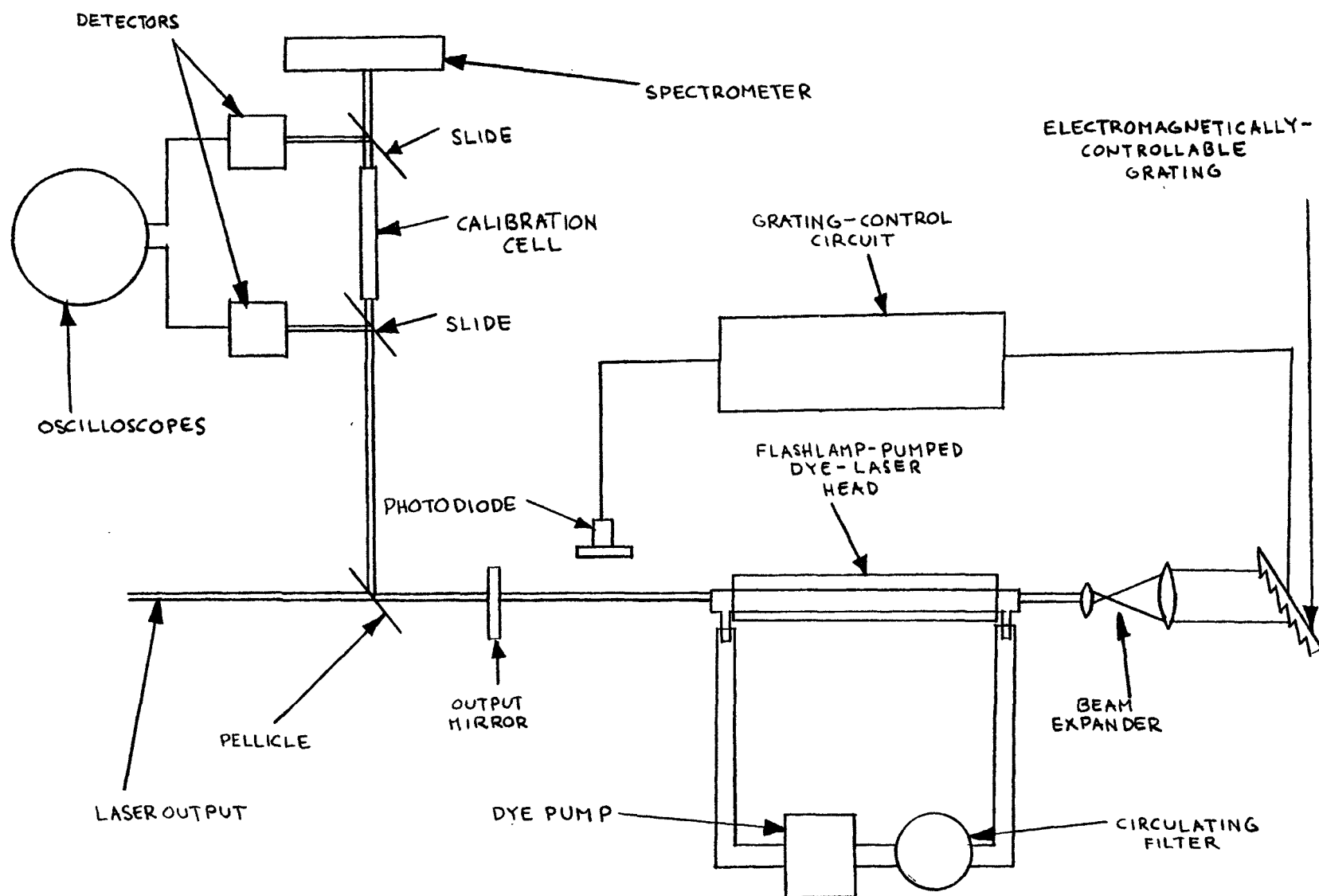
DYE PUMP

CIRCULATING
FILTER

FIGURE 3.4:1   THE OVERALL TRANSMITTING SYSTEM WITH CALIBRATION SETUP FOR SEQUENTIAL OPERATION

LIDAR operating mode.

The thermal factors affecting the signals are summarized below:[58]

1. Beam steering--angular deviation of the beam from the line-of sight path, causing the beam to miss the receiver. See Fig. 3.5:2.

2. Image dancing--variations in the beam-arrival angle, causing the focus to move in the image plane.

3. Beam spreading--small angle scattering, incresing the beam divergence and causing a decrease in spatial power density at the receiver. See Fig. 3.5:1.

4. Beam scintillation--small scale destructive interference with-in the beam cross section, causing variations in the spatial power density at the receiver. See Fig. 3.5:3.

The effects of scintillation on laser beam propagation have been studied both experimentally and theoretically.[62,64] However, atmospheric scintillation effects involving 180-degree backscatter have received relatively little attention either theoretically or experimentally.

A recent survey article by Lawrence and Strohbehn demonstrates that under most conditions the power spectrum of intensity fluctuations for one-way propagation decreases above approximately 100 HZ, and is quite small above 1000 HZ.[64] In the abscence of data for two-way propagation, it is reasonable to assume that the high-frequency power spectra for one-way and two-way propagation are the same. Hence, the atmosphere can perhaps be considered stable insofar as scintillation is concerned for time intervals smaller than 1 ms.[62]
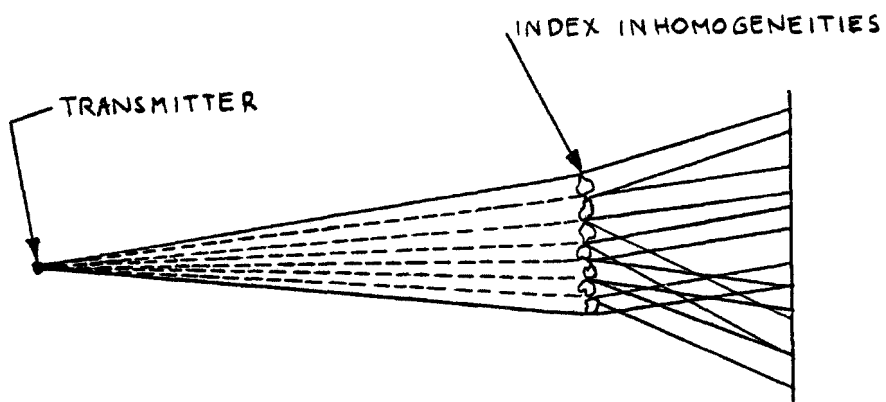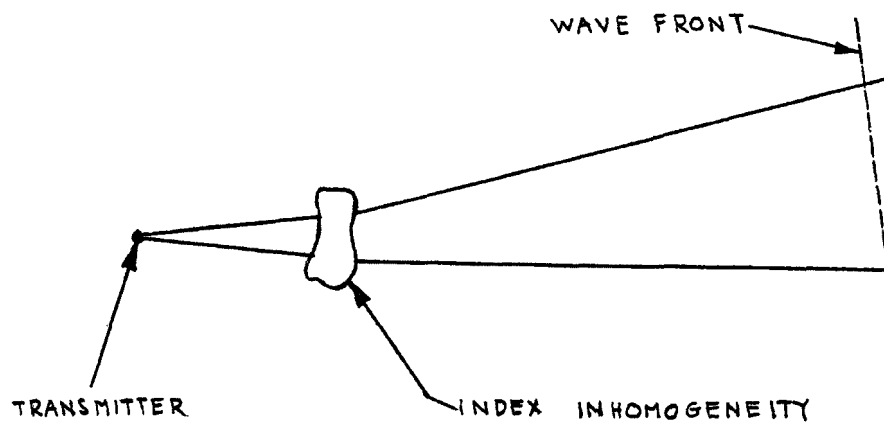
FIGURE 3.5:1 BEAM SPREADING

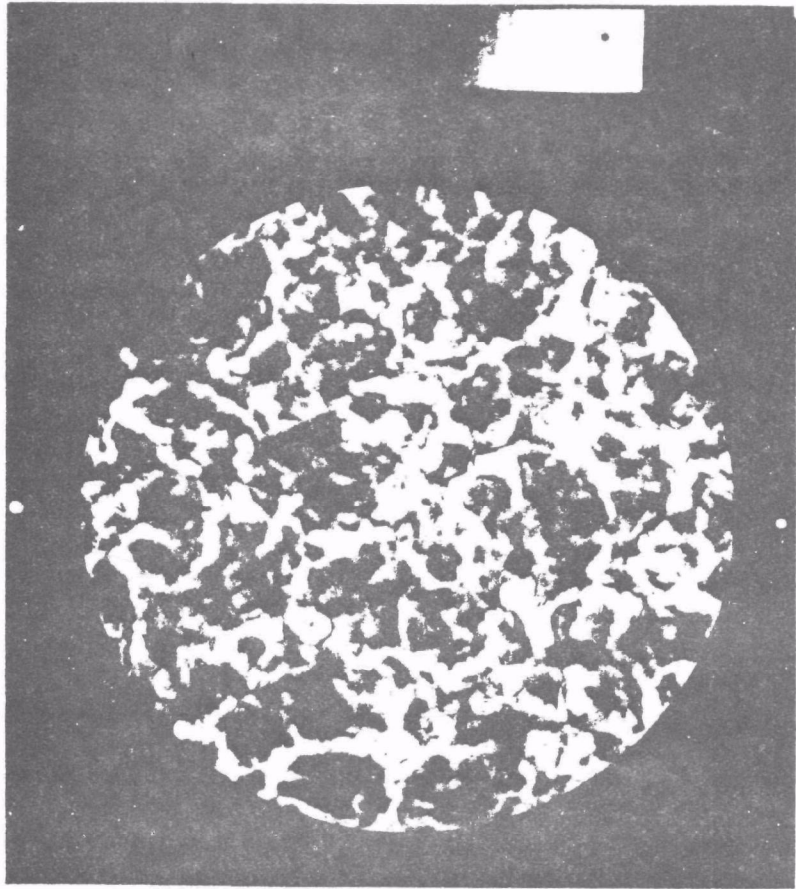**FIGURE 3.5:2** BEAM STEERING

63

FIGURE 3.5:3   BEAM SCINTILLATION [58]

Therefore, to be unaffected by scintillation the differential absorption measurement must be completed within this time interval. The optimum manner to meet this requirement is to emit two pulses (of slightly differing wavelengths) simultaneously. Spatial fluctuations within each sampled depth will be averaged out for each pulse, and in any case variations from one sampled depth to another will be the same for both wavelengths, and therefore will not affect the results.

3.5.2 Cavity Design

3.5.2.1 Introduction

To obtain laser action at the two wavelengths simultaneously, the arrangement shown in Figs. 3.5:4a and b, with a polarizing beam-splitting prism in the laser cavity, was evolved and used successfully.[65,66] With the prism splitting the light into two beams polarized at right angles to each other, each of the two wavelengths lases along one of the polarizations. Competition, in the form of bandwidth changes, between the two wavelengths is observed and is discussed in Sect. 3.6.

Two types of polarizing beam splitters were tested for this application:

1. a polarizing beam-splitting cube utilizing dielectric coatings,
   and

2. an air-spaced Glan-Taylor prism.

While both provided simultaneous laser action for close-lying wavelengths in the 4500 $\overset{\circ}{A}$ spectral region, it was found that each suffered some drawbacks. Both types of beam splitters are examined further below.
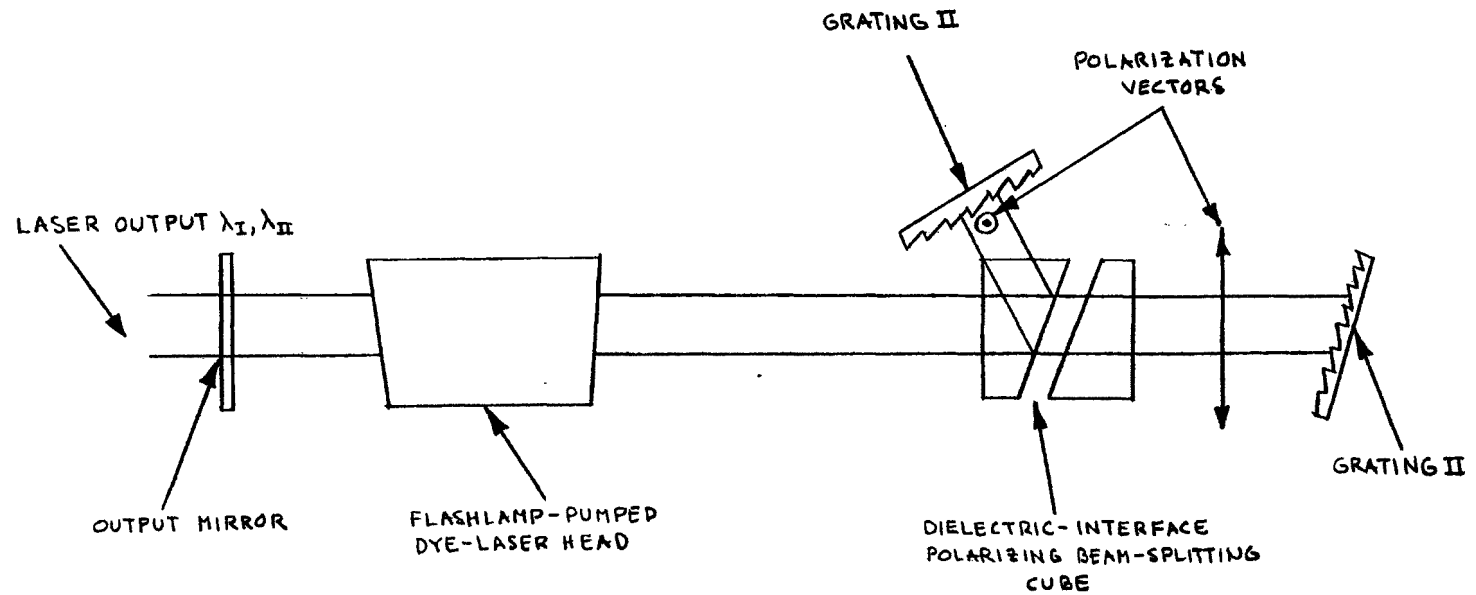
FIGURE 3.5:4a OPTICAL ARRANGEMENT FOR SIMULTANEOUS TWO-WAVELENGTH OUTPUT
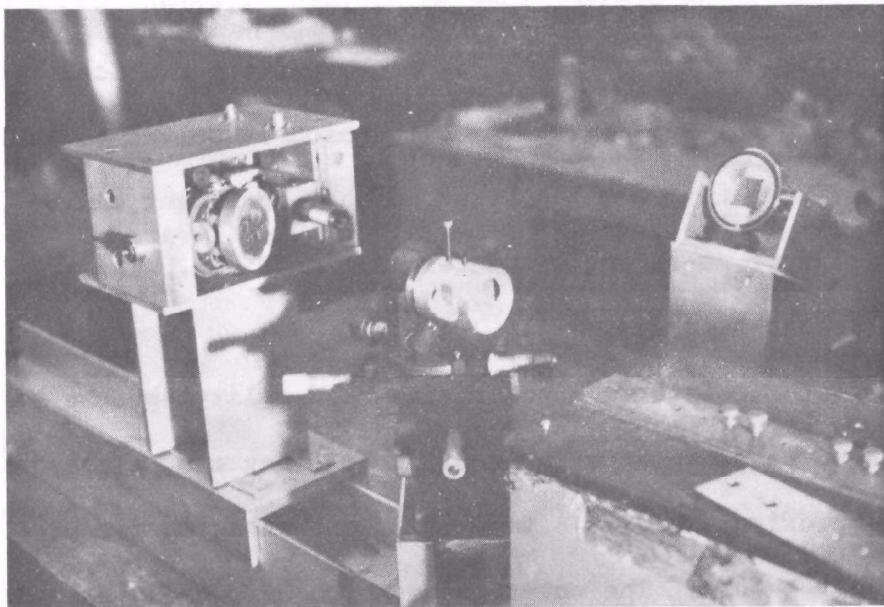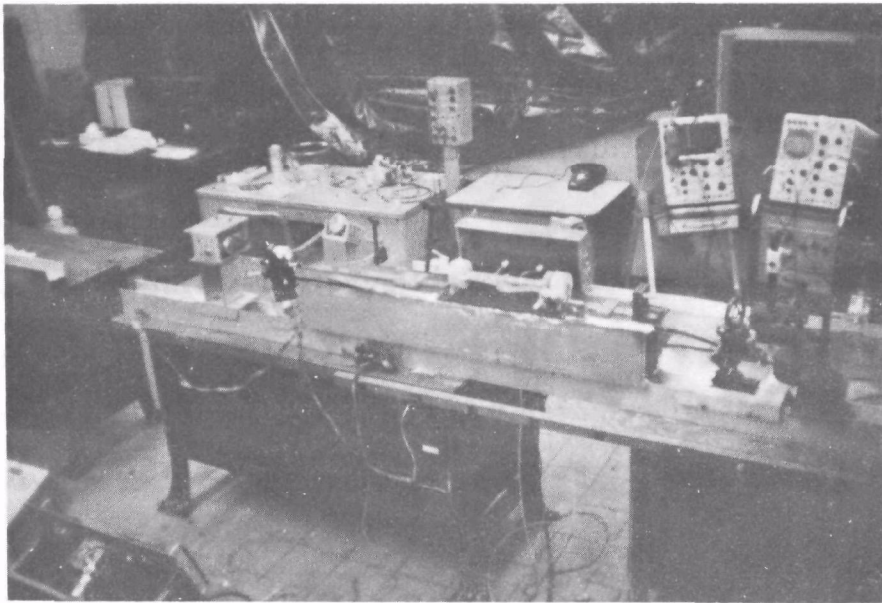
FIGURE 3.5:4b PHOTOGRAPHS OF THE OPTICAL ARRANGEMENT FOR SIMULTANEOUS
TWO-WAVELENGTH OUTPUT

3.5.2.2 Dielectric-Interface Polarizing Beam-Splitting Cube

The principle of this device is that it is always possible to find an angle of incidence so that the Brewster condition for an interface between two materials of differing refractive index is satisfied. When this occurs, the reflectance for the parallel-plane (p) of polarization vanishes. Perpindicularly-polarized (s) light is partially reflected and transmitted. To increase the s-reflectance, retaining the p-transmittance at or very near unity, the two materials are then made into a multilayer stack. The layer thicknesses are quarter-wave optical thicknesses at the appropriate angle of incidence.

When the Brewster angle for normal thin-film materials is calculated, it is found to be greater than 90 degrees referred to air as the incident medium. In other words, it is beyond the critical angle for the materials. This presents a problem which is solved by building the multilayer filter into a glass prism so that the light can be incident on the multilayer at an angle greater than critical. The type of arrangement is shown in Fig. 3.5:5.

The dielectric-interface polarizing beam-splitting cube tested was found to have an acceptance angle of up to 5 degrees, a passband extending from approximately 2245 Å to 6739 Å, and whose center wavelength is approximately 4490 Å. The entrance and both exit faces were polished to $\lambda/10$, and were antireflex coated for 4490 Å.

Utilizing the dielectric-interface polarizing beam-splitting cube, simultaneous two-wavelength operation was readily achieved. Fig. 3.5:6 is a picture taken from a 1/2 m Jarrell-Ash scanning spectrometer, and shows the two beams of close-lying wavelengths (the signal to the right is
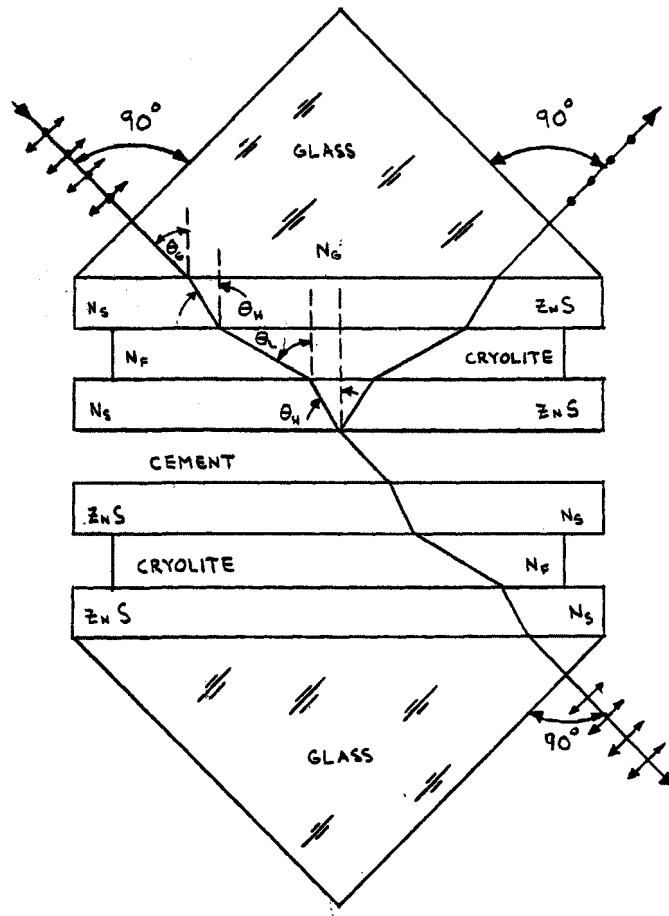
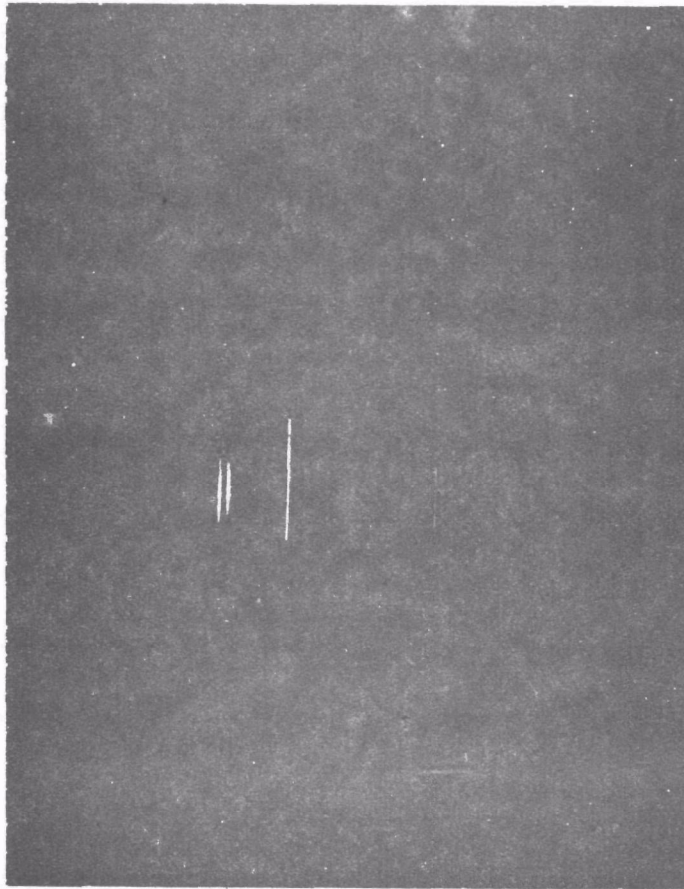**FIGURE 3.5:5 DIELECTRIC-INTERFACE POLARIZING BEAM-SPLITTING CUBE**

69

FIGURE 3.5:6 SPECTROMETER PHOTOGRAPH OF THE SIMULTANEOUS
TWO-WAVELENGTH OUTPUT UTILIZING THE DIELECTRIC-
INTERFACE POLARIZING BEAM-SPLITTING CUBE

centered at 4478.5 Å and to the left at 4500 Å) operating in the simultaneous mode, and obtained using the dielectric-interface polarizing beam-splitting cube. Both beams have output energies of approximately 100 mj, and bandwidths of 5 Å.

3.5.2.3 Air-Spaced Glan-Taylor Prism

The power handling capabilities of the air-spaced Glan-Taylor prism far exceed that of the dielectric-interface prism, since the medium sandwitched betweem the two prisms is air rather than a delicate dielectric coating. This prism is in fact comprised of two linearly birefringent calcite ($CaO \cdot CO_2$) prisms separated by the air gap.

In each prism the optic axis is perpindicular to the incident beam and to the lateral faces. The operation of the device may be readily understood in view of Fig. 3.5:7. This shows the air-spaced prism, its optic axis, and the incident unpolarized beam. When an unpolarized laser beam is incident upon the input face, two refracted orthogonally linearly-polarized beams are produced. The E-ray, the refracted beam whose polarization direction is parallel to the optic axis, experiances no change in index as it propagates through the prism-air-gap-prism combination.

The O-ray, the refracted beam whose polarization direction is perpindicular to the optic axis, experiences a large change in index at the calcite-air-gap interface and is thus totally internally reflected.

Use is made of both the E and O-rays to simultaneously obtain laser action on beams polarized at right angles to each other with gratings terminating the laser cavities beyond each prism. The optical arrange-
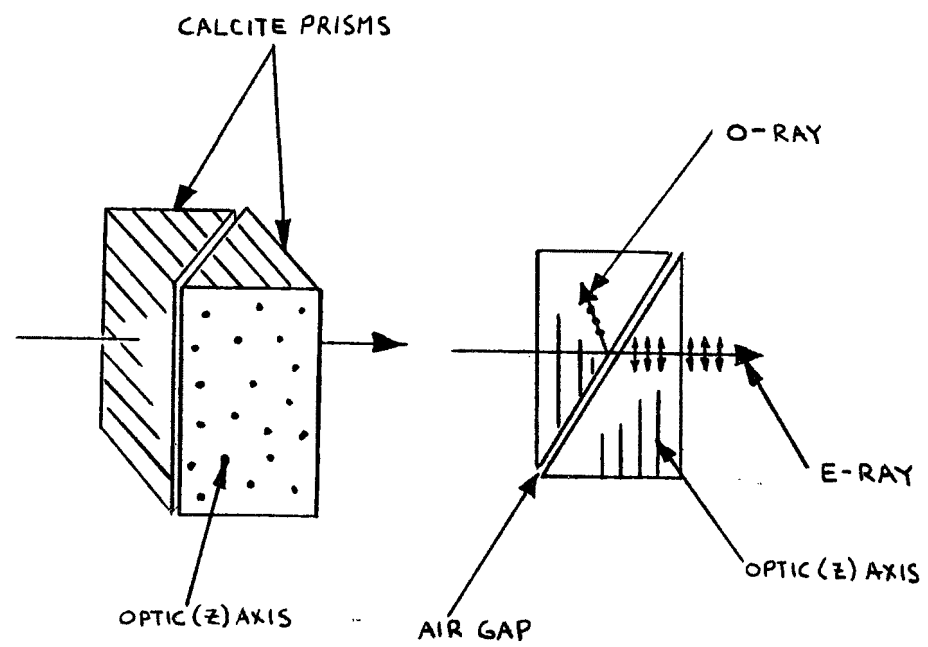
71

CALCITE PRISMS

O-RAY

E-RAY

OPTIC (Z) AXIS

OPTIC (Z) AXIS

AIR GAP

FIGURE 3.5:7 **AIR-SPACED GLAN-TAYLOR PRISM**

ment is shown in Fig. 3.5:4.[65,66]

In the manufacture of the air-spaced prism it was only possible to polish the input face and the axial output face to within $\lambda/4$ because of the crystal structure. The lateral faces are perpindicular to the optic axis, and since calcite belongs to the hexagonal crystallographic system, attempts to polish these faces to better than $\lambda/4$ would result in hexagonal pitting, giving rise to large scattering losses.

The high losses on the lateral face meant that for geometrically identically optical arrangements the low-loss axial resonator dominated, and laser action was restricted to it. When the axial resonator was blocked however, laser action was also obtainable in the lateral resonator.

By greatly reducing the off-axial resonator length it was possible to obtain laser action simultaneously in both resonators. Under these conditions, competition effects were clearly observed between the two resonators. Fig. 3.5:8 shows simultaneous two-wavelength operation as displayed in the spectrometer using the air-spaced Glan-Taylor prism.

Thus, when the axial resonator was blocked the output energy of the lateral resonator increased and vice versa. Similar competition effects were previously reported.[65-69] The interaction between the two laser beams of perpindicular polarizations in the amplifying medium is possible because the orientation relaxation time of the dye molecule (approximately 300 ps in ethanol) in the solvent is much shorter than the lifetime of the first excited singlet state (approximately 5 ns).[70,71]

Because of the high losses associated with the lateral faces, it was found that when conditions were arranged to obtain equal energies
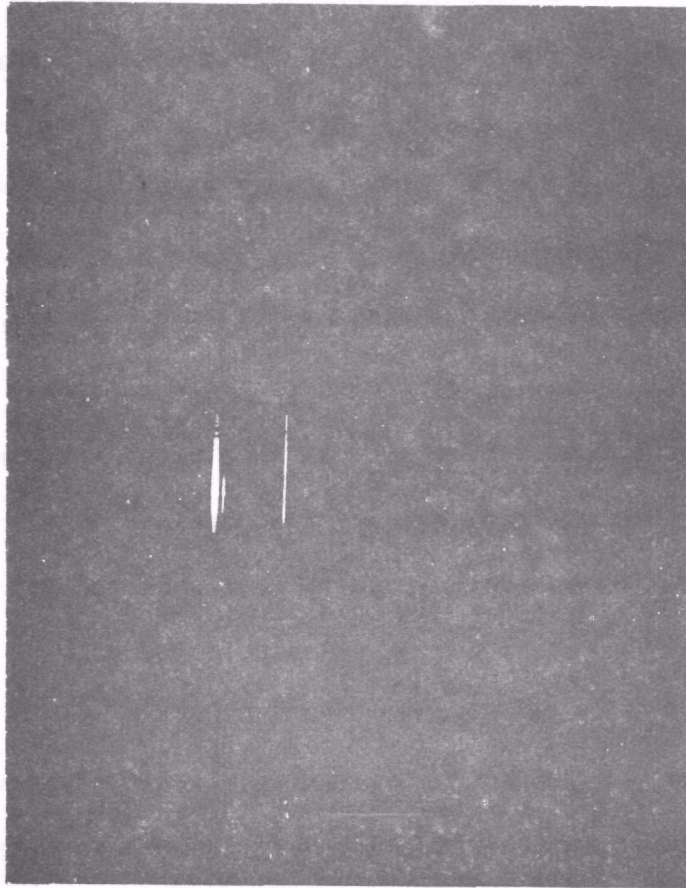
FROM LEFT TO RIGHT: LASER LINES, 4500 Å, 4478.5 Å; HG LINES, 4358 Å, 4078 Å, AND 4047 Å

FIGURE 3.5:8 SPECTROMETER PHOTOGRAPH OF THE SIMULTANEOUS TWO-
WAVELENGTH OUTPUT UTILIZING THE AIR-SPACED GLAN-
TAYLOR PRISM

and equal linewidths from both resonators simultaneously, the output energies were too low to be useful. See Fig. 3.5:9.

Thus, in spite of the higher power-density handling capabilities of the air-spaced prism, it was decided to abandon its use in favor of the dielectric-interface prism.

With this prism simultaneous two-wavelength outputs of approximately 100 mj were obtained at 4478.5 Å and 4500 Å with linewidths of approximately 5 to 6 Å. Fig. 3.5:6 shows the simultaneous outputs displayed on the spectrometer. It was with the dielectric-coated prism that the field experiments described in later sections were carried out.

3.6 Calibration

3.6.1 The Need for Calibration

In order to obtain accurate pollution measurements, it is necessary that we know from shot to shot what the absorption cross section is for a given pollutant for the actual laser bandwidth emitted. In performing the experiment to achieve simultaneous laser action, it was noticed that the output bandwidths varied from shot to shot. These variations in bandwidths depend upon:

1. The bias voltage applied to the charging circuit, i.e., the energy discharged in each flash.

2. The length of time between shots.

3. The degradation of the dye molecules due to repeated exposure to the pump source.

Two experiments were performed to determine:

75
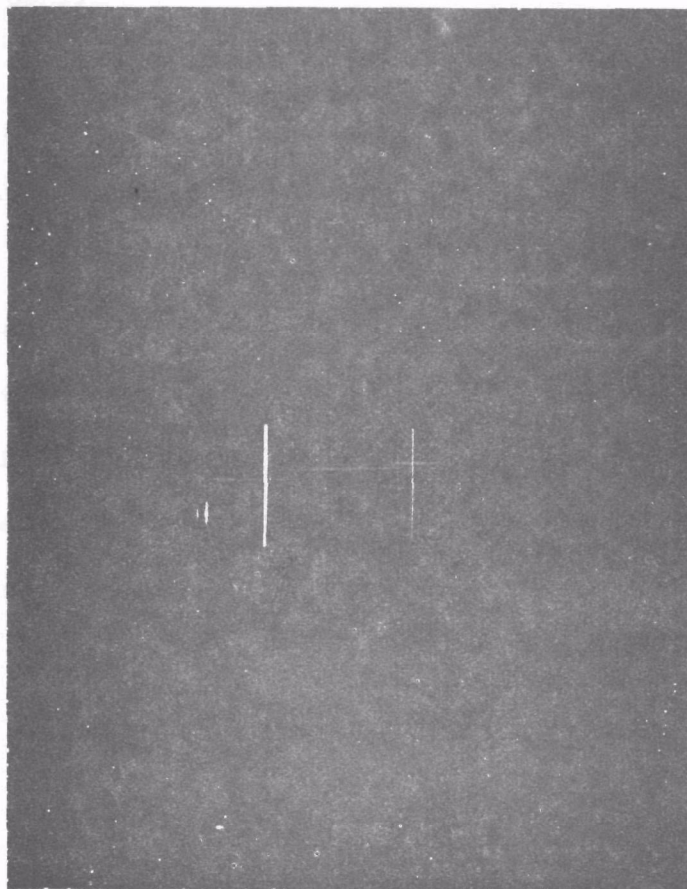
FROM LEFT TO RIGHT: LASER LINES, 4500 Å, 4478.5 Å; HG LINES, 4358 Å, 4078 Å, AND 4047 Å

FIGURE 3.5:9 SPECTROMETER PHOTOGRAPH OF THE SIMULTANEOUS TWO-WAVELENGTH OUTPUT UTILIZING THE AIR-SPACED GLAN-TAYLOR PRISM FOR EQUAL OUTPUT ENERGIES IN EACH LASING LINE

1. If any frequency pulling occurs between the two lasing wavelengths.

2. The extent of any laser bandwidth variations and frequency shifts from shot to shot for the simultaneous mode of operation. The purpose of this experiment was to determine whether a calibration system was needed to monitor each of the outgoing wavelengths.

The experimental setup is shown in Figs. 3.6:1a and b. The laser is set for simultaneous operation. The two perpindicularly polarized beams are diverted by a beam-steering mirror mount through a variable polarizer, a variable neutral density filter, and a 1 m focal length lens which focuses it onto a Corning 3850 filter and diffusion plate. Following the diffusion plate is a 1/2 m Jarrell-Ash scanning spectrometer whose input and output slits are set at 10 u each. A camera attachment is used and the results are recorded photographically.

To observe any frequency shifts, the laser lines were compared with known Hg lines: 4047 Å, 4078 Å, and 4358 Å. The Hg lines were initially exposed onto the film by directing the output of an Hg lamp into the spectrometer through the 3850 Corning filter which blocked out any unwanted harmonics. The laser lines were then superimposed onto the film which remained stationary during both exposures.

In the first experiment, an investigation was made of whether frequency shifts occur between the cases where each wavelength lases separately and when both lase simultaneously (with the same grating settings naturally).

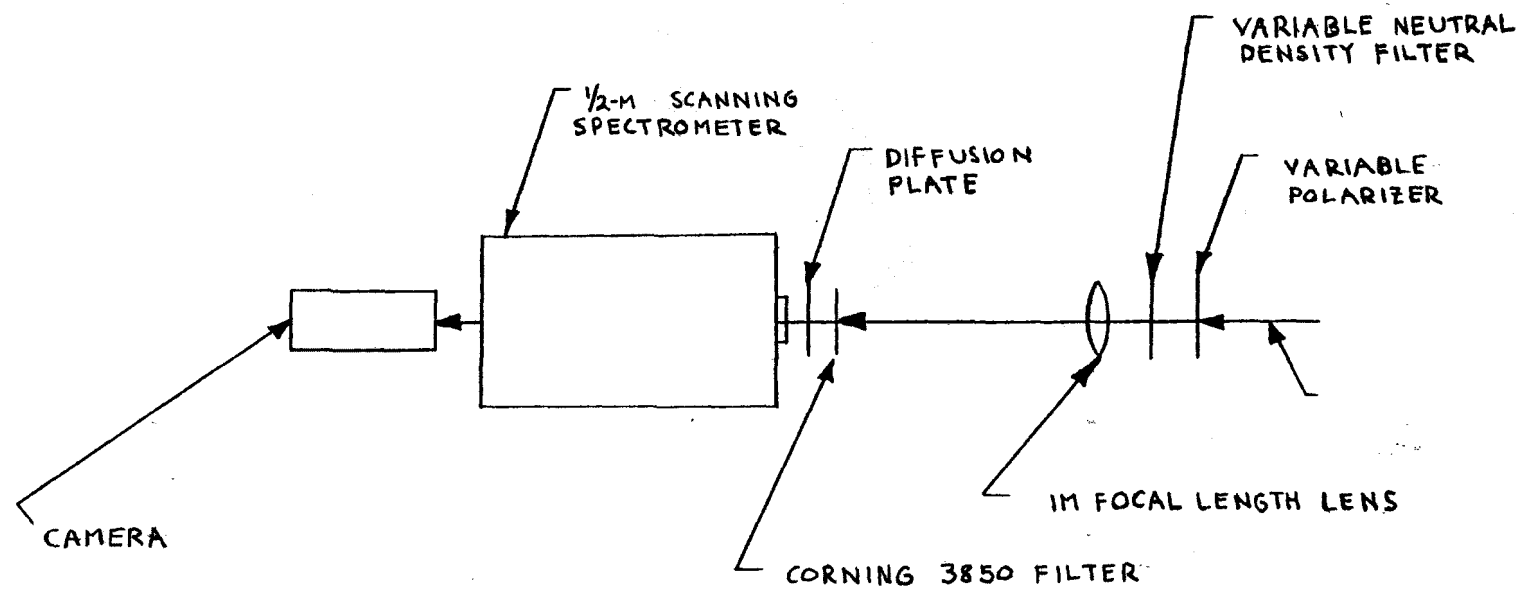To carry out the experiment, the laser was allowed to lase simul-

FIGURE 3.6:1a EXPERIMENTAL SETUP FOR MONITORING LASER FREQUENCY SHIFTS AND BANDWIDTH CHANGES
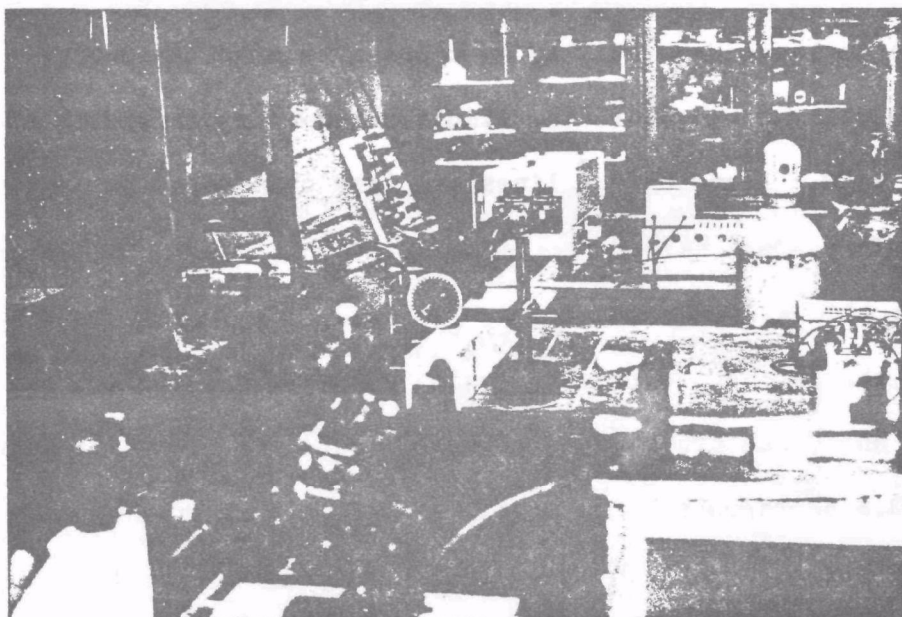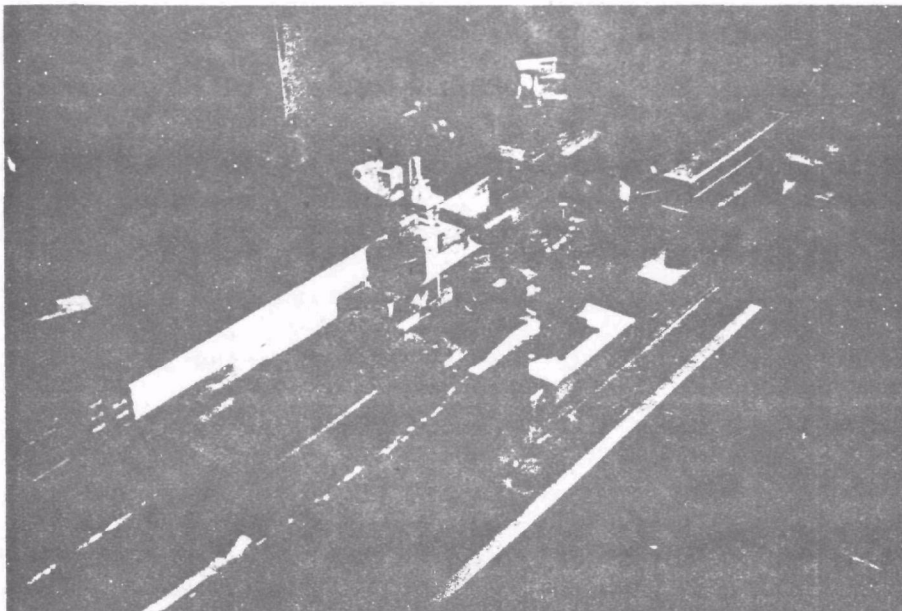
FIGURE 3.6:1b PHOTOGRAPHS OF THE EXPERIMENTAL SETUP FOR MONITORING LASER FREQUENCY SHIFTS AND BANDWIDTH CHANGES

taneously, but only one polarization was allowed to pass through the variable polarizer and onto the film. The exposed film was then compared to another exposure from a sequential lase at the same wavelength. Any frequency shifts would be obtained by observing the relative changes, if any, from the Hg lines to which both films were exposed. Figs. 3.6:2, 3,4, and 5 show respectively the 4478.5 Å line lasing sequentially then simultaneously, and the 4500 Å line lasing sequentially then simultaneously. There were no frequency shifts noted between the lines when lasing sequentially as to compared to when they lased simultaneously, but bandwidth changes did however occur, i.e., there was a change in laser bandwidth (along with a monotonic change in output energy) when the system lased sequentially as opposed to simultaneously. As can be Figs. 3.6:2 through 3.6:5 the simultaneous-mode bandwidths and energies of the 4478.5 Å and 4500 Å lines are less than those for the sequential mode. They are: 4478.5 A: sequential 10 A, 200 mj; simultaneous 7 A, 100 mj; 4500 A: sequential 7 A, 100 mj; simultaneous 4 A, 50 mj.

In the second experiment, lasing occurred simultaneously. Any frequency and bandwidth changes were observed in the same manner as above. Figs. 3.6:6a through 1 are photographs that show no frequency shifts existed but bandwidth changes did occur from shot to shot. The bandwidth changes depend upon:

1. bias voltage, i.e., the energy discharged in each flash,

2. time between pulses, and

3. degradation of the dye molecules due to repeated exposure to the pump source.

As can be seen from the photographs the bandwidths varied as much as 43
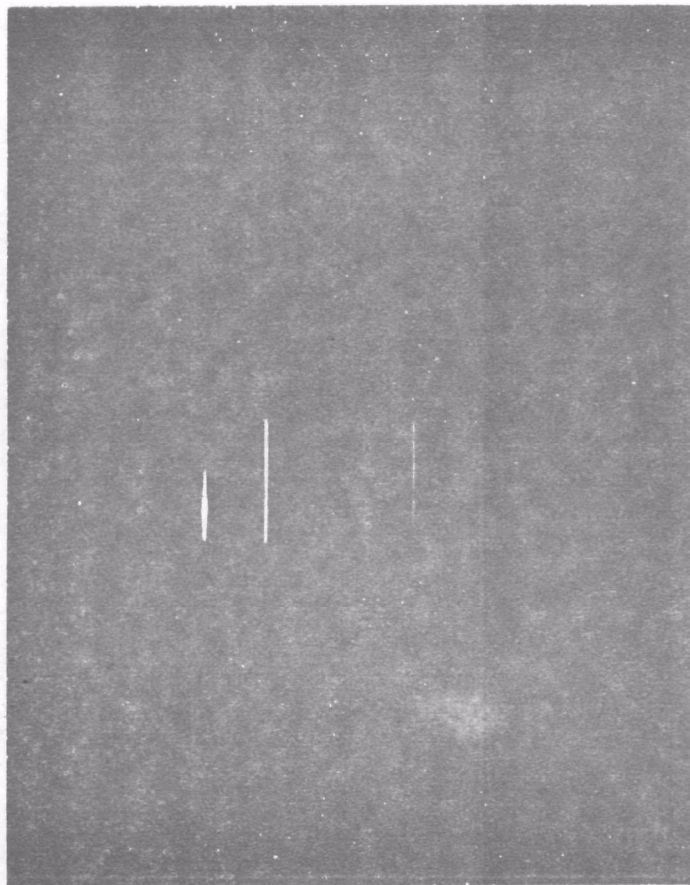
FROM LEFT TO RIGHT: 4478.5 Å, 4358 Å, 4078 Å, AND 4047 Å

FIGURE 3.6:2   SPECTROMETER PHOTOGRAPH OF THE 4478.5
Å LASER LINE FOR SEQUENTIAL OPERATION
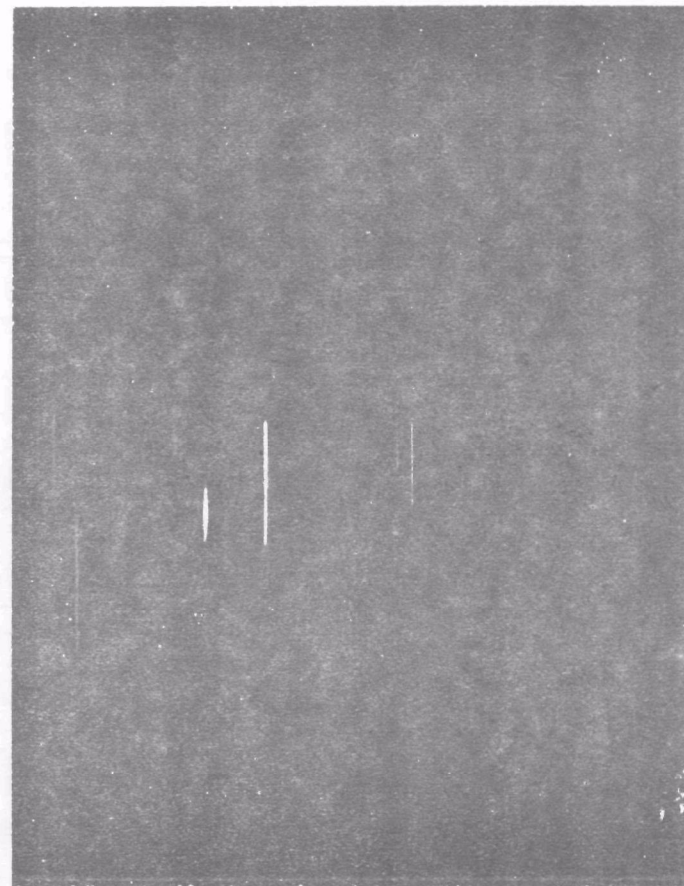
FROM LEFT TO RIGHT: 4478.5 Å, 4358 Å, 4078 Å, AND 4047 Å

FIGURE 3.6:3   SPECTROMETER PHOTOGRAPH OF THE
4478.5 Å LASER LINE FOR SIMUL-
TANEOUS TWO-WAVELENGTH OPERATION

FROM LEFT TO RIGHT: 4500 Å, 4358 Å, 4078 Å, AND 4047 Å

FIGURE 3.6:4   SPECTROMETER PHOTOGRAPH OF THE 4500
Å LASER LINE FOR SEQUENTIAL
OPERATION
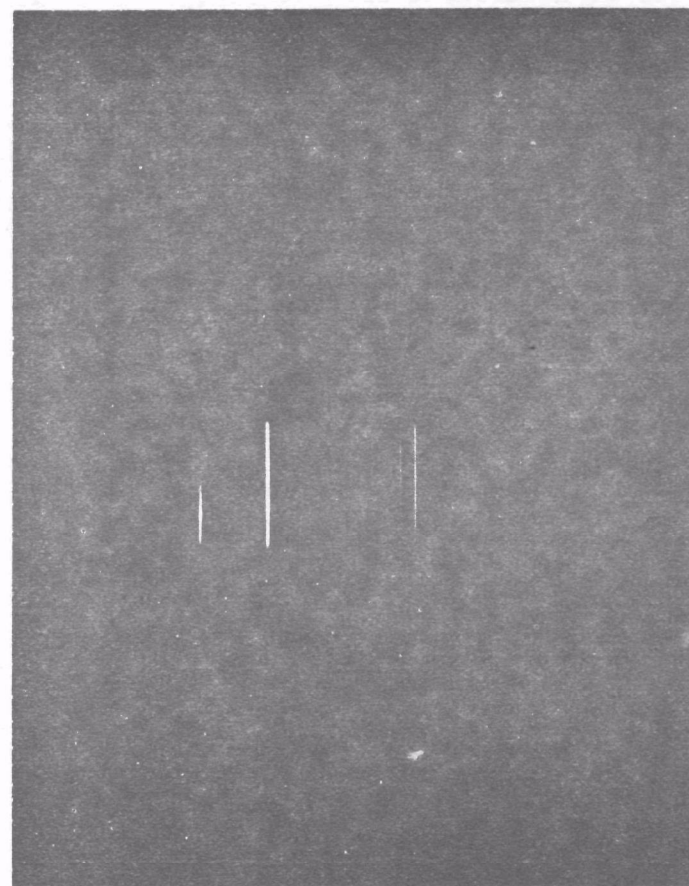
FROM LEFT TO RIGHT: 4500 Å, 4358 Å, 4078 Å, AND 4047 Å

FIGURE 3.6:5   SPECTROMETER PHOTOGRAPH OF THE 4500
Å LASER LINE FOR SIMULTANEOUS TWO-
WAVELENGTH OPERATION
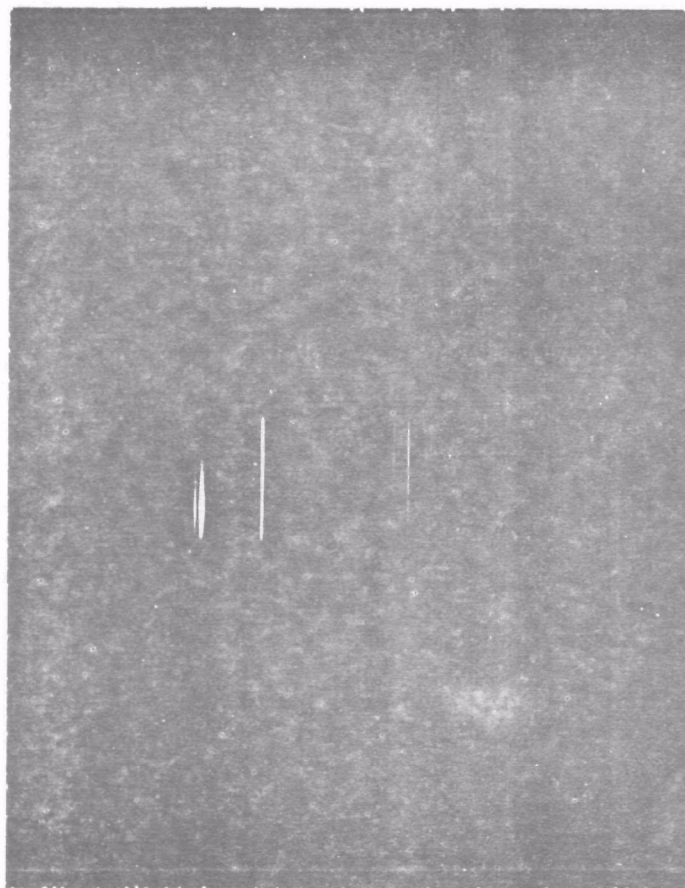
FROM LEFT TO RIGHT: 4500Å, 4478.5Å, 4358Å, 4078Å, AND 4047Å

FIGURE 3.6:6a SPECTROMETER PHOTOGRAPH OF THE
SIMULTANEOUS TWO-WAVELENGTH OUTPUT,
BIAS VOLTAGE = 20 KV, FIRST SHOT

FIGURE 3.6:6b BIAS VOLTAGE = 20 KV, SECOND SHOT

FIGURE 3.6:6c   BIAS VOLTAGE = 20 KV, THIRD SHOT

FIGURE 3.6:6d   BIAS VOLTAGE = 20 KV, FOURTH SHOT

FIGURE 3.6:6e BIAS VOLTAGE = 19 KV, FIRST SHOT

FIGURE 3.6:6f BIAS VOLTAGE = 19 KV, SECOND SHOT

FIGURE 3.6:6g BIAS VOLTAGE = 19 KV, THIRD SHOT

FIGURE 3.6:6h BIAS VOLTAGE = 19 KV, FOURTH SHOT
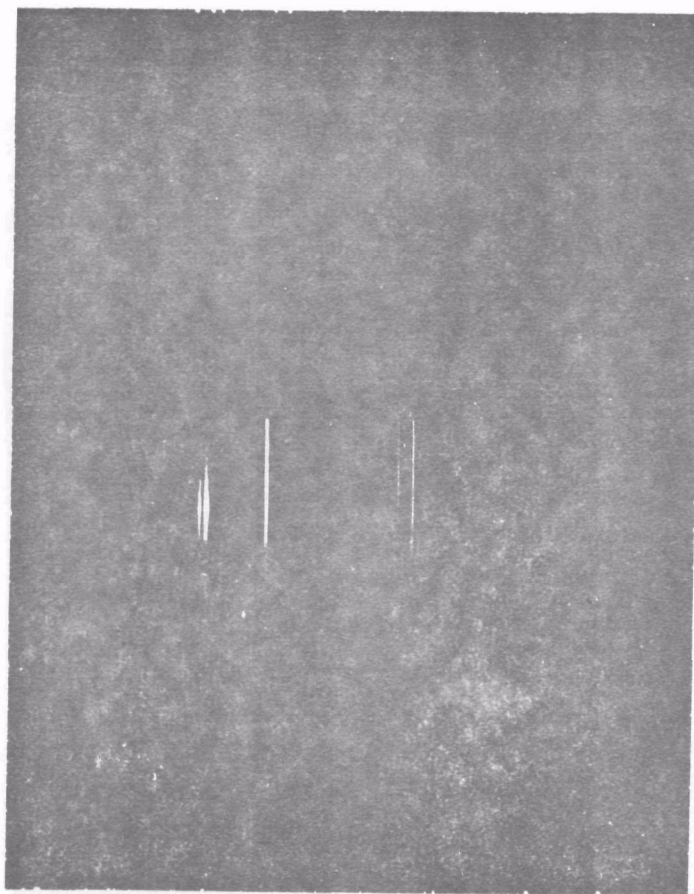
FIGURE 3.6:6i BIAS VOLTAGE = 18 KV, FIRST SHOT
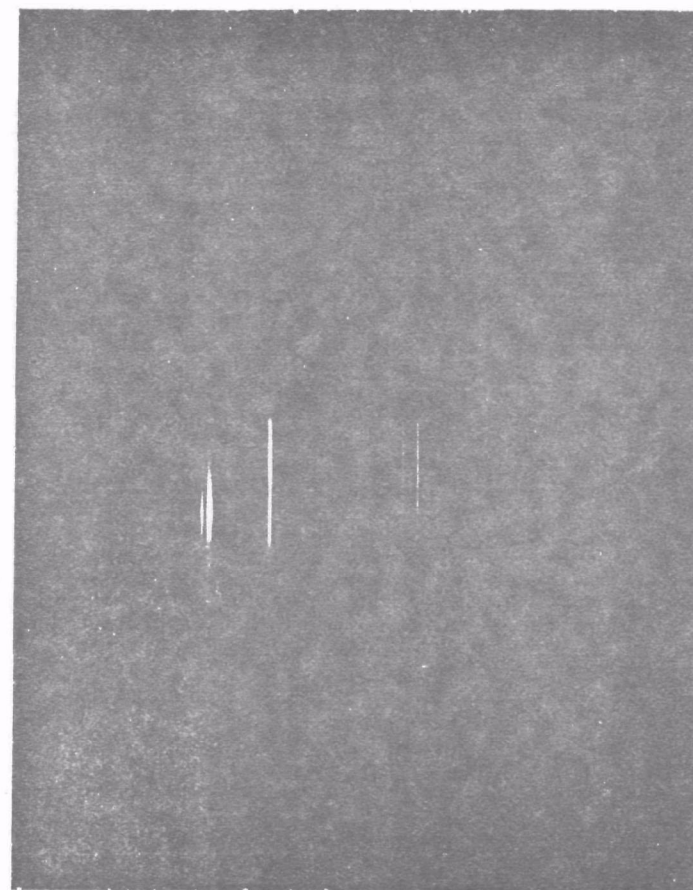
FIGURE 3.6:6j BIAS VOLTAGE = 18 KV, SECOND SHOT

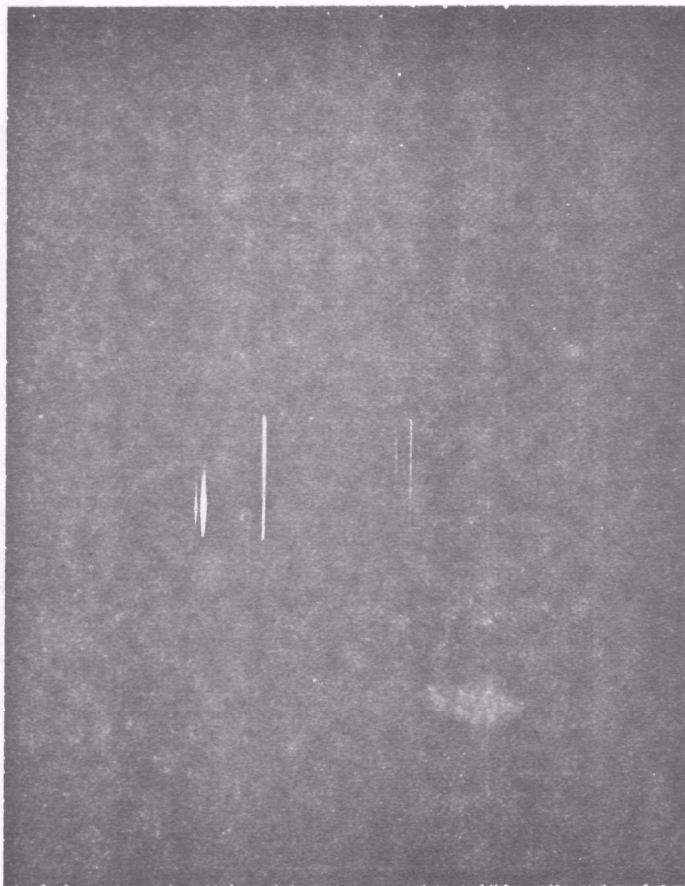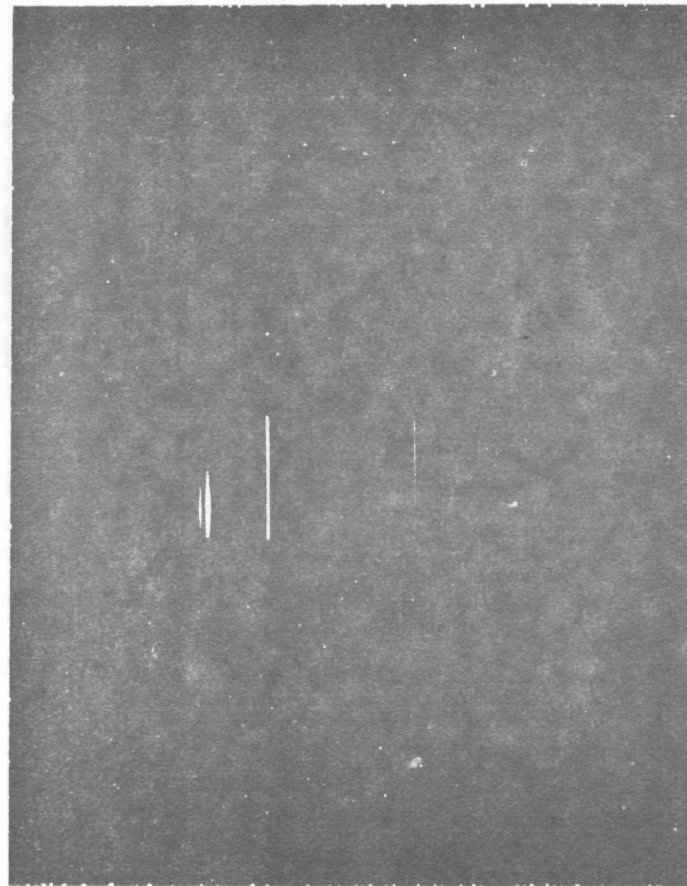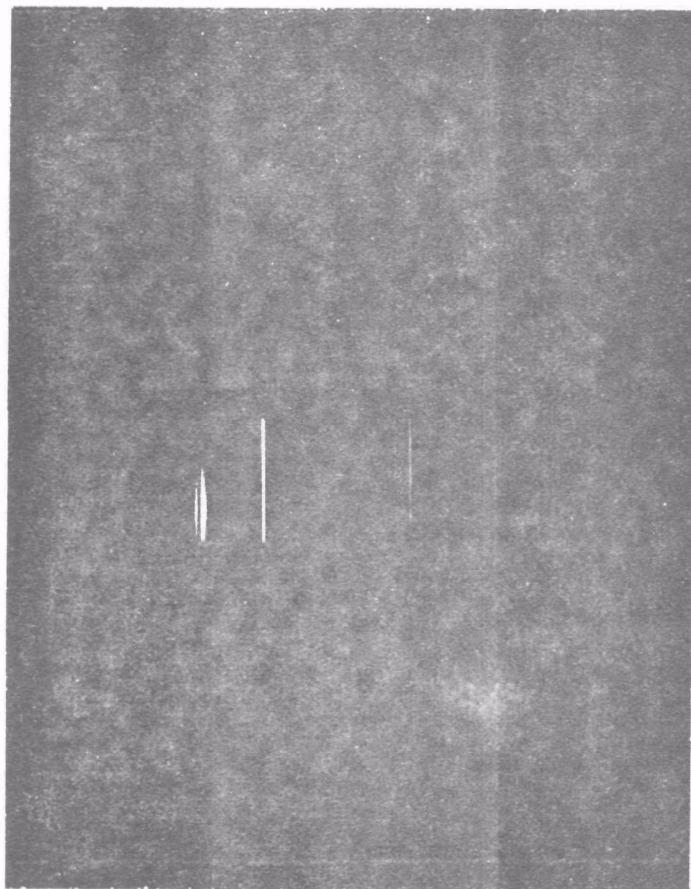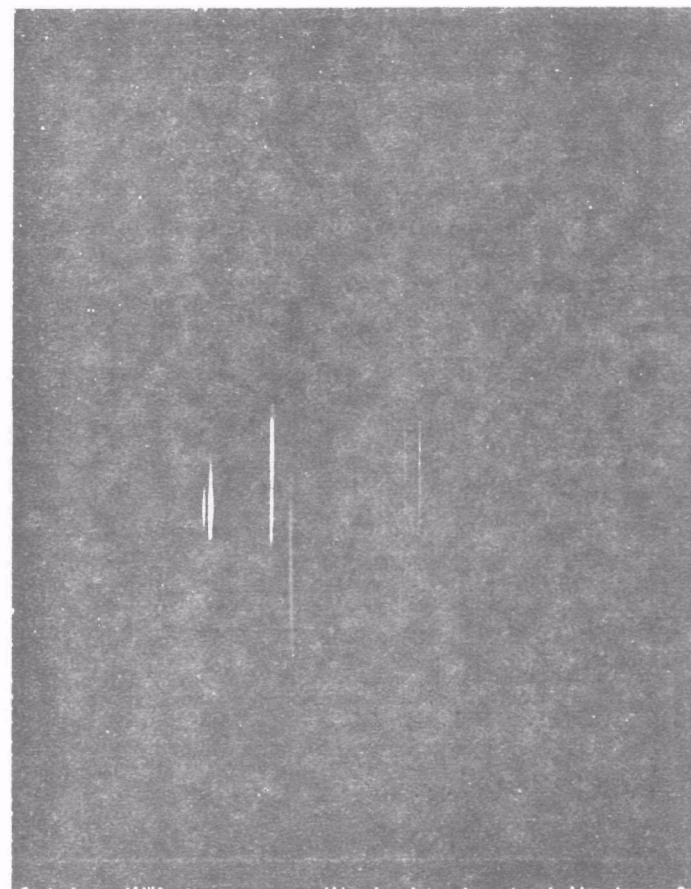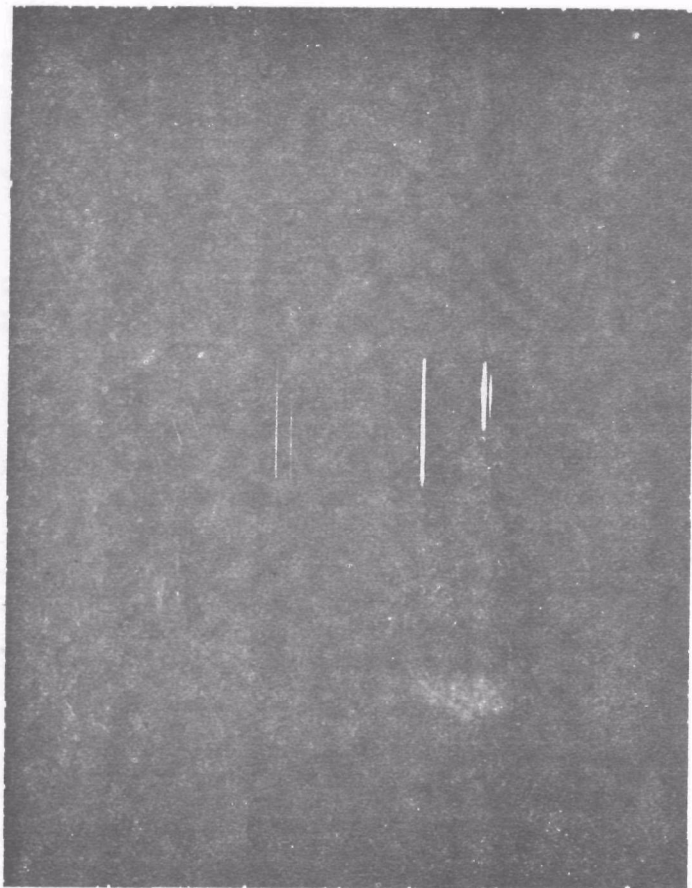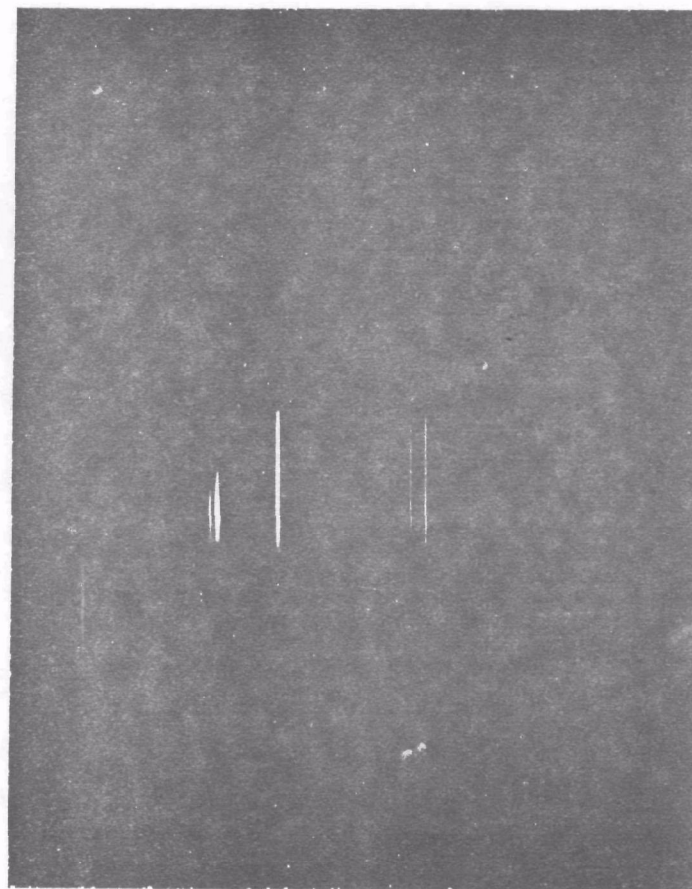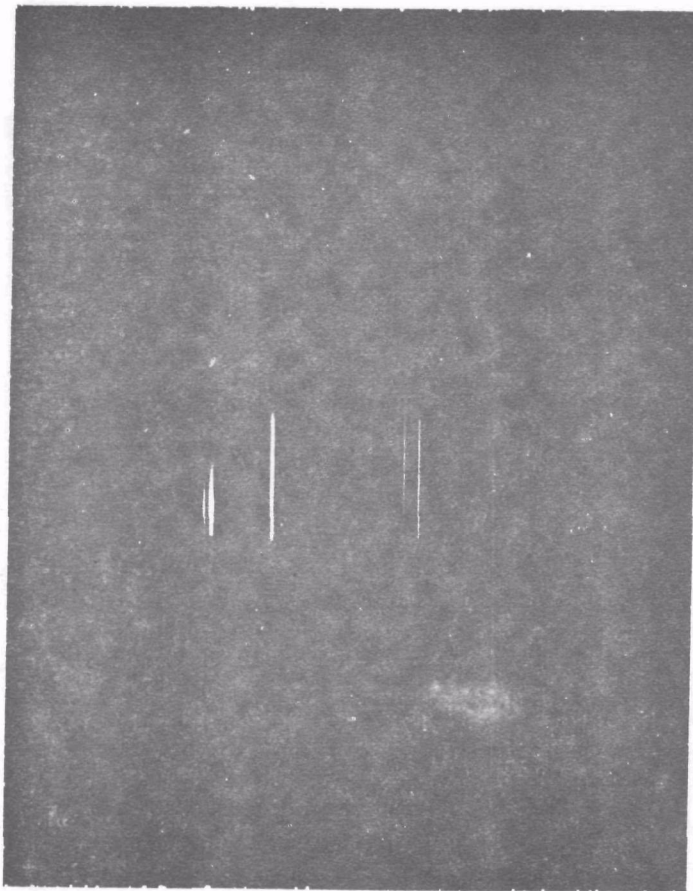FIGURE 3.6:6k BIAS VOLTAGE = 18 KV, THIRD SHOT
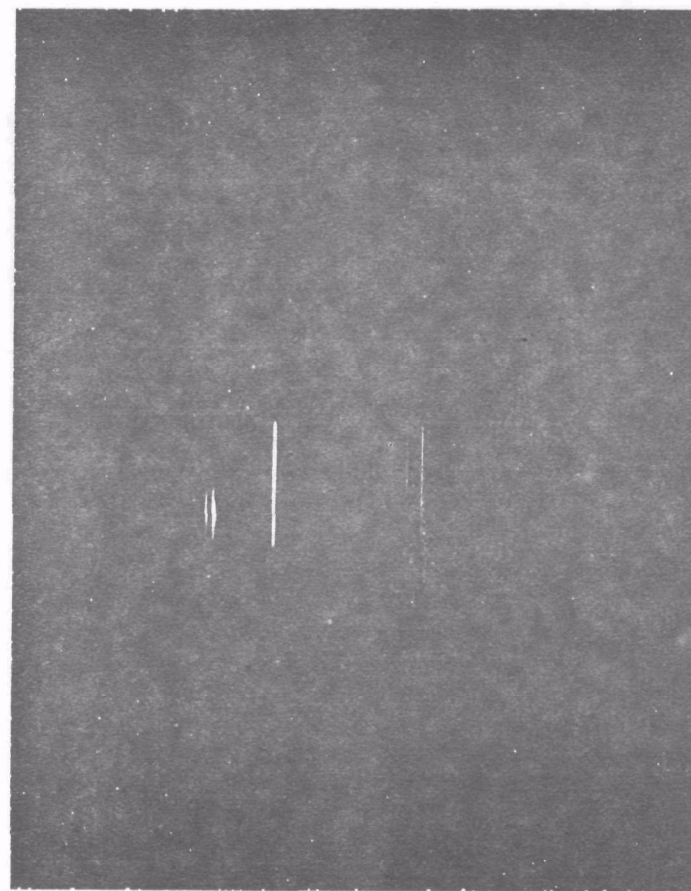
FIGURE 3.6:6l BIAS VOLTAGE = 18 KV, FOURTH SHOT

percent.

As a result of these experiments, it was therefore concluded that since significant bandwidth changes did occur from shot to shot during simultaneous operation, a calibration system must be used in the LIDAR system in order to allow for these changes. The next two sections describe the calibration system devised for this purpose, and tuning techniques used to obtain bandwidths and center-frequency requirements.

3.6.2 The Calibration System

To ensure accurate results which are independent of variations in laser operation which occur from shot to shot, and which affect bandwidth, a calibration system was devised. This is shown schematically in Figs. 3.6:7a and b. This calibration system analyses both output beams simultaneously and permits the effective NO_2 absorption cross sections to be calculated from the data obtained.

Operationally, two beams of mutually-orthogonal polarizations at the close-lying wavelengths λ_1 (4478.5 Å) and λ_2 (4500 Å) enter the shielded encasement through the variable iris. Both beams impinge upon an air-spaced Glan-Taylor prism by which the beams are spatially separated. The perpindicularly polarized beam, λ_1, is directed through slide #1 by a beam-steering mirror. Four percent of that beam is tapped off by slide #1 and is focused by the 15-cm focal-length lens #1 onto an RCA IP39 vacuum-tube photodiode through neutral density filters and diffusion plate #1. The remaining portion of the beam passes through a 1/2 m glass cell in which flows 609 ppm of NO_2 in N_2 at just above atmospheric pressure. The beam is then focused onto RCA IP39 photo-

89
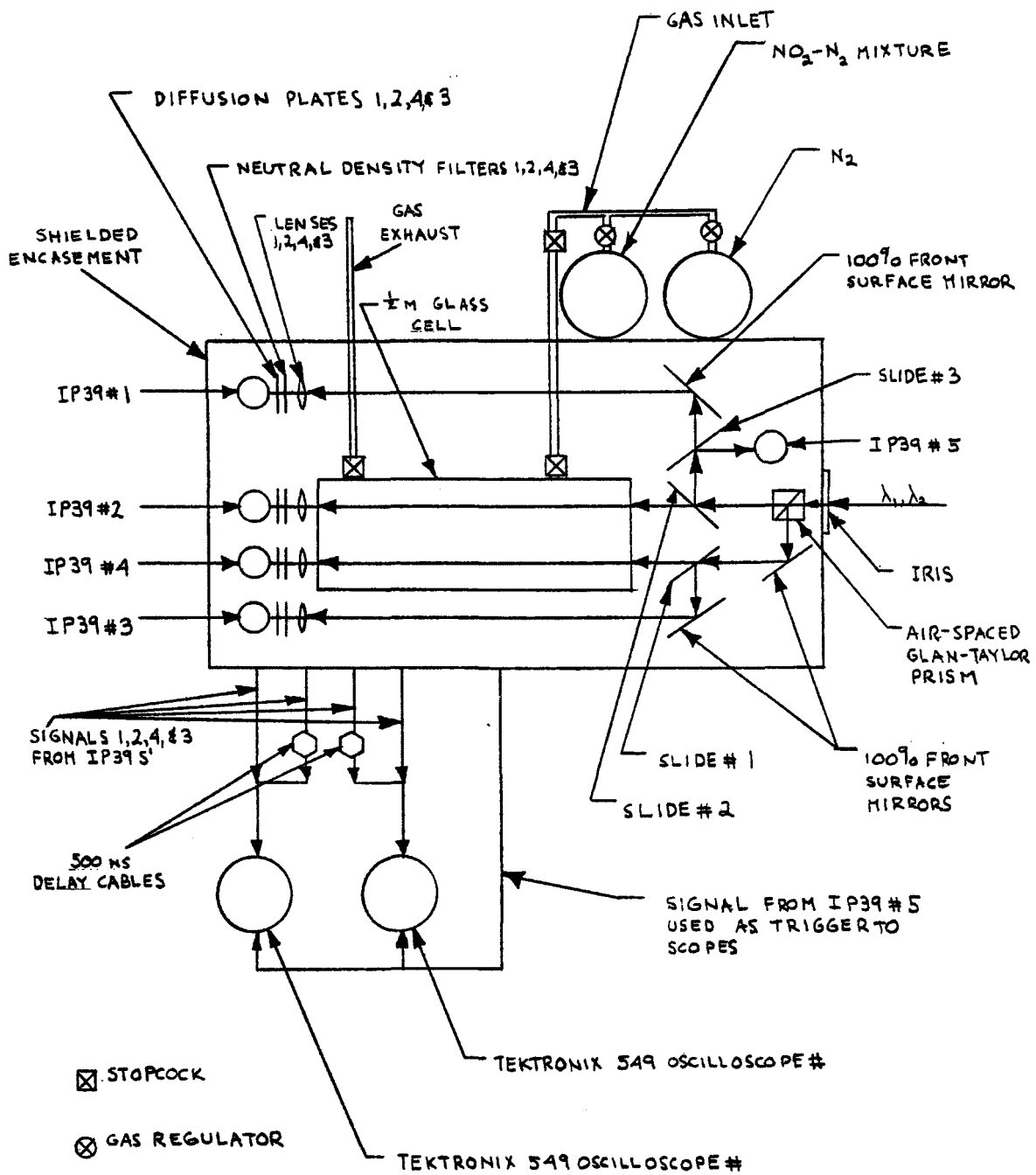
FIGURE 3.6:7a THE CALIBRATION SETUP
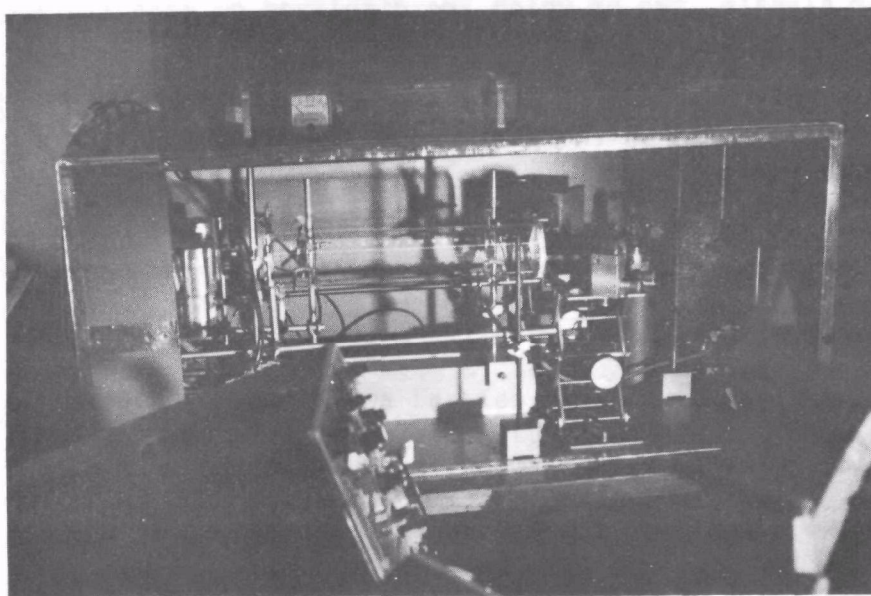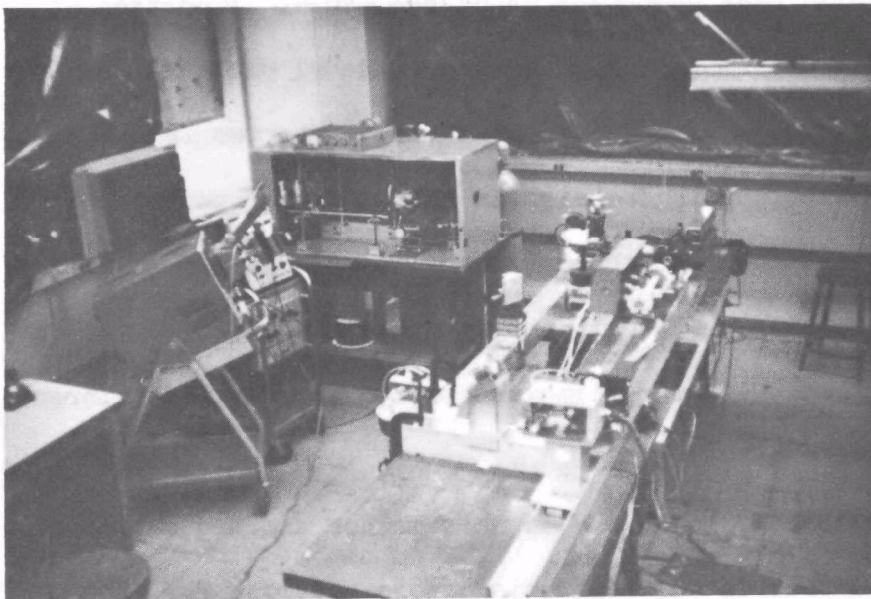
FIGURE 3.6:7b PHOTOGRAPHS OF THE CALIBRATION SETUP

diode #2 through neutral density filters and diffusion plate #2.

The same type of configuration applies to the parallel-polarized beam, λ_2, which uses component numbers 3 and 4. A portion of the parallel-polarized beam is tapped off by slide #3 onto RCA IP39 photovacuum diode #5, whose signal acts as a trigger to two Tektronix type 549 storage oscilloscopes. The signals corresponding to the portion of the beams that propagate through the cell are delayed in time by two 500 ns delay cables. The signals are then displayed on the two storage scopes along with the signals corresponding to the reference beams that bypassed the cell.

The type of data obtained in this manner and the method of calculating the effective NO_2 absorption cross sections for each lasing line from shot to shot are described below:

1. Four signals, two of which are displayed on each storage scope, are obtained.

2. The two signals on the first scope correspond to the 4478.5 Å laser line. The first signal on storage scope 1 is used for normalizing for any power fluctuations that may occur from shot to shot. This allows relative measurements to be made. The second signal, which is delayed approximately 500 ns, is partially absorbed by the NO_2-N_2 mixture in the cell.

3. The two signals on storage scope 2 correspond to the 4500 Å laser line. As before, the first signal is used for normalization. The delayed signal is partially absorbed by the NO_2-N_2 mixture, but not as much as the 4478.5 Å laser line.

4. To calculate the percent absorption and therefore the effective

NO_2 absorption cross section for each laser pulse for each laser line, it is necessary to know what losses are attributed to the NO_2 in the mixture and what losses are attributed to the cell itself. It is for this reason that an initial reading is necessary for each lasing wavelength when only N_2 is flowing through the cell.

5. To calculate the percent absorption for each wavelength (which is related to the effective absorption cross section) only relative measurements are required. The percent absorption is calculated using Eq. 3.6:1 below:

$$\% \text{ absorption} = 1 - \frac{\left.\frac{A}{B}\right|_W}{\left.\frac{A}{B}\right|_{W/O}} , \qquad (3.6:1)$$

where,

$\left.A/B\right|_W$ = the ratio of the signal that propagates through the cell containing the NO_2-N_2 mixture (the delayed signal) divided by the signal that bypasses the cell.

$\left.A/B\right|_{W/O}$ = the ratio of the signal that propagates through the cell containing only the N_2 (the delayed signal) divided by the signal that bypasses the cell. This is done for each of the lasing wavelengths.

6. To obtain the percent transmission of each lasing wavelength from shot to shot, each $\left.A/B\right|_W$ reading from each scope obtained during each shot is normalized by the initial $\left.A/B\right|_{W/O}$ reading.

93

To obtain the percent absorption the ratio of the above ratios is subtracted from unity.

7. The effective absorption cross section is related to the percent absorption by:

$$\sigma_{EFF} = \frac{-\ln(1 - \% \text{ absorption})}{Nl} \ (cm^2), \qquad (3.6:2)$$

where,

N = the concentration of NO_2 in the cell (cm^{-3}), and

l = the length of the cell (cm).

Figs. 3.6:8 a and b, and 3.6:9 a and b show curve traces of photographs of the signals from the storage scopes in the calibration system. Figs. 3.6:8a and b correspond to the readings without NO_2 but with N_2 in the cell for the lines centered about 4478.5 Å and 4500 Å respectively. Figs. 3.6:9a and b correspond to the readings with the NO_2-N_2 mixture in the cell for these lines. The effective absorption cross sections for the lines centered about 4478.5 Å and 4500 Å for this particular set of measurements are 6.36 X 10^{-19} cm^2 and 3.54 X 10^{-19} cm^2 respectively.

Knowing the calibrated values of the effective NO_2 absorption cross sections for each of the simultaneous laser wavelengths for each laser firing, permits allowance to be made for any variations of laser bandwidths which occur from shot to shot.

3.6.3 Tuning Technique

For operation of the LIDAR system, it is necessary that:

1. The center frequencies of both laser lines coincide with the

FIGURE 3.6:8a CALIBRATION SIGNALS FOR SIMULTANEOUS TWO-WAVELENGTH
OPERATION FOR THE 4478.5 Å LASER LINE WITH N_2 IN THE
CALIBRATION CELL
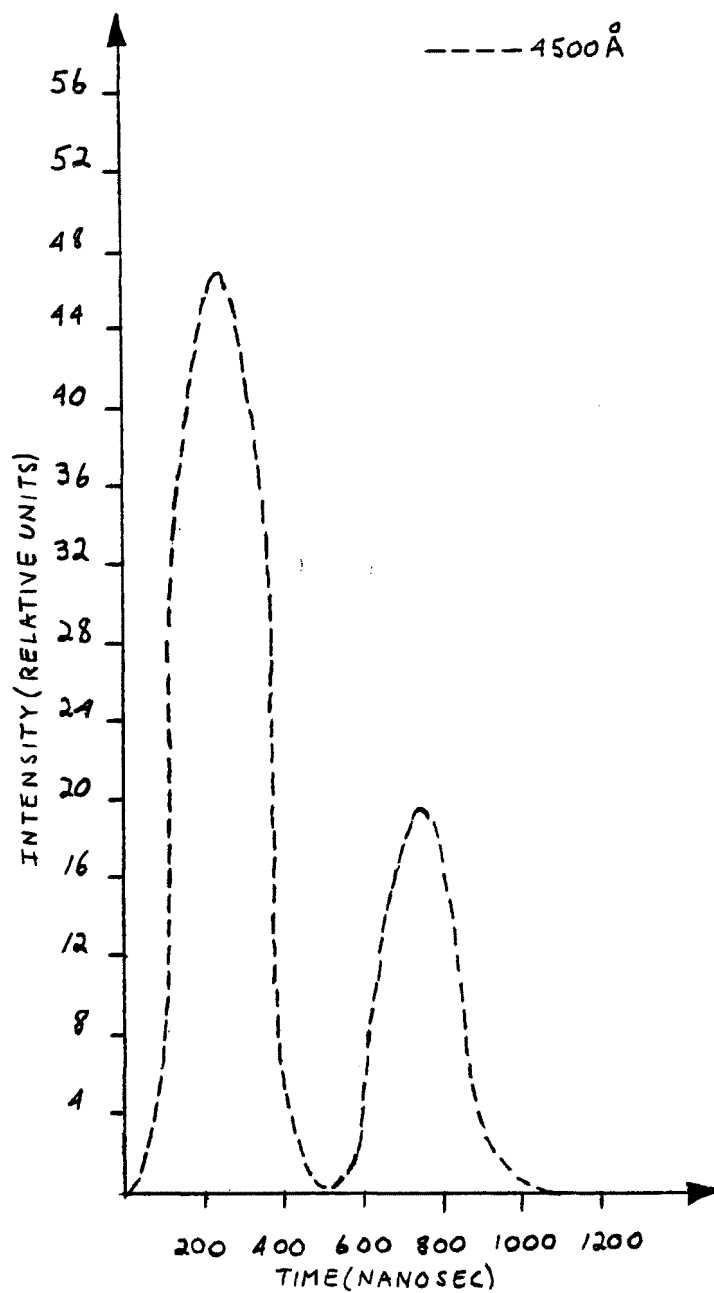
FIGURE 3.6:8b   CALIBRATION SIGNALS FOR SIMULTANEOUS TWO-WAVELENGTH
OPERATION FOR THE 4500 Å LASER LINE WITH N_2 IN THE
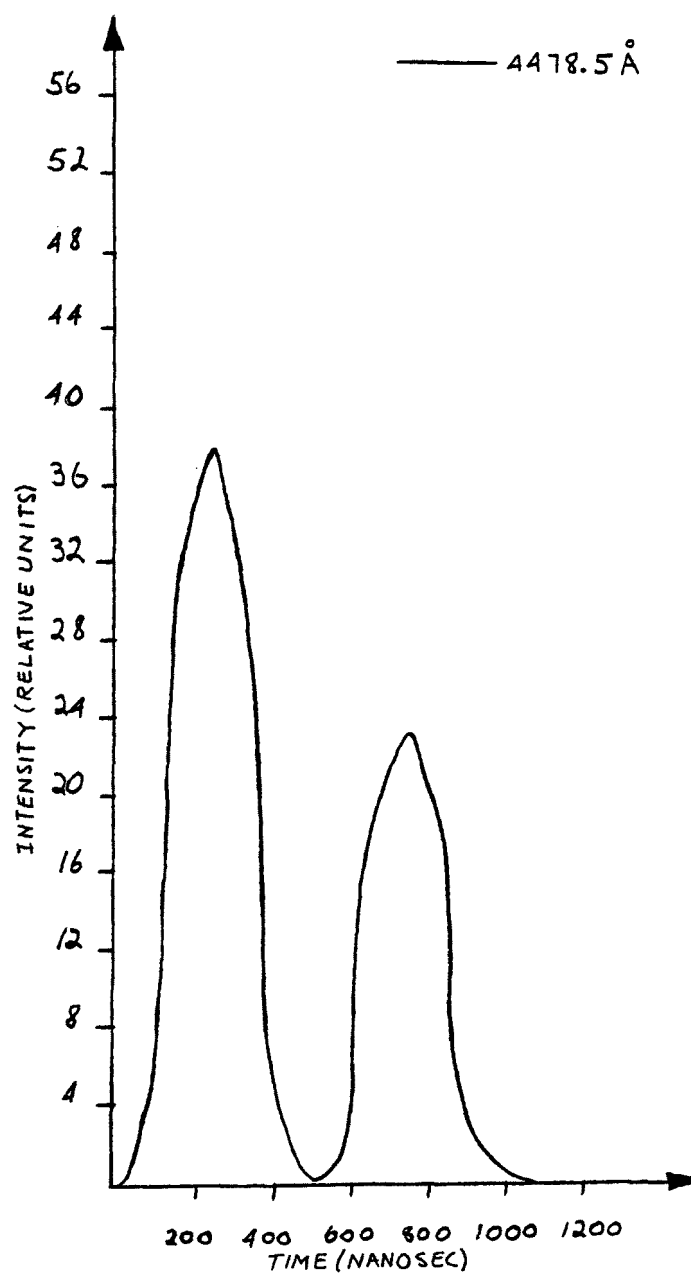CALIBRATION CELL
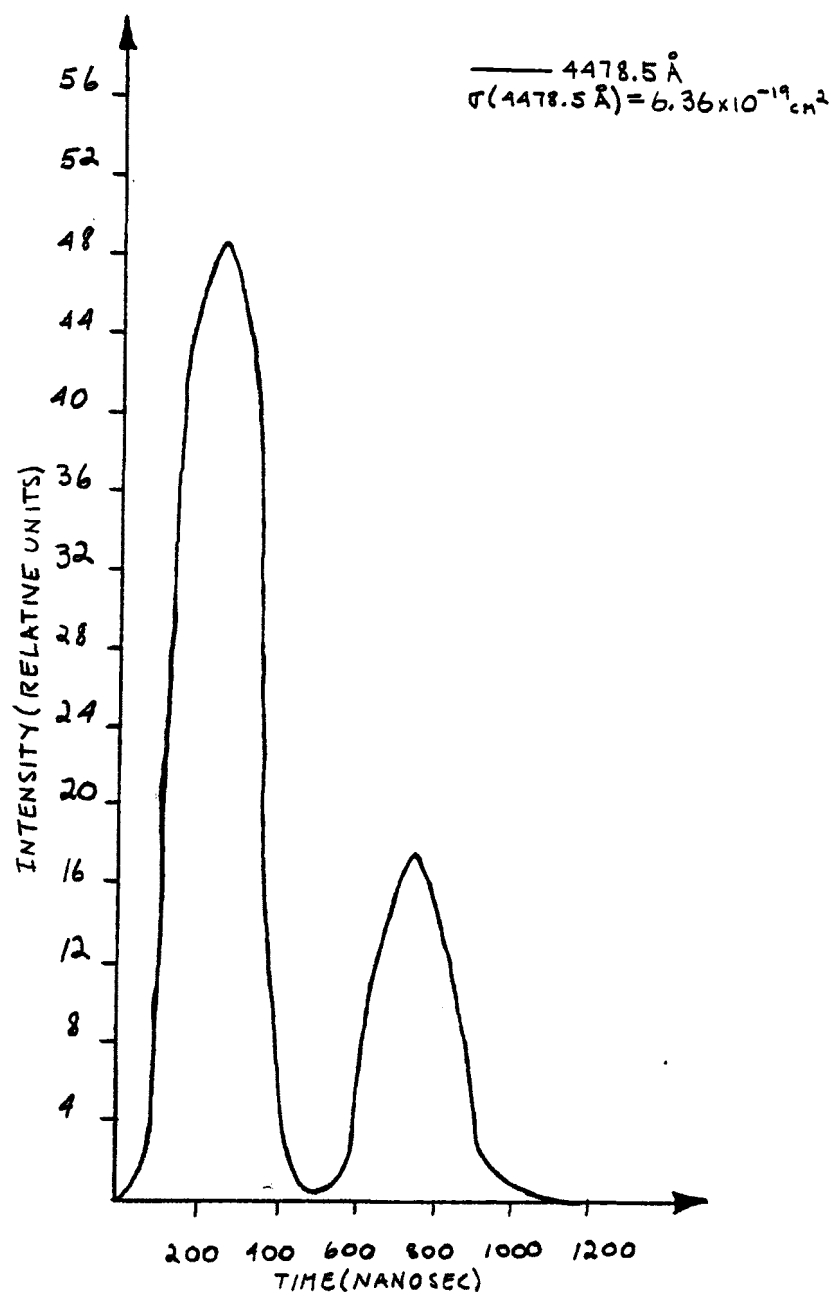
FIGURE 3.6:9a   CALIBRATION SIGNALS FOR SIMULTANEOUS TWO-WAVELENGTH OPERATION FOR THE 4478.5 Å LASER LINE WITH NO₂-N₂ MIXTURE IN THE CALIBRATION CELL
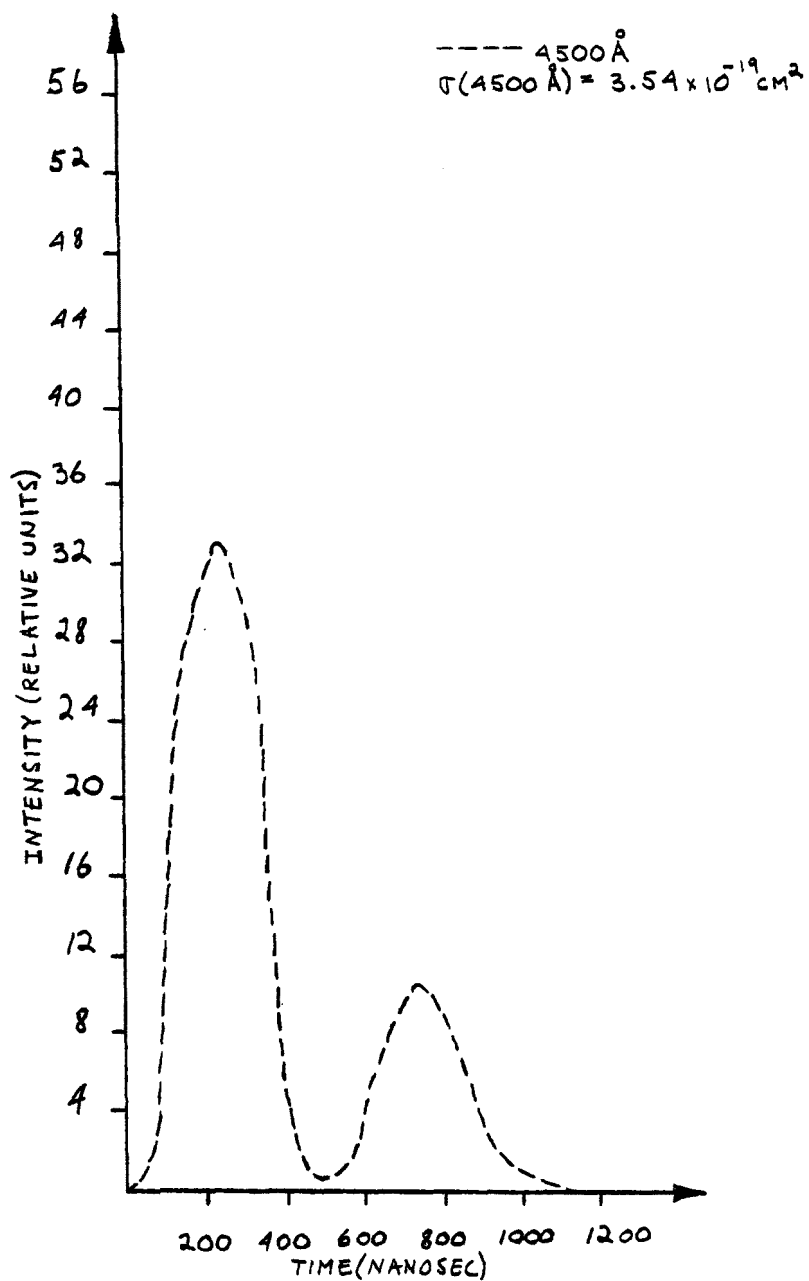
FIGURE 3.6:9b CALIBRATION SIGNALS FOR SIMULTANEOUS TWO-WAVELENGTH
OPERATION FOR THE 4500 Å LASER LINE WITH NO_2-N_2
MIXTURE IN THE CALIBRATION CELL

center frequencies of the two interference filters in the receiver.

2. The bandwidths of both laser lines must be less than the bandwidths of the respective interference filters.

3. Any increase in laser bandwidths must result in bandwidths that remain less than the bandpass of the interference filters.

If the laser bandwidths are larger than the bandpass of the filters, erroneous readings would result, i.e., the data obtained from the calibration system corresponds to the actual effective absorption cross sections, whereas the receiver would be detecting only a certain portion of the laser signal spectrum.

The operating characteristics of the receiving system could have been designed so as to require both lasing bandwidths to be much larger than the interference filter bandpass. This would eliminate the need for a calibration system in the following manner. If both laser-line bandwidths were larger than the filter bandpass, then known spectral quantities would be detected and determined exactly by the filter bandpass. The exact effective absorption cross sections would then be known and would not vary since they were determined by the filter characteristics.

There are three reasons why this approach was not used. First, when operating a LIADR system, it is desirable to obtain readings from useful ranges (up to 10 km). When detecting only a portion of the laser backscatter, the signal is reduced and the attainable range is decreased. Second, the signal to noise ratio for a given range decreases, since the signal is decreased. Third, in dye-laser systems,

the dye lasing medium degrades due to repeated exposure to the pump source. This has the effect of monotonically decreasing the laser bandwidth over a period of time. Therefore, there is a difficulty in maintaining laser output signals whose bandwidths are much larger than those of the receiver interference filters.

The tuning scheme was therefore developed to achieve:

1. Laser line center frequency and filter bandpass coincidence.

2. Desirable laser bandwidths.

3. Laser bandwidth fluctuations that continue to keep bandwidths below the bandpass of the interference filters.

Fig. 3.6:10 shows the experimental setup used to check the system. With the laser operated in the simultaneous mode, fractions of both beams of mutually orthogonal polarizations were tapped off by slide #1 and were directed through variable polarizer #1, variable neutral density filter #1, and lens #1 (1 m focal length). The beams were then focused onto diffusion plate #1, neutral density filter #1, and were detected by an RCA 6217 photomultiplier attached to a 1/2 m Jarrell-Ash scanning spectrometer. The input and output slits were set at 10μ each to give a detectable resolution of $0.16 \overset{o}{A}$. To compensate for any laser power fluctuations, the signal obtained through the spectrometer was normalized by a signal from a RCA IP39 vacuum-tube photodiode used as the trigger source in the calibration system. A portion of the main beam was tapped off with a pellicle and directed into the calibration system where it was detected by the IP39 photodiode. Signals from the spectrometer and the IP39 were recorded photographically on two Tektronix type 549 storage oscilloscopes.
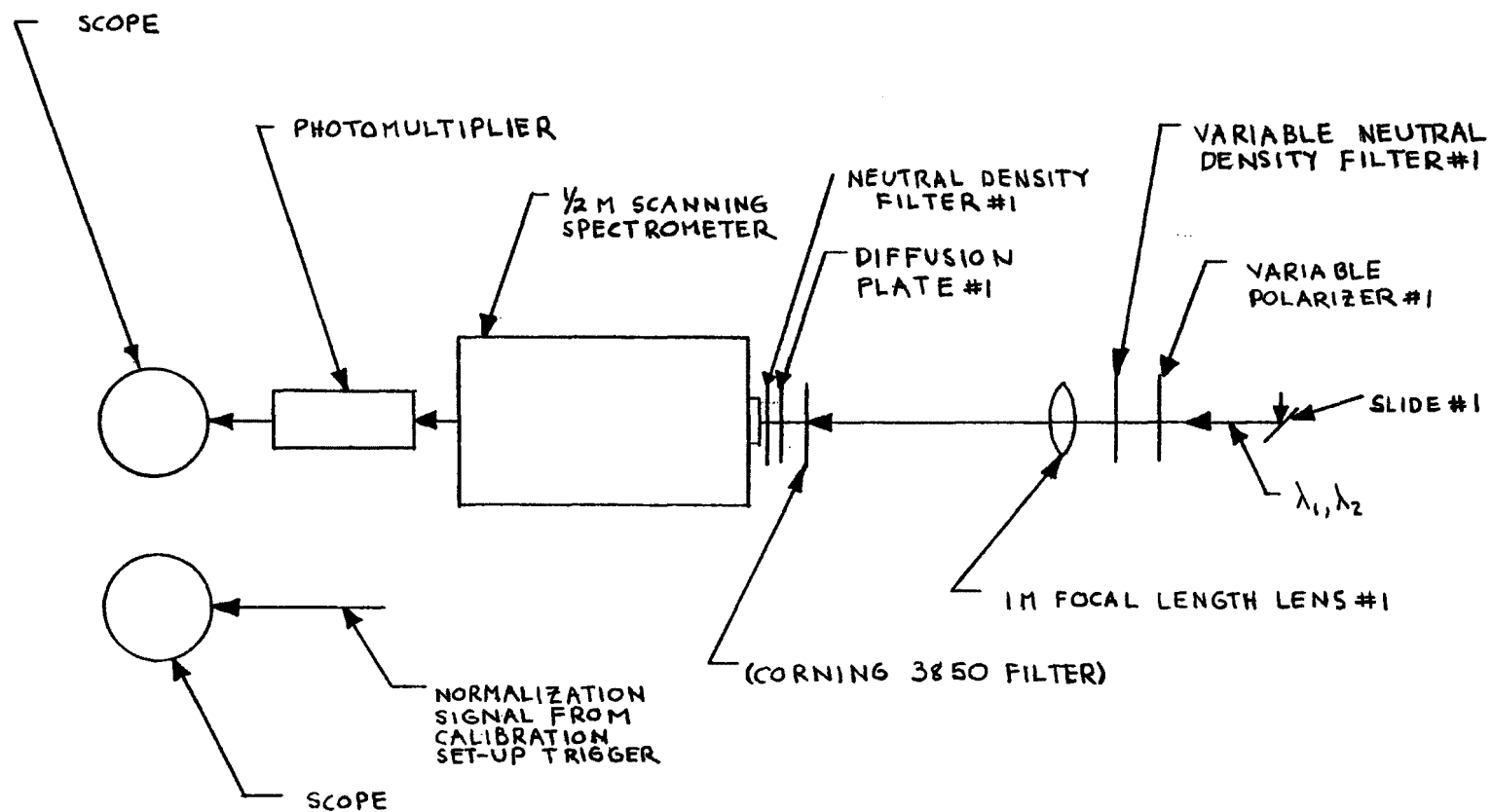
FIGURE 3.6:10   EXPERIMENTAL SETUP USED FOR FINE FREQUENCY TUNING

The spectrometer was initially calibrated using an Hg lamp and was then manually set to detect the 4478.5 Å line. With the laser operating in the simultaneous mode, both beams were tapped off, but only the line desired to lase at 4478.5 Å was allowed to pass through variable polarizer #1 initially. The laser line was initially sighted by eye through the view port on the spectrometer. Coarse tuning was accomplished by observing the spectral shift while the grating's rotational position was changed. Once having achieved the desired spectral center line frequency, within visual approximation, the desired laser bandwidth, approximately 5 Å, was sought. As mentioned earlier, the bandwidths must be less than the bandpass of the interference filters. If the laser bandwidths were initially set at 5 Å with the bias voltage set at the maximum to be used, and knowing that the bandwidths monotonically decrease due to repeated exposure of the lasing medium to the pump source, the laser bandwidths would be ensured to always be within the bandpass of the filters.

Initially, the laser bandwidths were adjusted for maximum width, approximately 20 Å, by setting the grating positions as close as possible to the polarizing prism. To obtain the desired 5 Å bandwidths, the distance of the gratings need only be increased relative to the polarizing prism. To check the bandwidths each time the grating positions were moved, a camera was attached to the view port on the spectrometer, and the laser spectral widths were recorded photographically. Initial exposure of the film to an Hg lamp through a Corning 3850 filter and the spectrometer served as a calibration check on the bandwidth readings. The resolution obtained on the film was 16 Å/mm. Initially, the

two laser lines might partially overlap since the bandwidths were orig-
inally set at approximately 20 Å. Therefore, variable polarizer #1 was
set to allow only one polarization to pass into the spectrometer initially.
Through repeated adjustments of the axial positions of the gratings, the de-
sired bandwidths were obtained with the center-line frequencies set vis-
ually at 4478.5 Å and 4500 Å. Figs.3.6:11a through i show the run to
obtain the 5 Å bandwidths for each of the simultaneous laser frequencies.

Having obtained the desired bandwidths, the next step was to finely
adjust the laser frequencies using the tuning technique described earlier
in the section. The rotational positions of the gratings were finely adjusted
using micrometers and the normalized readings of the scopes were maxi-
mized. Figs. 3.6:12a and b and 3.6:13a and b show the first and final scope
readings for fine center line adjustment for the simultaneous laser fre-
quencies 4478.5 Å and 4500 Å respectively. Fig. 3.6:14 shows the desir-
ed simultaneous output with each line approximately 5 Å wide and the
line center frequencies set at 4478.5 Å and 4500 Å.

In conclusion, the results of the experiments to determine whether
frequency shifts and bandwidth changes occur from shot to shot during
LIDAR operation, definitely show the necessity for a calibration system.
If meaningful pollution readings are to be obtained, calibrated output
signals must be used.

In the following chapter, calibrated LIDAR returns are interpreted
and pollution concentrations at various ranges from the LIDAR site are
given.

FROM LEFT TO RIGHT: 4478.5 Å, 4358 Å, 4078 Å, AND 4047 Å

FIGURE 3.6:11a SPECTROMETER PHOTOGRAPH OF THE SIMUL-
TANEOUS TWO-WAVELENGTH OUTPUT TO GET
5 Å BANDWIDTHS IN EACH LINE--4478.5 Å
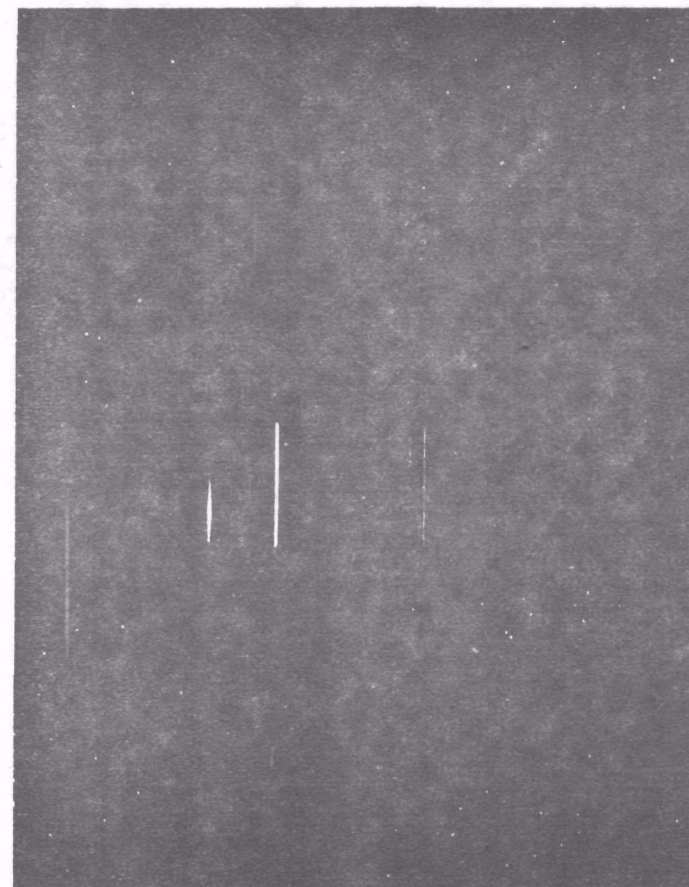
FIGURE 3.6:11b --4500 Å
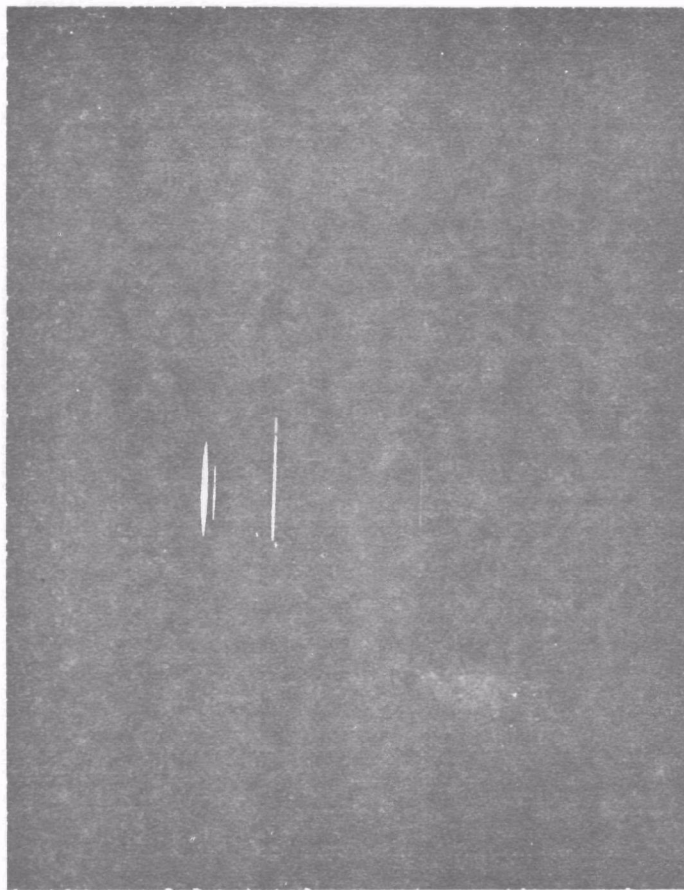
FROM LEFT TO RIGHT: 4500Å, 4478.5Å, 4358Å, 4078Å, AND 4047Å

FIGURE 3.6:11c --THE 4478.5 Å AND 4500 Å LASER
LINES
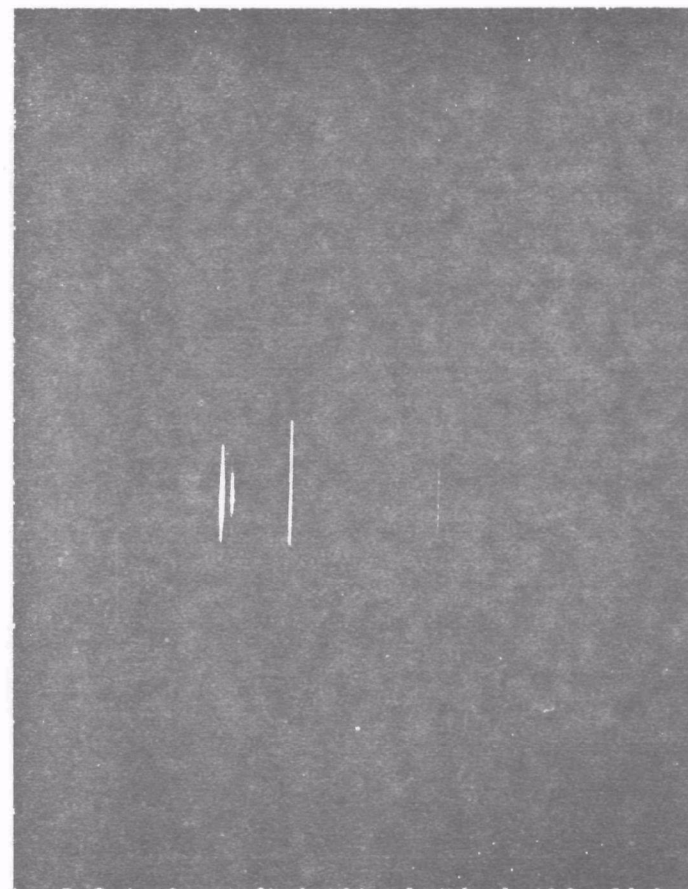
FIGURE 3.6:11d --THE 4478.5 Å AND 4500 Å LASER
LINES
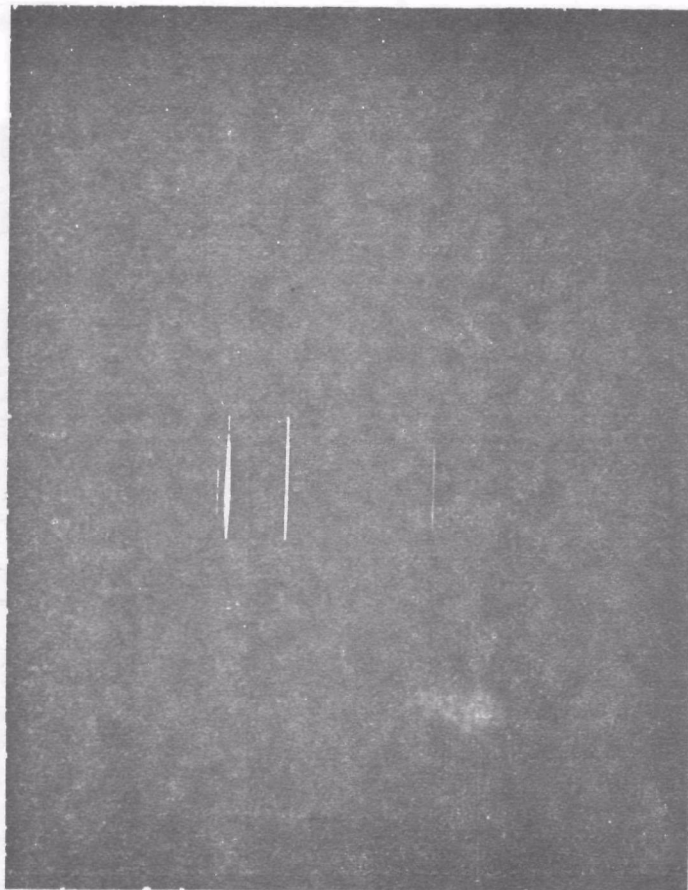
FIGURE 3.6:11e --THE 4478.5 Å AND 4500 Å LASER LINE
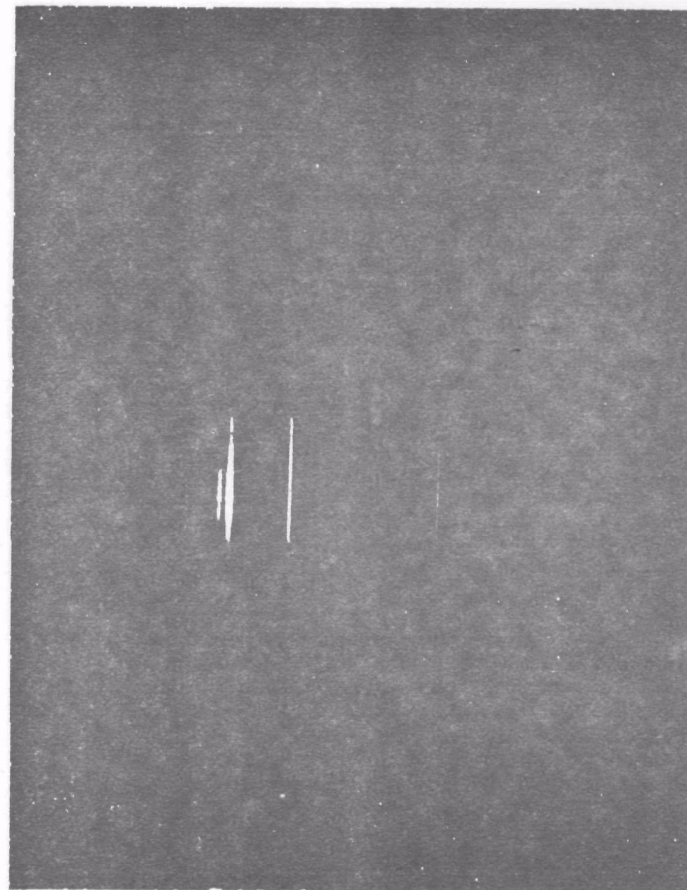
FIGURE 3.6:11f --THE 4478.5 Å AND 4500 Å LASER LINE
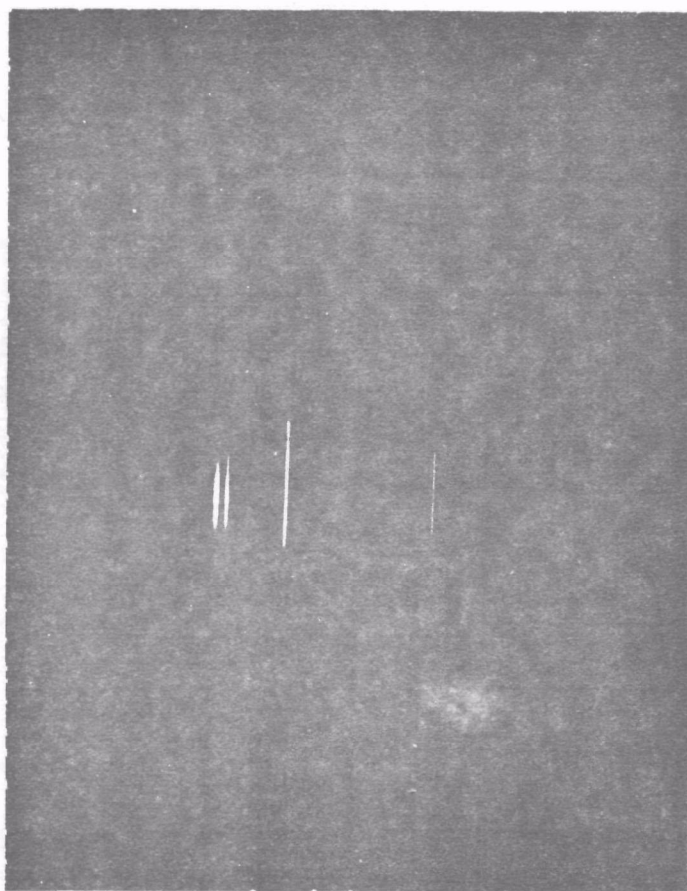
FIGURE 3.6:11g --THE 4478.5 Å AND 4500 Å LASER
LINE
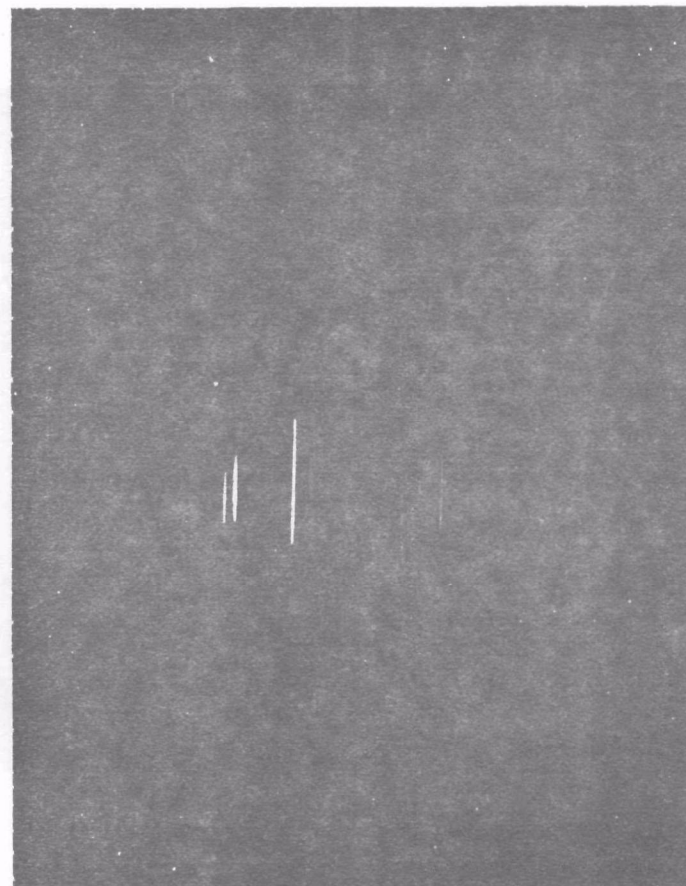
FIGURE 3.6:11h --THE 4478.4 Å AND 4500 Å LASER
LINE
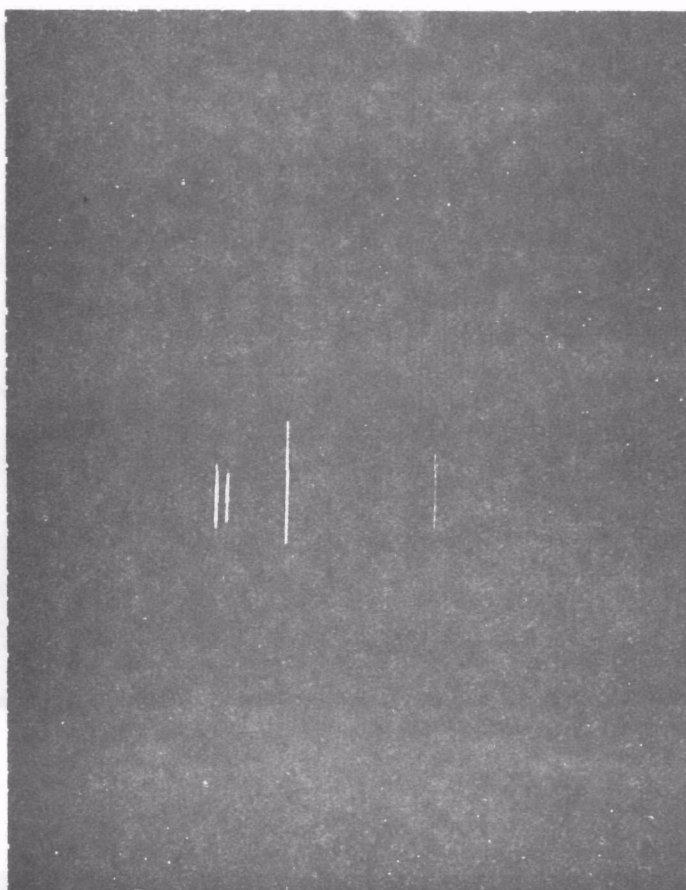
FIGURE 3.6:11i --THE 4478.5 Å AND 4500 Å LASER LINE
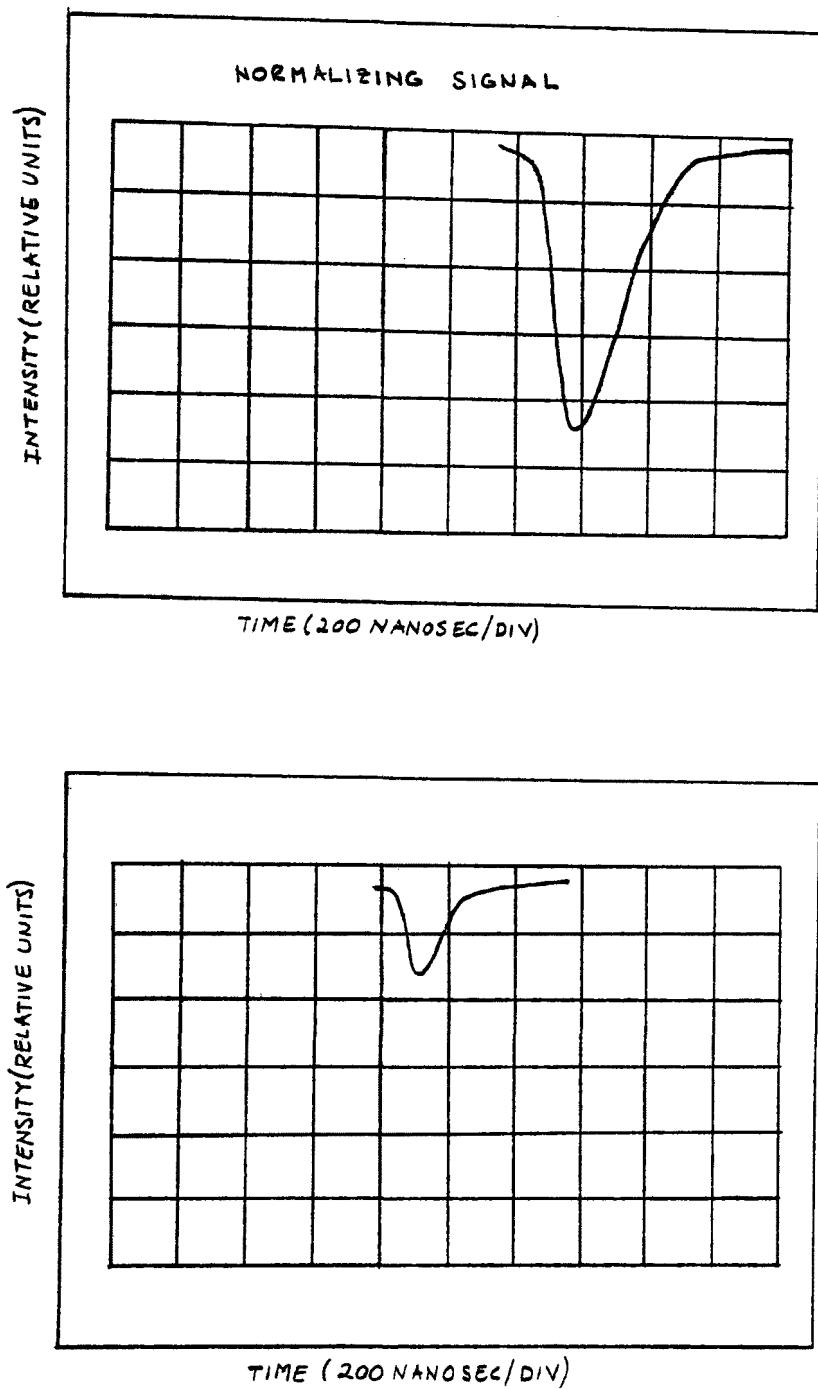
FIGURE 3.6:12a   THE INITIAL FINE TUNING SIGNALS FOR SIMULTANEOUS TWO-
WAVELENGTH OPERATION FOR OBTAINING FREQUENCY COINCI-
DENCE FOR THE 4478.5 Å LASER LINE

NORMALIZING SIGNAL

INTENSITY(RELATIVE UNITS)

TIME (200 NANOSEC/DIV)

INTENSITY(RELATIVE UNITS)

TIME (200 NANOSEC/DIV)
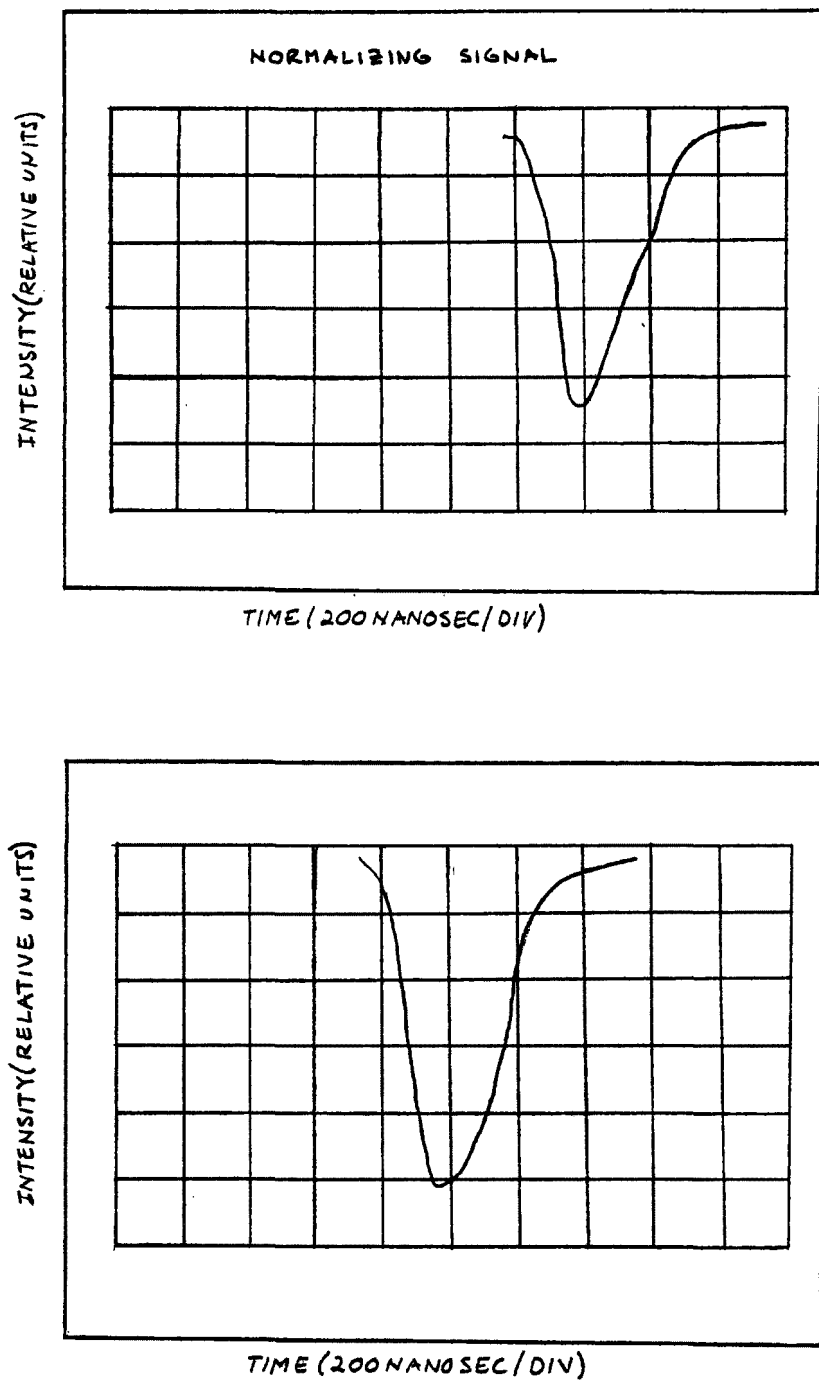
FIGURE 3.6:12b THE FINAL FINE TUNING SIGNALS FOR SIMULTANEOUS TWO-WAVELENGTH OPERATION FOR OBTAINING FREQUENCY COINCIDENCE FOR THE 4478.5 Å LASER LINE

NORMALIZING SIGNAL

INTENSITY(RELATIVE UNITS)

TIME (200 NANOSEC/DIV)

INTENSITY(RELATIVE UNITS)

TIME (200 NANOSEC/DIV)
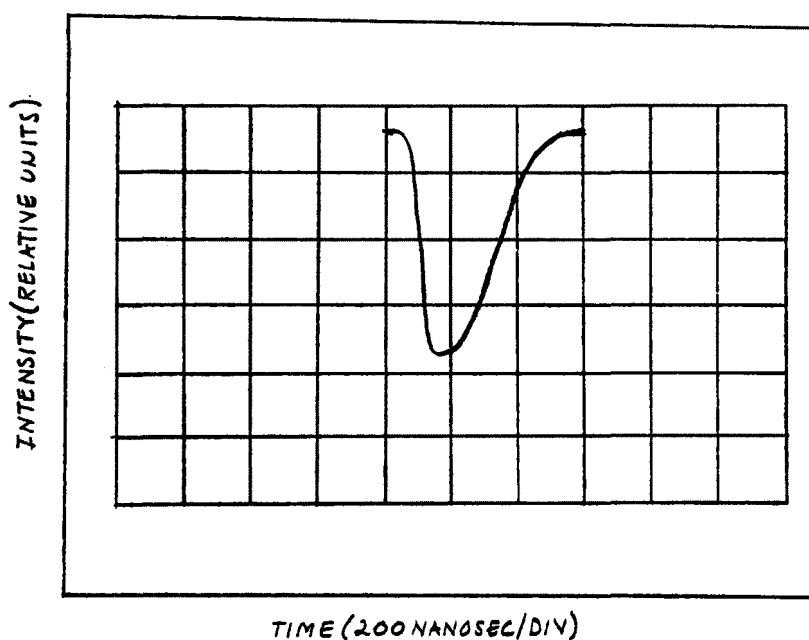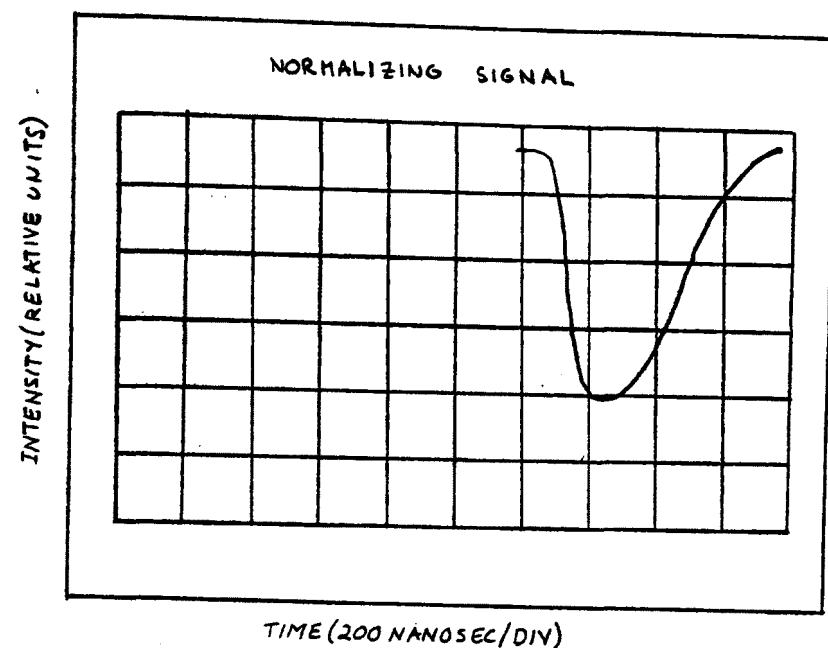
FIGURE 3.6:13a   THE INITIAL FINE TUNING SIGNALS FOR SIMULTANEOUS TWO-
WAVELENGTH OPERATION FOR OBTAINING FREQUENCY COINCI-
DENCE FOR THE 4500 Å LASER LINE

111

NORMALIZING SIGNAL

INTENSITY (RELATIVE UNITS)

TIME (200 NANOSEC/DIV)

INTENSITY (RELATIVE UNITS)

TIME (200 NANOSEC/DIV)
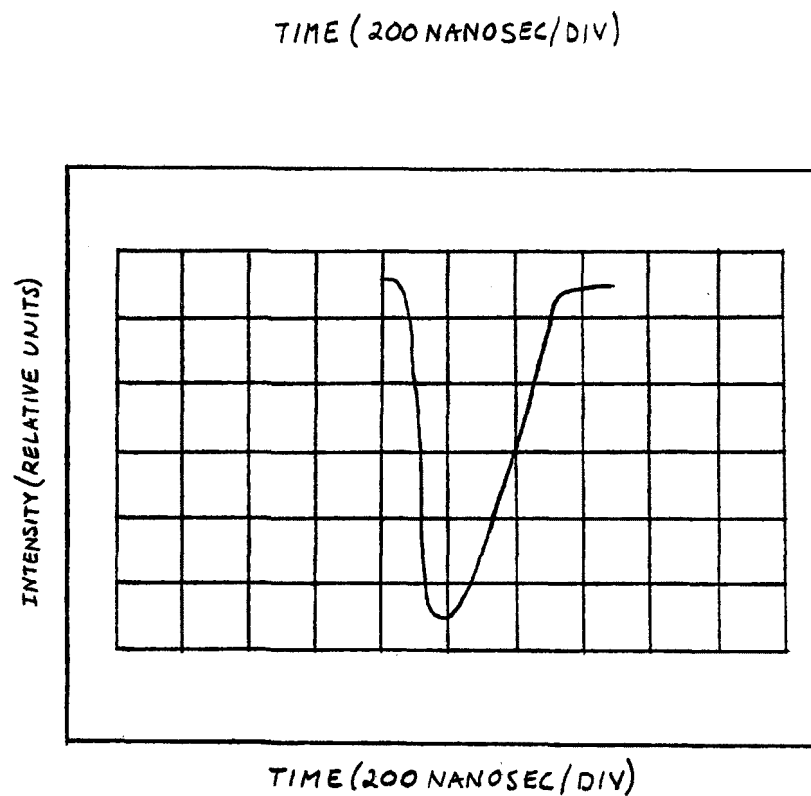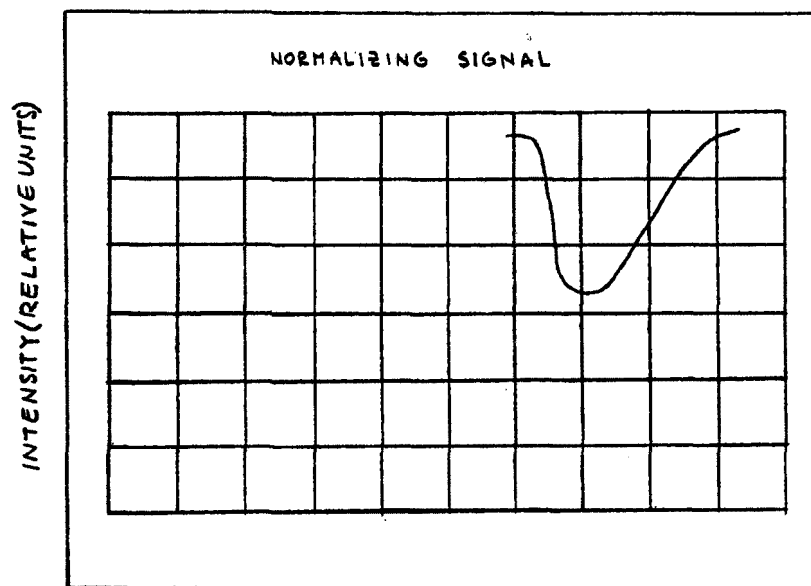
FIGURE 3.6:13b   THE FINAL FINE TUNING SIGNALS FOR SIMULTANEOUS TWO-WAVELENGTH OPERATION FOR OBTAINING FREQUENCY COINCIDENCE FOR THE 4500 Å LASER LINE
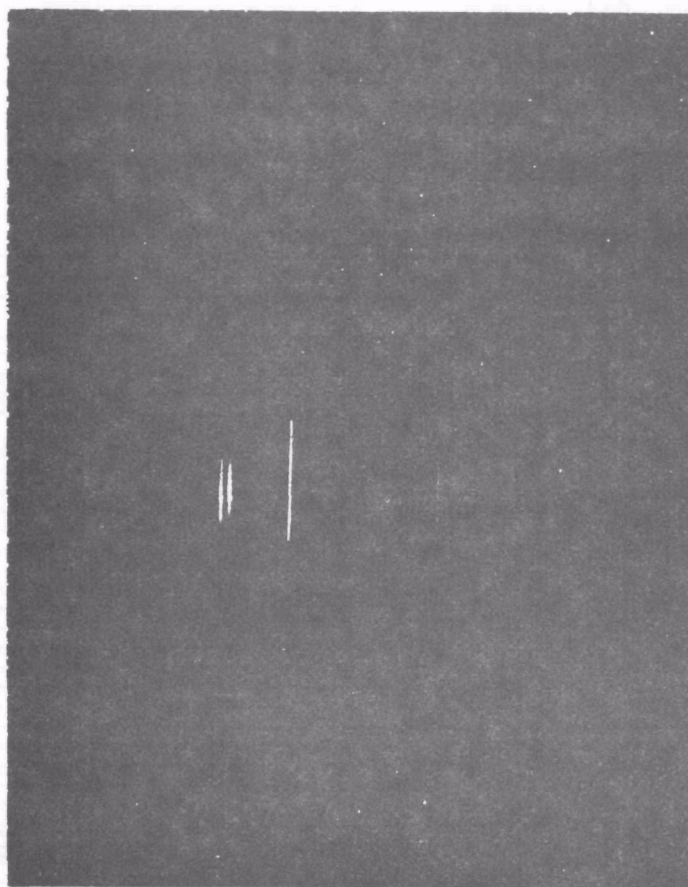
FROM LEFT TO RIGHT: 4500 Å, 4478 Å, 4358 Å, 4078 Å, AND 4047 Å

FIGURE 3.6:14   SPECTROMETER PHOTOGRAPH OF THE SIMULTANEOUS

TWO-WAVELENGTH OUTPUT WITH LASER FREQUENCIES

FINE TUNED TO 4478.5 Å AND 4500 Å WITH APPROX-

IMATELY 5 Å BANDWIDTHS

EFFICIENCY–PERCENT

100

E⊥

50

E //

MASTER =24 FR
1800 g/mm

0

| 0.3 | 0.4 | 0.5 | 0.6 | 0.7 |

WAVELENGTH – MICRONS
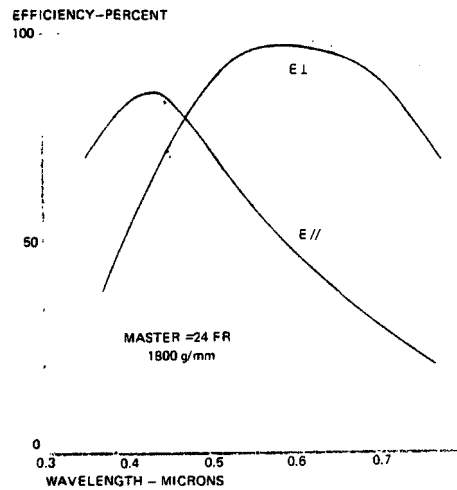
GRATING TYPE	LASER POWER CONTINUOUS	LASER POWER PULSED	MAXIMUM TEMPERATURE
Replica on pyrex aluminum coating	50 W/cm^2	2 MW/cm^2 on 20 - 30 ns	100°C

Grating Characteristics

FIGURE 3.6:15   SPEC. SHEET 3.6:1

114

TEST INSTRUMENT _____ *Eazy 14*

DATE _*10/26/74*_ TECHNICIAN _____

AMBIENT TEMP. _____ °C CHART SPEED _*20*_ Ang/Div.

CALIBRATION CORRECTION FACTOR _____ Ang

PEAK WAVELENGTH _____ *4480* Ang
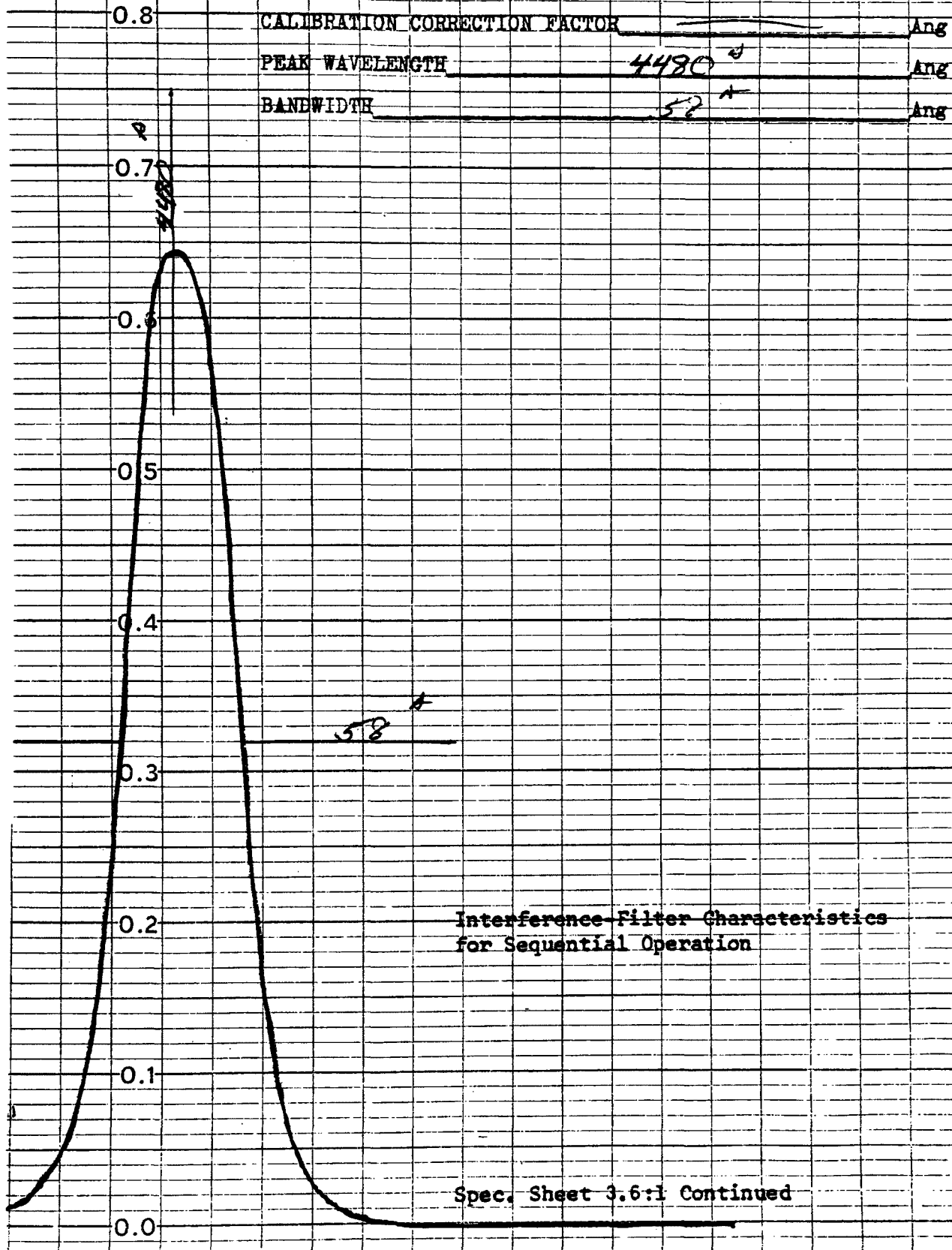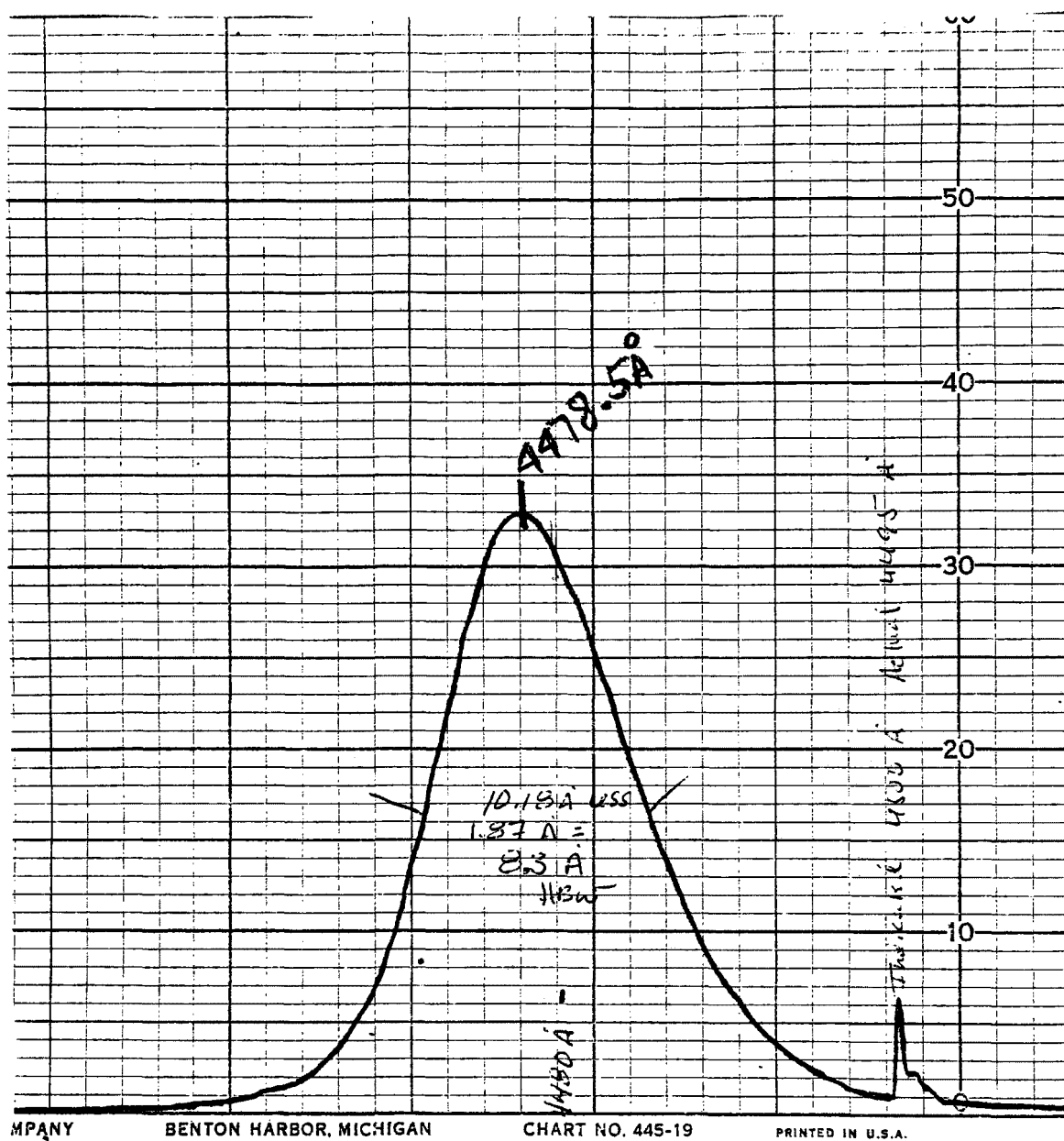
BANDWIDTH _____ *52* Ang

Interference-Filter Characteristics
for Sequential Operation

Spec. Sheet 3.6:1 Continued

115

Interference-Filter Characteristics for Simultaneous Two-Wavelength
Operation

Spec. Sheet 3.6:1 Continued

116

Interference-Filter Characteristics for Simultaneous Two-Wavelength Operation

Spec. Sheet 3.6:1 Continued

117

CHAPTER 4 NO_2 MEASUREMENTS

4.1 Introduction

Measurements on NO_2 were carried out using laser outputs at 4478.5 Å and 4500 Å. These were optimized using the procedure described in Sect. 3.6.3.

Alignment of the outgoing laser beam with the receiver telescope was carried out by using a water tower on top of a building over 2 km away as a target and adjusting the alignment of the receiver telescope to obtain the maximum return signal from the tower. The outgoing beam goes out eastwards from a corner window in our laboratory, and passes over upper Manhattan and the East River.

4.2 Results of Field Tests

4.2.1 Sequential Measurements

Measurements were carried out in the sequential mode of operation with pulses fired at intervals of approximately 5 seconds. The laser was fired in trains of three pulses: on-peak, off-peak, and on-peak. Measurements were only considered valid when the first and the third pulse returns were nearly identical, indicating that no substantial scene change had occurred between pulses.

With the LIDAR system pointing out of the laboratory window, measurements of the LIDAR backscatter returns at 4478.5 Å and 4500 Å were carried out. The return signal, the output of the photomultiplier tube in the receiver system, was displayed on the oscilloscope and recorded photographically.

Fig. 4.2:1 shows a curve trace from an oscilloscope photograph of a typical return signal. The peak occurring at 16 µs represents the reflection from the water tower on top of a building some 2400 m away from the LIDAR site.

Fig. 4.2:2 shows the trace of the return signal when a number of chimneys below the beam path were emitting smoke.

Fig. 4.2:3a and b show respectively two curves plotted from oscilloscope photographs of the returns at 4478.5 Å and 4500 Å, and the calibration signals obtained for these readings. As can be seen from the curves, the signal at 4478.5 Å, which is on the absorption peak, was clearly attenuated more than the signal at 4500 Å, which is off the absorption peak.

The different attenuations may be noticed immediately by looking at the reflection peaks from the building 2400 m (16 us) away.

The relative attenuation is largest over a 450 m region extending from a range of approximately 1050 to 1500 m. Below the LIDAR beam in that region are several avenues with heavy traffic. NO_2 densities over that region are calculated from the curves to be approximately 0.46 ppm.

The overall average density to the building and back is approximately 0.09 ppm. Measurements of this type show a correlation within 30 percent of the sample measurements made at a fixed-site, the Department of Air Resources monitoring station situated near the area.

4.2.1.1 Factors Affecting Accuracy

In the initial field tests, the laser beam was paraxial with the optical receiver axis. This arrangement was used to avoid local scat-
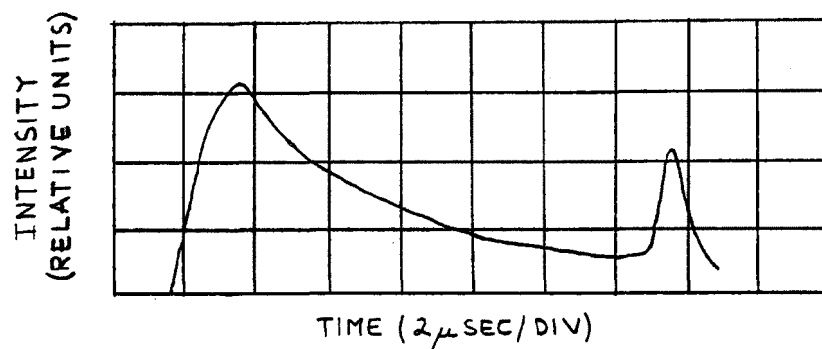
FIGURE 4.2:1   TYPICAL LIDAR RETURN SIGNAL
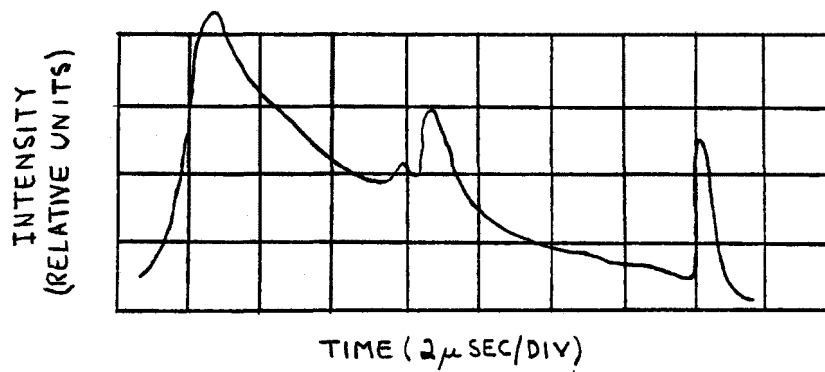
FIGURE 4.2:2   TYPICAL LIDAR RETURN SIGNAL WITH CHIMNEYS BELOW BEAM

PATH
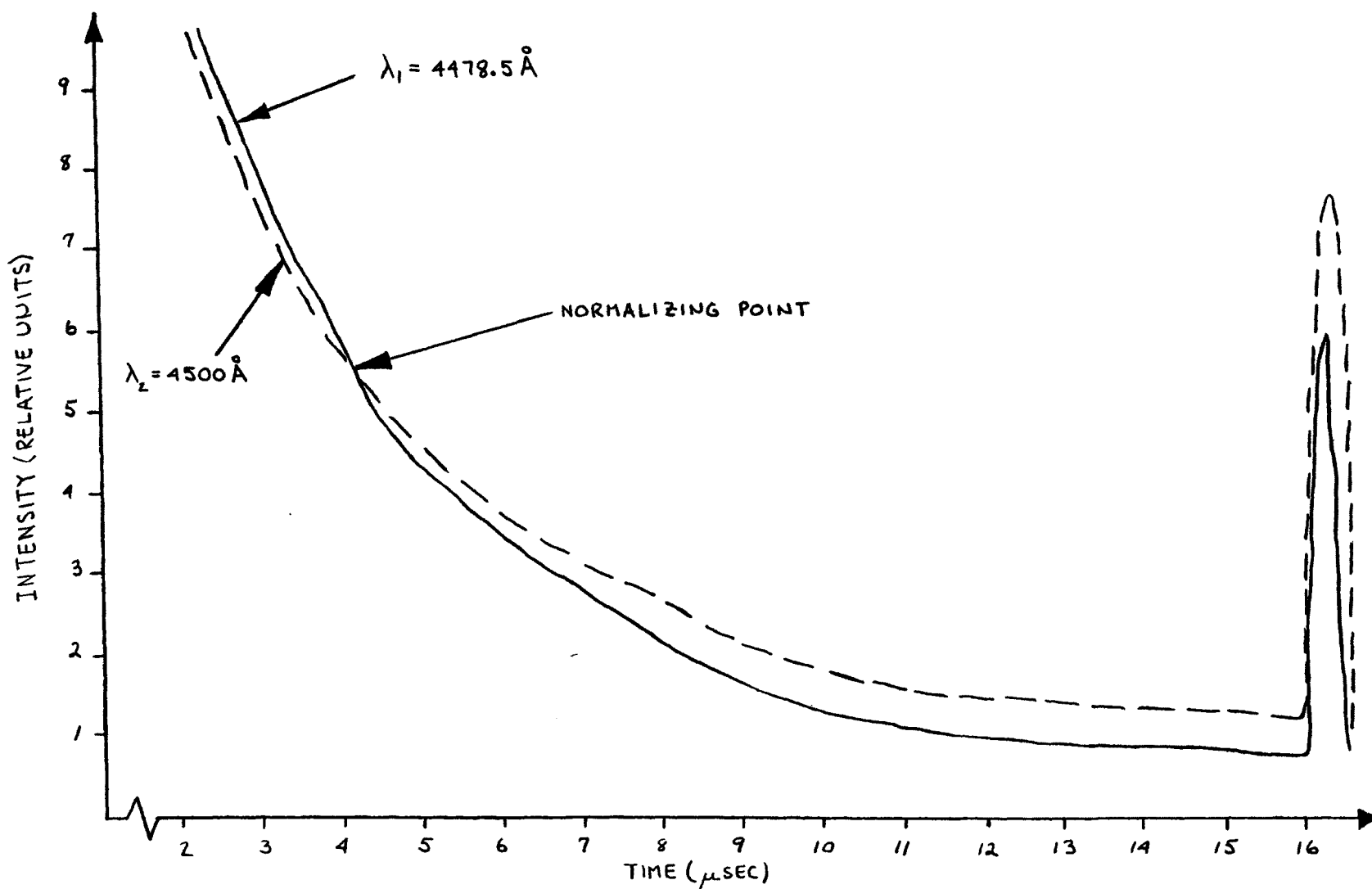
FIGURE 4.2:3a   SEQUENTIAL LIDAR RETURN SIGNALS AT 4478.5 Å AND 4500 Å
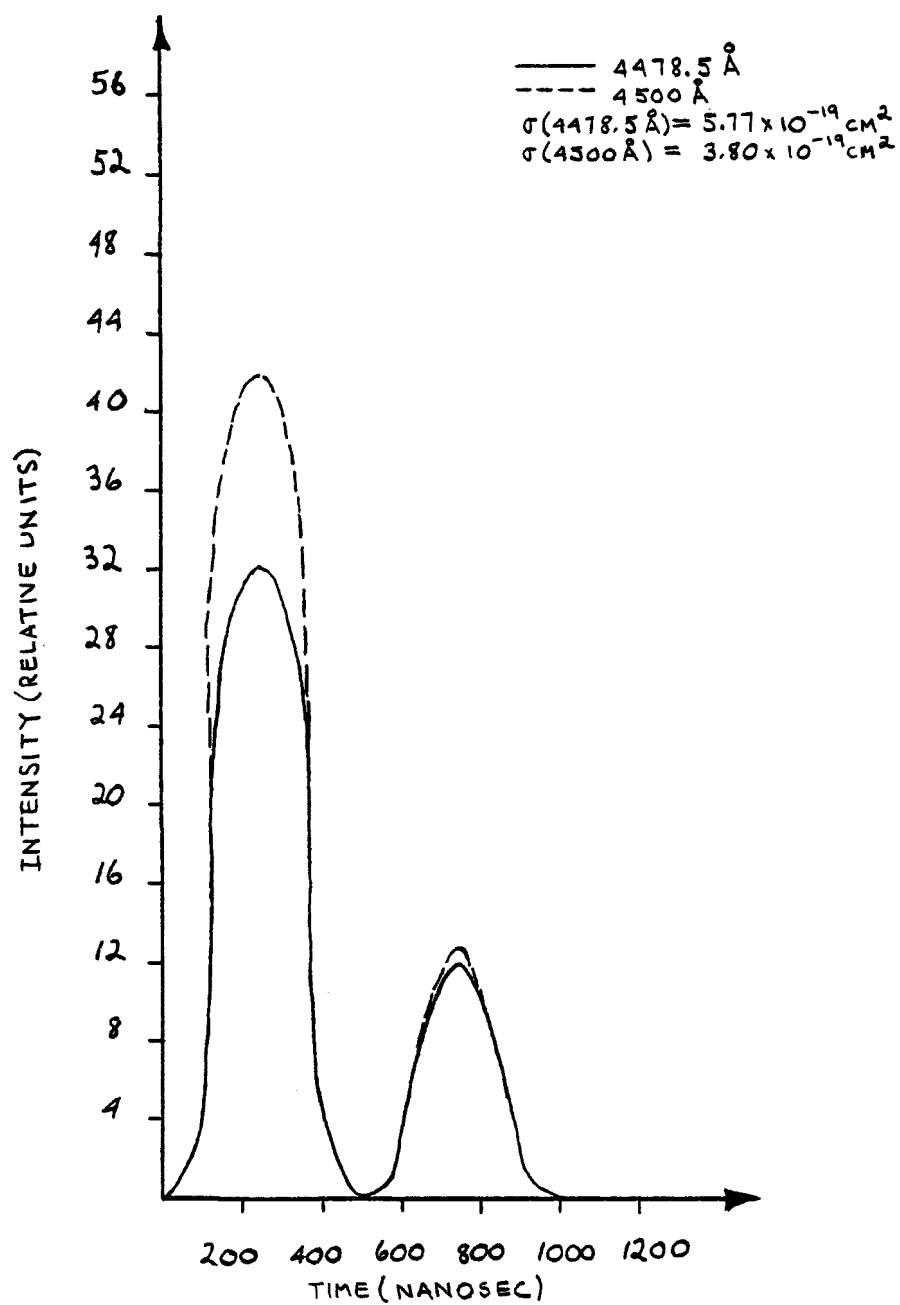
FIGURE 4.2:3b   SEQUENTIAL CALIBRATION SIGNALS AT 4478.5 Å AND 4500 Å

122

tering from the outgoing beam into the receiver. This scattering problem was overcome with a redesigned optical arrangement with the outgoing beam collinear with the optical receiver axis. This permitted the use of a much more collimated output beam along with a smaller acceptance angle for the optical receiver field of view. This has resulted in improved signal-to-noise ratios as well as reducing the importance of shot to shot repeatability of the geometric intensity distribution of the laser output pulse.

Other factors were also found to affect the accuracy of measurements. With sequential operation, changes in the region probed by the laser beam in the time interval between shots obviously cause errors. Changes are of two types:

1. Scintillation effects, which cause rapid changes in the transmission of the beam and backscattered signal through the atmosphere.

2. More gradual changes due to particulates and pollutants being blown by wind.

Scintillation effects are particularly bad when there are large temperature gradients across the beam path.

To check that neither of these effects is causing substantial errors when sequential measurements are being made, the laser is operated in groups of three pulses, with the first pulse being off-resonance, the second on-resonance, and the third pulse off-resonance again, to ensure no substantial changes with the first. It is found that these conditions prevail particularly when there are no patches of particulates, e.g., smoke drifting across the scene being viewed, and when

123

there are no strong temperature gradients causing scintillation effects. The curves of Figs. 4.2:1 and 4.2:3a were obtained under such conditions.

For conditions where the scene or optical path is changing rapidly, which is frequently the case, there appears to be no remedy but to use simultaneous wavelength operation, so that both wavelengths are traversing the same optical path at the same time.

4.2.2 Simultaneous Two-Wavelength Measurements

A series of field tests were carried out operating the laser in the simultaneous two-wavelength mode of operation. For this purpose, the arrangement described in Sect. 3.5.2 and Figs. 3.5:4a and b was used, as well as the calibration cell arrangement described in Sect. 3.6.2 and Figs. 3.6:7a and b.

Figs. 4.2:4a through o each show typical pairs of curves plotted from oscilloscope photographs of the LIDAR returns and the calibration signals at 4478.5 Å and 4500 Å for various times during the day.

During the field tests it was noted that the readings from the calibration system indicated that there was a monotonic narrowing in laser bandwidth with the number of laser firings. This can readily be seen in view of Figs. 4.2:4b, d, f, h, j, l, and n. These curves show that the difference in effective absorption cross sections increased with the number of times the laser was fired.

The effective NO_2 absorption cross sections therefore varied from 5.43×10^{-19} cm^2 and 4.17×10^{-19} cm^2 to 6.36×10^{-19} cm^2 and 3.54×10^{-19} cm^2 for the 4478.5 Å and 4500 Å lines, respectively. This effect was expected, and as explained in Sect. 3.6 is due to solarization of
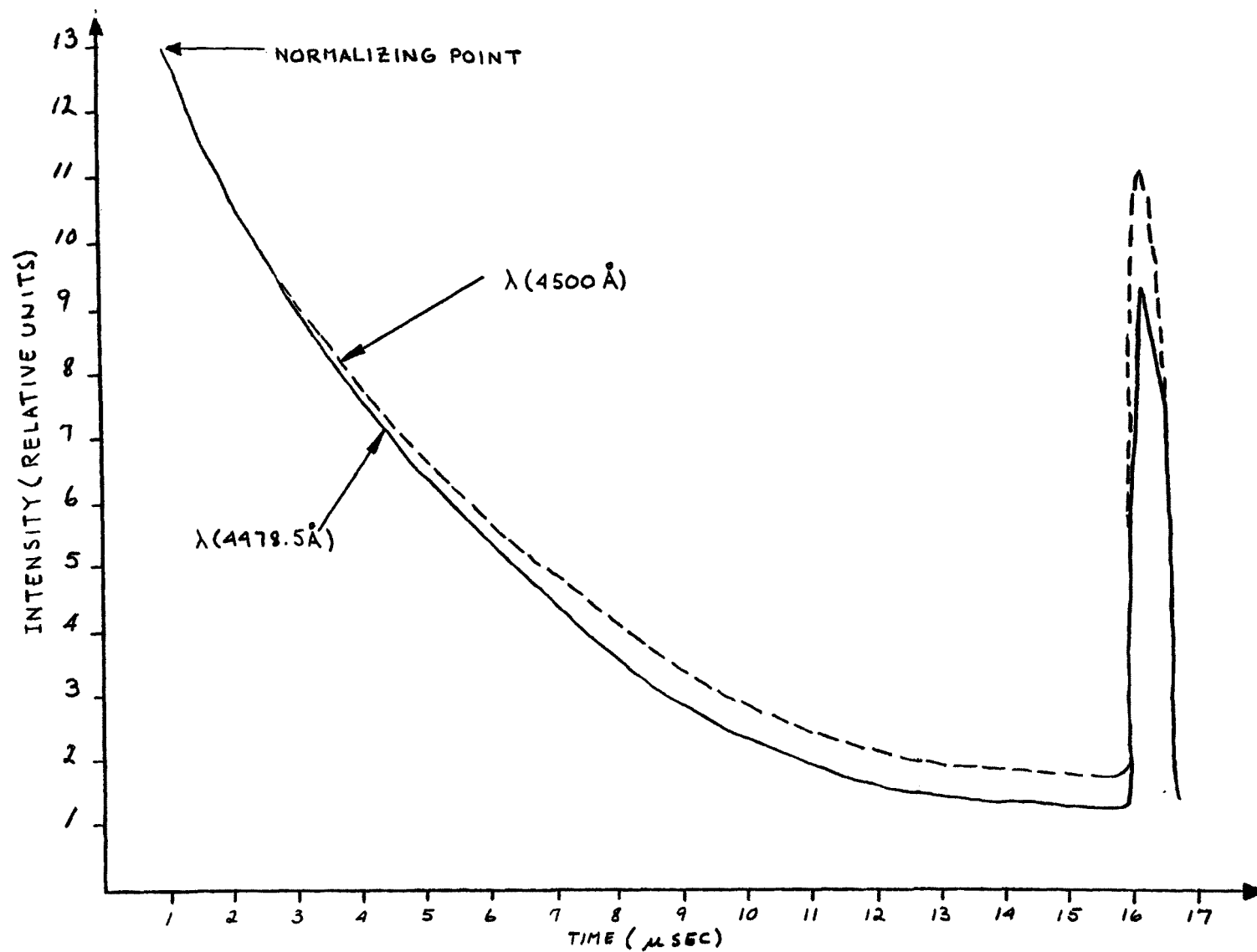
FIGURE 4.2:4a   SIMULTANEOUS LIDAR RETURN SIGNALS AT 4478.5 Å AND 4500 Å, TIME: 8:45 A.M.
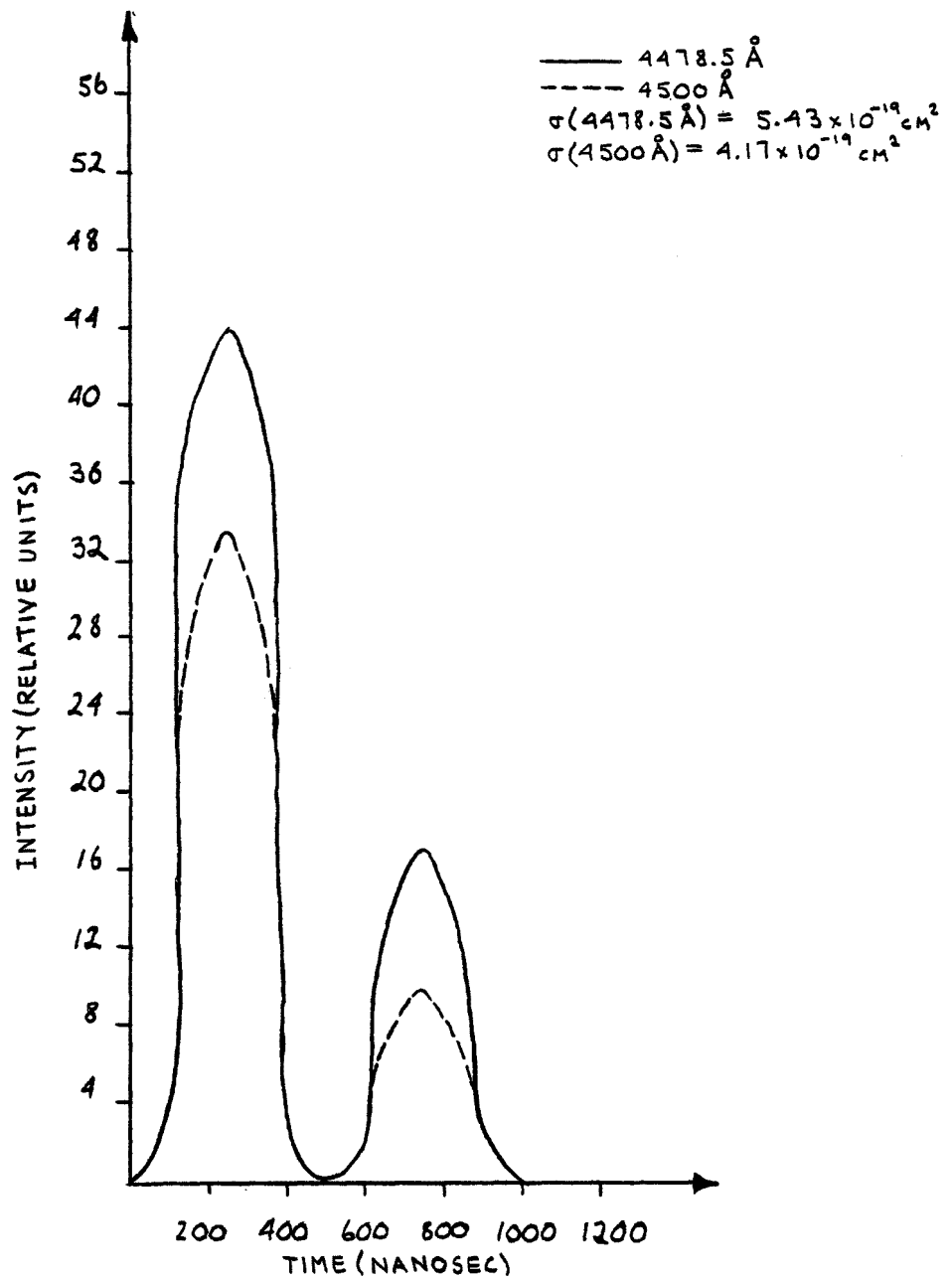
FIGURE 4.2:4b SIMULTANEOUS CALIBRATION SIGNALS FOR 4478.5 Å AND 4500 Å, TIME: 8:45 A.M.

NORMALIZING POINT

λ(4500 Å)

λ(4478.5 Å)

INTENSITY (RELATIVE UNITS)

TIME (μ SEC)
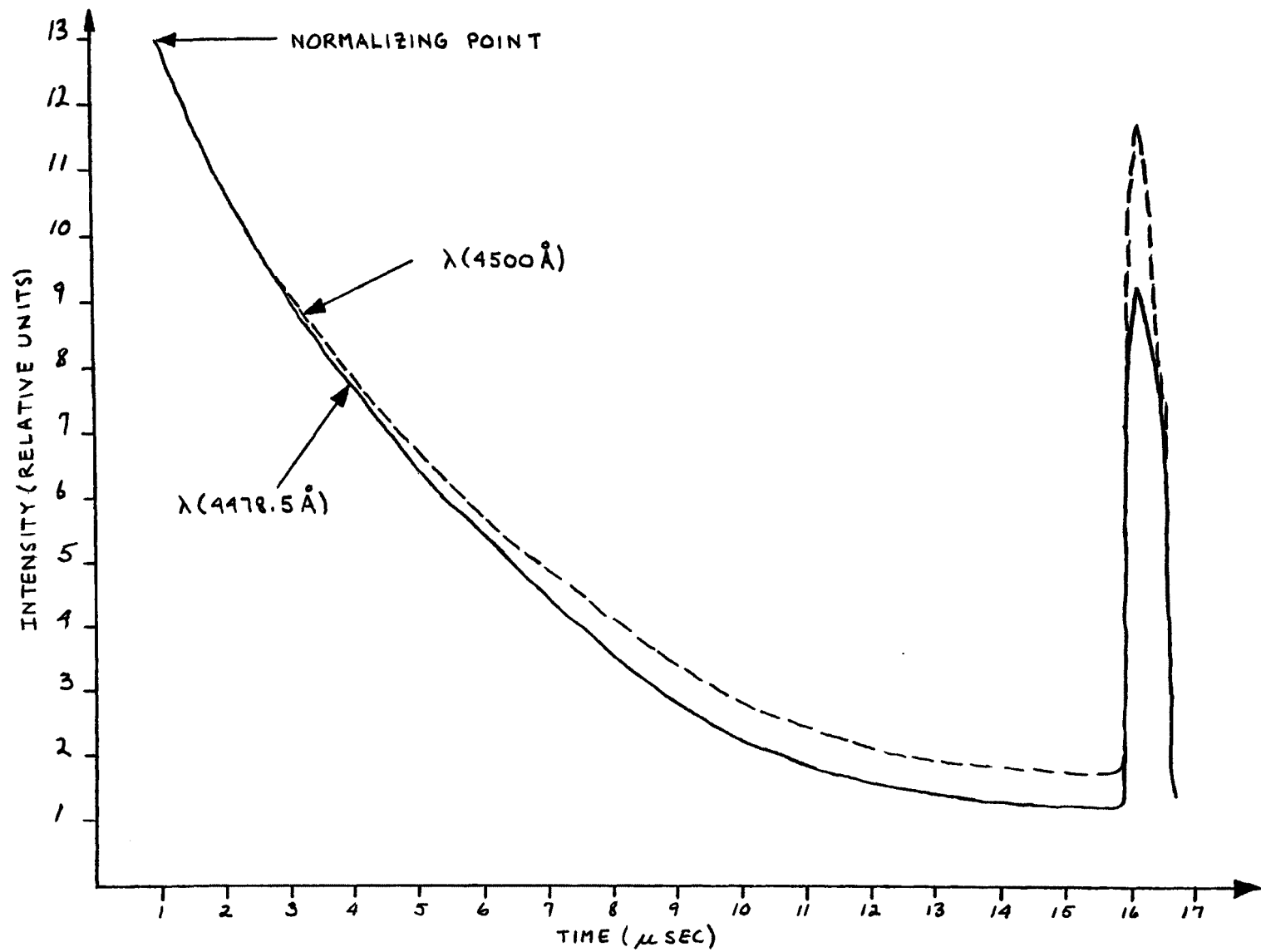
FIGURE 4.2:4c   SIMULTANEOUS LIDAR RETURN SIGNALS AT 4478.5 Å AND 4500 Å, TIME: 9:00 A.M.

127
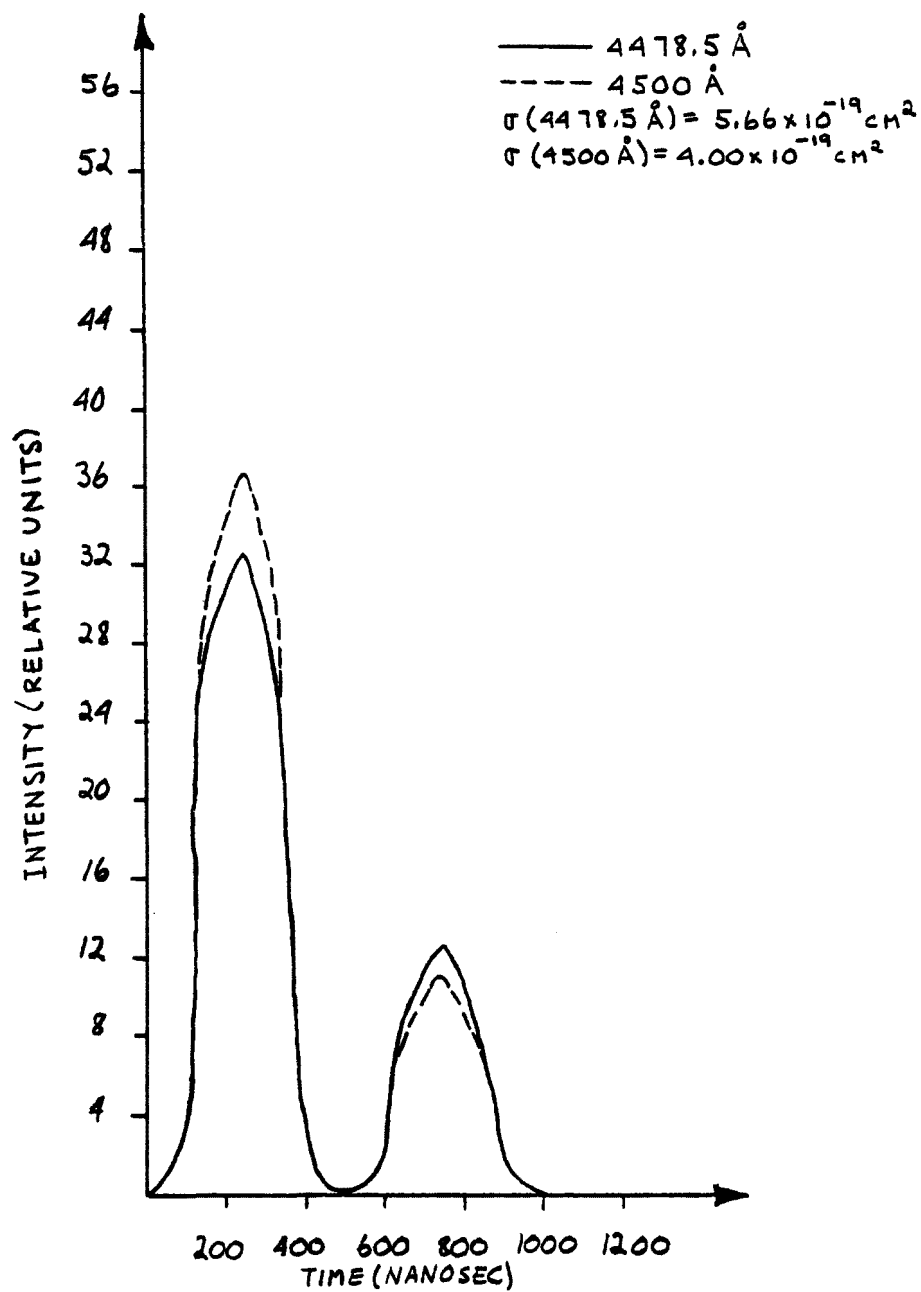
FIGURE 4.2:4d   SIMULTANEOUS CALIBRATION SIGNALS FOR 4478.5 Å AND 4500

Å, TIME: 9:00 A.M.
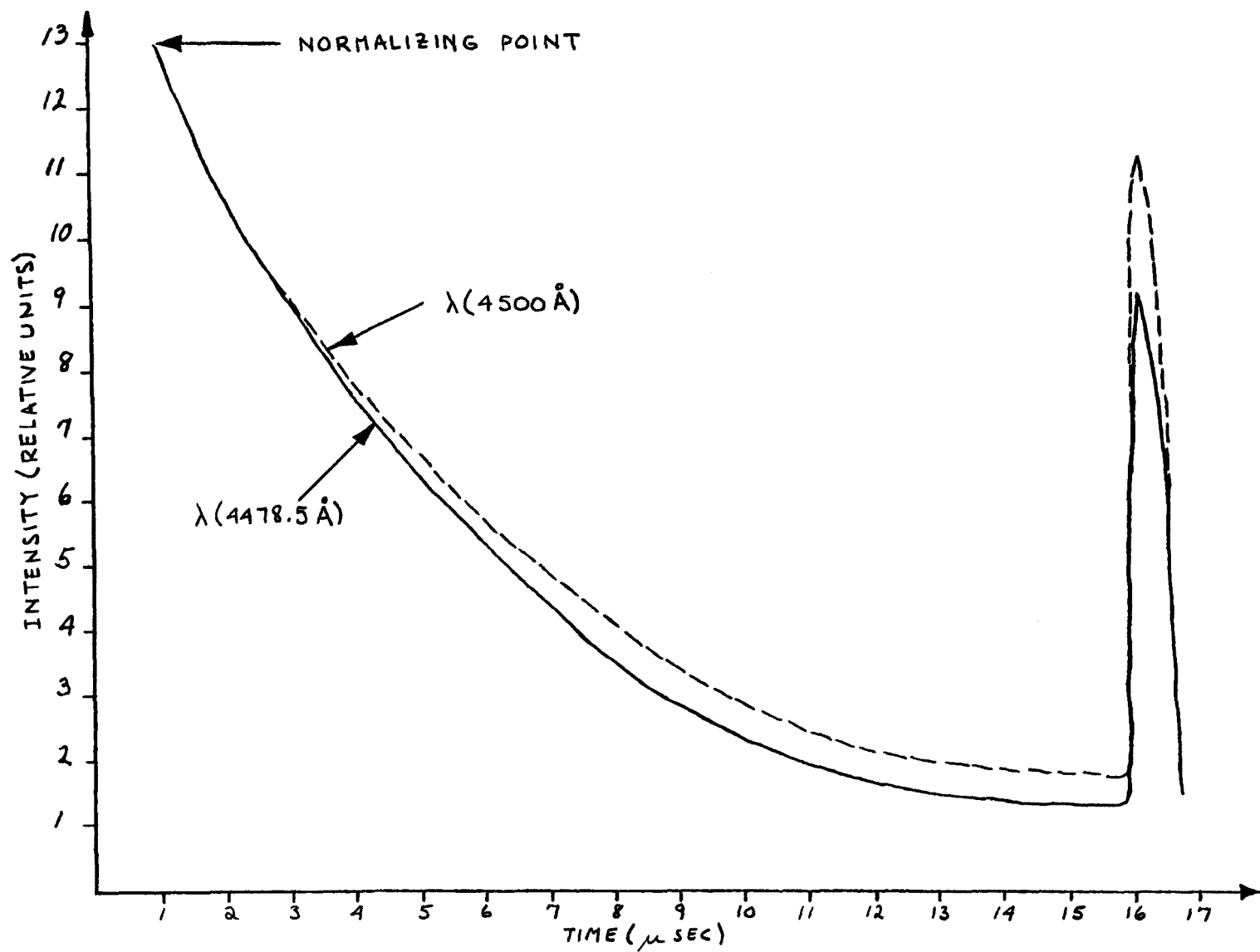
FIGURE 4.2:4e   SIMULTANEOUS LIDAR RETURN SIGNALS AT 4478.5 Å AND 4500 Å, TIME: 9:30 A.M.
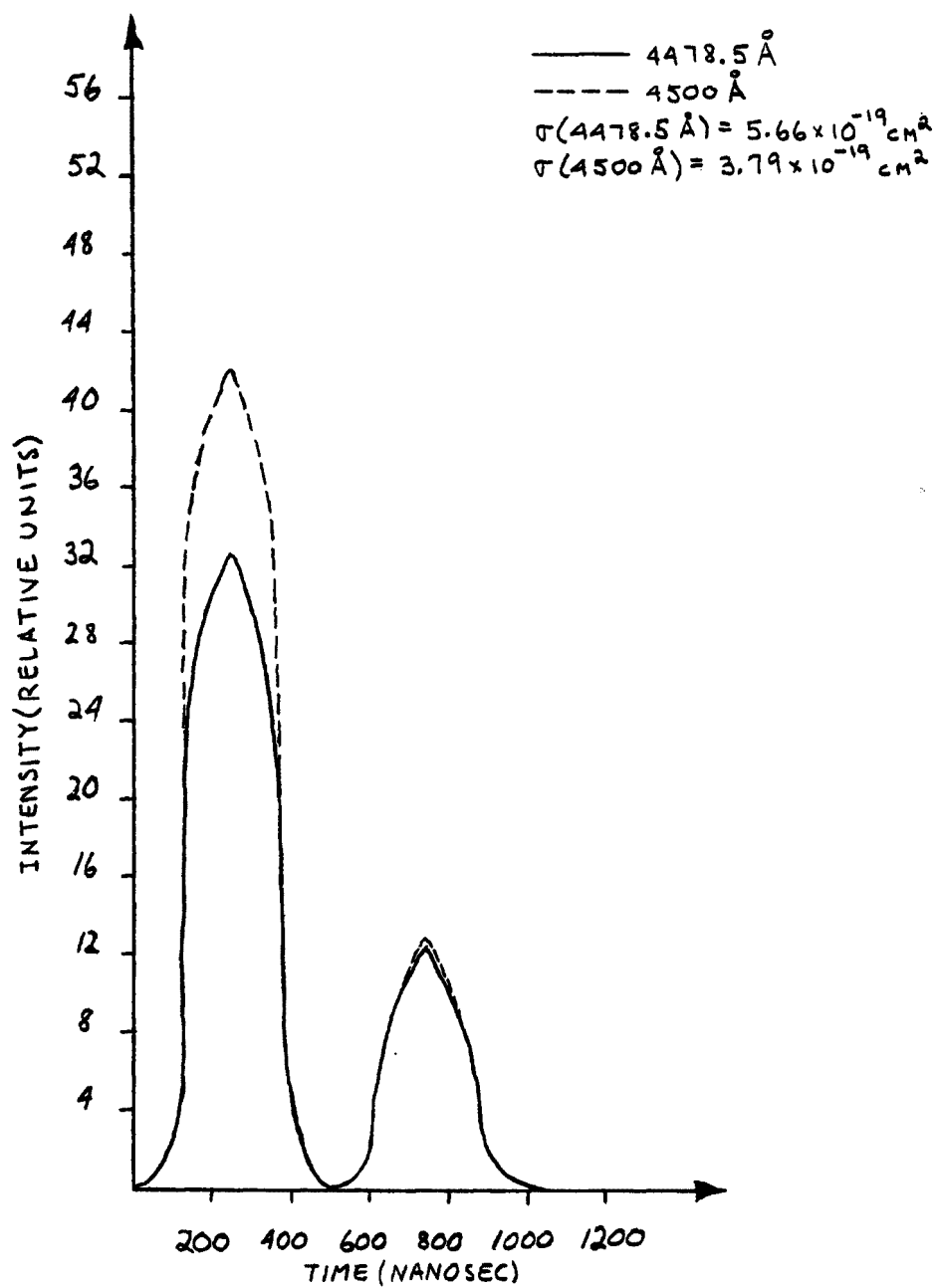
FIGURE 4.2:4f SIMULTANEOUS CALIBRATION SIGNALS FOR 4478.5 Å AND 4500 Å, TIME: 9:30 A.M.

130
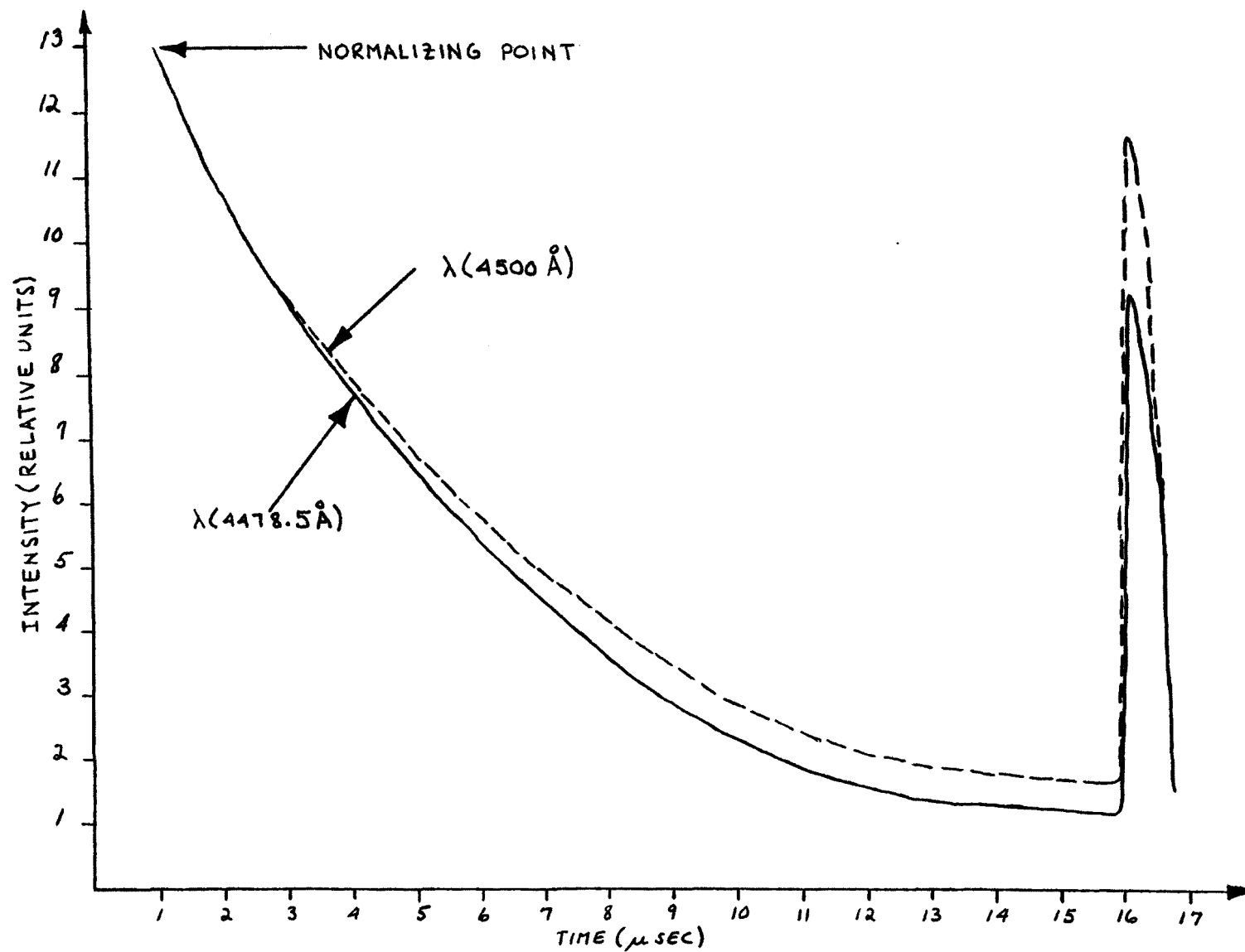
FIGURE 4.2:4g   SIMULTANEOUS LIDAR RETURN SIGNALS AT 4478.5 Å AND 4500 Å, TIME: 5:30 P.M.
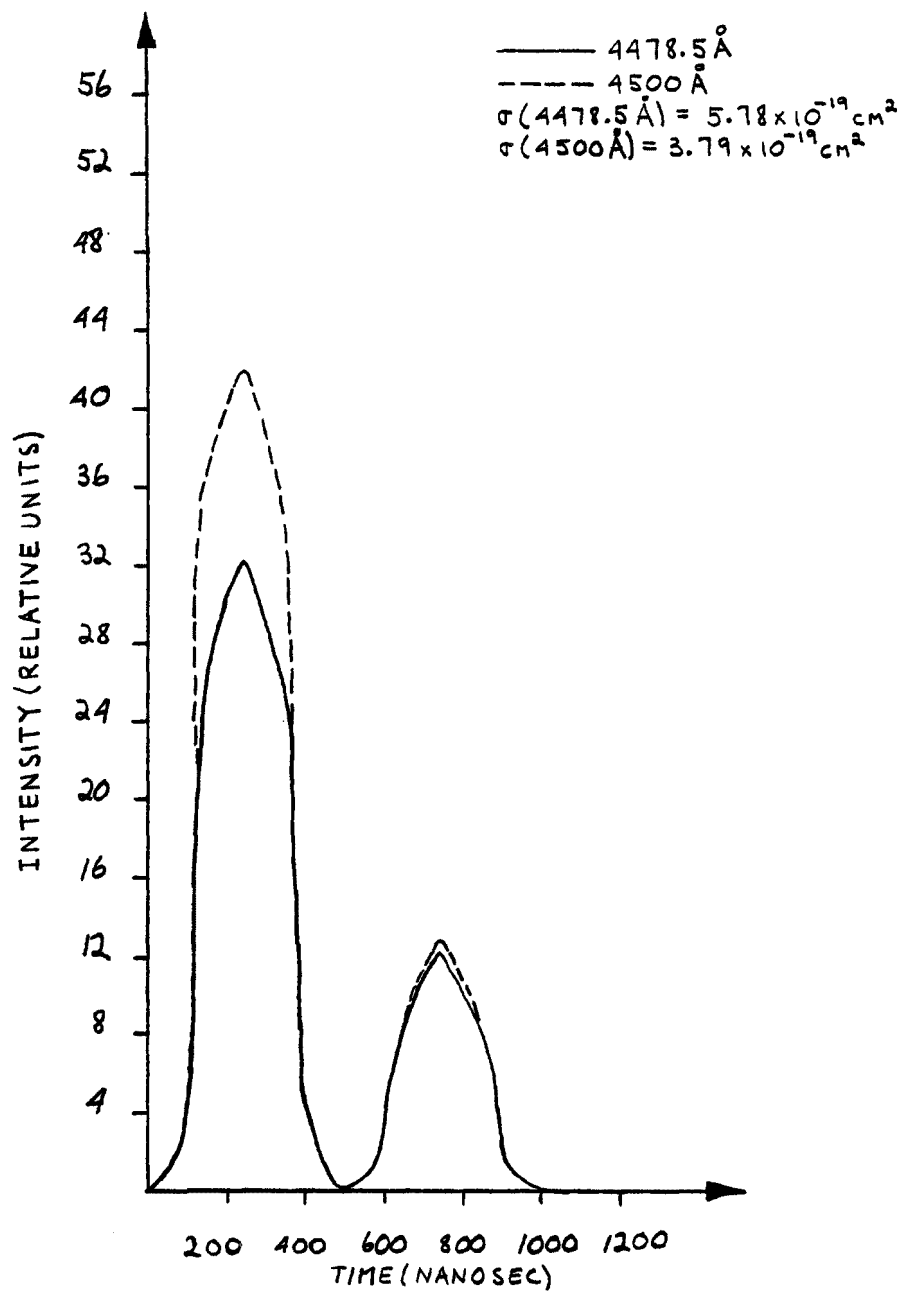
FIGURE 4.2:4h SIMULTANEOUS CALIBRATION SIGNALS FOR 4478.5 Å AND 4500

Å, TIME: 5:30 P.M.

132
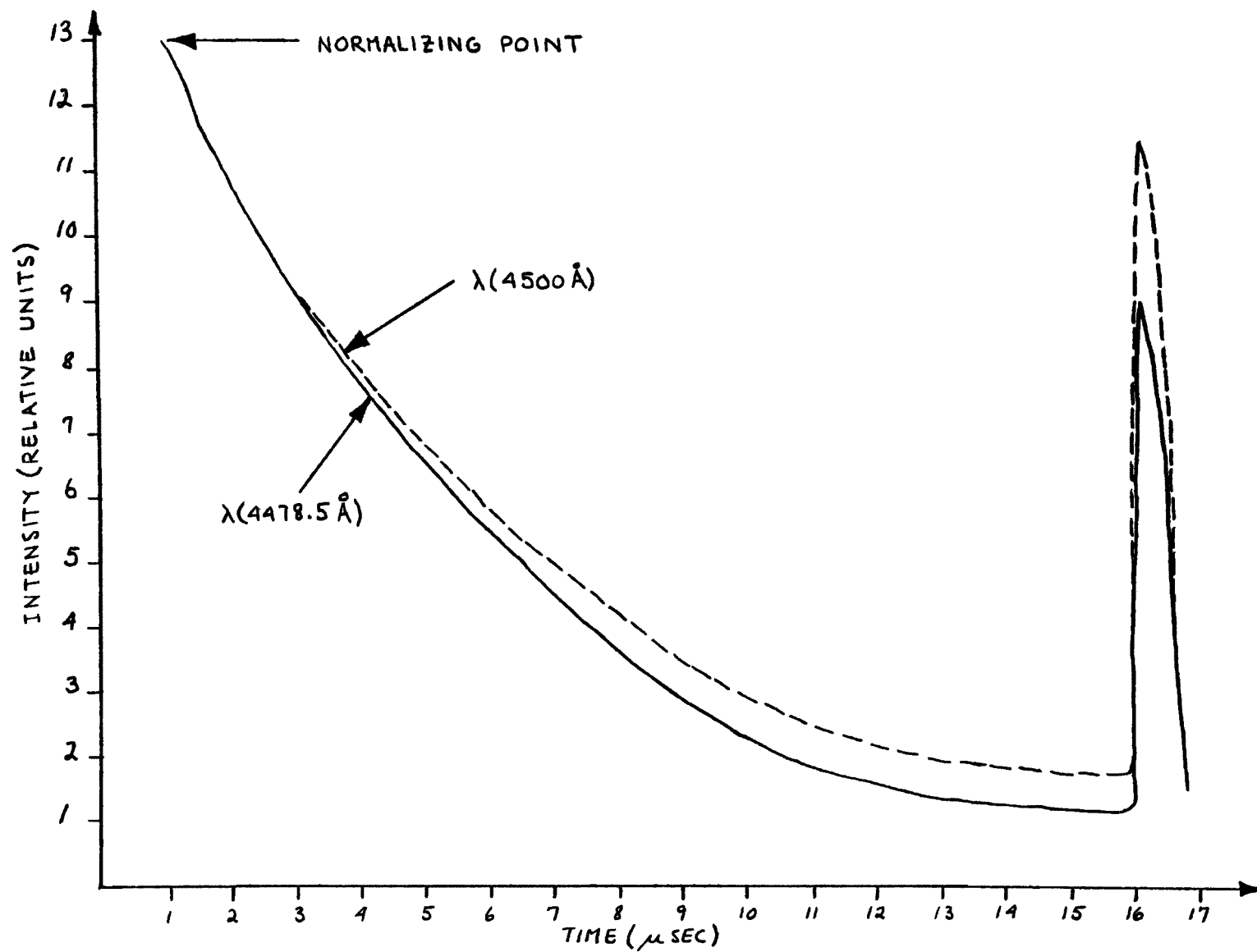
FIGURE 4.2:41   SIMULTANEOUS LIDAR RETURN SIGNALS AT 4478.5 Å AND 4500 Å, TIME: 6:00 P.M.
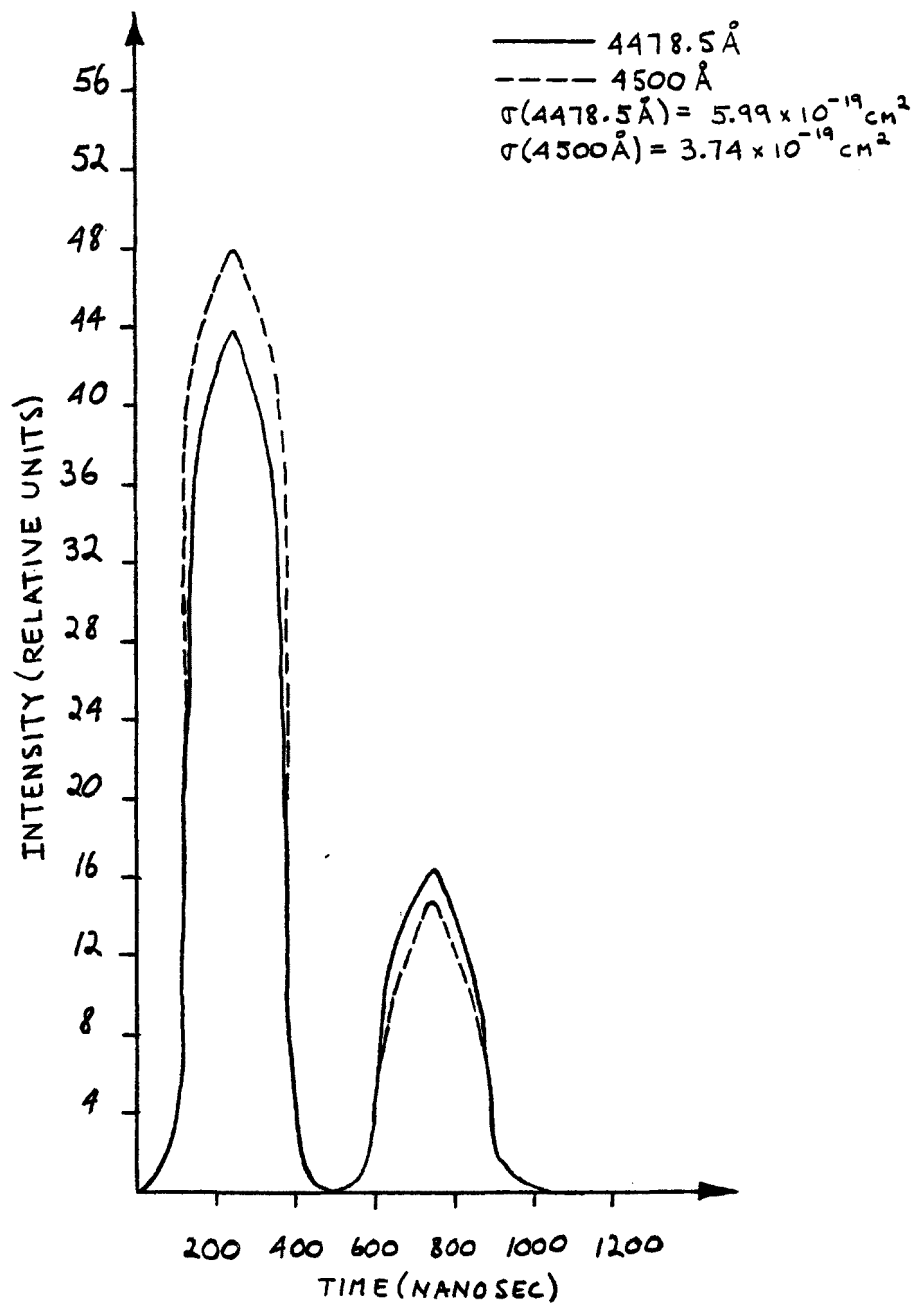
FIGURE 4.2:4j   SIMULTANEOUS CALIBRATION SIGNALS FOR 4478.5 Å AND 4500 Å, TIME: 6:00 P.M.
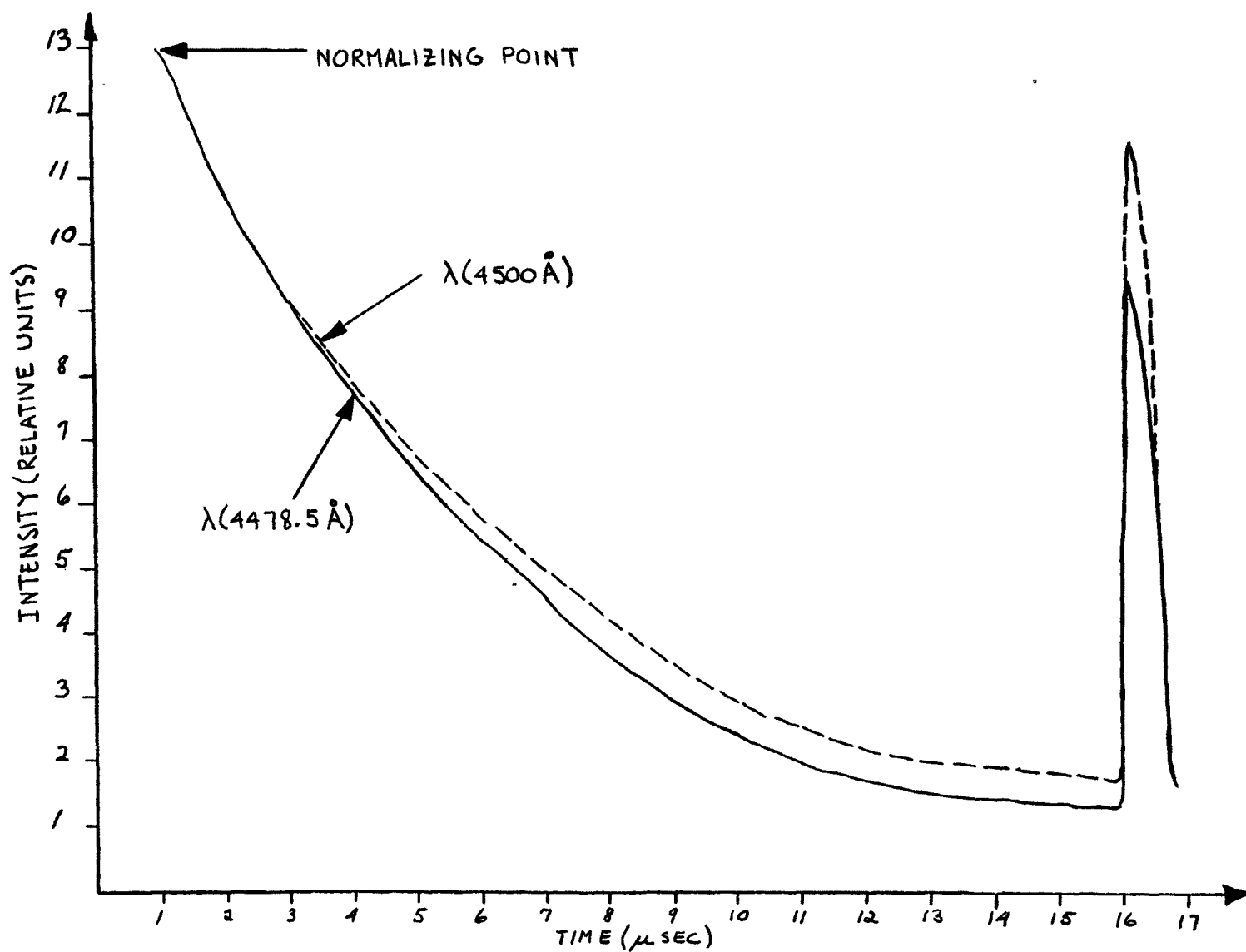
FIGURE 4.2:4k   SIMULTANEOUS LIDAR RETURN SIGNALS AT 4478.5 Å AND 4500 Å, TIME: 6:30 P.M.
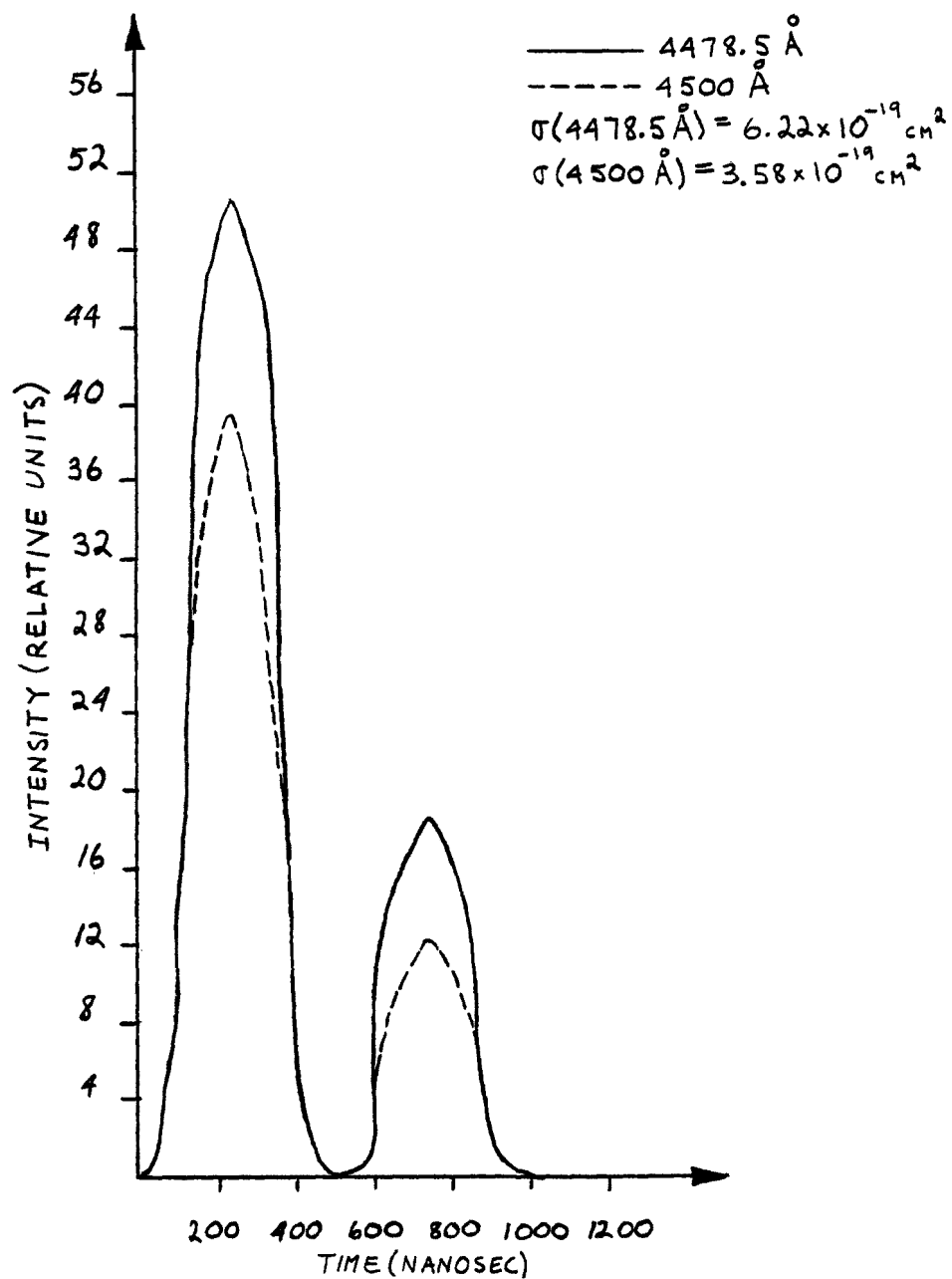
FIGURE 4.2:41 SIMULTANEOUS CALIBRATION SIGNALS FOR 4478.5 Å AND 4500

Å, TIME: 6:30 P.M.

136
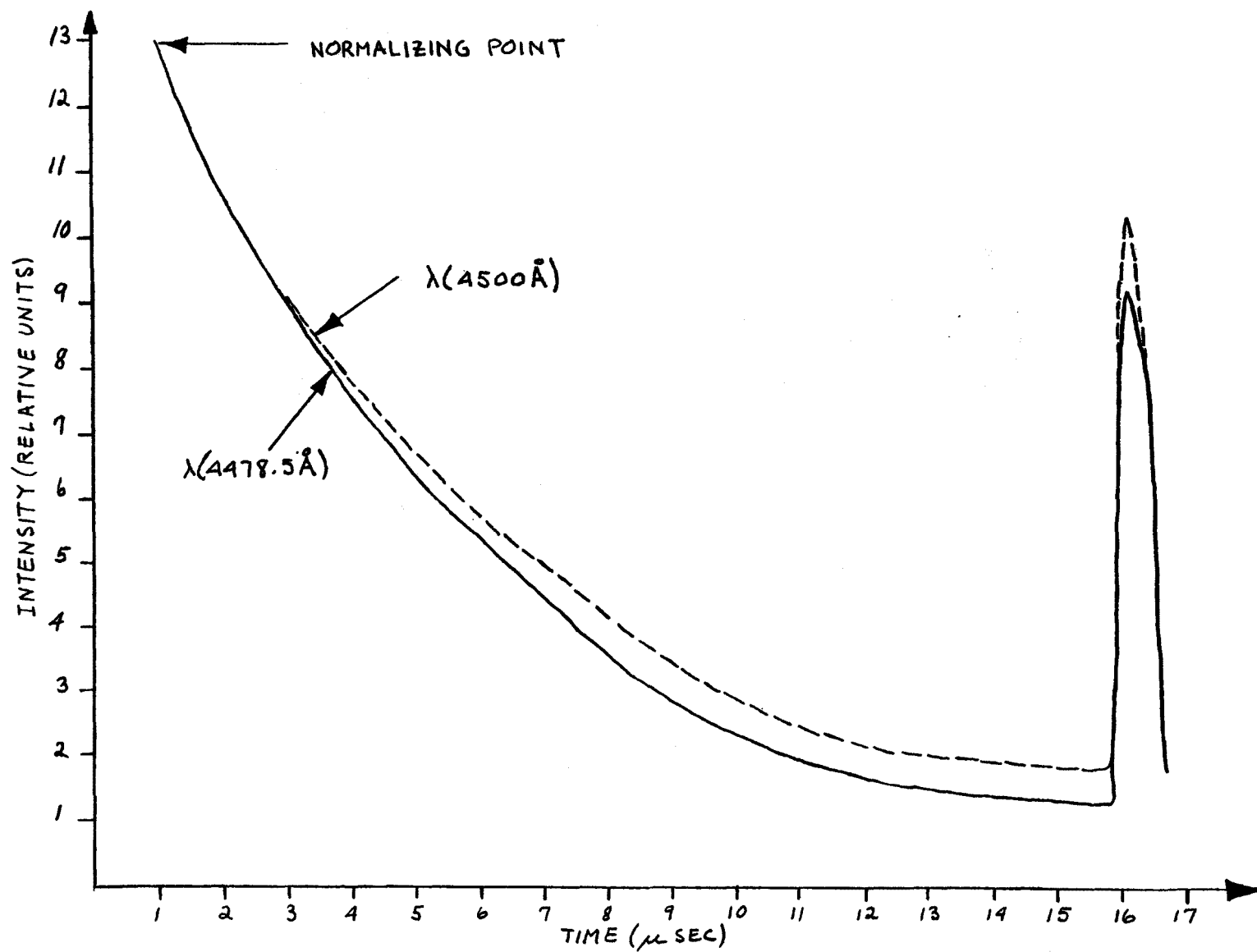
FIGURE 4.2:4m SIMULTANEOUS LIDAR RETURN SIGNALS AT 4478.5 Å AND 4500 Å, TIME: 8:00 P.M.

137
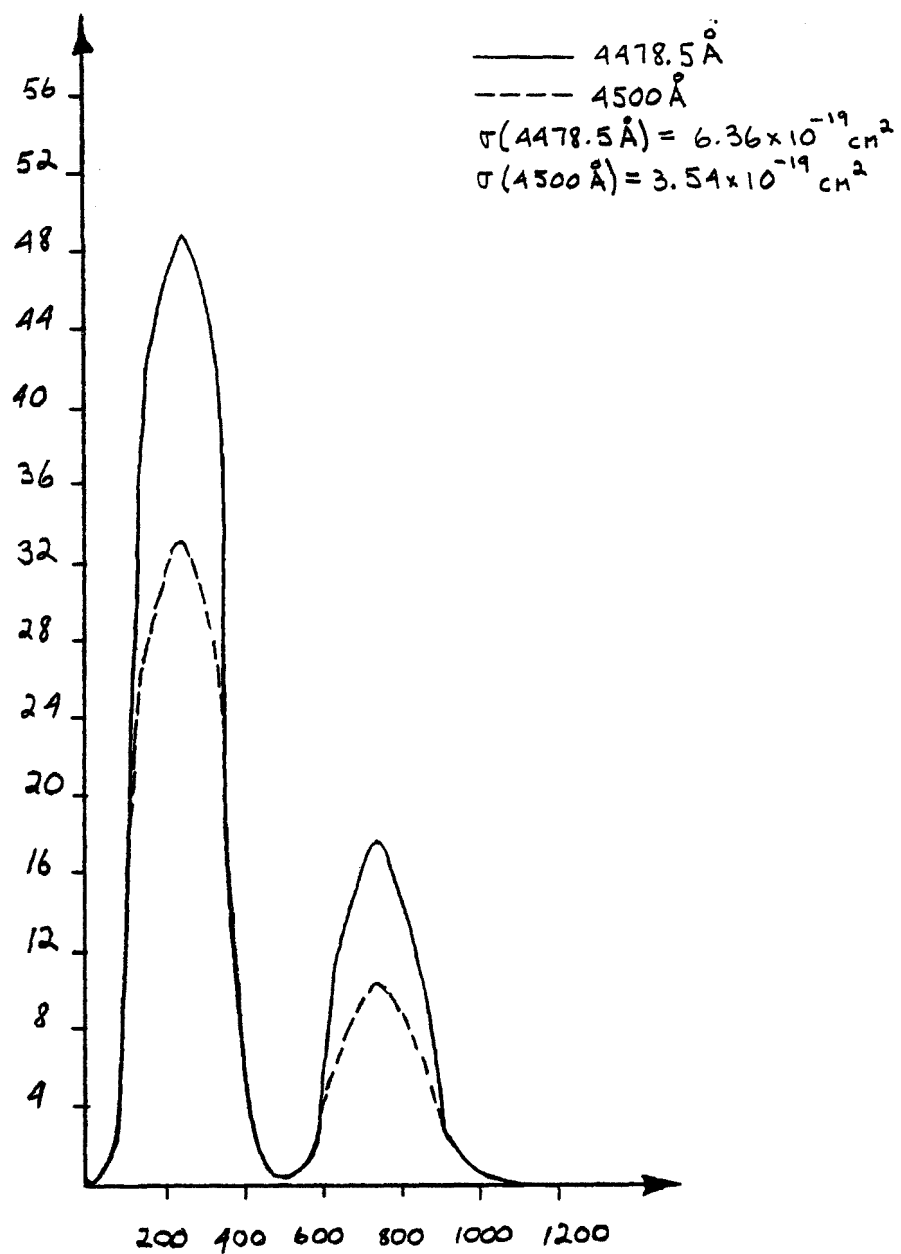
FIGURE 4.2:4n   SIMULTANEOUS CALIBRATION SIGNALS FOR 4478.5 Å AND 4500

Å, TIME: 8:00 P.M.
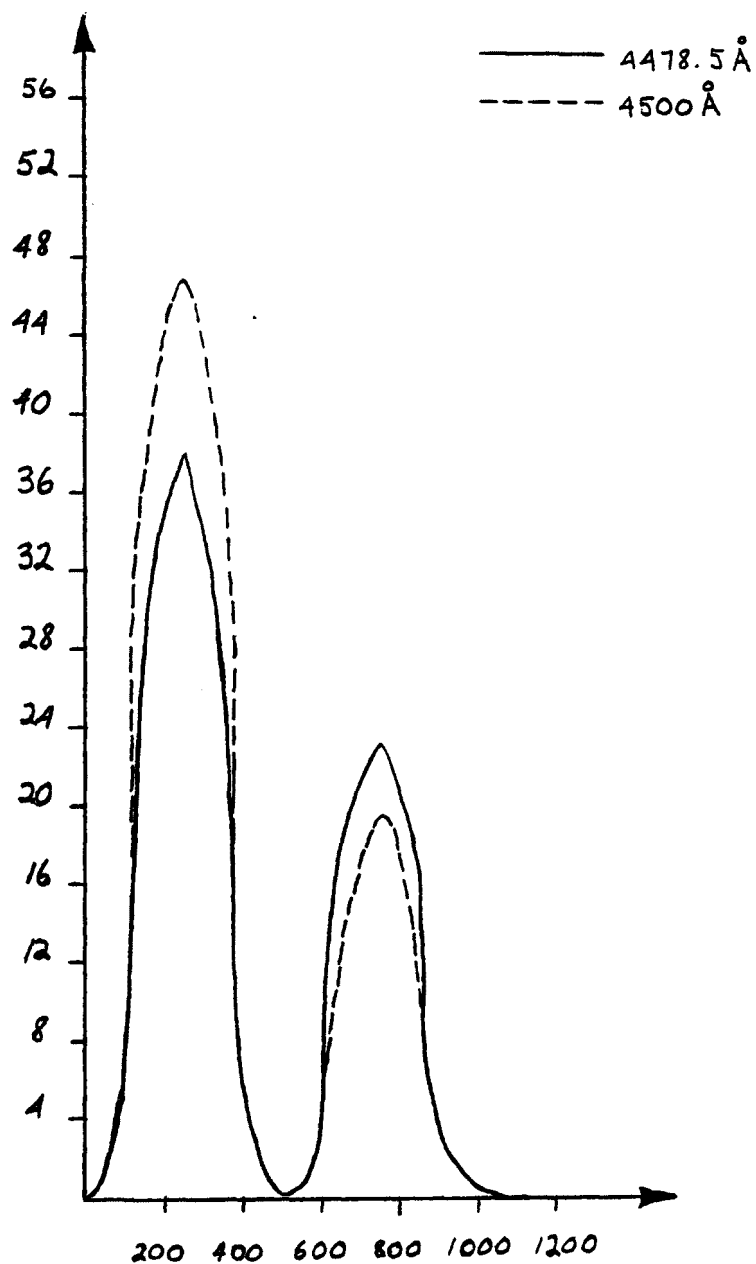
FIGURE 4.2:40   SIMULTANEOUS CALIBRATION SIGNALS FOR 4478.5 Å AND 4500

Å FOR NORMALIZATION (WITH N_2 IN THE CALIBRATION CELL)

r (m)	r (m)	Time	NO_2 Concentration (ppm)	Uncertainity (ppm)
1050	450	8:45 A. M.	0.29	0.05
		9:00 A. M.	0.31	
		9:30 A. M.	0.21	
		5:30 P. M.	0.26	
		6:00 P. M.	0.24	
		6:30 P. M.	0.15	
		8:00 P. M.	0.14	
750	300	8:45 A. M.	0.31	0.07
		9:00 A. M.	0.22	
		9:30 A. M.	0.22	
		5:30 P. M.	0.19	
		6:00 P. M.	0.15	
		6:30 P. M.	0.16	
		8:00 P. M.	0.11	
FROM LIDAR SITE TO BLDG.	2400	8:45 A. M.	0.11	0.009
		9:00 A. M.	0.11	
		9:30 A. M.	0.09	
		5:30 P. M.	0.09	
		6:00 P. M.	0.08	
		6:30 P. M.	0.06	
		8:00 P. M.	0.06	

TABLE 4.2:1   RANGE, RESOLUTION, NO_2 POLLUTION CONCENTRATION,

AND UNCERTAINTIES FOR VARIOUS TIMES DURING THE DAY

the dye and degradation of gain following many laser firings during the course of the day.

From the traces of the LIDAR returns, Figs. 4.2:4a, c, e, g, i, k, and m, it is seen that in each case the relative attenuation is largest over a 450 m region extending from a range of approximately 1050 m to 1500 m. This result corresponds well with the fact that over that region the LIDAR beam crosses over several avenues with heavy traffic.

Table 4.2:1 lists the pollution concentration measured at various times during a typical day. The range location of particular interest to observe pollution changes during rush hours is located approximately 1200 m from the LIDAR site (the region where areas of heavy traffic exist). Table 4.2:1 shows that the readings obtained at the range of 1050 m and depth resolution of 450 m do in fact evidence peaks in pollution levels during the morning and evening rush hours, while dropping lower thereafter. From 8:45 a.m. to 9:00 a.m. the pollution level remained approximately the same (0.29 ppm to 0.31 ppm respectively), then declined to 0.21 ppm at 9:30 a.m.. During the evening rush hours the peak NO_2 concentration reached 0.26 ppm at 5:30 p.m. then declined to 0.24 ppm at 6:00 p.m.. Thereafter, the level of NO_2 pollution reduced steadily from 0.15 ppm at 6:30 p.m. to 0.14 ppm at 8:00 p.m.. The overall average NO_2 density observed from the building (2400 m or 16 us away) to the LIDAR site ranged from 0.11 ppm to 0.06 ppm from 8:45 a.m. to 8:00 p.m. respectively.

These average density results were generally found to be within 30 percent of the values measured by the New York City Department of Air Resources fixed-site monitoring station situated a short distance to the south of the LIDAR beam trajectory.

141

4.3 Error Analysis

For the practical interpretation of the LIDAR pollution measurements it is useful to know the uncertainity that is associated with the measurement. Towards this end, an experiment was performed in which a known concentration of NO_2 was monitored by the LIDAR system.

The experimental setup is shown in Fig. 4.3:1. The simultaneous laser output passed through a 1/2 m sample cell which contained 609 ppm of NO_2 in N_2. The output was then directed into the atmosphere and the backscattered returns were monitored by the receiving system. Each output pulse was monitored by the calibration system and the signals obtained from detectors 1 and 3 in the calibration setup served as the before-cell signals for both the calibration and sample cells. The experiment was performed on a windy clear night such that clear-air conditions existed, and that the output signals would not be further attenuated by ambient levels of NO_2.

By knowing the before cell readings and the signals backscattered from the atmosphere, the pollutant concentration in ppm·Δr(m) was obtained for a series of 5 shots. The mean value of the deviations from the known concentration in the cell (609 ppm in 1/2 m = 304.5 ppm·Δr (m)), was calculated to be 21 ppm·Δr(m) or 0.021 ppm·Δr(km). Fig. 4.3:2 shows the results of the experiment.

Knowing the uncertainity associated with a given depth resolution, Δr, the corresponding values were calculated for the pollution readings and are shown in Table 4.2:1.

In conclusion, the results obtained from the LIDAR field measurements were what were expected. The NO_2 pollution level peaked at rush
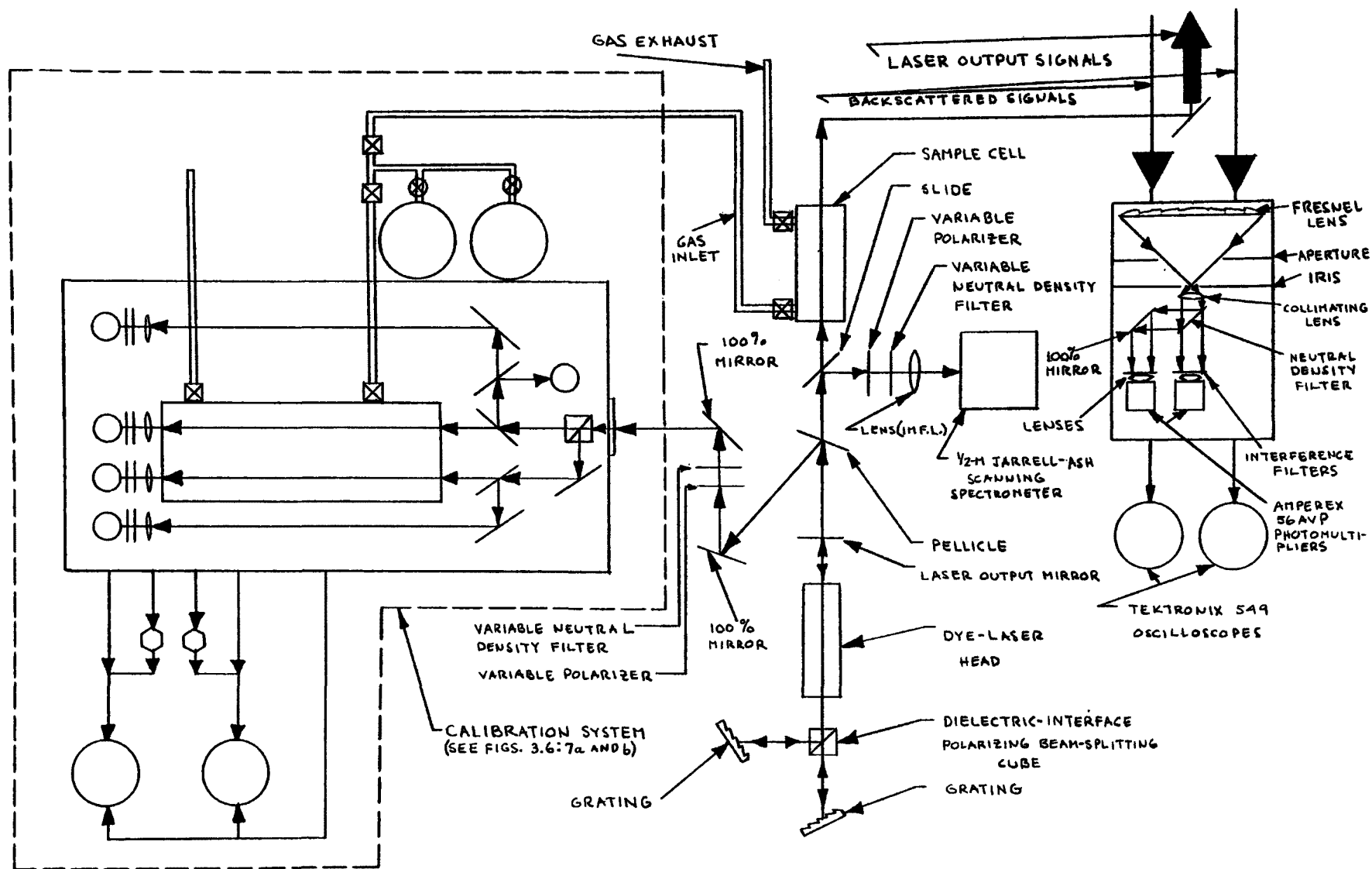
FIGURE 4.3:1 EXPERIMENTAL SETUP FOR DETERMINATION OF LIDAR-READING UNCERTAINTIES

143
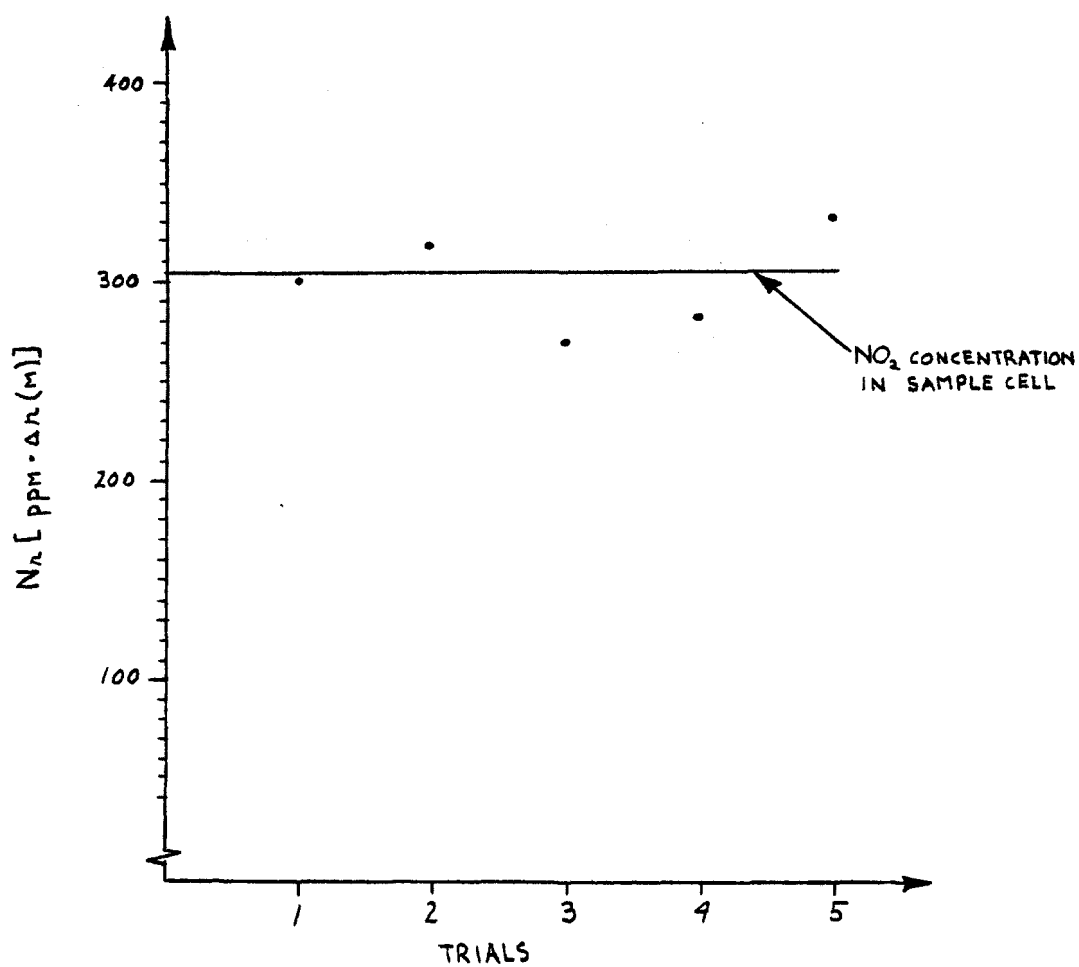
FIGURE 4.3:2   ERROR PLOT FOR DETERMINATION OF LIDAR-READING

UNCERTAINTIES

hour times and leveled off thereafter. The pollution levels calculated from the returns are typical of the levels found at intersections and avenues of heavy traffic.

An experiment was performed to obtain quantitative uncertainties associated with each pollution reading obtained in the simultaneous mode of operation. The variations in the readings obtained by the LIDAR system in monitoring the known concentration of NO_2 were primarily attributed to ambient levels of NO_2 present during the time of the experiment.

CHAPTER 5 SIMULTANEOUS MULTIWAVELENGTH OUTPUTS FROM ENERGY-TRANSFER
DYE-MIXTURE LASERS

5.1 Introduction

In a second generation LIDAR system it would be desirable to have
the capability of monitoring several pollutants simultaneously. This
can be accomplished by lasing simultaneously in the spectral regions
necessary to monitor the pollutants of interest.

Thus, though the work being reported here centered primarily on the
detection of NO_2, an experimental program was carried out on dye mix-
tures for the purpose of:

> Obtaining simultaneous outputs at two pairs of wavelengths, one
>
> in the 4500 Å spectral region (for monitoring NO_2) and the oth-
>
> er in the 6200 Å spectral region. (The outputs in the 6200 Å
>
> region could then be used, in conjunction with frequency dou-
>
> bling, for monitoring SO_2 and O_3 in the 3100 Å spectral region.)

The program carried out was successful and simultaneous laser opera-
tion was obtained at two and even three wavelengths (in the three pri-
mary colors) for the first time.[77]

To achieve these results, use was made of energy transfer processes
in organic dye mixtures. Energy transfer processes in organic dyes have
received some consideration in the past.[74-89] The results of the exper-
iments described below conclusively demonstrate that:

1. In a mixture of two or more dyes in a solution, excitation ener-
    gy may be very efficiently transferred from an excited molecule
    of one species to another, and that the process may be repeated

successively to a third dye with the excitation energy being efficiently cascaded to still longer wavelengths.

2. Furthermore, simultaneous outputs at several widely separated spectral regions may be obtained from a dye-mixture laser.

3. Dye mixtures can be used to reduce the required concentration of the lasing dye, while still maintaining effective absorption of the pump soruce radiation. The reduced concentration of the lasing dye reduces self-absorption losses at the laser wavelengths. This in turn reduces threshold upper level population density requirements, and therefore the required pump source intensity.

A second series of experiments was carried out to define the energy transfer processes involved. Possible processes were either radiative or nonradiative resonance transfer or a combination of the two. Two experiments were devised which required only static measurements to be performed.

The next section considers the theoretical background for energy transfer processes that could occur at the concentrations found optimum for simultaneous laser action in dye-mixture lasers.

5.2 Energy Transfer Mechanisms

5.2.1 Introduction

The characteristics of a donor-acceptor system in which intermolecular energy transfer plays the dominant role are illustrated schematically in Fig. 5.2:1. There, the fluorescence emission spectrum of donor molecule D overlaps its own absorption spectrum as well as that of the
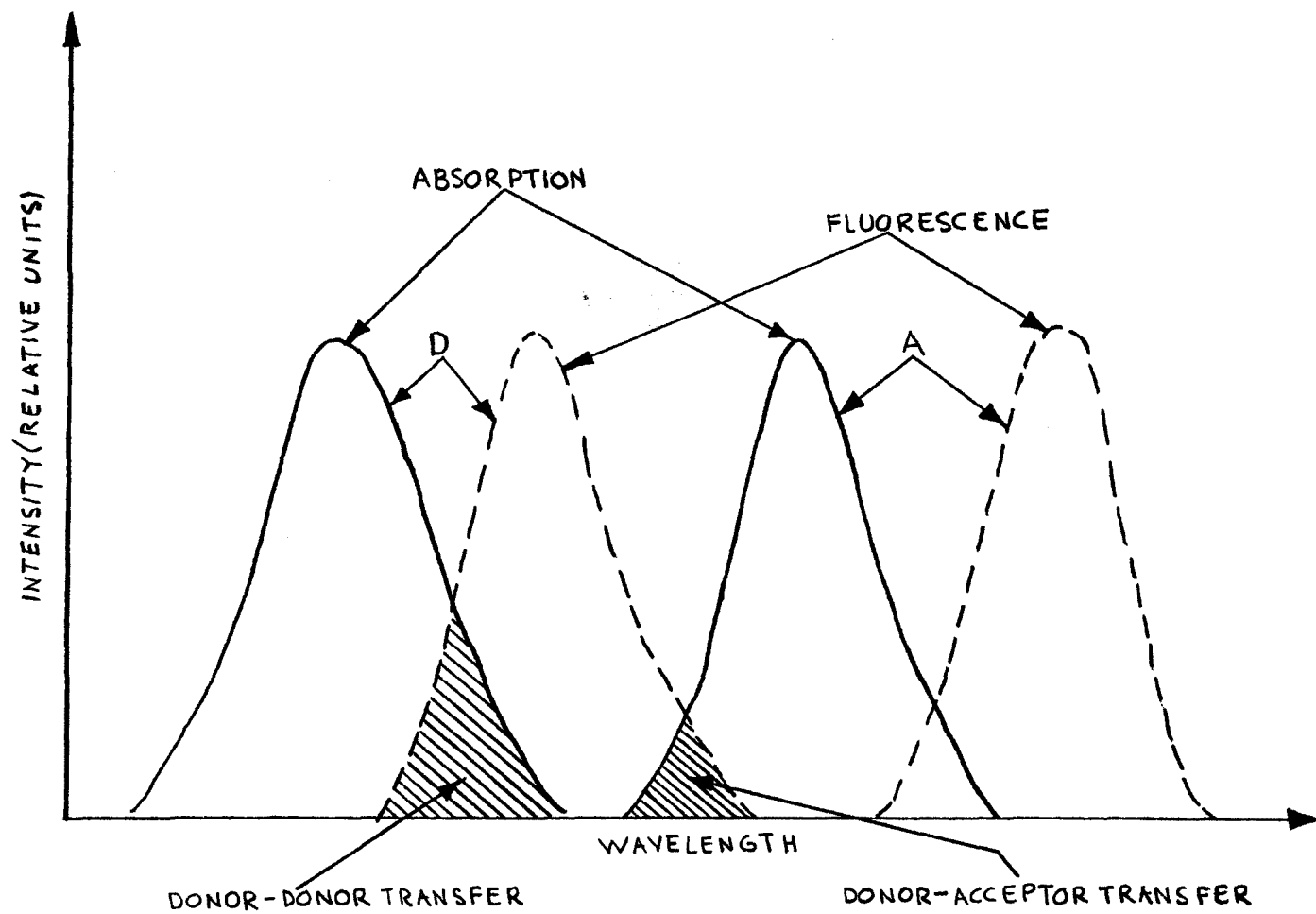
FIGURE 5.2:1 DONOR-ACCEPTOR SYSTEM OF TWO ORGANIC DYES WITH OVERLAPPING FLUORESCENCE AND ABSORPTION BANDS

acceptor molecule A. These spectra indicate an overlap in the energy manifolds of the transitions in D and the absorptive transitions in D and A, thus permitting excitation transfer from D to D and from D to A. Energy transfer along a chain of donor to donor molecules and from donor to acceptor molecules are therefore possible. It is also clear that such a process can be cascaded down through several dyes, e.g., D to A to B to C. This is shown in Fig. 5.2:2.

A second type of dye mixture in which simultaneous emission is possible is illustrated in Fig. 5.2:3. In this case the absorption bands of dyes D and A overlap, while the emission bands are widely separated. Thus, excitation of such a mixture will result in simultaneous excitation of, and emission (and possibly laser emission under the appropriate conditions) from both dyes.

The main mechanisms that can be responsible for the intermolecular energy transfer between the donor-donor pairs and donor-acceptor pair molecules are:[76,90-92]

1. radiative transfer by means of radiation by the donor dye and reabsorption by the donor and acceptor dyes.

2. singlet-singlet nonradiative transfer between donor and donor molecules and between donor and acceptor molecules due to coulombic interactions (dipole-dipole etc.) and exchange or collision induced nonradiative decay back to $^1S_0$ (ground state).

5.2.2 Radiative and Nonradiative Energy Transfer

In the case of radiative transfer, excitation transfer rates are related in a relatively straightforward manner by the values of the absorp-
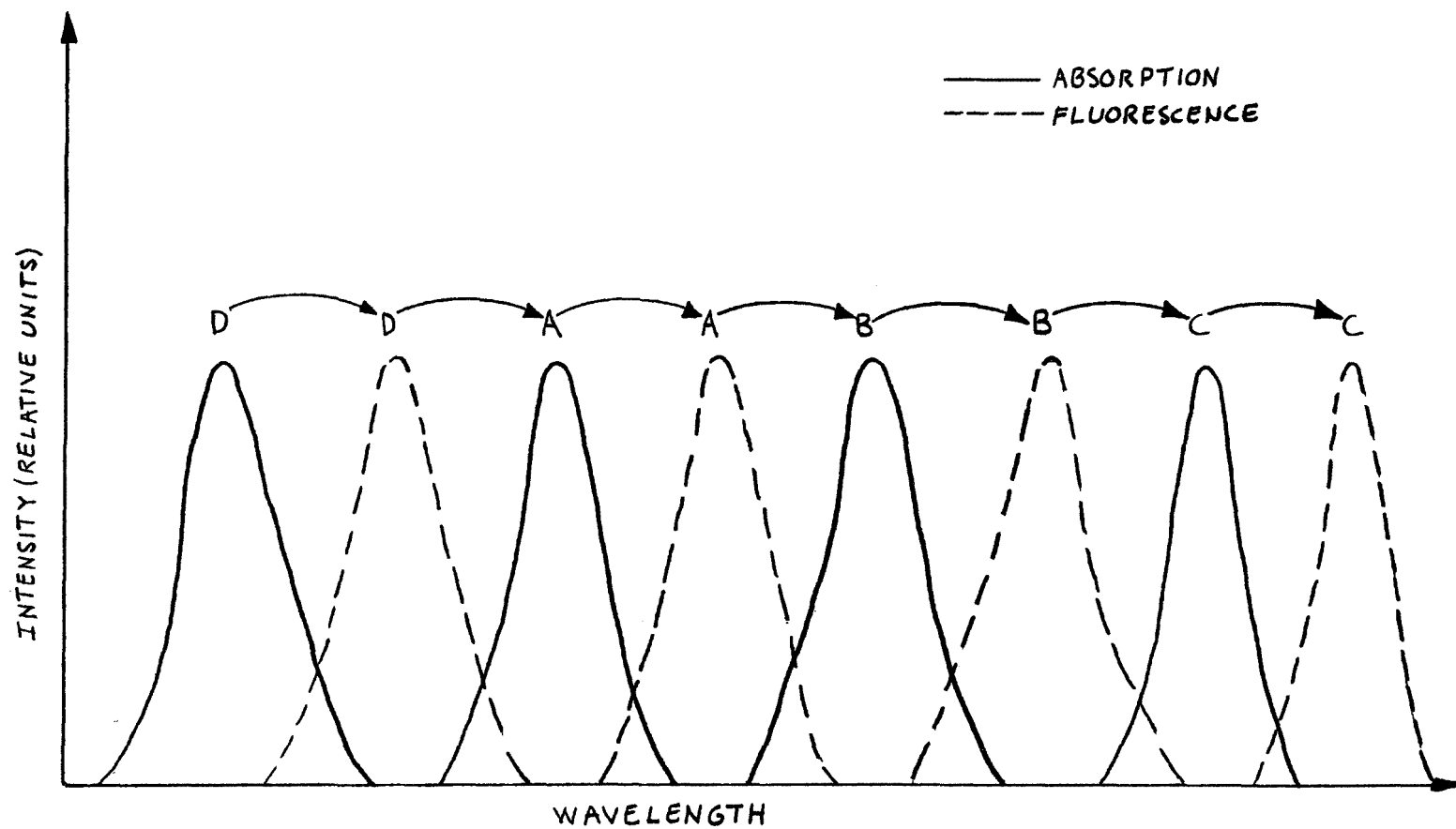
FIGURE 5.2:2   DONOR-ACCEPTOR SYSTEM OF FOUR ORGANIC DYES WITH OVERLAPPING FLUORESCENCE AND ABSORPTION BANDS
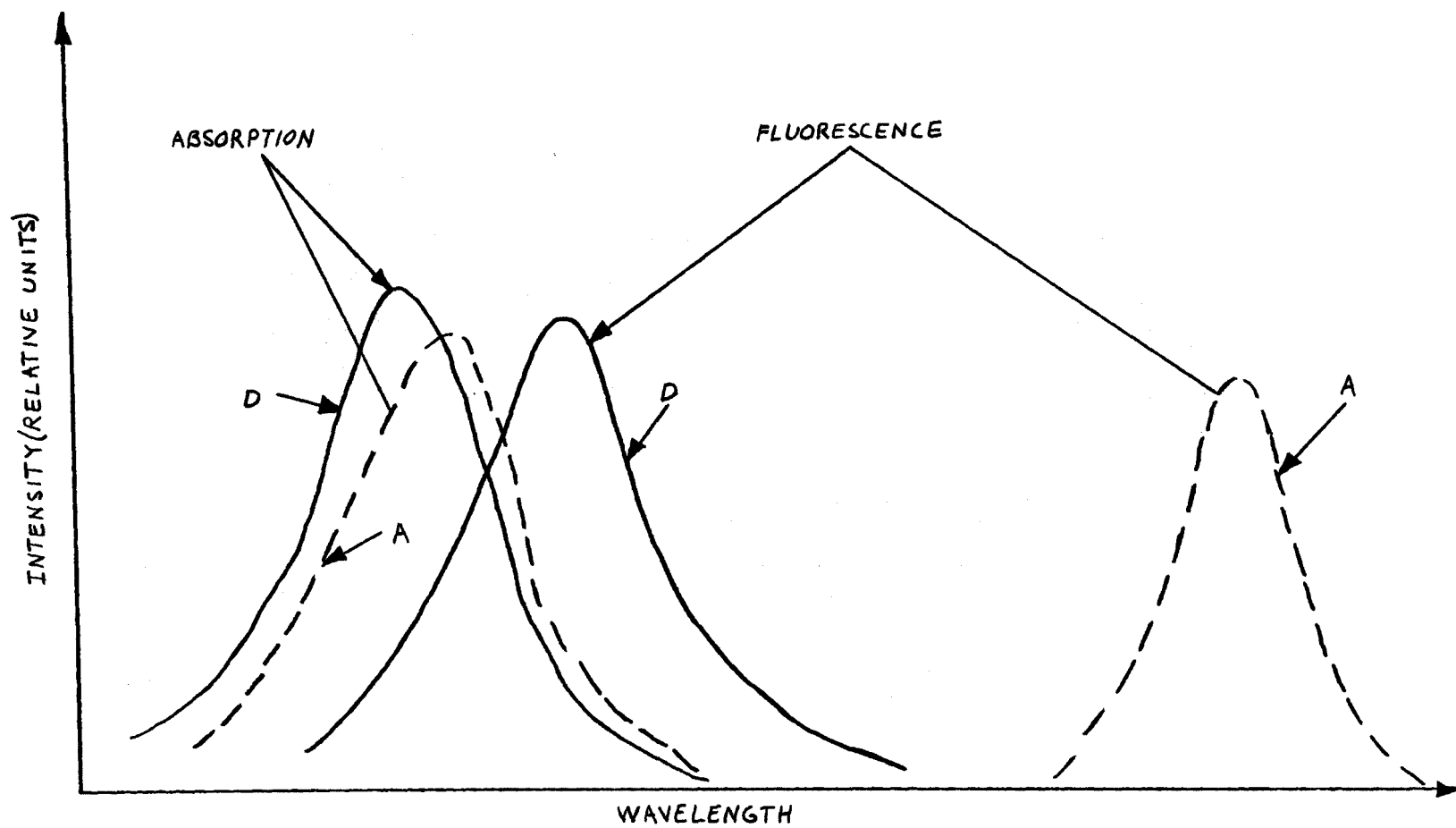
FIGURE 5.2:3 DONOR-ACCEPTOR SYSTEM WITH OVERLAPPING ABSORPTION BANDS

tion and emission cross sections of the acceptor and donor dye and their extent of overlap, and takes place over distances greater than 50 to 100 Å.

Analysis of these factors show that the probability of radiative transfer, $K_{ET}(RAD)$, is given by:[90]

$$K_{ET}(RAD) \approx \frac{2.303[N_A]l}{Q_D} \int_0^\infty f_D(\vee)E_A(\vee)d\vee, \qquad (5.2:1)$$

where,

l = the specimen thickness,

f_D = the donor normalized fluorescence spectrum,

E_D = the acceptor absorption coefficient,

$[N_A]$ = the molar concentration of acceptors, and

Q = the quantum efficiency of the donor.

The mechanism of singlet state transfer of energy between donor and acceptor molecules was analyzed by Forster.[93] According to Forster, the probability of nonradiative transfer from a donor to an acceptor molecule is proportional to the overlap of the fluorescence band of the donor and the absorption band of the acceptor molecule. This is a resonance transfer mechanism and is illustrated in Fig. 5.2:4. Radiationless transfer due to coulombic interaction takes place over distances less than 50 to 100 A depending upon the molecules involved in the process. The probability of nonradiative energy transfer, $K_{ET}(NONRAD)$, from an excited fluorescent molecule D to an acceptor molecule A is expressed below:

$$K_{ET}(NONRAD) = \frac{1}{\tau_0}\left(\frac{R_0}{R}\right)^6, \qquad (5.2:2)$$

where,
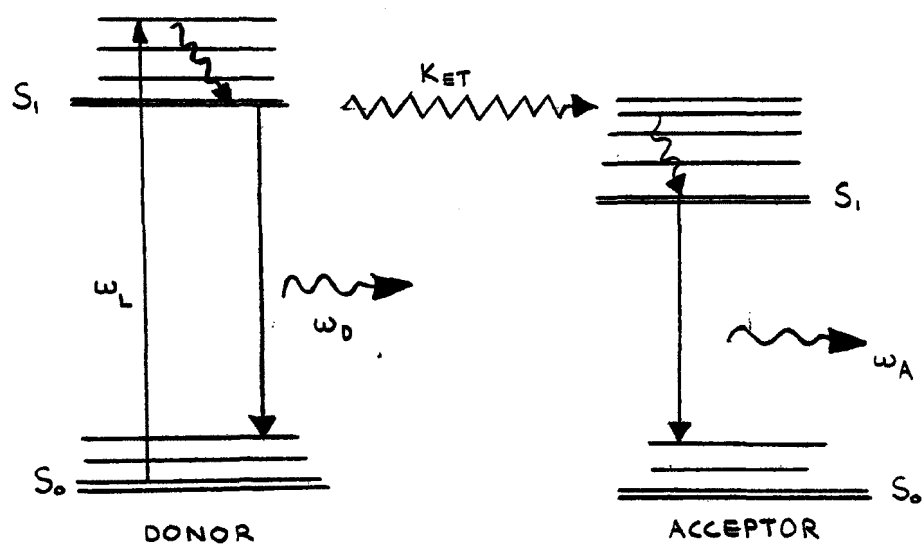
FIGURE 5.2:4   DONOR AND ACCEPTOR ENERGY LEVELS

153

$$R_0^6 = \frac{(9000 \ln 10)\chi^2}{128(\pi^5)(n^4)N} \int_0^\infty \frac{f_D(\nu)E_A(\nu)d\nu}{\nu^4},$$

(5.2:3)

where,

τ_0 = the fluorescence lifetime of isolated donors,

R = the distance between D and A,

n = the refractive index,

f_D = the normalized fluorescence intensity of D,

E_A = the absorption coefficient of A,

χ = a geometrical factor ($\langle \chi^2 \rangle$ = 2/3), and

R_0 = the critical transfer distance at which there is equal

probability of radiative or nonradiative resonance trans-

fer to occur.

5.3 Multiwavelength Laser Action in Dye Mixtures--Experimental Results

In the first series of experiments carried out, dye mixtures were

chosen from which simultaneous laser outputs at useful spectral combi-

nations could be obtained. A mixture of 7--diethylamino-4 methyl coumarine,

Acriflavine, and Rhodamine B allowed dye laser outputs to be obtained at

three primary colors.[77]

Fig. 5.3:1 shows the absorption and fluorescence spectra of these

three dyes. The absorption bands of Acriflavine and Rhodamine are seen

to overlap the fluorescence bands of the Coumarine and the Acriflavine

respectively. This overlap in the energy gaps of these dyes would per-

mit, in principle, excitation energy transfer from Coumarine to the

Acriflavine and from the Acriflavine to Rhodamine B either by radiative

or nonradiative resonance transfer.

154
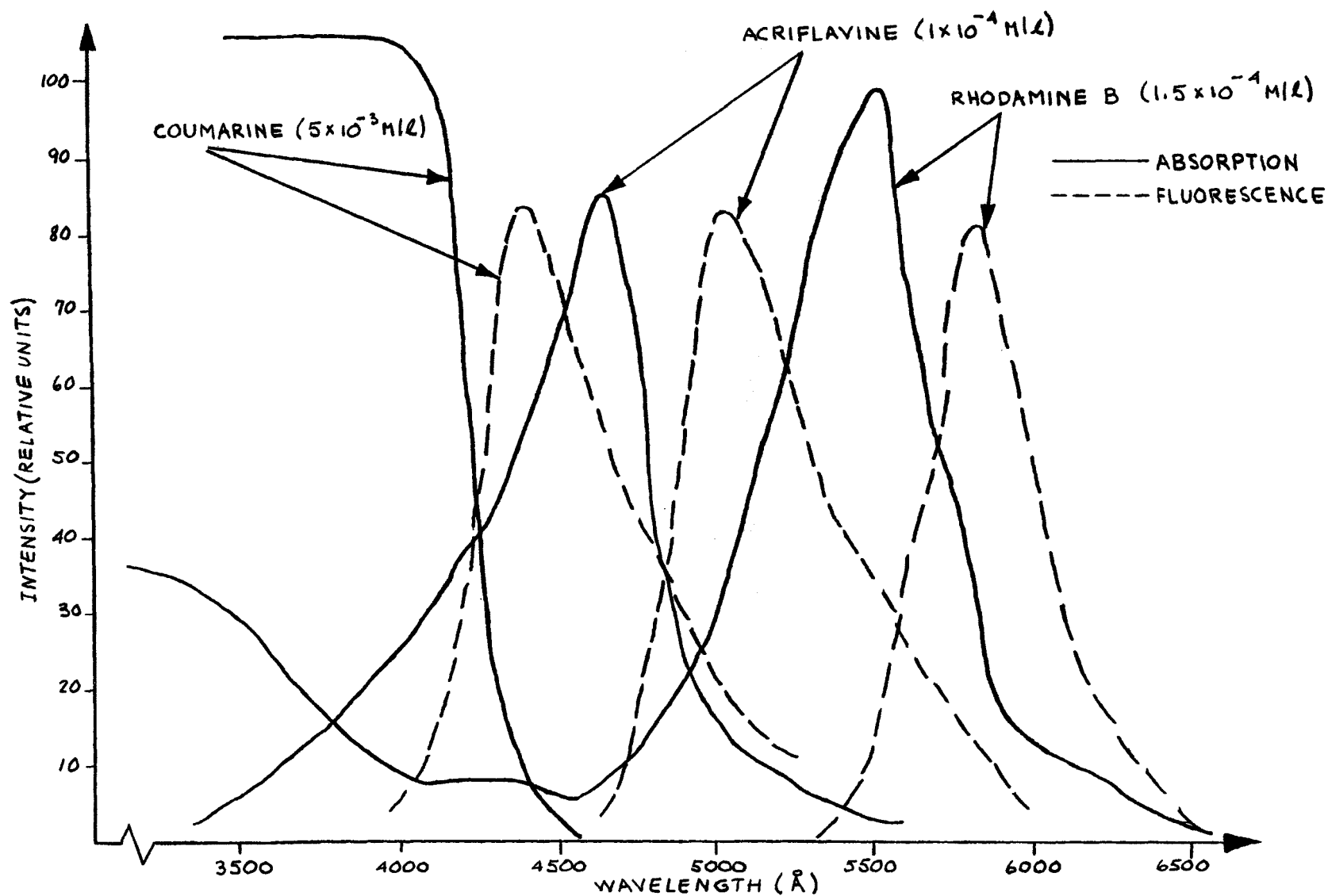
FIGURE 5.3:1 ABSORPTION AND FLUORESCENCE SPECTRA OF THE THREE DYES AT OPTIMUM CONCENTRATIONS FROM WHICH SIMULTANEOUS LASER OUTPUTS WERE OBTAINED IN THE THREE PRIMARY COLORS

155

It was therefore possible to use the 3371 Å output of an N$_2$ laser to excite the Coumarine dye and obtain excitation transfer to, and simultaneous emission (including laser emission) from, all three dyes in a mixture with appropriate concentration ratios.

Fig. 5.3:2 shows the absorption and fluorescence spectrum of this three-dye mixture at concentrations found optimum for three-color laser operation. The absorption curve shown is for a 1.0 mm optical path length, and ethanol was the solvent used. Excitation for the front surface fluorescence measurements depicted in Fig. 5.3:2 was by means of the 3650 Å output obtained from an Hg discharge lamp. This is absorbed by the Coumarine, which transfers excitation to the Acriflavine, which in turn transfers excitation to the Rhodamine B. Fig. 5.3:3 shows the experimental setup used to obtain the absorption and emission curves of the dyes.

The different concentrations used for each of the three dyes arises from the fact that the excitation source for laser action in the dye mixture was the 200-kw 30-ns 1-HZ N$_2$ laser output at 3371 Å. The absorption of this pump light was therefore predominantly by the Coumarine dye, hence its large concentration requirements relative to the other two dyes. Thus, in this case, the type of dye mixture used would be a combination of the types depicted in Figs. 5.2:1, 2, and 3. With this three dye mixture, laser action was obtained simultaneously at three wavelengths centered at 4400 Å, 4900 Å, and 6200 Å. These outputs could be individually tuned over a range of approximately 15 Å, as shown in Fig. 5.3:3.

That excitation transfer is the predominant mechanism for exciting
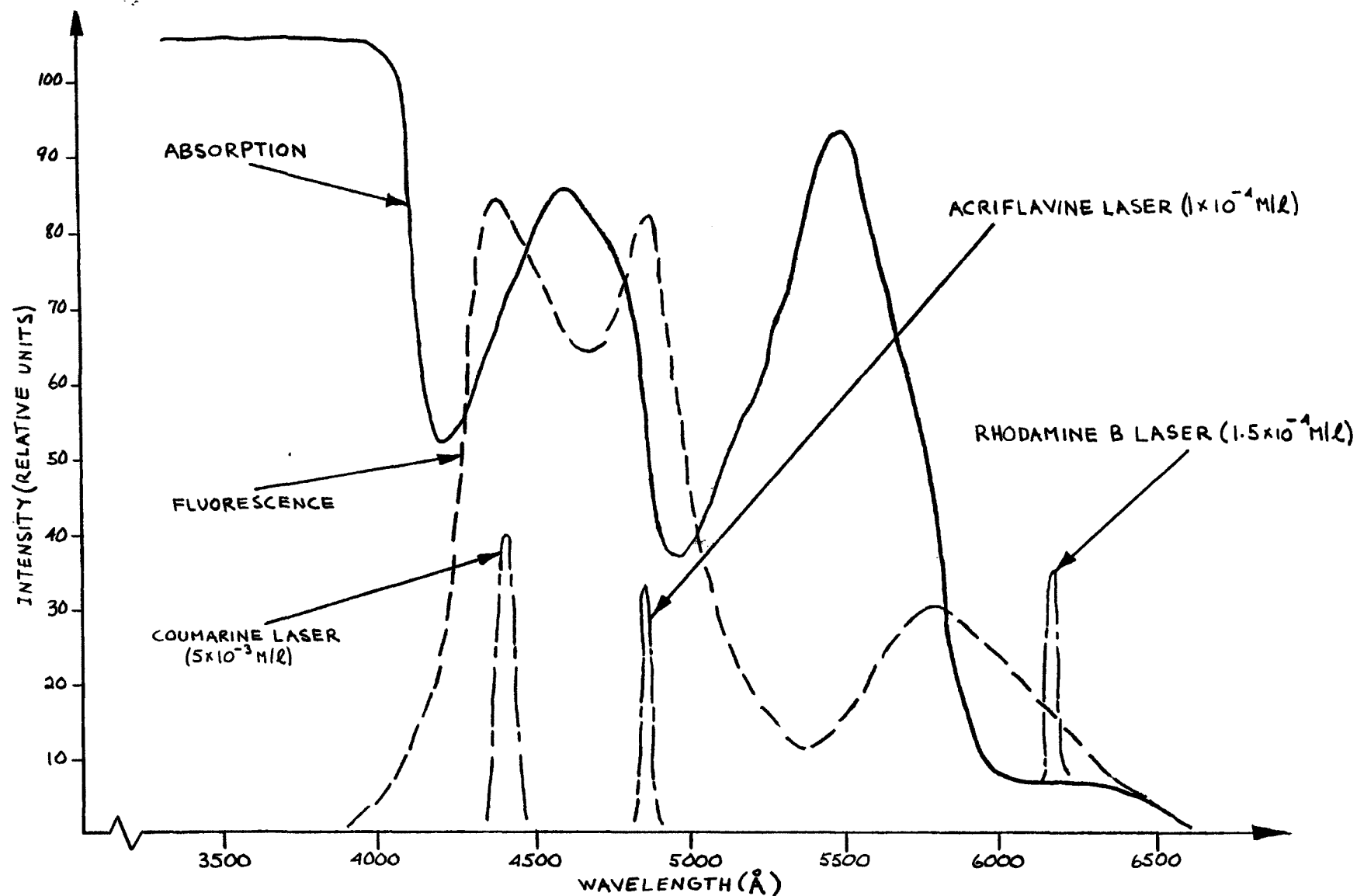
FIGURE 5.3:2 ABSORPTION AND FLUORESCENCE SPECTRA OF THE THREE-DYE MIXTURE AT OPTIMUM CONCENTRATIONS FROM WHICH SIMULTANEOUS LASER OUTPUTS WERE OBTAINED IN THE THREE PRIMARY COLORS
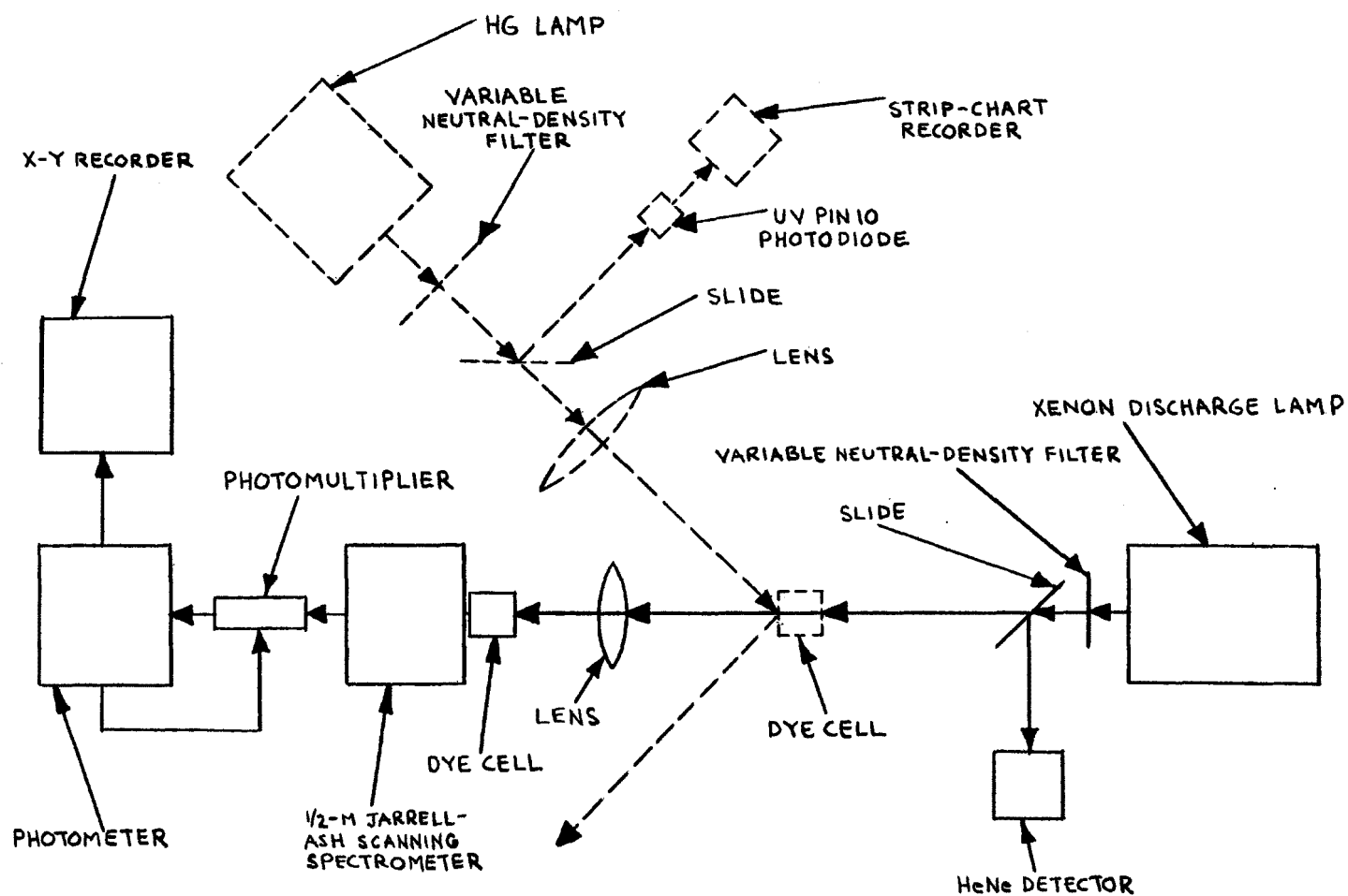
FIGURE 5.3:3 EXPERIMENTAL SETUP FOR OBTAINING FLUORESCENCE AND ABSORPTION SPECTRA

laser action in the Acriflavine and Rhodamine B is confirmed by the fact that it was not possible to obtain laser action from Acriflavine alone, at any concentration, using the 3371 Å N_2 laser output for excitation, while laser action by direct excitation at 3371 Å of Rhodamine B alone was found to require an order of magnitude higher concentration of Rhodamine B with the same optical arrangement used. See Fig. 5.3:4.

For two-wavelength operation in the 4500 Å and 6200 Å region, the concentration of the center dye, Acriflavine, was reduced, and that of the Rhodamine B increased. This resulted in effective laser operation at the desired spectral regions. Fig. 5.3:5 shows the spectrum of the dye mixture for two-wavelength operation. An optical arrangement suitable for getting simultaneous laser action at two pairs of wavelengths in each of the spectral regions of interest is shown in Fig. 5.3:6.

By comparing the fluorescence quantum yield for each of the three dyes alone with the fluorescence quantum yield for the dye mixtures, it was found that the fluorescence quantum yield for the single-step transfer process, Coumarine to Acriflavine, was approximately 90 percent. The yield for the two-step transfer process, Coumarine to Acriflavine to Rhodamine B, was approximately 80 percent.

5.4 Energy Transfer Mechanisms--Experimental Results

5.4.1 Radiative Energy Transfer

If energy transfer were predominantly a radiative process at the concentrations required for simultaneous laser action, the energy
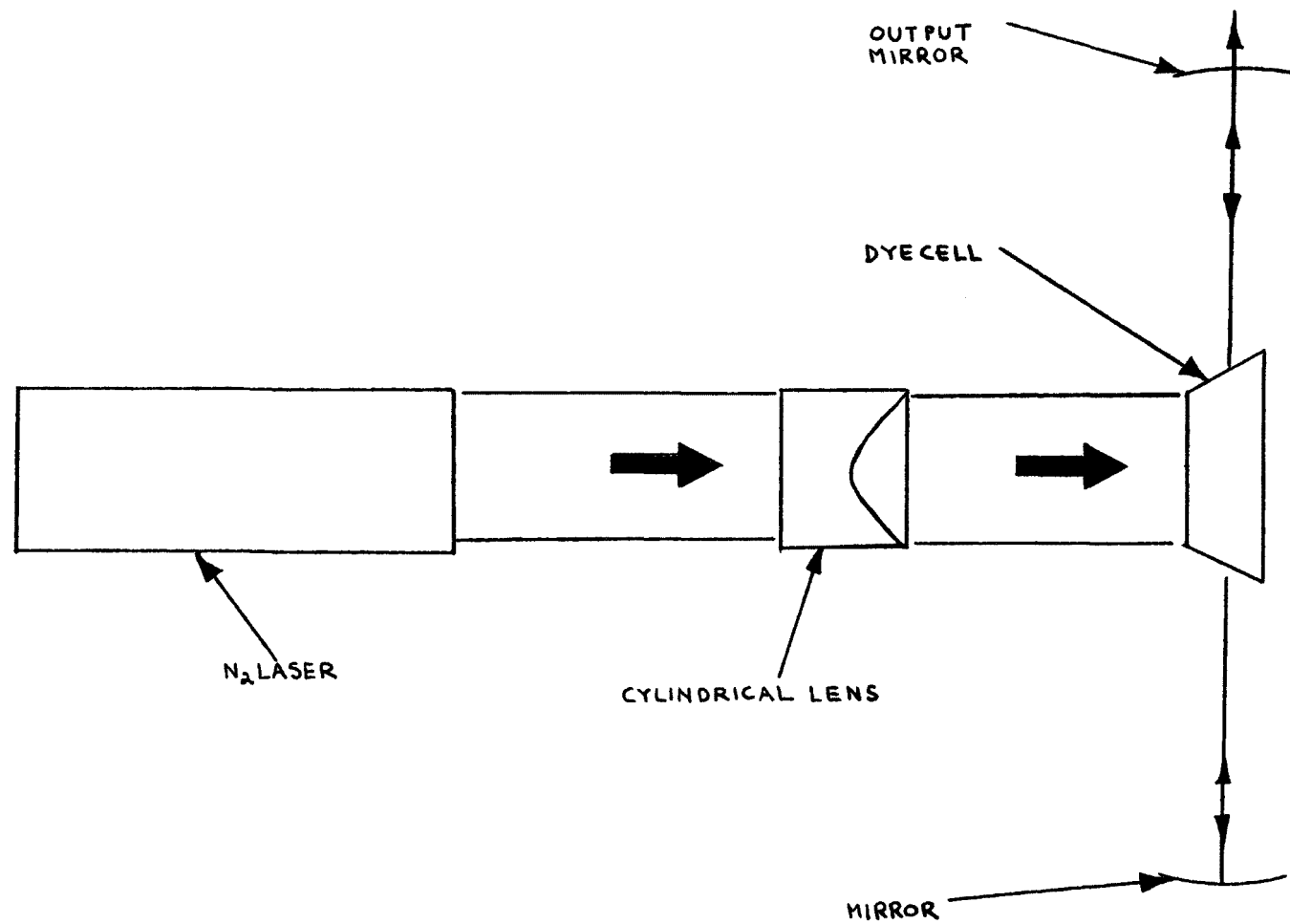
FIGURE 5.3:4   OPTICAL ARRANGEMENT FOR OBTAINING SIMULTANEOUS THREE-COLOR OUTPUTS IN THE THREE PRIMARY

COLORS
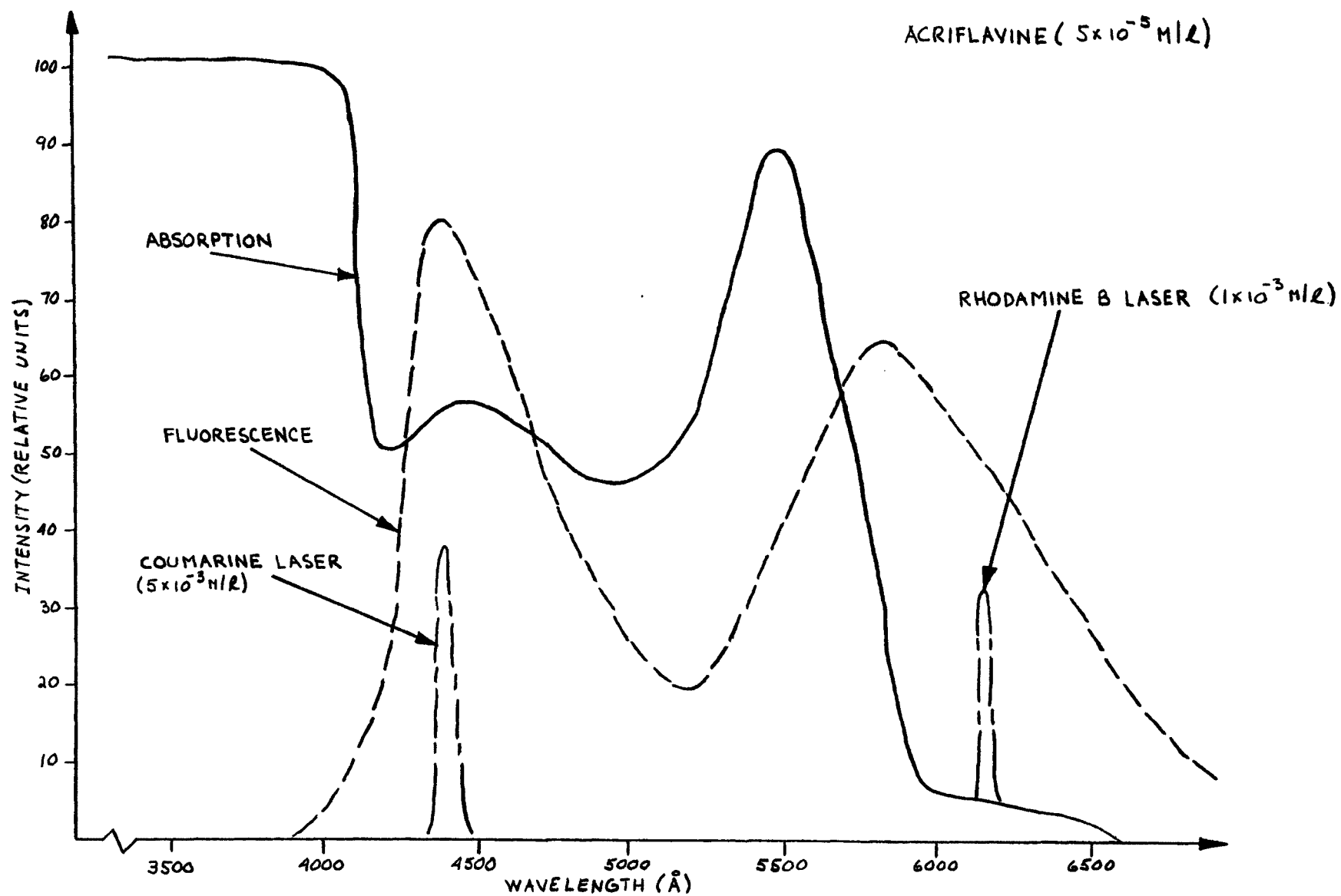
FIGURE 5.3:5   ABSORPTION AND FLUORESCENCE SPECTRA FOR SIMULTANEOUS TWO-WAVELENGTH OUTPUT
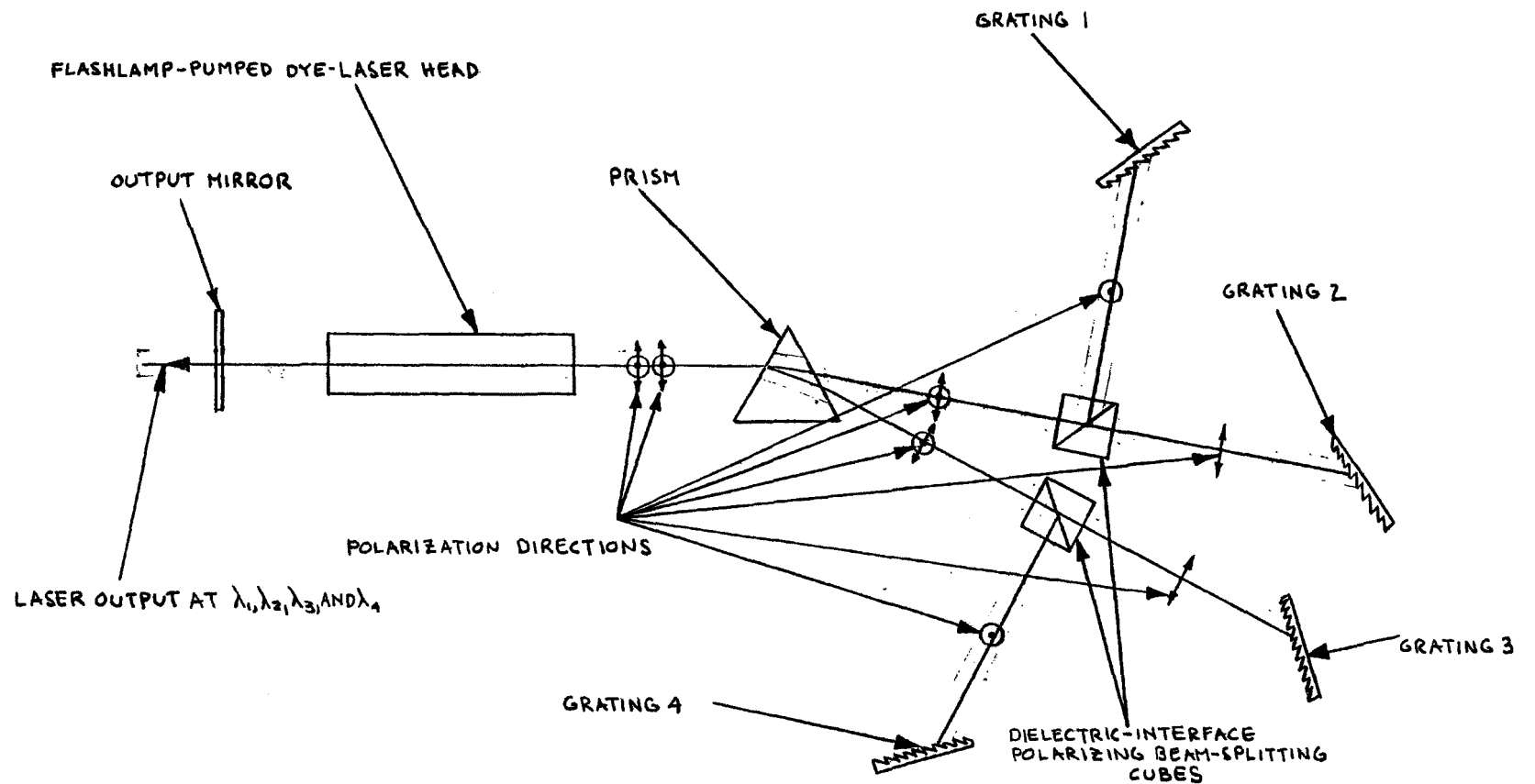
FIGURE 5.3:6   OPTICAL ARRANGEMENT FOR OBTAINING TWO PAIRS OF WAVELENGTHS SIMULTANEOUSLY

transfer rate would be given by Eq. 5.2:1. The energy transfer rate from D to A would be directly proportional to the overlap integral, P, as defined in Eq. 5.2:1. Thus, the emission from the acceptor molecules, A, would be proportional to the product of the quantum efficiency of A and the overlap integral P.

Two pairs of dyes were chosen such that the absorption spectrum of each acceptor dye overlapped the flourescence spectrum of the same donor dye differently. Relative measurements were made to determine the dominant mechanism for energy transfer in the following manner:

$$\frac{P_1 n_{Q1}}{P_2 n_{Q2}} = \frac{\text{Fluorescence of } A_1 \text{ in mixture 1}}{\text{flourescence of } A_2 \text{ in mixture 2}},$$

$$(5.4:1)$$

where,

A_1 = acceptor dye #1,

A_2 = acceptor dye #2,

$P_{1,2}$ = the overlap integrals of the fluorescence spectrum of donor dye, D, with the absorption spectrum of acceptor dye, $A_{1,2}$, and

$n_{Q1,2}$ = the quantum efficiencies of the acceptor dyes $A_{1,2}$.

If Eq. 5.4:1 holds, it can then be concluded that the dominant mechanism for energy transfer is by the radiative process.

In the experiments performed, Dichlorofluorescein was chosen as the donor, and Rhodamine B and DODC as acceptors. Ethanol was used as the solvent. The exciting line was the 4880 Å output of an argon-ion laser which excited the donor alone. Fig. 5.4:1 shows the experimental set-up used to determine the absorption and front fluorescence spectra of the dyes. The experiment was run with both dyes in both mixtures at
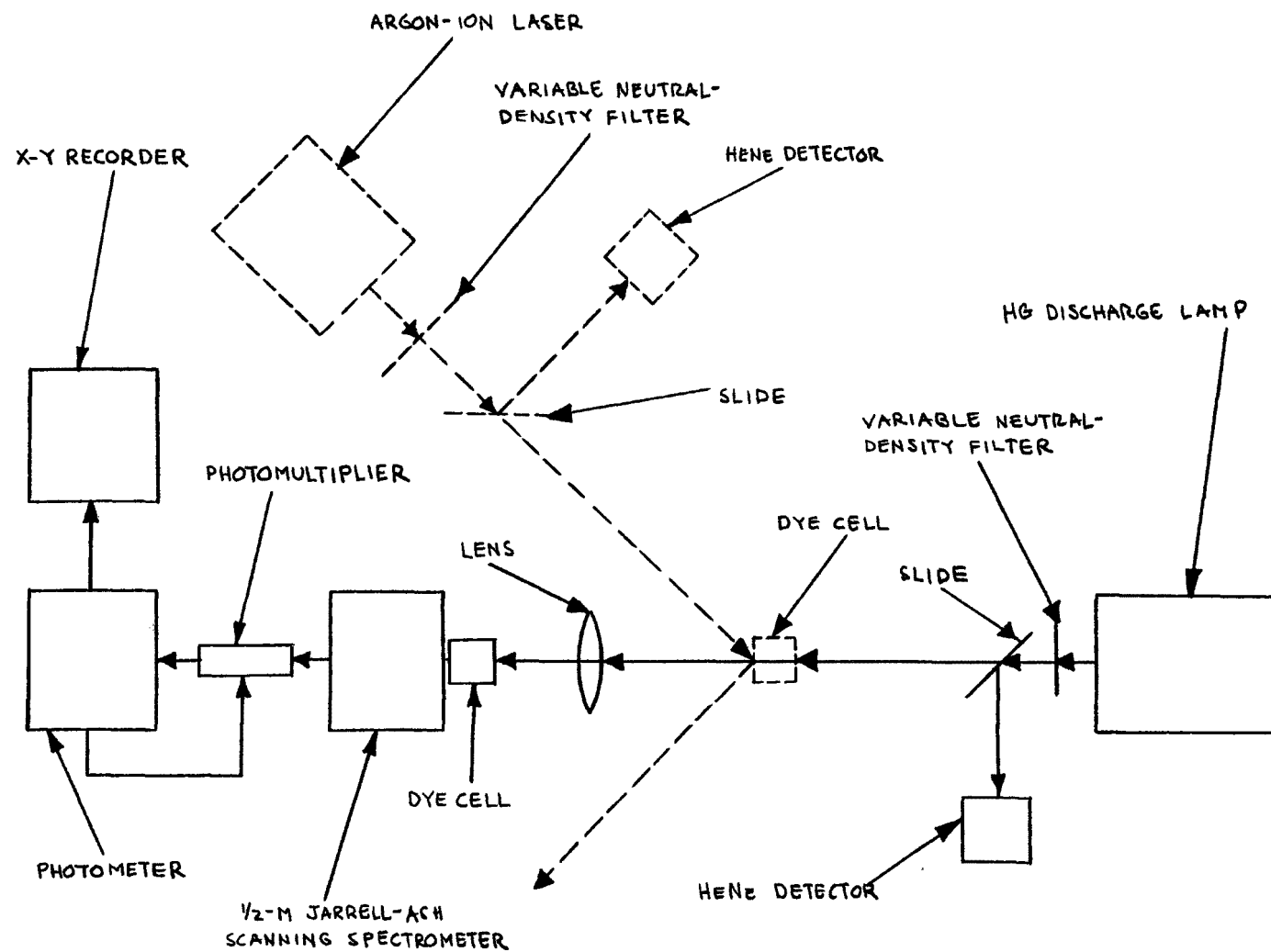
FIGURE 5.4:1 EXPERIMENTAL SETUP FOR OBTAINING FLUORESCENCE AND ABSORPTION SPECTRA

the same concentration. The first mixture consisted of Dichloroflu-
orescein (2×10^{-2} M/l), donor, and DODC (5.52×10^{-5}), acceptor, in
ethanol. The second mixture consisted of Dichlorofluorescein (2×10^{-2} M/l), donor, and Rhodamine B (5.52×10^{-5} M/l) in ethanol.

Figs. 5.4:2 and 3 show the absorption and fluorescence spectra
and the overlap integrals of Dichlorofluorescein with DODC and Di-
chlorofluorescein with Rhodamine B in the concentrations stated above.
Figs. 5.4:4 and 5 show the fluorescence spectra of DODC and Rhodamine
B in the appropriate mixtures respectively.

Inserting the appropriate terms into Eq. 5.4:1 yields:

$$1.00 \approx 0.92 \qquad\qquad (5.4:2)$$

This result confirms the fact that, at the concentrations needed for
lasing, radiative transfer plays the dominant role in the mixtures
used.

5.4.2 Nonradiative Energy Transfer

The next experiment performed was designed to determine at what
concentration of donor molecules nonradiative resonance energy trans-
fer would initiate. Energy transfer in dye mixtures takes place at
various concentrations of donor and acceptor dyes.

If the acceptor concentration were kept constant and the donor con-
centration increased--or equivalently the mean distance between accept-
or-acceptor, $\overline{\overline{R}}$, kept constant, between donor-donor, $\underline{\overline{R}}$, and between do-
nor-acceptor, $\overline{R}$, varied--there would be a donor concentration reached
at which nonradiative energy transfer would initiate. This would be
noted by an increase in the normalized fluorescence yield of the ac-
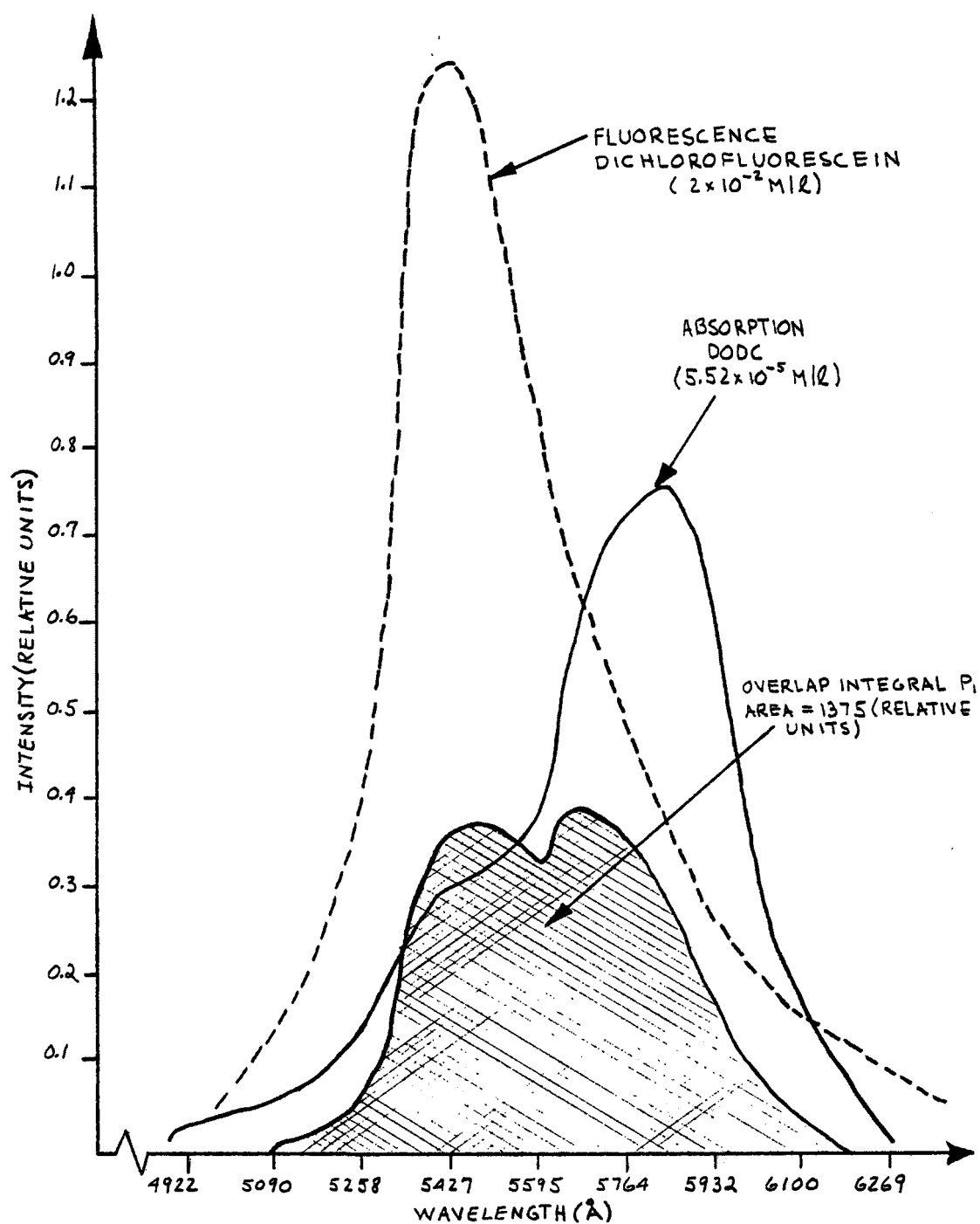
FIGURE 5.4:2   OVERLAP INTEGRAL OF DICHLOROFLUORESCEIN (DONOR) AND DODC

(ACCEPTOR)

166
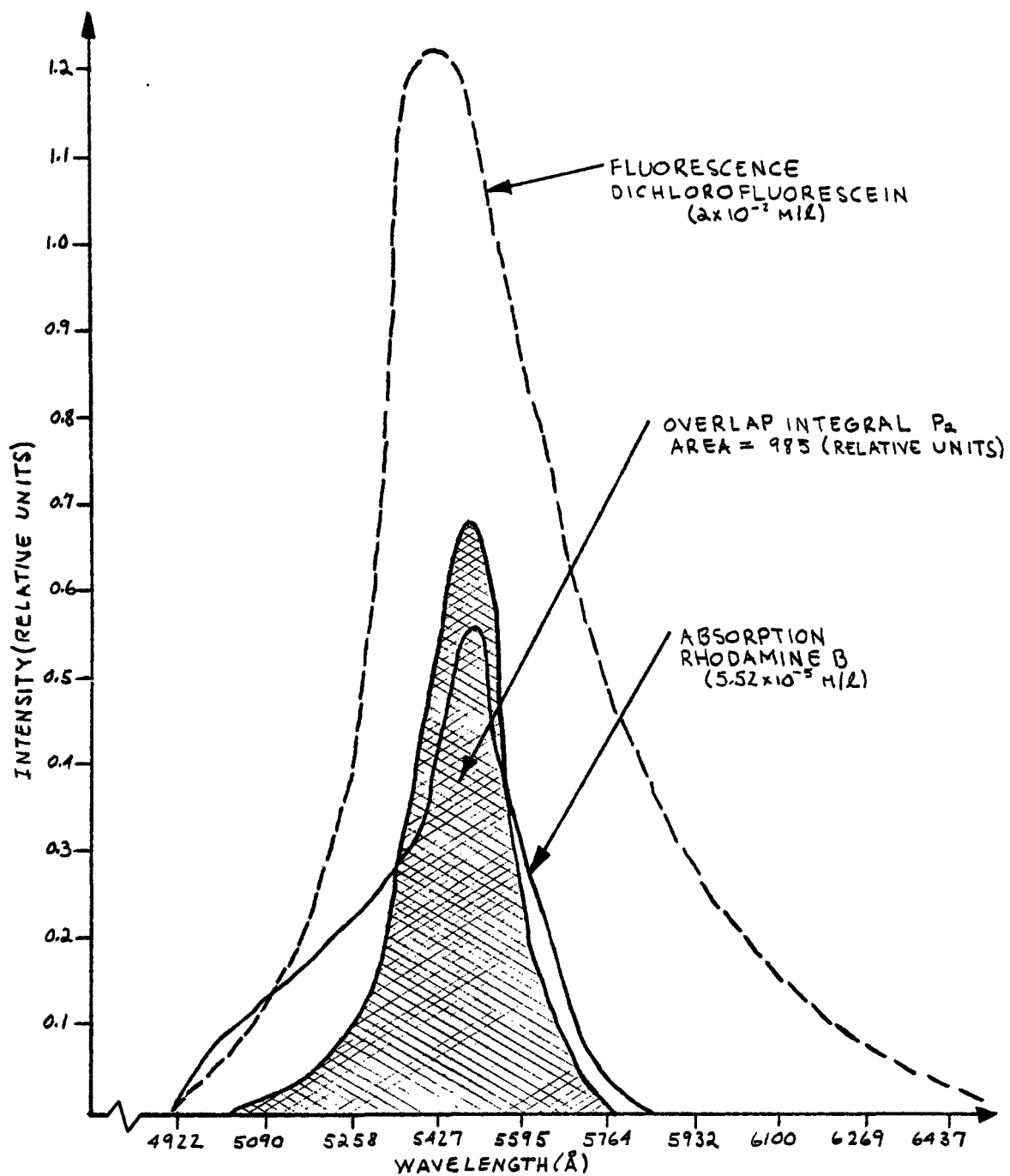
FIGURE 5.4:3 OVERLAP INTEGRAL OF DICHLOROFLUORESCEIN (DONOR) AND

RHODAMINE B (ACCEPTOR)
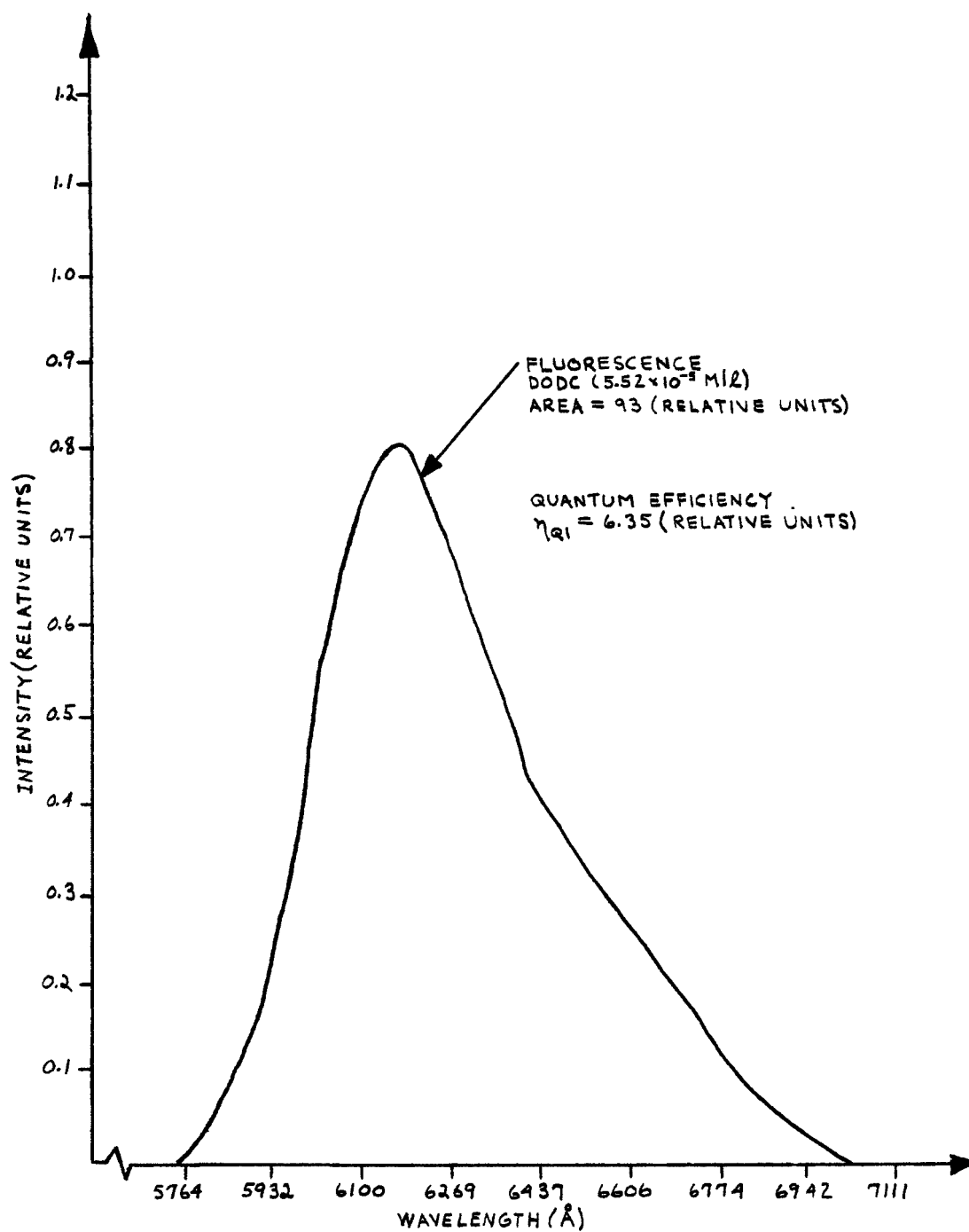
FIGURE 5.4:4   FLUORESCENCE QUANTUM YIELD OF DODC IN THE MIXTURE WITH

DICHLOROFLUORESCEIN

168
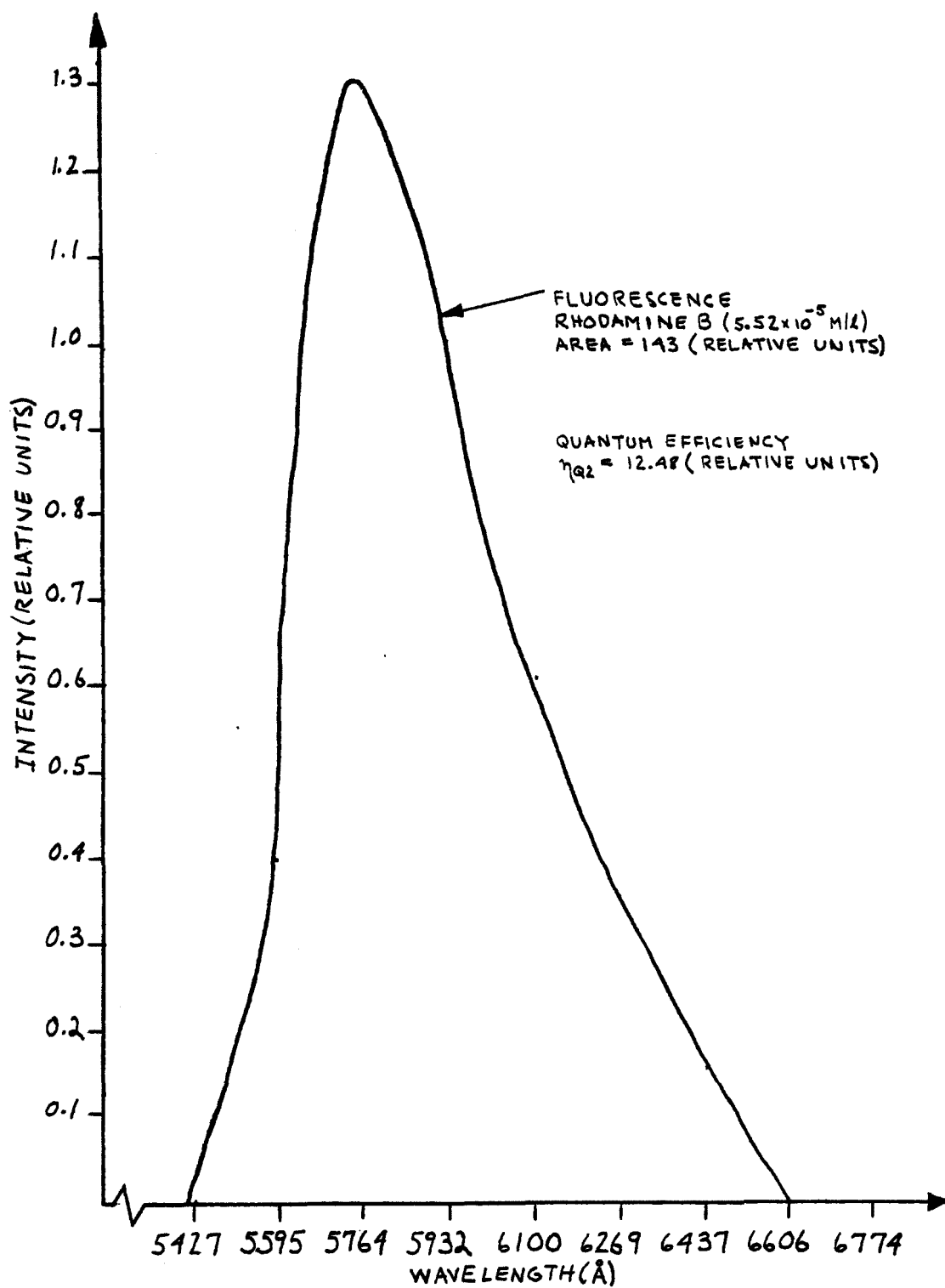
FIGURE 5.4:5   FLUORESCENCE QUANTUM YIELD OF RHODAMINE B IN THE MIXTURE
WITH DICHLOROFLUORESCEIN

169

ceptor relative to the fluorescence of the donor in the same mixture. Before this critical concentration, energy transfer would take place by the radiative process. The emission of the donor would be partially absorbed by the acceptor. As the donor concentration is increased and the mean distance between donors decreases (along with a decrease in donor-acceptor distance), a point will be reached at which the energy transfer flow would take place from donor to donor to donor to... to acceptor. This "hopping" phenomenon is observed during the process of photosynthesis but at concentrations much higher than those used in dye-mixture lasers.

Two organic dyes were chosen such that the fluorescence band of the donor overlapped the absorption band of the acceptor, and that the acceptor would not absorb at the pump wavelength. 7-diethylamino-4 methyl coumarine and DODC were chosen as the donor and acceptor dyes respectively. Ethanol was used as the solvent throughout. The acceptor concentration was kept constant at 1×10^{-4} M/l ($\overline{\overline{R}} = 158$ Å), while the donor concentration varied from 1×10^{-4} M/l ($\underline{\overline{R}} = 158$ Å, $\overline{R} = 126$ Å) to 5×10^{-2} M/l ($\underline{\overline{R}} = 20$ Å, $\overline{R} = 20$ Å). Fluorescence curves were obtained for the pure donor, and the donor and acceptor in the same mixture. The experimental setup used to obtain the fluorescence curves is shown in Fig. 5.4:6. The pump light, 3700 Å and 50 Å bandwidth, was obtained from a xenon-lamp 1/4-m Jarrell-Ash monochrometer combination. The output of the monochrometer went through a variable neutral density filter and was then focused onto a 1 cm quartz cell containing the dye solutions. The cell was pointed at such an angle that the reflection of the pump light from the front surface of the cell would not be picked up by the detection system. The detection system used to monitor the

170
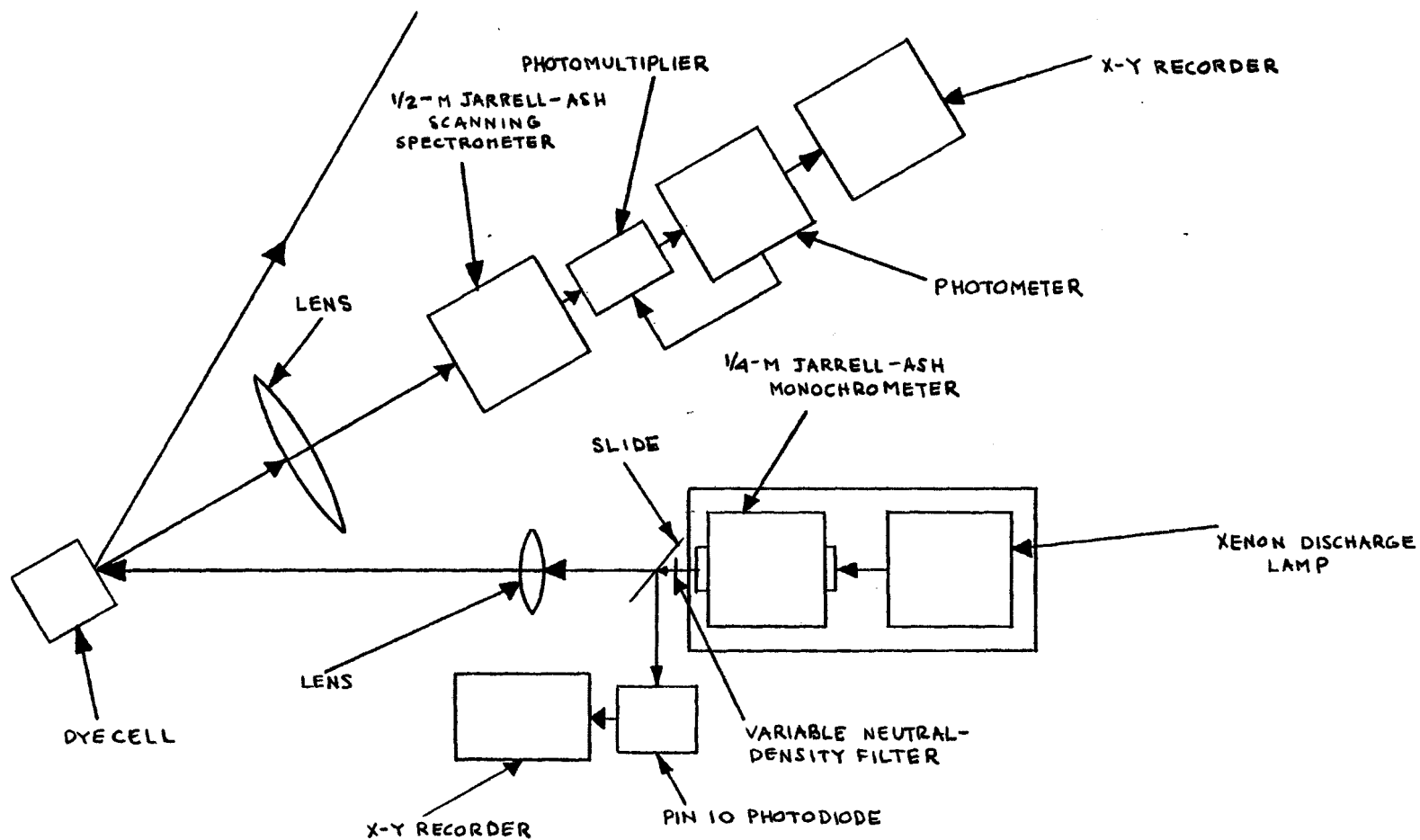
FIGURE 5.4:6   EXPERIMENTAL SETUP FOR OBTAINING FLUORESCENCE SPECTRA

front surface fluorescence of the mixtures consisted of a 1/2-m Jarrell-Ash scanning spectrometer whose light output was detected by an RCA 6217 photomultiplier. The output of the photomultiplier went to a photometer, the output of which went to an x-y recorder.

The results of the experiment are shown in Figs. 5.4:7 through 11. Fig. 5.4:7 shows the effect of concentration quenching of pure solutions of the donor dye, 7-diethylamino-4 methyl coumarine.[90,94] Fig. 5.4:8 shows the quantum yield of the donor in mixtures with the acceptor dye, DODC. The slope in Fig. 5.4:8 is steeper than in Fig. 5.4:7 indicating energy transfer to the acceptor.[90.94] For dilute concentrations of the donor, the energy transfer is due to the radiative process.[90] This can be seen in Fig. 5.4:11, which is the quantum yield of the acceptor dye normalized with respect to the fluorescence of donor dye in the same mixtures. The flat portion of the curve extending from donor concentration of 1×10^{-4} M/l to 2×10^{-2} M/l is due predominantly to the radiative process. As the donor-donor distance decreases still further there is an increase in the relative quantum yield of the acceptor. If the radiative process were the dominant energy transfer mechanism in this region, 2×10^{-2} M/l to 5×10^{-2} M/l, the curve would have remained flat. The increase in the quantum yield starting at 2×10^{-2} M/l is therefore due to the nonradiative process. At the donor concentration of 5×10^{-2} M/l the nonradiative process is the dominant energy transfer mechanism.

Hence, the dominant energy transfer mechanisms found for various regions of donor-donor concentrations are as follows:

1. radiative transfer for the region extending from 1×10^{-4} M/l to
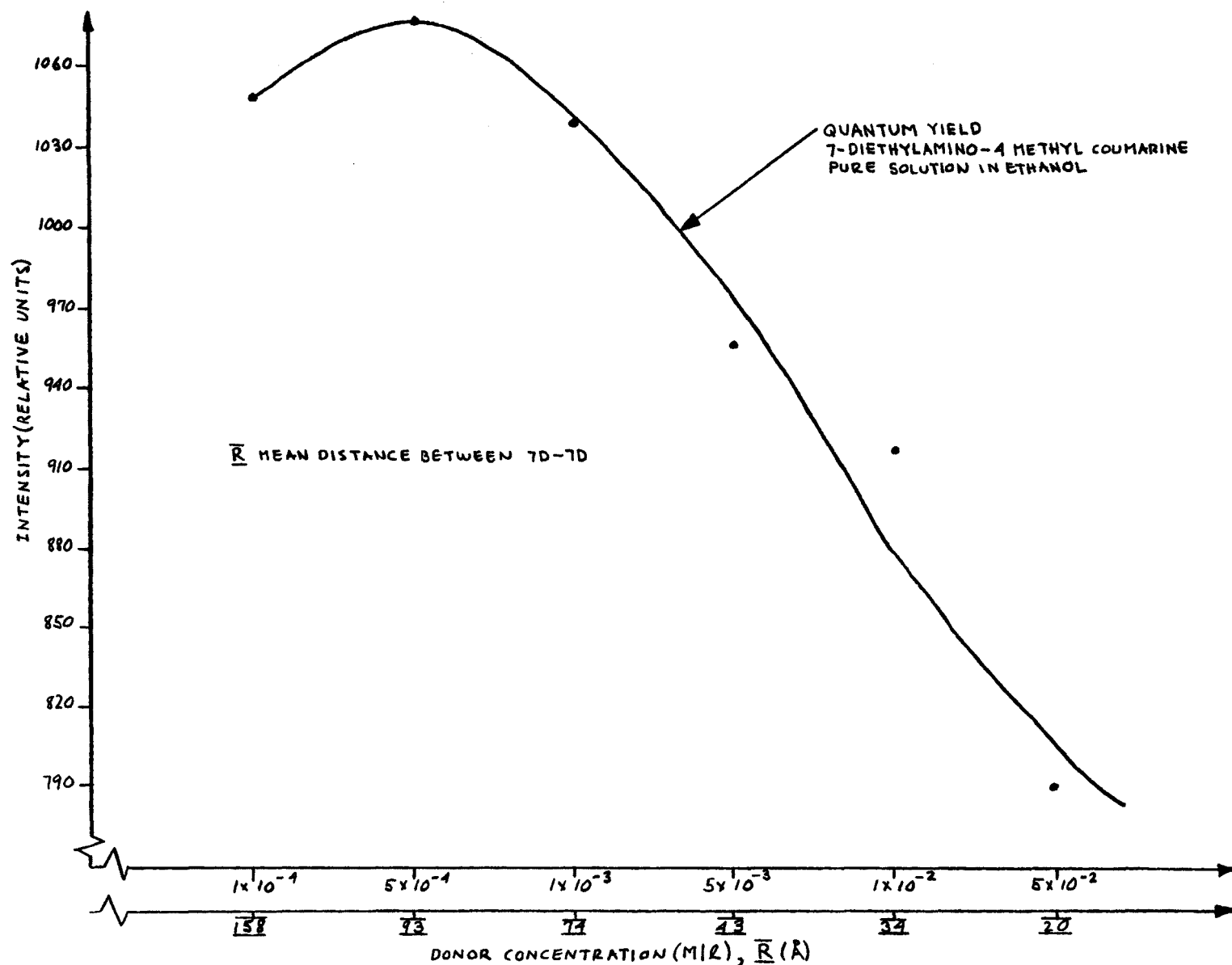
FIGURE 5.4:7   FLUORESCENCE QUANTUM YIELD OF 7-DIETHYLAMINO-4 METHYL COUMARINE VERSUS CONCENTRATION

173
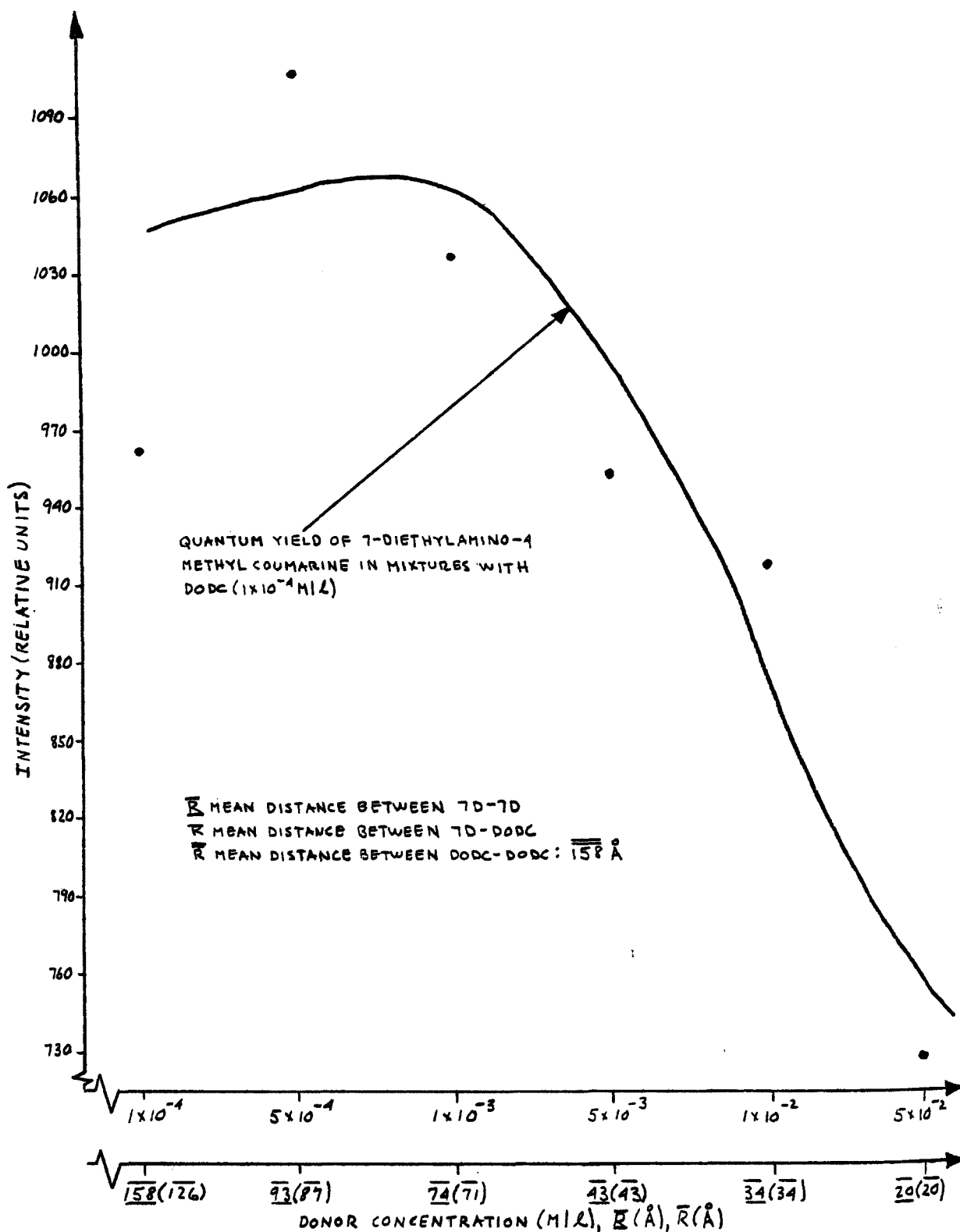
FIGURE 5.4:8 FLUORESCENCE QUANTUM YIELD OF 7-DIETHYLAMINO-4 METHYL
COUMARINE (DONOR) IN MIXTURES WITH DODC (ACCEPTOR, 1 X 10⁻⁴
M/1) VERSUS DONOR CONCENTRATION

174
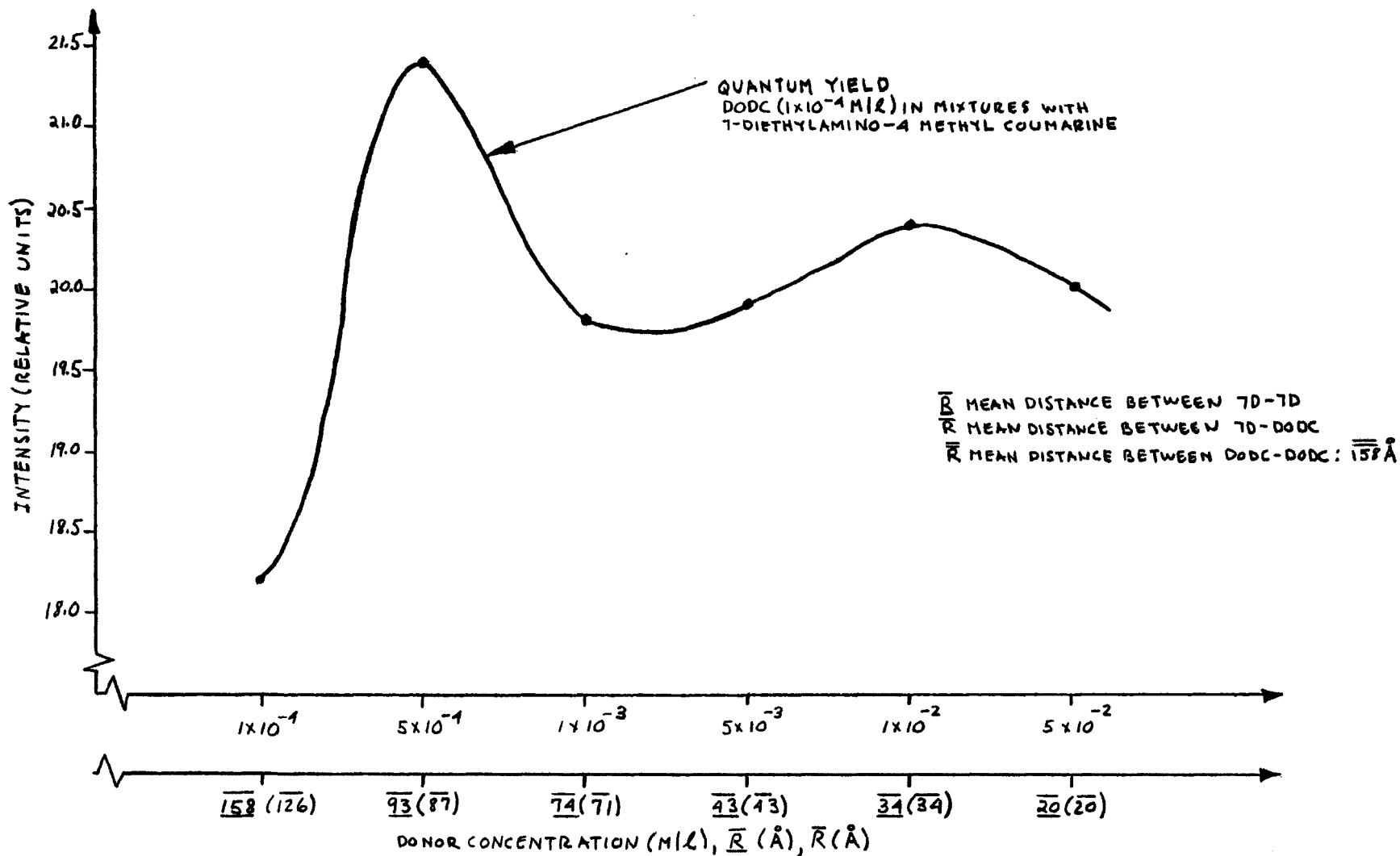
FIGURE 5.4:9   FLUORESCENCE QUANTUM YIELD OF DODC (ACCEPTOR, 1 X 10⁻⁴ M/l) IN MIXTURES WITH 7-DIETHYL-

AMINO-4 METHYL COUMARINE (DONOR) VERSUS DONOR CONCENTRATION

Figure content labels:

NORMALIZED QUANTUM YIELD OF DODC (1×10^{-4} M/l) IN MIXTURES WITH 7-DIETHYLAMINO-4 METHYL COUMARINE WITH RESPECT TO QUANTUM YIELD OF PURE SOLUTION OF 7-DIETHYLAMINO-4 METHYL COUMARINE

$\underline{\underline{R}}$ MEAN DISTANCE BETWEEN 7D-7D
$\overline{R}$ MEAN DISTANCE BETWEEN 7D-DODC
$\overline{\overline{R}}$ MEAN DISTANCE BETWEEN DODC-DODC : $\overline{\overline{158}}$ Å

Y-axis: (RELATIVE UNITS) — 18, 19, 20, 21, 22, 23, 24, 25

X-axis: 1×10^{-4}, 5×10^{-4}, 1×10^{-3}, 5×10^{-3}, 1×10^{-2}, 5×10^{-2}

$\underline{158}(\overline{126})$ $\underline{93}(\overline{87})$ $\underline{74}(\overline{71})$ $\underline{43}(\overline{43})$ $\underline{34}(\overline{34})$ $\underline{20}(\overline{20})$

CONCENTRATION (M/l), $\underline{R}$ (Å), $\overline{R}$ (Å)

FIGURE 5.4:10 NORMALIZED FLUORESCENCE QUANTUM YIELD OF DODC (ACCEPTOR, 1×10^{-4} M/l) IN MIXTURES WITH 7-DIETHYLAMINO-4 METHYL COUMARINE (DONOR) WITH RESPECT TO THE FLUORESCENCE QUANTUM YIELD OF PURE SOLUTION OF THE DONOR VERSUS DONOR CONCENTRATION
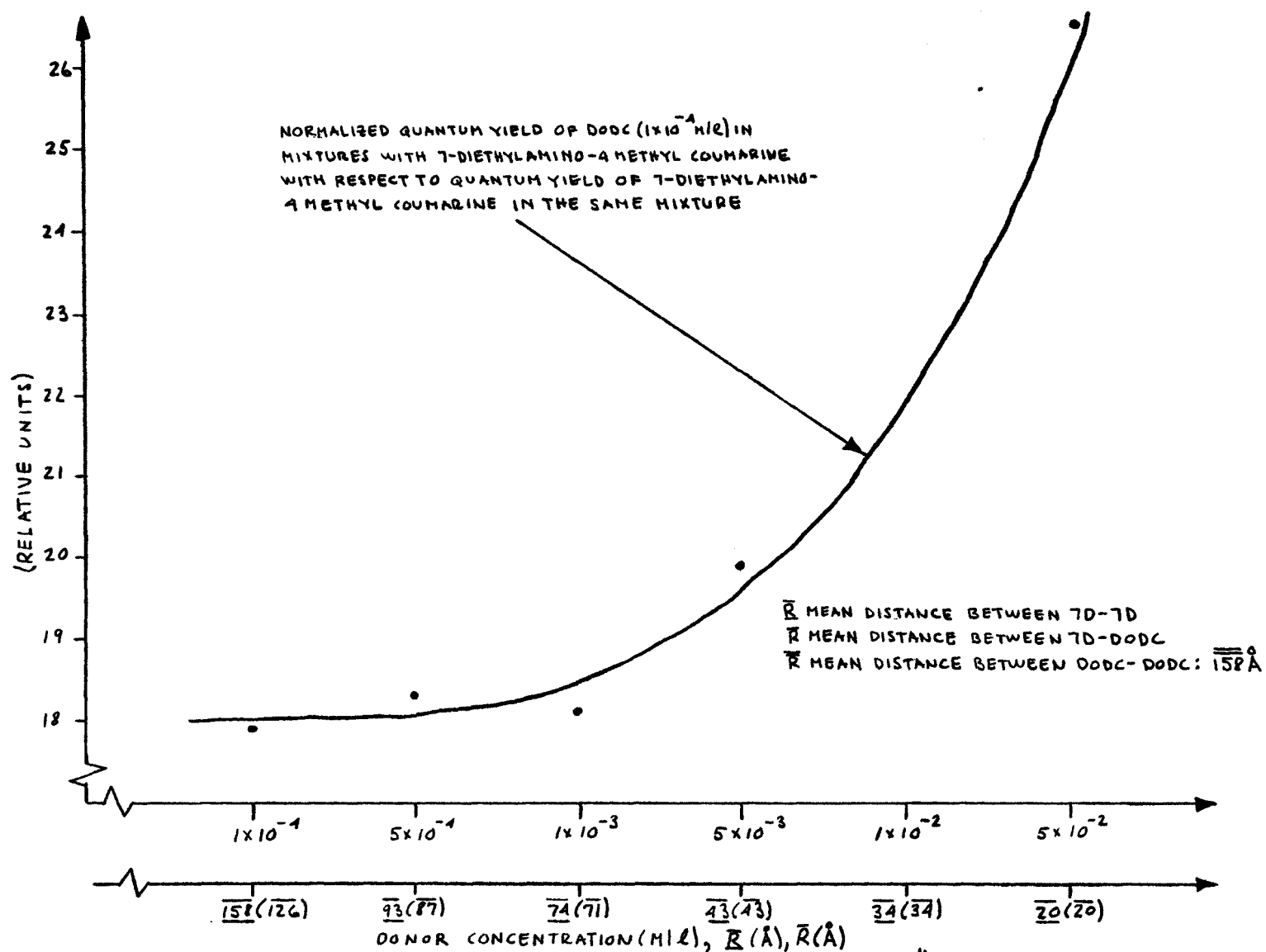
FIGURE 5.4:11 NORMALIZED FLUORESCENCE QUANTUM YIELD OF DODC (ACCEPTOR, 1 X 10^{-4} M/1) IN MIXTURES WITH 7-DIETHYLAMINO-4 METHYL COUMARINE (DONOR) WITH RESPECT TO THE FLUORESCENCE QUANTUM YIELD OF THE DONOR IN THE SAME MIXTURE VERSUS DONOR CONCENTRATION

2×10^{-2} M/l,

2. the onset of nonradiative resonance transfer at approximately 2×10^{-2} M/l, and

3. nonradiative resonance transfer at 5×10^{-2} M/l.

In conclusion, experiments were designed to obtain simultaneous outputs at two (and three) wavelength regions. The experiments were successful in that multiwavelength dye-mixture lasers were developed in spectral regions necessary to monitor the pollutants of interest, namely, NO_2, SO_2, and O_3.

Investigations of the energy transfer processes in dye-mixture lasers were carried out. Successful determination of the dominant energy transfer mechanisms was achieved.

To explore the dynamic flow of energy transfer in dye-mixture lasers, use would have to be made of time resolved spectroscopy using picosecond laser techniques. By pumping the donor dye with a picosecond laser pulse and observing the rise of the acceptor dye's fluorescence at various acceptor concentrations, the radiative and nonradiative energy transfer rates could be determined. Only static measurements were made in this work. This is suggested as another topic for future studies.

The LIDAR system developed in this work was designed to monitor ambient levels of NO_2. It would be desirable if the LIDAR system had the capability of simultaneously monitoring several pollutants, for example, NO_2, SO_2, and O_3. Use could be made of the results obtained in achieving simultaneous laser action in dye mixtures and the investigation of the processes involved. The spectral regions obtained in

the dye-mixture lasers that could be used in pollution detection would be at 4500 Å and 6200 Å. The 4500 Å region could be used to monitor NO_2, and the 6200 Å region could be frequency doubled into the ultra-violet to 3100 Å to monitor SO_2 and O_3. This would be an attractive feature of an integrated LIDAR system, and is suggested as another topic for future studies in the LIDAR area.

CHAPTER 6. DASE LIDAR SYSTEM APPLIED TO OZONE AND SULFUR DIOXIDE MEASUREMENTS

6.1 Absorption Spectra of Ozone and Sulfur Dioxide

The ozone molecule shows strong absorption in the infrared and the ultra-violet regions of the spectrum. In the ultra-violet, (Fig. 6.1.1) the main bands are known as the Huggins band, which begins at 3450Å and extends to approximately 3000Å, and the Hartley band which overlaps the Huggins band and represents the strongest ozone absorption. The Hartley band consists of a broad continuum extending between 3000Å and 2200Å with a high peak near 2550Å.

In contrast to ozone, sulfur dioxide has strong, discrete and sharp absorption bands in the near ultra-violet region, Fig. 6.1.1.

The ozone continuum corresponds to the dissociation of the molecule while in the sulfur dioxide case a similar dissociation occurs at slightly higher energies (2280Å).

In considering the application of the DASE system to the measurement of ozone and sulfur dioxide, it is clear that the interference of the two absorption spectra (of ozone and sulfur dioxide) must be taken into account.

Table 6.1.1 shows the absorption coefficients of ozone and sulfur dioxide in cm^{-1} atm^{-1}.

For measurements of ozone concentration the wavelength pair at 2923 Å and 2940 Å were chosen. At these wavelengths, the absorption due to sulfur dioxide is the same and hence its effect will cancel out for ozone measurements.
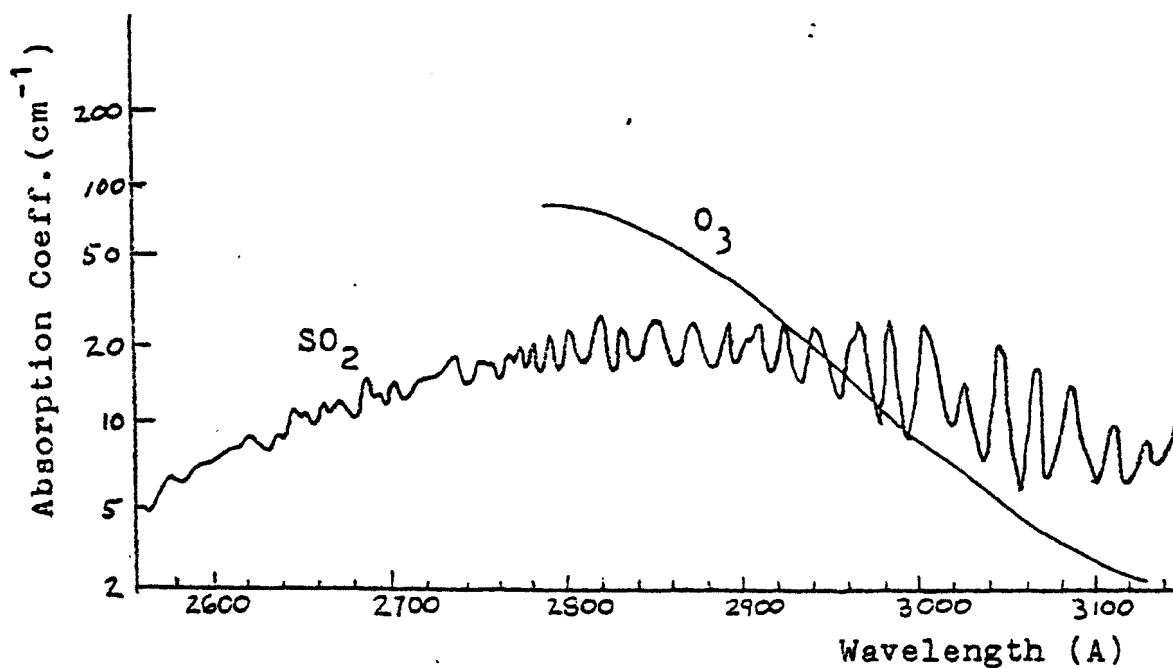
Fig. 6.1.1 Absorption coefficients of SO_2 and O_3

Wavelength $\overset{\circ}{A}$	Absorption Coefficient SO_2, cm atm^{-1}	Absorption Coefficient O_3, cm atm^{-1}
2923	26	28
2933	14	24.4 ✓
2940	26	22
2952	12.5	19.5 ✓

Fig. 6.1.1 Absorption Coefficients of SO_2 and O_3

at specific wavelengths.

For ozone,

$$\sigma(\text{at } 292.3) - \sigma(\text{at } 294) = 6 \text{ cm}^{-1} \text{ atm}^{-1}$$

These represent the values to be used for calculation of ozone concentrations from Lidar measurements at these two wavelengths.

For measurements of sulfur dioxide concentrations, the situation is different. The ozone spectrum is continuous and monotonically decreasing in the spectral ranges of interest, where sulfur dioxide shows significant absorption, Fig. 6.1.1.

To determine sulfur dioxide concentrations, it is therefore necessary to first determine (or allow for) ozone interference. Measurements at three wavelengths are therefore required: two at 292.3 and 294.0 nanometers to determine ozone concentration, plus one additional reading at 293.3 nanometers which is an absorption trough for sulfur dioxide with $\sigma = 14 \text{ cm}^{-1} \text{ atm}^{-1}$.

The results of measurements at 2933 $\overset{\circ}{A}$ can then be taken in conjunction with the previous measurements at 2923 $\overset{\circ}{A}$, where σ sulfur $= 26 \text{ cm}^{-1} \text{atm}^{-1}$, corrected for ozone interference, and used to calculate sulfur dioxide concentrations in the usual manner.

6.2.1 Lidar System Design for Ozone and Sulfur Dioxide Measurements

The system used for ozone and sulfur dioxide measurements is shown schematically in Fig. 6.2.1. It consists of the same flashlamp pumped dye laser used for the nitrogen dioxide measurements, but now containing Rhodamine$_B$ and lasing in the 6000 $\overset{\circ}{A}$ range and whose output frequency is doubled by means of a temperature tuned 90° phase-matched ADA crystal.

Frequency doubling of the dye laser output is necessary, since the 2900$\overset{\circ}{A}$ - 3000$\overset{\circ}{A}$ ranges needed for ozone and sulfur dioxide monitoring are

Fresnel Lens (15")

Mirror

Aperture Filter Photomultiplier

Collimating
Lens

Oscilloscope

Dispersive element
(prism or grating)

Temp. Oven
& ADA crystal

Mirror

Collimator

Mirror

Flashlamp Pumped
Dye Laser

Temp. Oven controller

183
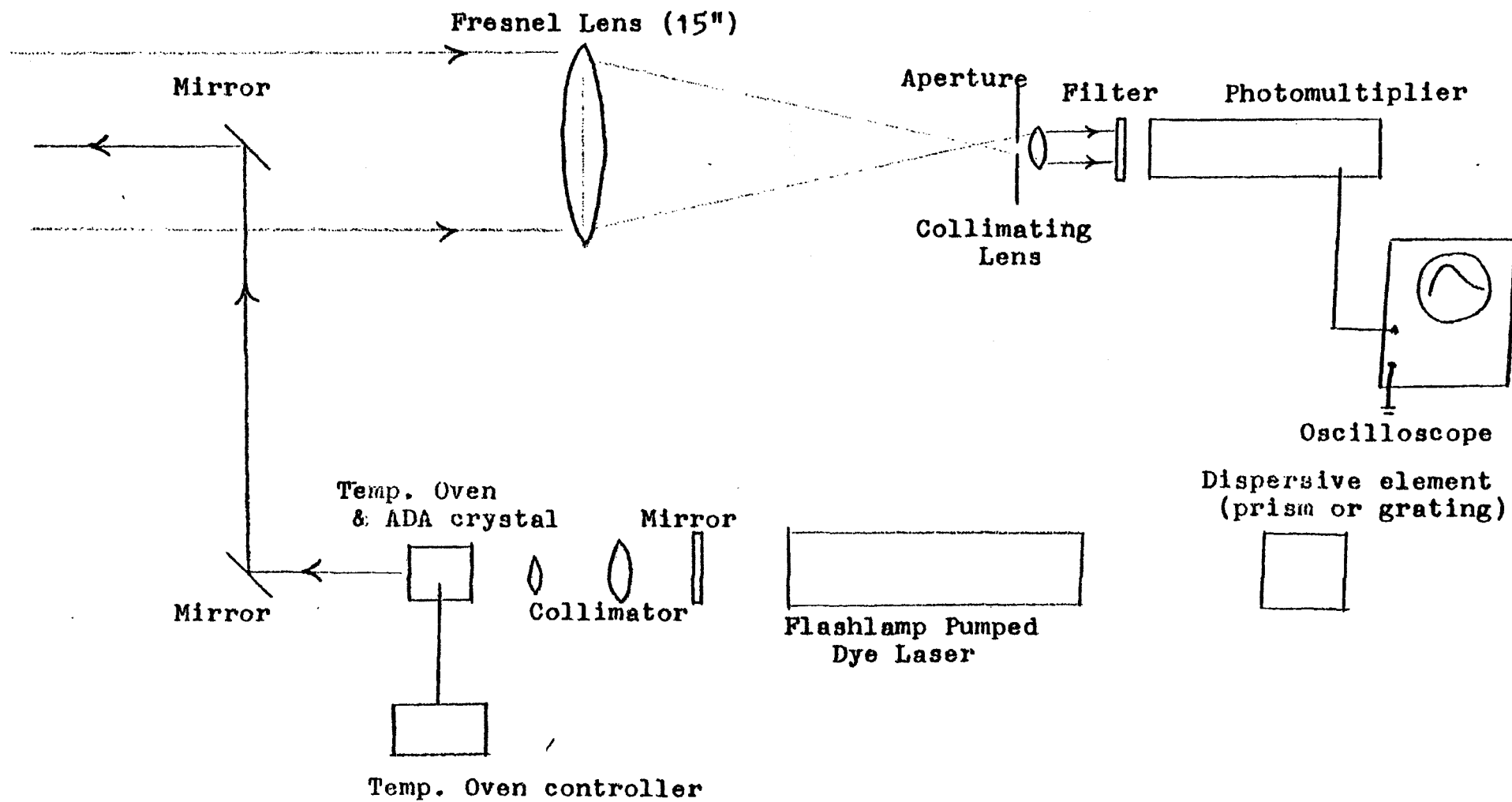
Fig. 6.2.1   Lidar System components

unobtainable directly from flashlamp pumped dye lasers. Because of the

high cost of the temperature tuned ADA frequency doubling element, and

the financial constraints on the project, it was decided to use only one

crystal to carry out the measurements for ozone and sulfur dioxide by

transmitting different required wavelengths sequentially. While not as

desirable as using tow simultaneous near-uv wavelengths which could have

been obtained by using two temperature-tuned frequency-doubling crystals

in conjunction with the beam-splitting prism arrangement used for the

nitrogen dioxide measurements, it was still possible to successfully

demonstrate the viability of the systems for ozone and sulfur dioxide by

averaging series of sequential measurements at the desired wavelengths.

The optical receiver used was the same as that used for nitrogen

dioxide but with a 15" diameter, uv transmitting, acrylic Fresnel lens;

a 1-1/2" uv transmitting collimating lens; together with a uv transmitting

filter and a Centronic photomultiplier.

The center wavelength and bandwidth of the filter are such that all

the ozone and sulfur dioxide probe wavelengths are passed by it.

The same dispersive elements used for the nitrogen dioxide measure-

ments were used to select the wavelengths necessary for the

DASE system and to obtain the narrow linewidth required for efficient

harmonic generation.

The return signal is displayed on an oscilloscope and recorded

photographically as for the nitrogen dioxide measurements.

6.3.1 Harmonic Generation and Choice of Crystal

Since the pioneering work of Franken[96], there has been extensive

research, both theoretically and experimentally, in the field of non-

linear optics, particularly second harmonic generation (SHG).

The appearance of a second harmonic is basically due to the nonlinear

polarization of the crystal. The linear dependence between the polarization

and the electric field (the basis of pre-laser optics) is no more than an approximation. A better picture is:

$$\bar{P} = \bar{P}_1 + \bar{P}_{nl}$$

where, $\bar{P}_1 = \chi E$ and $\bar{P}_{nl} = \chi^{(2)} \overline{EE} + \chi^{(3)} \overline{EEE} + ...$, with χ the linear susceptibility and χ the susceptibility tensor.

The second harmonic is then described by the first term in the non-linear polarization, $\bar{P}_{nl}$. The electric field is determined by the in-homogeneous wave equation:

$$\Delta \times \Delta \times E - \partial \bar{\epsilon} \overline{E} / t = \partial P / \partial t$$

where, $\bar{\epsilon}$ is the permittivity tensor.

The classical model of radiation of slowly moving dipoles can be used in calculating the ratio of the power densities at the second harmonic and fundamental. The result is [16]:

$$\eta = (d_{36}^2 \ |E_1|^2 / n_1 n_2)(16 \pi^3 z^2 / \lambda_1^2) \ \sin^2(\pi z / L_c) / (\pi z / L_c)^2 \qquad (6.3.1)$$

for $P(2\omega) << P(\omega)$. Where d_{36} is the piezoelectric constant, related to the susceptibility by $\chi_{ij} = 2 \ d_{ij}$; n_1, n_2 are the indices of refraction at λ_1 and λ_2, respectively; z is the distance into the medium, and L_c is the coherence length ($L_c = \lambda / 2 |n_1 - n_2|$).

In a dispersive medium, $n_2 \neq n_1$, the intensity of the second harmonic increases only when $z < L_c$ and oscillates with distance for $z > L_c$ and oscillates with distance for z L_c (Maker oscillations). Eq. 6.3.1 is a maximum when $L_c \to \infty$, (phase matching condition).

This condition can be obtained in some crystals by making use of the birefringence, that is, the variation of index of refraction with polarization and direction with respect to the optic axis (z axis).

185

The direction in which $n_2^e(\theta)=n_1^o$ is known as the direction

of collinear phase matching. However, the Poynting vectors for the funda-

mental (o wave) and second harmonic (e wave) are not in the same direction.

This has the effect of reducing the interaction between the two waves,

thereby decreasing the efficiency by a factor of $\sin^2(\theta)$. It is difficult

in practice to achieve sufficiently good alignment to avoid losses due to this

factor. These losses can be minimized by choosing a crystal whose phase

matching angle is $90°$. Because of the variation of index with temperature,

this can easily be accomplished by temperature tuning of the crystal

The tuning ranges of several crystals for $90°$ phase matching are

shown in Fig. 6.3. As can be seen, the spectral ranges required for

ozone and sulfur dioxide measurements, 2900–3000 $\overset{o}{A}$ lie at the center

of the tunable band for ADA. In addition, the nm linear coefficient for

ADA is a relatively high 0.75. These factors led to the choice of a

temperature-tuned ADA crystal as the frequency doubling element.

6.4.1 Factors Affecting Second Harmonic Generation Power Saturation

Equation 6.3.1 shows that efficiency of frequency doubling increases

linearly with input power (if beam depletion is neglected). At very

high power densities, saturation effects can be predicted theoretically.

However, the damage threshold of the doubling crystal is generally

reached well below the saturation value. In the experiments carried out,

the input power to the frequency doubling crystal was as large as was

permissible without damaging the crystal.
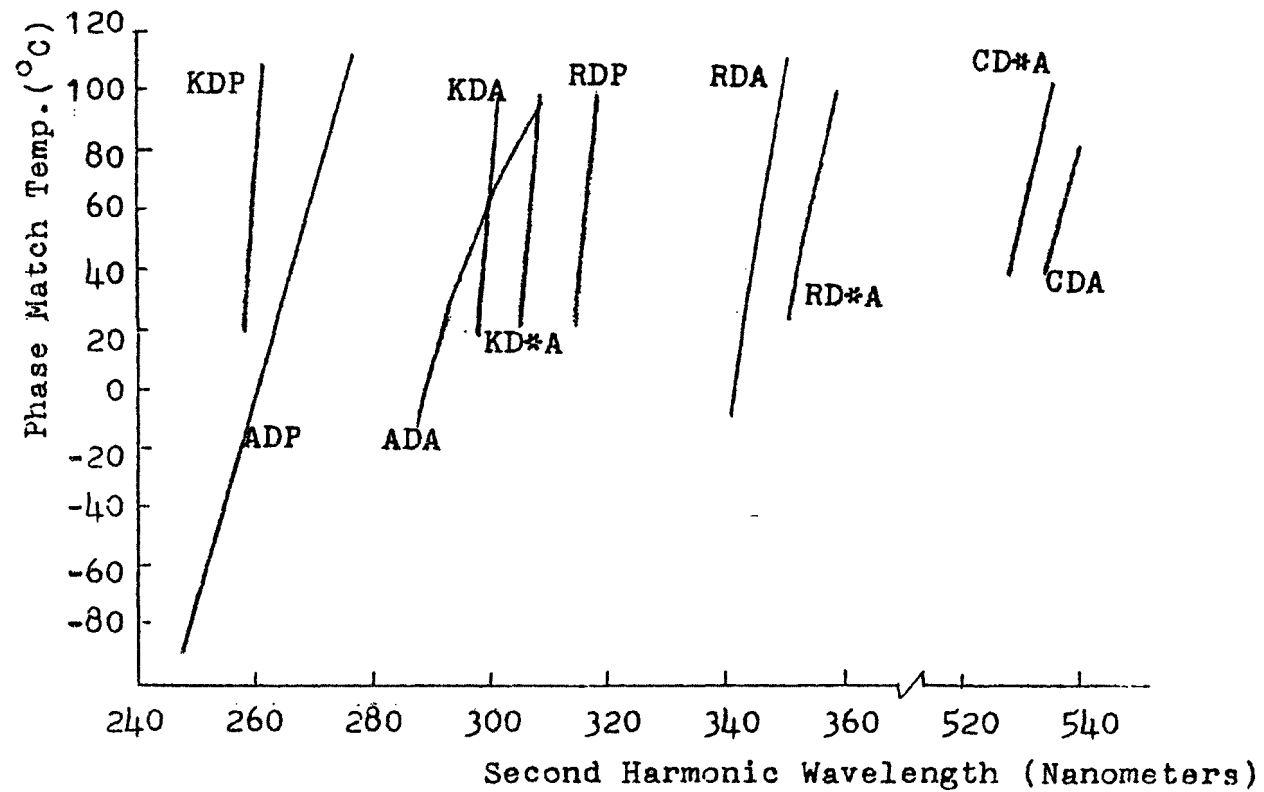
Fig. 6.3.1   Phase Matching Temperatures for 90° PM,
              KDP Homologs   (Reference 19)

Beam Divergence and Diffraction

Beam divergence of the fundamental pump wavelength effectively causes a mismatch from the optimum 90° phase matched condition and would therefore reduce the efficiency of the frequency doubling. Among the factors affecting divergence is diffraction.

For a collinear flashlamp pumped dye laser the diffraction is large (> 10mr) and varies from shot to shot. The shot to shot variation is caused by the non-uniform heating of the dye which arises because energy is absorbed non-uniformly and therefore the dye solution closest to the flashlamp is heated the most, causing refractive variations, radially, and producing a lens effect. It has also been conjectured that a shock wave is produced within the dye solution which causes a larger index variation than is produced by non-uniform heating of the dye.

To minimize these effects, a circular adapter cell was fitted around the dye cell, Fig. 6.4.1. This had the effect of concentrating the same flashlamp output into a smaller base laser cell which had a smaller beam divergence and was less susceptible to distorting effects of temperature gradients and shock waves.

6.5.1 Experimental Results

Field measurements in ozone and sulfur dioxide ware carried out over the same optical paths as in the nitrogen dioxide experiments described in previous sections. The probe wavelengths used were: 2923 Å and 2940 Å for ozone, and 2923 Å and 2933 Å for sulfur dioxide.

Coolant In

Coolant Out

Annular Region of Flash

Window

Dye In

Dye Out

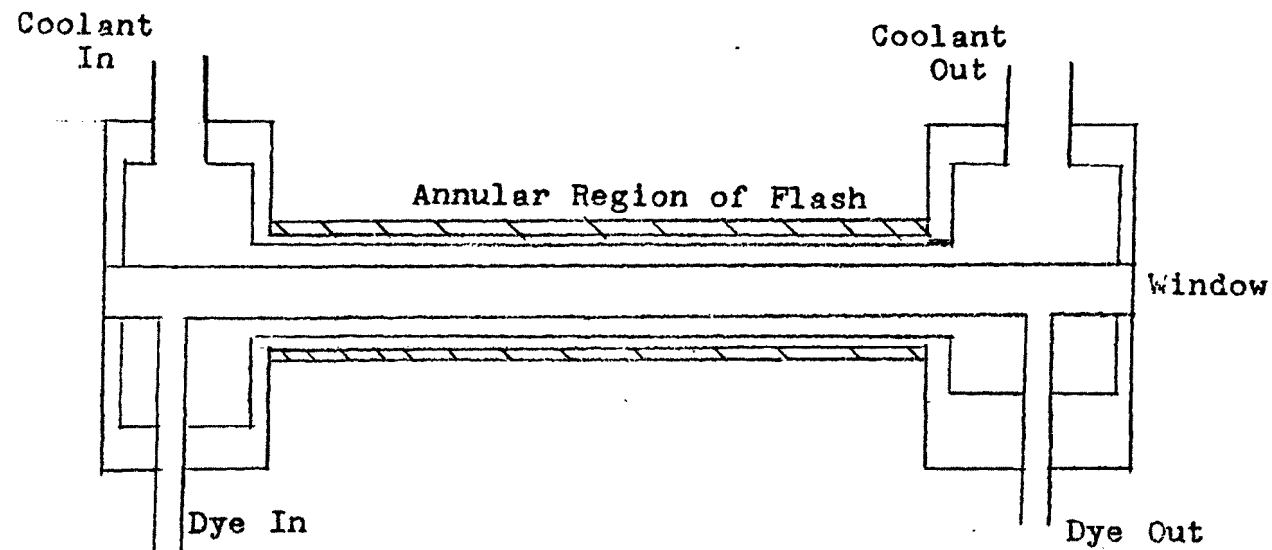Fig. 6.4.1   Flashlamp fitted with adaptor to further isolate dye solution from the annular region of the flash (Crossectional view). The coolant and dye sollution temperatures are kept within 1^{0} of each other by flowing both through the same cool water bath.

As discussed in Section 6.2.1 above, financial constraints permitted the purchase of only one temperature tuned ADA crystal, consequently measurements at the three different wavelengths were carried out sequentially.

The experimental arrangements for carrying out the measurements was that shown schematically in Fig 6.2.1. The procedure used was essentially the same as that used earlier to carry out sequential measurements of nitrogen dioxide which was described previously in Section 4.2.1.

For the measurements at each wavelength at least 6 laser probe shots were fired and the returns recorded. After each set of measurements at one wavelength, the grating at the end of the laser cavity was then rotated, and the ADA crystal temperature changed to obtain the next wavelength at which measurements were to be taken. The information required at each wavelength was then obtained by taking the average of each set of 6 (or more) recorded returns.

For the ozone measurements the probe wavelengths at 2923 $\overset{o}{A}$ and 2940 $\overset{o}{A}$ were used in conjunction with a calibration cell containing sulfur dioxide.

The use of the calibration cell with sulfur dioxide ensured that the absorption due to the sulfur dioxide was the same at both these wavelengths and that its effects were therefore cancelled out as far as ozone calculations were concerned, as discussed in Section 6.1.1 above.

To obtain the sulfur dioxide concentrations additional measurements were made at the 2933 $\overset{o}{A}$ probe wavelength, again in conjunction with the sulfur dioxide calibration cell. Along with the returns at the 2923 $\overset{o}{A}$ and 2940 $\overset{o}{A}$ wavelengths this permitted the attenuation due to ozone

to be allowed for and the sulfur dioxide concentration to be calculated as discussed in Section 6.1.1.

Several series of tests were carried out in which measurements of sulfur dioxide and ozone were made. The results of two of these series, which were typical are presented below.

The two series of measurements were each carried out on summer afternoons a few days apart. For each of the series twenty five lidar returns were obtained at each required probe wavelength. Figs. 6.5.1 through 6.5.6 show the first four returns for each of the three probe wavelengths, for each series.

The relative attenuation was measured in each photograph between the time intervals of $3-4\,\mu$ sec and $5-6\,\mu$ sec. These time intervals correspond approximately to ranges of 550 m and 850 m respectively, with a range resolution (or sample length) of 150 m. These attenuation values were then averaged (over the 25 pictures) and used (in conjunction with the absorption coefficient obtained from the calibration cell) to calculate the ozone concentration by means of equation 2.4.11.

These calculations yielded the following ozone concentrations:

First Series

      0.09 ppm at 550 m (or $3-4\,\mu$ sec)

and   0.1 ppm at 850 m (or $3-4\,\mu$ sec)

Second Series

      0.08 ppm at 550 m (or $3-4\,\mu$ sec)
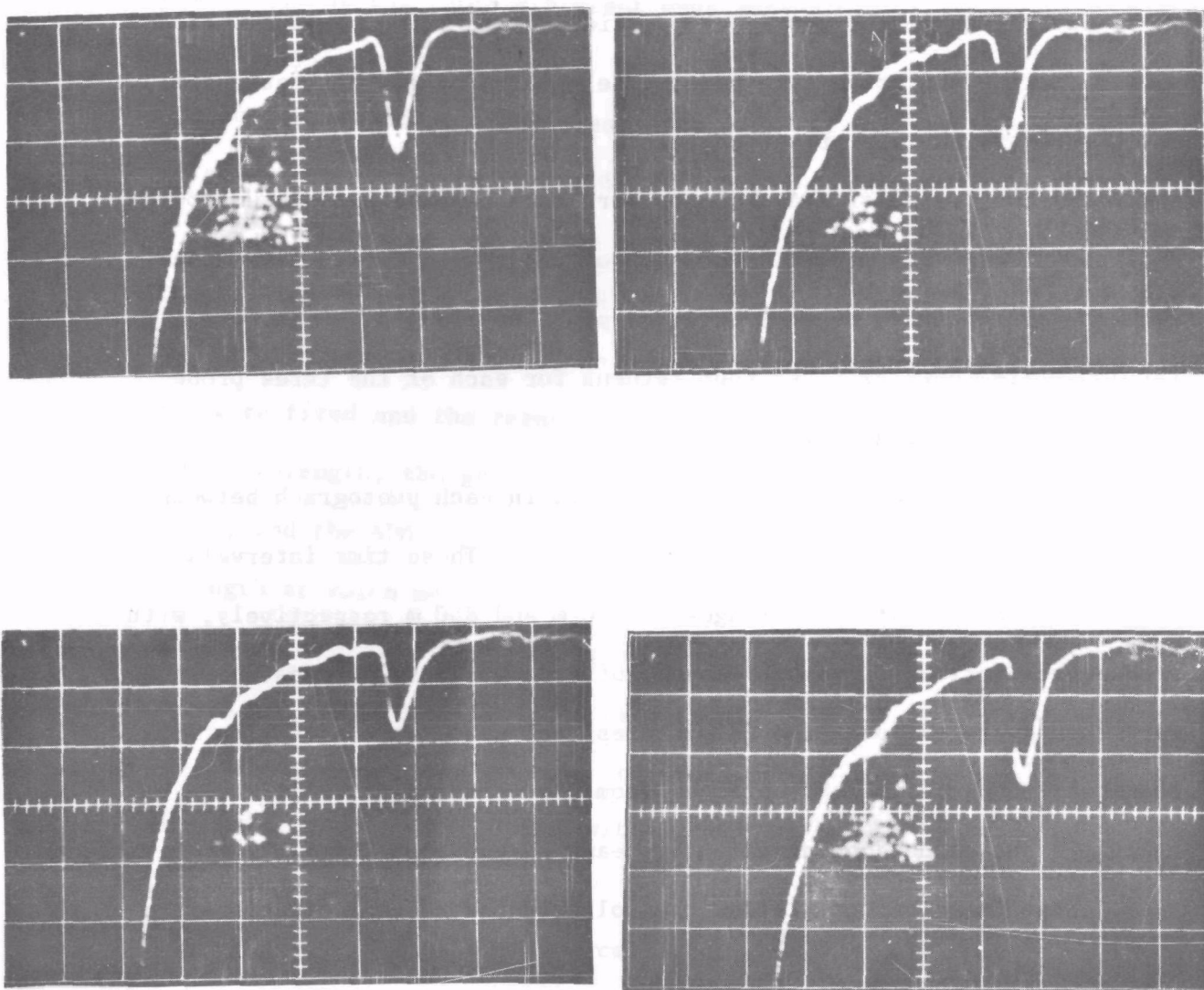
and

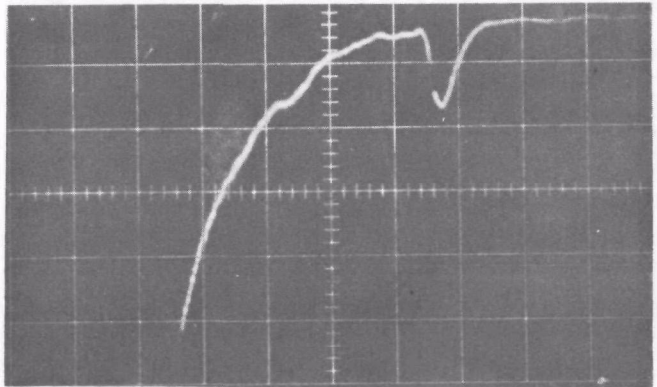   0.09 ppm at 850 m (or $5-6\,\mu$ sec)

Figure 6.5.1 LIDAR returns at 2933A for first series.
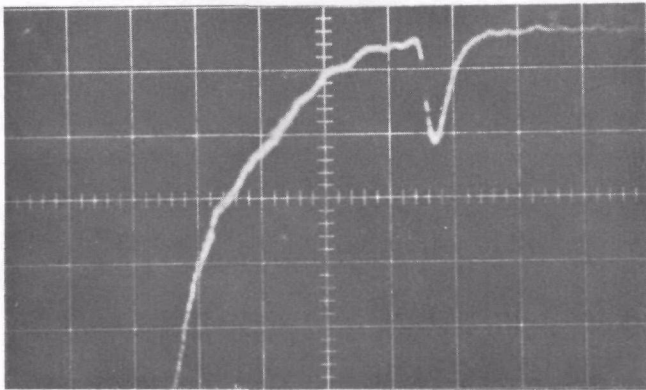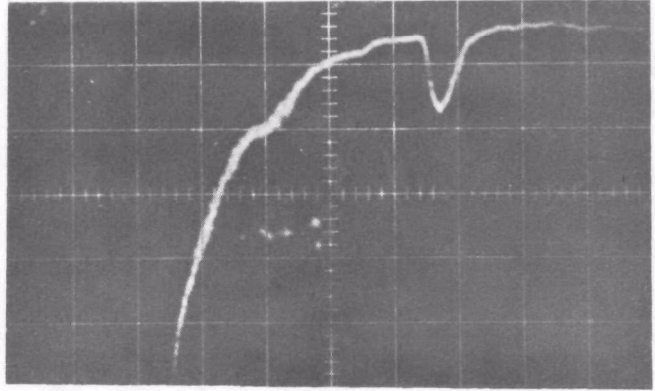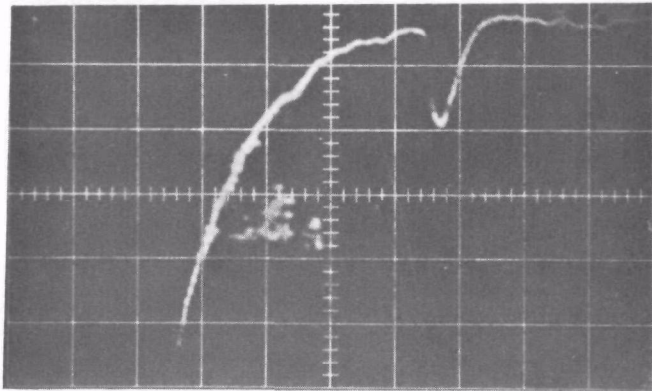
Figure 6.5.2 LIDAR returns at 2940A for first series.
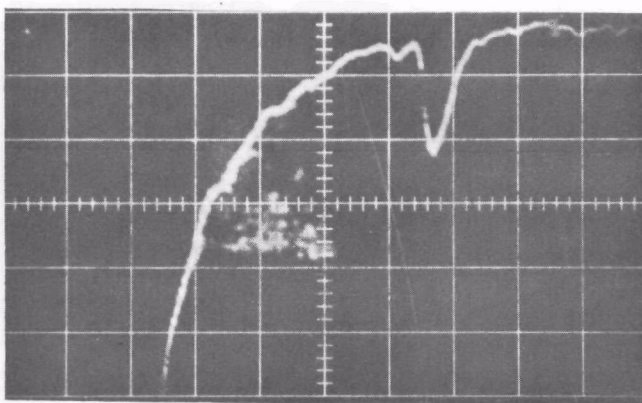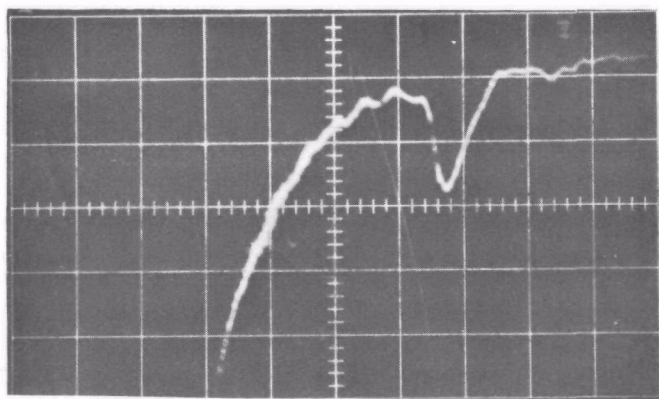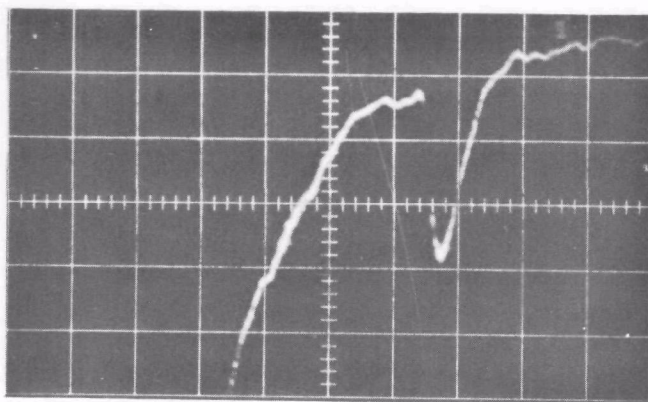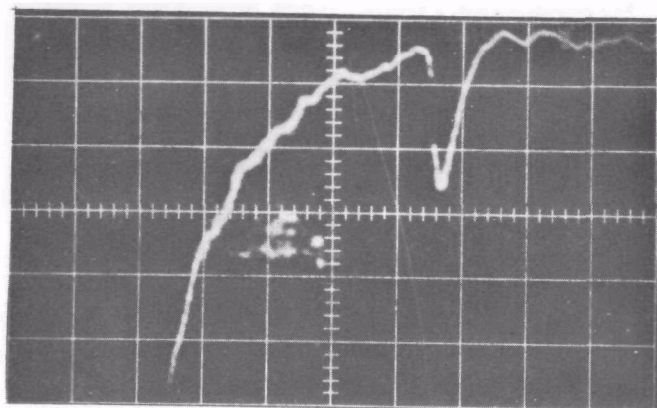
Figure 6.5.3 LIDAR returns at 2952A for first series.
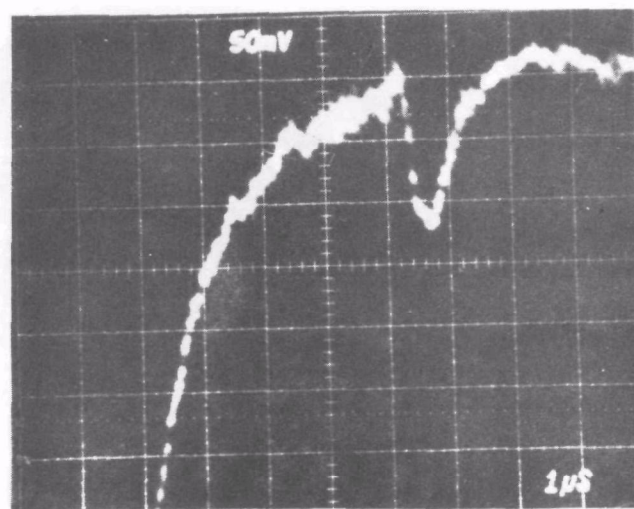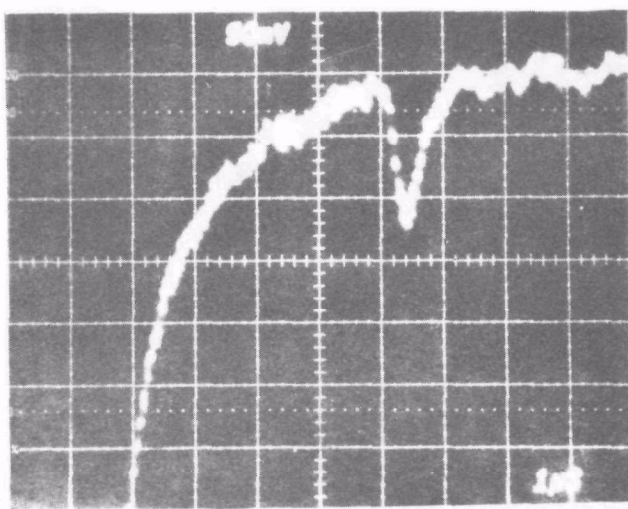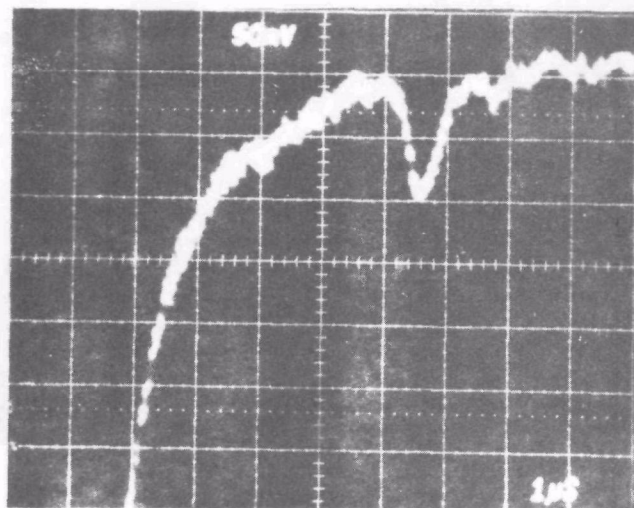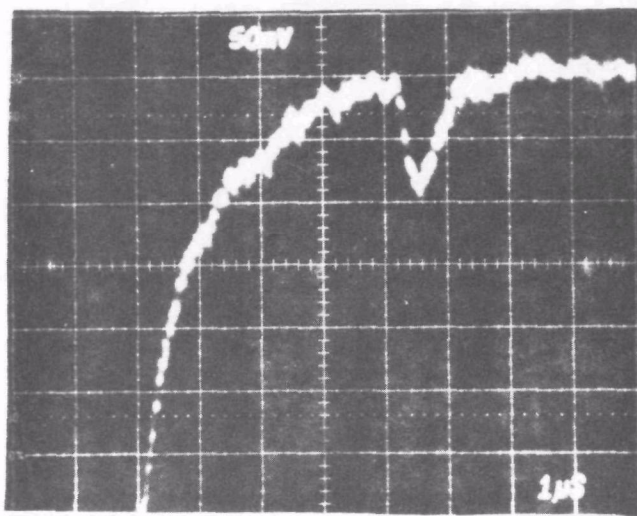
Figure 6.5.4 LIDAR returns at 2923A for second series

195
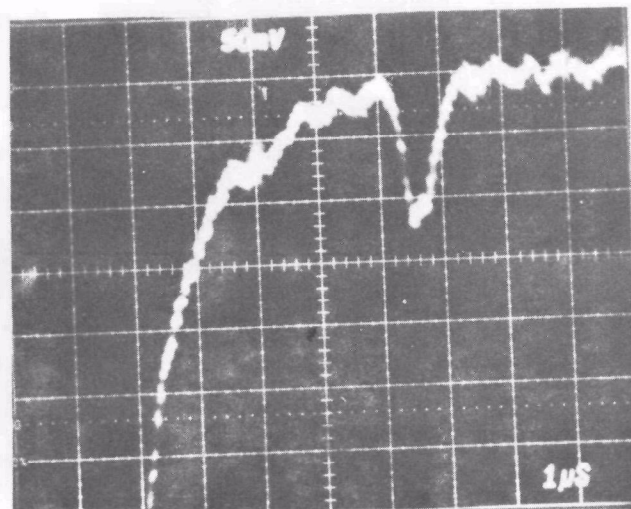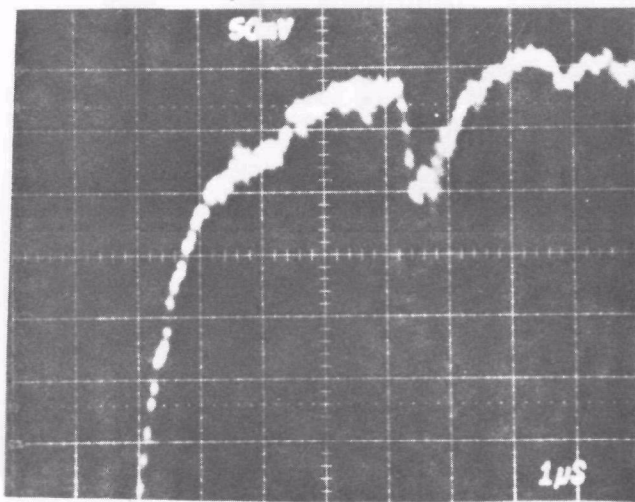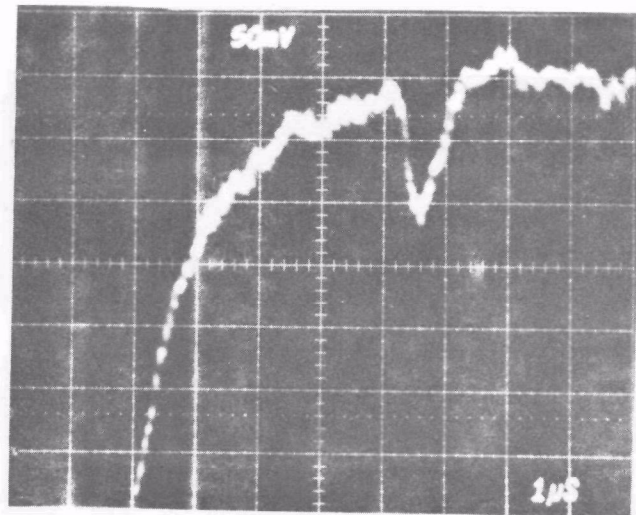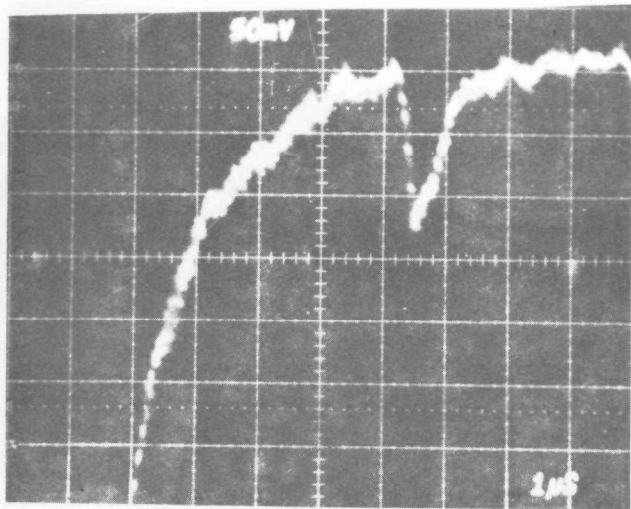
Figure 6.5.5 LIDAR returns at 2933A for second series
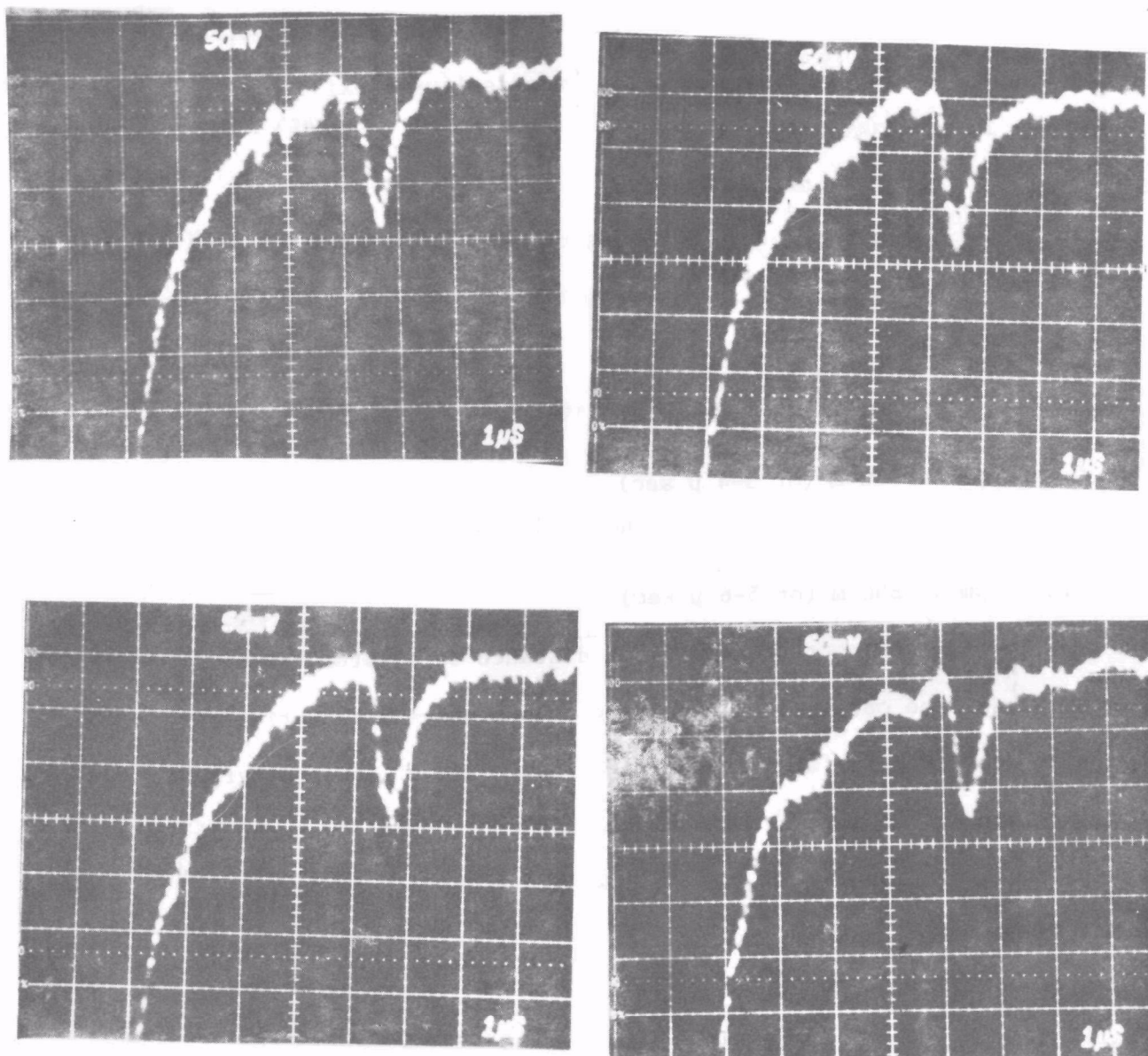
Figure 6.5.6 LIDAR returns at 2940A for second series

197

Using these concentrations and averaging the attenuation in the returns for the third wavelength, at 2933 $\overset{\circ}{A}$ and making use of the absorption coefficient obtained from the calibration cell, equation 2.4.11 was again used to obtain the following sulfur dioxide concentrations:

First Series

0.05 ppm at 550 m (or 3.4 μ sec)

and

0.08 ppm at 850 m (or 5-6 μ sec)

Second Series

0.048 ppm at 550 m (or 3-4 μ sec)

and

0.047 ppm at 850 m (or 5-6 μ sec)

The average concentration over the distance to a water tower 1 km away was also obtained by examining the relative attenuation of the pulse echo from it (seen at the right hand side of the photographs of the returns). Making use of the attenuation averaged over the 25 returns, and equation 2.4.28, the following average concentrations were obtained for ozone and sulfur dioxide over the 1 km path to the water tower:

First Series

ozone : 0.08 ppm

and

sulfur dioxide : 0.06 ppm

<u>Second Series</u>

    ozone : 0.06 ppm

and

  sulfur. dioxide : 0.05 ppm

The results reported by the New York City Department of Air

Resources for the City College – Upper Manhattan area were obtained

and were averaged over the same period that the lidar measurements were

made. This yielded the following average concentrations:

<u>First Series</u>

    ozone : 0.07 ppm

and

  sulfur dioxide : 0.05 ppm

<u>Second Series</u>

    ozone : 0.065 ppm

and

  sulfur dioxide : 0.04 ppm

As can be seen the long path average absorption results and the

Department of Air Resources results agree fairly well. The discrepancy

is greater for the DASE measurements at the 550 m and 850 m ranges.

This, however is to be expected since the DASE system measured pollution

at specific points (over 150 m sampling lengths) where local traffic

and other pollution conditions could be expected to vary from the averages

for the Upper Manhattan region.

In contrast the long path absorption method (to the water tower)

can be expected to yield the average concentrations over the Upper

Manhattan region. This is in fact borne out by its closer agreement

with the averaged readings from the Department of Air Resources over

approximately the same region for the same period.

SUMMARY

Introduction

A single-ended laser radar (LIDAR) system was designed, built and successfully operated to measure NO_2, SO_2 and O_3 concentrations in the atmosphere. The LIDAR technique used was the Differential Absorption of Scattered Energy (DASE) technique. In its simplest form, the DASE LIDAR technique determines the concentrations of a pollutant along the transmitted LIDAR beam by examining the selective attenuation of outgoing LIDAR signals, transmitted at different wavelengths, by the pollutant molecules present. More specifically, the concentration of pollutant present in an incremental path length (or sample length) in space (along the LIDAR beam path) is obtained by determining the relative attenuation (across the sample length) of two colinear laser beams at close lying wavelengths, each respectively on and off the resonance absorption of the pollutant molecule in question. The relative attenuation is determined from comparisons, (at the LIDAR receiver) of the Rayleigh and Mie atmospheric elestic backscatter of the two outgoing laser beams as they traverse the sample length. Appropriate temporal resolution at the receiver then permits determination of the range and spatial resolution of the pollutant distribution.

The LIDAR System

The basic LIDAR system was built around a flashlamp-pumped organic dye laser as the source of laser energy. For measurements of NO_2, whose absorption spectrum lies in the 4500 Å spectral regions, it was possible to use the output of the dye laser directly for the transmitted LIDAR signals. For the measurements of SO_2 and O_3, whose absorption spectra

lie in the near ultraviolet (2900 Å) spectral regions, it was necessary

to frequency-double the output of the dye laser, by means of a

temperature controlled ADA crystal frequency doubler, to obtain the

transmitted LIDAR wavelenghts required.

The LIDAR system as used for the NO_2 measurements was designed to

be capable of operation in two basic modes. In the first mode, the outputs

at the two required wavelengths, 4500 Å and 4478.5 Å, respectively on and

off the resonance absorption of NO_2 are obtainable, in rapid sequence with

frequency selection being carried out by an electromechanically-driven

diffraction grating, whose position at one-end of the organic dye laser

may be rapidly and accurately changed between laser shots.

In the second mode of operation, an intra-cavity dielectric-

interface polarizing beam-splitter was used to simultaneously obtain the

pair of close lying wavelengths at 4500 Å and 4478.5 Å required from

the laser. The use of this system represented the first successful use

of a DASE LIDAR system operating in a simultaneous two wavelength mode.

In this mode of operation, errors due to scintillation effects and

particle and aorosol drift are effectively reduced.

The systems developed for both sequential and simultaneous operation

incorporated an automatic calibration feature which allowed for the

variations in bandwidth which inevitably occur from shot to shot with dye

lasers. Experimental results are presented, which show the necessity and

advantages of this automatic calibration approach. The calibration system

operates by sampling the transmission of part of each outgoing laser pulse

through a test cell containing samples of known concentrations of the

pollutant being measured by the LIDAR system. This approach automatically

allows for the variations in laser bamdwidths and determines the effective

202

pollutant absorption cross-section for each outgoing laser pulse. Again, this work represented the first reported use of this automatic calibration approach which we believe to be essential to the successful operation of LIDAR systems of this type.

The LIDAR system receiver was designed and built using a 15 inch diameter and 24 inch focal length acrylic Fresnel lens as the primary lens. This lens is capable of forming a sharp image for objects near the optical axis. This is appropriate, since LIDAR receivers do not require a wide field of view for collecting the backscattered light from the outgoing laser beam. The light from the Fresnel lens is the collected and collimated then split onto two photomultipliers with appropriate optical filters to match the transmitted wavelengths.

Measurements of NO_2, SO_2 and O_3

With the errors in the system minimized through the use of simultaneous two wavelength operations, NO_2 measurements were made with the LIDAR transmitter directed out of a laboratory window across the upper East Side of Manhattan. Several readings were obtained for various times during the day to observe changes in pollution levels over areas of heavy vehicular traffic.

From the LIDAR returns obtained and recorded, range-resolved calculations were made of pollution concentrations in the atmosphere at distances of 250 and 1000 meters from the LIDAR receiver. In addition average pollution concentrations between the LIDAR transmitter and a fixed target (the water tower on a building) 2400 m away were also calculated. Concentrations varying from 0.06 to 0.31 ppm were obtained depending on the time of day. The highest numbers were for the

concentrations calculated for the range-resolved returns from 700 m and 1000 m, which are from the atmosphere above heavily trafficked areas.

Measurements of SO_2 and O_3 were carried out using the frequency doubled output of the dye laser. Because of financial constraints only one temperature tuned ADA crystal was available for frequency doubling. Measurements of SO_2 and O_3 were therefore carried out in a sequential mode of operation. Because of overlap of the absorption spectrum of SO_2 and O_3, it is first necessary to determine O_3 concentrations then SO_2 concentrations. This procedure required LIDAR returns to be obtained at three different wavelengths in the 2900 $\overset{o}{A}$ spectral region. These returns were obtained sequentially and results averaged for a series of (typically 25) laser shots at each wavelength.

From these averaged returns, range resolved atmospheric concentrations of O_3 and SO_2 were calculated at distances of 550 m and 850 m respectively. Average concentrations between the LIDAR transmitter and a fixed target (building) 1000 m distant were also calculated. SO_2 concentrations varied from 0.04 to 0.08 ppm, while O_3 concentrations varied from 0.07 to 0.1 ppm depending on the location and time of day (with the highest numbers being obtained for the 850 m range).

To compare the results of the LIDAR measurements, information was obtained from the New York City Department of Air Resources on pollution levels recorded at their various monitoring stations on the upper East Side, at the same time that the LIDAR measurements were being carried out. It was found that the averaged readings for these stations, which cover the area of the LIDAR tests, were generally within 15 percent of the average concentrations obtained by the LIDAR technique for the same region.

Dye Mixture Lasers

To examine the potential for second generation LIDAR systems capable of operating simultaneously in two and three spectral regions for the simultaneous monitoring of several pollutants, a program of experiments on dye-mixture lasers was also carried out. The objective of this was to use energy transfer mechanisms that were considered feasible in dye mixtures to obtain simultaneous laser action at widely separated spectral regions. The program was successful, with simultaneous laser action being obtained for the first time at widely separated spectral regions, including simultaneous outputs at the three primary colors. Analysis of the experimental results showed that radiative energy transfer was dominant at the concentrations found optimum for simultaneous two and three-wavelength operation in dye-mixture lasers. Nonradiative resonance energy transfer was found to dominate at higher concentrations.

Conclusion

The work reported here describes the development, design and construction of a LIDAR system operating in the visible and near ultra-violet spectral regions for the measurement of NO_2, SO_2 and O_3. Field tests with the system successfully demonstrated the potential for LIDAR methods based on the DASE technique to be used for range-resolved monitoring of ambient NO_2, SO_2 and O_3.

REFERENCES

1. L. B. Lave and E. P. Seskin, Science, 169, (1970), pp. 723-731.

2. H. Kildal and R. L. Byer, Proc. IEEE, 59, (1971), pp. 1644-1663.

3. T. Kobayashi and H. Inaba, 'Laser Beam Technology for Remotely Sensing Invisible Molecules in the Polluted Atmosphere', 11th Symposium on Electron, Ion and Laser Beam Technology, ed. R. F. M. Thornley, San Francisco Press, Inc., (1971), pp. 385-401; see also S. Nakahara, K. Ito, A. Fuke, S. Komatsu, H. Inaba and T. Kobayashi, Opto-electronics, 4, (1972), pp. 169-177.

4. R. T. H. Collins, Appl. Opt., 9, (1970), pp. 1782-1788.

5. C. S. Cook, Appl. Opt., 11, (1972), p. 1742.

6. G. Fiocco and L. D. Smullin, Nature (London), 109, (1963), pp. 1275-1276.

7. M. G. H. Ligada, Proc. Conf. Laser Tech., 1st San Diego, California, U. S. Navy ONR, (1963), p. 62.

8. D. A. Leonard, Nature, 216, (1967), pp. 142-143.

9. J. A. Cooney, Appl. Phys. Letts., 12, (1968), pp. 40-42; see also J. Appl. Meteorology, 9, (1970), pp. 182-184.

10. S. H. Melfi, J. D. Lawrence, Jr. and M. P. McCormick, Appl. Phys. Letts., 15, (1969), pp. 295-297.

11. H. Inaba and T. Kobayashi, Nature, 224, (1969), p. 170; see also Opto-electronics, 2, (1970), pp. 45-46.

12. T. Kobayashi and H. Inaba, Appl. Phys. Letts., 17, (1970), pp. 139-141.

13. J. A. Cooney, J. Appl. Meteorology, 10, (1971), pp. 301-308.

14. R. G. Strauch, V. E. Derr and R. E. Cupp, Appl. Opt., 10, (1971), pp. 2665-2669.

15. S. H. Melfi, Appl. Opt., 11, (1972), pp. 1605-1610.

16 T. Hirschfeld, E. R. Schildleraut, H. Tannenbaum and D. Tannenbaum, Appl. Phys. Letts., 22, (1973), pp. 38-40; see also T. Hirschfeld and S. Klainer, Opt. Spect., (1970), pp. 63-66.

17. T. Hirschfeld, Appl. Opt., 13, (1974), pp. 1435-1437.

18. R. L. Byer, Opt. and Quant. Elect., 7, (1975), pp. 147-177.

19. G. B. Jacobs and L. R. Snowman, IEEE J. Quant. Elect., QE-3, (1967), pp. 603-605.

20. P. L. Hanst and J. A. Morreal, J. Air Pollut. Cont. Ass., 18, (1968), pp. 754-759.

21. P. L. Hanst, Appl. Spect., 24, (1970), pp. 161-174.

22. S. Zaromb, Proc. Electro-Optical Systems Design Symposium, Sept., (1969), p. 609.

23. S. Nakahara and K. Ito, International Quantum Electronics Conf. Digest Tech. Papers, Sept., (1970), p. 226.

24. H. Inomata and T. Igarashi, Trans. Tech. Group on Quant. Elect. of the Inst. Elect. Comm. Engr. (IECE) of Japan, QE-70-36, Dec.

25. J. A. Hodgeson, W. A. McClenney and P. L. Hanst, Science, 182, (1973), p. 248.

26. R. L. Byer and M. Garbuny, Appl. Opt., 12, (1973), pp. 1496-1505.

27. E. D. Hinkley, Appl. Phys. Letts., 16, (1970), pp. 351-354; see also K. W. Nill, F. A. Blum, A. R. Calowa and T. C. Harman, Appl. Phys. Letts., 19, (1971) pp. 79-82.

28. E. D. Hinkley and P. L. Kelley, Science, 171, (1971), pp. 635-639; see also I. Melngailis, IEEE Trans. on Geo. Sci. Elect., GE-10, (1972).

29. E. D. Hinkley, Opto-electronics, 4, (1972), pp. 69-86.

30. L. R. Snowman. Technical Report R72ELS-15, General Electric Electronic Laboratory, Syracuse, New York, March, (1972).

31. D. O'Shea and L. G. Dodge, Appl. Opt., 13, (1974), pp. 1481-1486.

32. T. Henningsen, M. Garbuny and R. L. Byer, Appl. Phys. Letts., 24, (1974), pp. 242-244.

33. M. R. Bowman, A. J. Gibson and M. C. W. Sandford, Nature, 221, (1969), p. 456; see also A. J. Gibson, J. Sci. Instr., 2, (1969), p. 802.

34. M. C. W. Sandford and A. J. Gibson, J. Atmos. Terr. Phys., 32, (1970), pp. 1423-1430.

35. A. J. Gibson and M. C. W. Sandford, J. Atmos. Terr. Phys., 33, (1971), p. 1675.

36. C. J. Schuler, C. T. Pike and H. A. Miranda, Appl. Opt., 10, (1971), pp. 1689-1690.

37. R. D. Hake, D. E. Arnold, D. W. Jackson, W. E. Evans, B. P. Ficklin and R. A. Song, J. Geophys. Res., 77, (1972), p. 6839.

38. J. E. Blamont, M. L. Chanin and G. Megie, Ann. Geophys., 28, (1973), pp. 833-838.

39. V. W. J. H. Kirchoff and B. B. Clemesha, J. Atm. Terr. Phys., 35, (1973), p. 1493.

40. A. J. Gibson and M. C. W. Sandford, Nature, 239, (1972), pp. 509-511.

41. F. Felix, W. Keenliside, G. Kent and M. C. W. Sandford, Nature, 246, (1973), p. 345.

42. C. M. Penney, W. W. Morey, R. L. ST. Peters, S. D. Silverstein, M. Lapp and D. R. White, Final Report for NASA CR-132363, prepared by General Electric Corporate Research and Development, Schenectady, New York.

43. R. M. Measures and G. Pilon, Opto-electronics, 4, (1972), pp. 141-153.

44. S. A. Ahmed and J. S. Gergely, 'Atmospheric Pollution Monitoring Using Tunable Dye Lasers', Proc. Tech. Prog., Electro-Opt. Systems Design Conf., New York, N. Y., Sept., (1973), pp. 275-282.

45. J. A. Gelbwachs, M. Birnbaum, A. W. Tucker and C. L. Fincher, Opto-electronics, 4, (1972), pp. 155-160.

46. R. M. Schotland, E. E. Chermack and D. T. Chang, Proc. First International Symp. of Humidity and Moisture, p. 569 (Reinhart Book Div., New York, N. Y., 1964); see also R. M. Schotland, Proc. Third Symp. on Remote Sensing of the Environment, Oct. 14-16, (1964), pp. 215-224, Univ. of Michigan, Ann Arbor, Mich.

47. S. A. Ahmed and J. S. Gergely, 'Laser Radar Study Using Resonance Absorption for Remote Detection of Air Pollutants', Fifth Conf. on Laser Radar Studies of the Atm., June 4-6, (1973), Williamsburg, Va.

48. S. A. Ahmed, Appl. Opt. 12, (1973), pp. 901-903.

49. M. L. Wright, E. K. Proctor, L. S. Gasiorek and E. M. Liston, Final Report for NASA CR-132724, Contract NA S1-11657, Stanford Research Institute, Menlo Park, California.

50. T. Igarashi, 'Laser Radar Study Using Resonance Absorption for Remote Detection of Air Pollutants', Fifth Conf. on Laser Radar Studies of the Atm., June 4-6, (1973), Williamsburg, Va.

51. K. W. Rothe, U Brinkmann and H. Walther, Proc. VIII ICPEAC, Beograd, july, (1973); see also Appl. Phys., 3, (1974), pp. 115-119.

52. W. B. Grant, R. D. Hake, Jr., E. M. Liston, R. C. Robbins and E. K. Proctor, Jr., Appl. Phys. Letts., 24, (1974), pp. 550-552

53. K. W. Rothe, U. Brinkman and H. Walther, Appl. Phys., to be published.

54. R. Penndorf, J. Opt. Soc. Am., 47, (1957), pp. 176-182.

55. R. F. Begley, A. B. Harvey and R. L. Byer, Appl. Phys. Letts., 25, (1974), pp. 317-390.

56. H. Inaba and T. Kobayashi, Opto-electronics, 4, (1972), pp. 101-123.

57. P. W. Kruse, L. D. McGlauchlin and R. B. McQuistan, 'Elements of Infra-Red Technology', Wiley, New York, (1963).

58. W. K. Pratt, 'Laser Communication Systems', Wiley, New York, (1969).

59. H. Walther and J. L. Hall, Appl. Phys. Letts., 17, (1970), p. 239.

60. R. C. C. Leite, Phys. Rev. Letts., 14, (1965), p. 7.

61. R. C. Damen, Phys. Rev. Letts., 14, (1965), p. 9.

62. R. M. Schotland, J. Appl. Meteorology, 13, (1974), pp. 71-77.

63. G. W. Grams and C. M. Wyman, J. Appl. Meteorology, 11, (1972), pp. 1108-1113.

64. R. S. Lawrence and J. W. Strohbehn, Proc. IEEE, 58, (1970).

65. H. S. Piloff, Appl. Phys. Letts., 21, (1972), pp. 339-340.

66. P. Dezauzier, A. Eranian and O. deWitte, Appl. Phys. Letts., 22, (1973), pp. 664-666.

67. A. A. Friesem, U. Ganiel and G. Neumann, Appl. Phys. Letts., 23, (1973), pp. 249-251.

68. P. Flamont and Y. H. Meyer, Opt. Comm. 13, (1975), pp.13-16.

69. H. Furtumoto and H. Ceccon, Appl. Phys. Letts. 13, (1968), pp. 335-337.

70. K. B. Eisenthal, Accounts of Chem. Res., 8, (1975), pp. 118-124.

71. I. B. Berlman, 'Handbook of Fluorescence Spectra of Aromatic Molecules', Academic Press, New York, (1965).

72. H. J. Bernstein, Paper presented at the 1973 Spring Meeting of the Optical Society of America, New York, N. Y., April 11-13.

73. H. P. Rosen, P. Robrish and O. Chamberlain, 'Feasibility of the Remote Detection of Pollutants Using Resonance Raman Scattering', Lawrence Berkeley Lab., Energy and Environment Div., U. C. Berkeley, California, (1975).

74. P. Bied-Charreton, C. R. Acad. Sci., Paris, 268, (1969), pp. 1377-1380.

75. C. E. Moeller, C. M. Verber and A. H. Adelman, Appl. Phys. Letts., 18, (1971), p. 278.

76. T. Urisu and K. Kajiyama, J. Appl. Phys., 47, (1976), p. 3563.

77. S. A. Ahmed, J. S. Gergely and D. A. Infante, J. Chem. Phys., 61, (1974), p. 1584.

78. T. Urisu and K. Kajiyama, J. Appl. Phys., 47, (1976), p. 3559.

79. J. M. Drake, E. M. Tam and R. I. Morse, IEEE J. Quant. Elect. (Correp.), QE-8, (1972), pp. 92-94.

80. W. W. Morey, IEEE J. Quant. Elect. (Corresp.), QE-8, (1972), pp. 818-819.

81. D. D. Whawalkar and L. Pandit, IEEE J. Quant Elect. (Corresp.), QE-9, (1973), pp. 43-46.

82. C. Lin and A. Dienes, J. Appl. Phys., 44, (1973), p. 5050.

83. F. B. Dunning and E. D. Stokes, Opt. Comm., 6, (1972), p.160.

84. E. D. Stokes, F. B. Dunning, R. F. Stebbings, G. K. walters and R. D. Rundel, Opt. Comm., 5, (1972), p. 267.

85. R. C. Hilborn and H. C. Brayman, J. Appl. Phys., 45, (1974), p. 4912.

86. A. Dienes and M. Madden, J. Appl. Phys., 44, (1973) p. 4161.

87. C. V. Shank A. Dienes and W.T. Silfvast, Appl. Phys. Letts., 17, (1970), p. 307.

88. O. G. Peterson and B. B. Snavely, Bull. Am. Phys. Soc., 13, (1968), p. 397.

89. J. B. Marling, D. W. Gregg and S. J. Thomas, IEEE J. Quant. Elect., QE-6, (1970).

90. J. B. Birks, 'Photophysics of Aromatic Molecules', edited by J. B. Birks (Wiley-Interscience, New York, 1970).

91. F. Wilkinson, 'Advances in Photochemistry', edited by W. A. Noyes, Jr., G. S. Hammond and J. N. Pitts, Jr. (Interscience, New York, 1964), Vol. III.

92. I. B. Berlman, 'Energy Transfer Parameters of Aromatic Molecules', Academic Press, New York, (1973).

93. Th. Forster, 'Light and Organic Crystals', Modern Quantum Chemistry, Sinanoglu, editor, Academic Press, (1965); Th. Forster, Ann. Phys., 2, (1948), p. 55; Z. Naturforsh, A 4, (1949), p. 32.

94. G. S. Beddard, S.E. Carlin and G. Porter, Chem. Phys. Letts., 43, (1976), pp. 27-32.

95. T. D. Wilkerson, B. Ercoli and F. S. Tomkins, 'Absorption Spectra of Atmospheric Gases', Tech. Note BN-784, Institute for Fluid Dynamics and Applied Mathematics, Feb., (1974).

TECHNICAL REPORT DATA
(Please read Instructions on the reverse before completing)

1. REPORT NO. EPA-600/2-80-049	2.	3. RECIPIENT'S ACCESSION NO.
4. TITLE AND SUBTITLE REMOTE MONITORING OF GASEOUS POLLUTANTS BY DIFFERENTIAL ABSORPTION LASER TECHNIQUES		5. REPORT DATE February 1980
		6. PERFORMING ORGANIZATION CODE
7. AUTHOR(S) S. A. Ahmed, J. S. Gergeley, and F. Barone		8. PERFORMING ORGANIZATION REPORT NO.
9. PERFORMING ORGANIZATION NAME AND ADDRESS Electrical Engineering Department The City College of the City University 140th Street and Convent Avenue New York, N. Y. 10031		10. PROGRAM ELEMENT NO. 1AD712 BA-041
		11. CONTRACT/GRANT NO. 803109
12. SPONSORING AGENCY NAME AND ADDRESS Environmental Sciences Research Laboratory - RTP, NC Office of Research and Development U. S. Environmental Protection Agency Research Triangle Park, N. C. 27711		13. TYPE OF REPORT AND PERIOD COVERED Final 6/74-6/78
		14. SPONSORING AGENCY CODE EPA/600/09

15. SUPPLEMENTARY NOTES

16. ABSTRACT

A single-ended laser radar (LIDAR) system was designed, built, and successfully operated to measure range-resolved concentrations of NO_2, SO_2, and O_3 in the atmosphere using a Differential Absorption of Scattered Energy (DASE) LIDAR technique. The system used a flash-lamp pumped dye laser as the primary source of laser energy. For the NO_2 measurements, the dye laser output was used directly in a novel simultaneous two wavelength output mode in which two wavelengths, one on and one off the resonance absorption of NO_2 molecules are transmitted simultaneously and the relative attenuation determined for the two backscattered signals detected. This mode of operation effectively reduces errors due to scintillation and aerosol drift. For the SO_2 and O_3 measurements, it was necessary to frequency double the output of the dye laser to match the absorption spectra of the SO_2 and O_3 molecules. Field measurements, which were carried out over the Upper East Side of Manhattan for all three pollutants, produced range-resolved concentrations at ranges of over two kilometers. The ambient pollutant concentrations measured ranged from 0.04 ppm to 0.31 ppm, depending on location and time of day. In general, these showed reasonably good correlation with measurements obtained from conventional pollution monitoring stations in the area and demonstrated the potential of DASE LIDAR systems for range-resolved ambient pollutant measurements.

17.	KEY WORDS AND DOCUMENT ANALYSIS	
a. DESCRIPTORS	b. IDENTIFIERS/OPEN ENDED TERMS	c. COSATI Field/Group
*Air pollution Nitrogen dioxide Sulfur dioxide Ozone *Remote sensing *Optical radar Development		13B 07B 14B 17H

18. DISTRIBUTION STATEMENT RELEASE TO PUBLIC	19. SECURITY CLASS (This Report) UNCLASSIFIED	21. NO. OF PAGES 226
	20. SECURITY CLASS (This page) UNCLASSIFIED	22. PRICE

EPA Form 2220-1 (9-73)